Time-Resolved Kerr Microscopy of Spin Waves Propagating in Magnetic Nanostructures

Dissertation

zur Erlangung des Doktorgrades
der Naturwissenschaften (Dr. rer. nat.)
der Fakultät für Physik
der Universität Regensburg

vorgelegt von

Helmut Sebastian Körner

aus Heilbronn

im Jahre 2017

Promotionsgesuch eingereicht am: 27.10.2017
Die Arbeit wurde angeleitet von: Prof. Dr. Christian Back

Prüfungsausschuss:	Vorsitzender:	Prof. Dr. Vladimir Braun
	1. Gutachter:	Prof. Dr. Christian Back
	2. Gutachter:	Prof. Dr. Christian Schüller
	weiterer Prüfer:	Prof. Dr. Dieter Weiss

Das Promotionskolloquium fand am 11.05.2018 statt.

Contents

Introduction

Spin waves (SWs)—and the associated bosonic quanta, the magnons—are collective spin excitations in a magnetically ordered system. SW studies have a successful history of more than 60 years [1, 2]. In the past 10–15 years, the interest in SWs experienced a renaissance under the name of "magnonics" [3, 4] driven by four major factors:

(i) the rapid advance in nanofabrication technology,

(ii) the availability of a variety of experimental techniques—e.g., time-resolved magneto-optical Kerr microscopy (TRMOKE) [5–7], Brillouin light scattering (BLS) [8–10], propagating spin wave spectroscopy (PSWS) [11–13] and scanning transmission X-ray microscopy (STXM) [14, 15]—which provide the required temporal, frequency, field, and/or spatial resolution to investigate high frequency magnetization dynamics in magnetic nanostructures,

(iii) the discovery of different physical phenomena such as the spin-transfer torque (STT) [16–18]—arising upon the interaction of a spin-polarized current with a noncollinear spin texture—as well as the spin Hall effect (SHE) [19–24] and the Dzyaloshinskii-Moriya interaction (DMI) [25, 26]—both originating from spin-orbit coupling (SOC)—and,

finally, from the application point of view,

(iv) the need for an alternative to the complementary metal-oxide semiconductor (CMOS) technology due to its fundamental limitations [27–31].

In the latter context, SWs are considered as potential data carriers in future computing devices, as they provide a variety of very interesting and promising features, including, for instance, wavelengths in the range from micrometers down to nanometers, frequencies, which are in the GHz frequency range used nowadays for applications in telecommunication systems and radars [32, 33], and which can even reach into the very promising low-THz range [34–36], Joule-heat-free transport of spin information [37] over macroscopic distances [38, 39], and, due to their wave nature and their abundant nonlinear properties, access to new and more efficient concepts for data processing, novel wave-based computing technologies, and logic circuits based on wave interference and nonlinear wave interaction [40–42].

Propagating SWs are characterized by their dispersion—the relation of the SW wave vector to its frequency—and their attenuation length—the propagation distance over which the SW amplitude decays to a factor $1/e$ due to the inherent magnetic damping. These two quantities crucially depend on the properties of the magnetic material, and can be tailored for instance by the magnitude of an external magnetic field, the magnetization direction, and the geometry and thickness of the magnetic structures [2]. In addition, the excitation of propagating SWs as well as the SW propagation characteristics and direction can be controlled by a variety of physical effects [7, 38, 43–47].
Moreover, as propagating SWs are the fundamental excitations in a magnetically ordered material, they are also regarded as an excellent experimental model system and sensitive tool to quantify those fundamental parameters, which govern and modify magnetization dynamics in different kinds of magnetic systems, including,

(i) the intrinsic Gilbert damping parameter α,

(ii) the spin polarization P and the nonadiabatic parameter β [11, 48, 49], which determine the strength of the adiabatic and nonadiabatic STT, respectively,

(iii) the spin Hall angle θ_{SH} [13, 50, 51], which is a measure for the efficiency of the conversion of an electric current into a spin current resulting from the SHE, and

(iv) the DMI constant D [52, 53], which quantifies the strength of an interfacial DMI arising in a magnetic system with broken inversion symmetry.

Since each parameter specifies the magnitude of a specific physical mechanism or phenomenon that affects the SW propagation in a special way, which, in turn, is reflected in the SW dispersion and/or the SW attenuation length, their values can be assessed by studying the characteristics of propagating SWs in detail.

Quantifying all these parameters precisely is not only of great interest to magnonics, but also to the research field of "spintronics" [54, 55], where the key concept is the simultaneous exploitation of the charge and spin degree of freedom of the electron for additional and novel functionality in future logic [56] and memory devices such as the STT-magnetic random access memory (MRAM) [57, 58], or the racetrack memory [59, 60], where either the bulk STTs or a combination of SHE-STT and DMI can be exploited for operation [61–63].

Within the framework of this thesis, on various kinds of magnetic nanostructures, in total, four different SW propagation experiments are performed.
Three of them focus on the determination of the values of the fundamental parameters governing magnetization dynamics in different kinds of magnetic materials and systems. This is achieved by studying in detail the impact of the underlying physical mechanism or phenomenon on the characteristics of the propagating SWs in combination with other sample characterization techniques and/or micromagnetic simulations.

The fourth one deals with the exploration of a novel excitation approach for the spatial addressing of propagating SWs in a plain magnetic film. For this purpose, real-space images of the propagating SWs are acquired to reveal how the SW excitation and propagation characteristics can be tailored.

This thesis is organized as follows:

The theoretical background to the different SW propagation experiments is covered in Ch. 1. It addresses the different magnetic energies, the equations of motion of field- and current-induced magnetization dynamics, and the characteristics of propagating (Damon-Eshbach[1]) SWs—dispersion and attenuation length. The influence of a spin-polarized electric current or an interfacial DMI on the SW characteristics is also discussed in detail. Moreover, the impact of lateral confinement and the excitation of propagating (Damon-Eshbach) SWs by microwave antennas are considered. This chapter closes with the theoretical description of the magneto-optical Kerr effect.

Ch. 2 deals with the experimental technique used for the investigation of the SW dynamics and characteristics in the magnetic nanostructures—TRMOKE—especially with the components of the setup and its modes of operation.

In Ch. 3–6, the results of the individual SW propagation experiments are presented. Each of these four chapters is structured as follows:
First, the motivation for the respective experiment is presented and the goals of the experiment are elucidated. Then, the preparation and characterization of the magnetic nanostructures is addressed. Subsequently, the implementation of the experiment is explained prior to the presentation, analysis and discussion of the experimental findings. If micromagnetic simulations needed to be performed to confirm and/or check the experimental observations, their implementation and results are discussed afterwards. At the end of each chapter, a conclusion is drawn.
In detail, Ch. 3–6 deal with the following SW propagation experiments:

In Ch. 3, the key STT parameters for $Ni_{80}Fe_{20}$ are determined by investigating in detail the changes in the characteristics of propagating Damon-Eshbach SWs resulting upon the interaction with a spin-polarized electric current.

In Ch. 4, the presence of an interfacial DMI at the Pt/Co interface in thin Pt/Co/Py/MgO stripes is evidenced and quantified by studying the characteristics of counterpropagating Damon-Eshbach SWs.

In Ch. 5, the magnetic damping in the poly-crystalline grown binary $3d$ transition metal alloy $Co_{25}Fe_{75}$ is quantified by in-plane ferromagnetic resonance measurements on a $Co_{25}Fe_{75}$ full film as well as by studying the propagation of Damon-Eshbach SWs in micrometer-wide $Co_{25}Fe_{75}$ stripes, where the attenuation length is the figure of merit.

[1] The Damon-Eshbach geometry is one of the three different geometries for propagating SWs [2], and it is the one, in which the different SW propagation experiments are performed.

In Ch. 6, it is demonstrated that it is possible to locally excite, tailor and steer multiple diffractive SW beams in a $Ni_{80}Fe_{20}$ full film using specially shaped non-uniform microwave antennas.

This thesis concludes with a summary. Additional information are provided in the Appendices A and B.

Chapter 1

Theoretical Background

Contents

In this chapter, the theoretical background for this thesis is provided. First, in Sec. 1.1 and 1.2, the micromagnetic description and the relevant magnetic energy terms are discussed. Then, in Sec. 1.3, the equations of motion are introduced, which describe field-induced and current-induced magnetization dynamics.

The main focus of this chapter is addressed in Sec. 1.4: SWs, in particular, Damon-Eshbach (DE) SWs. In Subsec. 1.4.1, the derivation of expressions for the characteristics of DE SWs—dispersion and attenuation length—is presented. In Subsec. 1.4.2 a peculiarity of propagating DE SWs—the nonreciprocity—is explained. Subsequent, the modifications in the characteristics of the DE SWs are discussed resulting from their interaction with a spin-polarized electric current [cf. Subsec. 1.4.3] or when they propagate in the presence of an interfacial Dzyaloshinskii-Moriya interaction (DMI) [cf. Subsec. 1.4.4]. Subsec. 1.4.5 deals with the excitation of these SWs using microwave antennas and the characteristic features of the excitation process. In Subsec. 1.4.6, it is elucidated how the characteristics of DE SWs are affected by lateral confinement and SW mode coupling affect, which occur when they propagate in magnetic stripes of finite width instead of plain magnetic films.

Finally, in Sec. 1.5, the origin and characteristics of the magneto-optical Kerr effect (MOKE) are explained.

1.1 Micromagnetic Description

In large systems, the number of spins is on the order of the number of atoms. To enable a convenient description of this system, Brown suggested a model, in which the individual spins $\vec{S}_i$ are replaced by a classical continuous magnetic vector field $\vec{M}(\vec{r})$ [64]. This micromagnetic approximation can be regarded as a transition from the sum over single spins to an integral over the continuous magnetization, which is valid if

- the system size is much larger than the atomic distances.
- quantum effects do not play a role so that $\vec{M}$ can be regarded as a classical vector.
- the temperature is much lower than the Curie temperature[2] so that $|\vec{M}|$ is identical with the saturation magnetization M_S.

1.2 Magnetic Energies

In the following, first, the various magnetic energies occurring in a magnetic system are discussed [cf. Sec. 1.2.1–1.2.4]. These energies are the basis for the derivation of Brown's equations of static equilibrium [cf. Sec 1.2.5].

[2] In case of the common $3d$ ferromagnets—Fe, Co and Ni—the respective Curie temperatures—1043 K, 1394 K and 631 K [65]—are much higher than room temperature.

1.2.1 Exchange Interaction

Magnetic exchange is the origin of (long-range) magnetic ordering. It cannot be explained classically. Its quantum-mechanical origin—the combination of Coulomb interaction and the Pauli principle—is discussed in terms of a simple model, where two electrons are located on lattice sites i and j with spins $\vec{S}_i$ and $\vec{S}_j$. The joint state of both electrons is described by an overall wavefunction—consisting of a spatial and a spin part—which needs to be anti-symmetric as electrons are fermionic particles. This condition implies a spin-dependent term in the corresponding "effective" Hamiltonian of the system, which can be written as [65]

$$\mathcal{H} = -2J_{ij} \cdot \vec{S}_i \cdot \vec{S}_j \tag{1.1}$$

with the exchange integral J_{ij}. Generalizing Eq. (1.1) to a many-body system yields the Hamiltonian of the Heisenberg model [65]:

$$\mathcal{H} = -2 \sum_{i>j} J_{ij} \cdot \vec{S}_i \cdot \vec{S}_j \,. \tag{1.2}$$

In this model, it is often possible to take J_{ij} to be equal to J for nearest neighbor spins and to be 0 otherwise. If $J < 0$, the (neighboring) spins favor an anti-parallel alignment with respect to each other, i.e., an anti-ferromagnetic order—$\ldots\uparrow\downarrow\uparrow\downarrow\uparrow\downarrow\uparrow\ldots$—while, if $J > 0$, the (neighboring) spins favor a parallel alignment, i.e., a ferromagnetic order—$\ldots\uparrow\uparrow\uparrow\uparrow\uparrow\uparrow\uparrow\ldots$. In the latter case, deviations from this perfectly ordered state cost exchange energy. In the continuum limit, it is given by [64–67]

$$E_{\text{ex}} = \int_V \mathrm{d}V \varepsilon_{\text{ex}} \tag{1.3a}$$

$$\text{with} \qquad \varepsilon_{\text{ex}} = \frac{A}{M_{\text{S}}^2} \left[\left(\vec{\nabla} M_x \left(\vec{r} \right) \right)^2 + \left(\vec{\nabla} M_y \left(\vec{r} \right) \right)^2 + \left(\vec{\nabla} M_z \left(\vec{r} \right) \right)^2 \right] , \tag{1.3b}$$

where ε_{ex} is the corresponding energy density. A is the exchange stiffness constant, which is proportional to the exchange integral J and a material-dependent quantity. The exchange energy is minimal in case of a homogeneous magnetization configuration.

1.2.2 Dzyaloshinskii-Moriya Interaction

Interatomic exchange—as described by the Hamiltonian of the Heisenberg exchange interaction [cf. Eq. (1.2)]—is usually symmetric in that the consequences of rotating the magnetization one way or the reverse are equivalent, i.e., it is isotropic. However, this symmetry is lost when the system is subjected to spin-orbit coupling (SOC) and exhibits a broken inversion symmetry. The resulting anti-symmetric component of the magnetic exchange interaction is referred to as Dzyaloshinskii-Moriya interaction (DMI) [25, 26]. The DMI between two atomic spins $\vec{S}_i$ and $\vec{S}_j$ is given by

$$\mathcal{H}_{\text{DMI}} = -\vec{D}_{ij} \cdot \left(\vec{S}_i \times \vec{S}_j \right) , \tag{1.4}$$

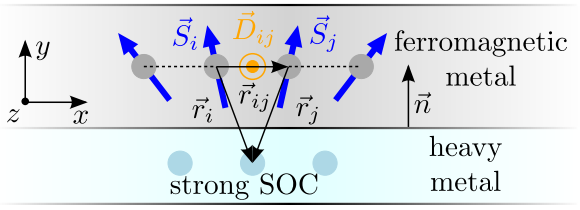

Figure 1.1. Schematic of a bilayer system consisting of a ferromagnetic metal layer on top of a nonmagnetic heavy metal layer with strong SOC. An interfacial DMI arises at the interface between both layers due to the broken inversion symmetry of the system along the y direction. The blue arrows indicate the local orientation of the spins $\vec{S}$ while the orange arrow marks the orientation of the DMI vector $\vec{D}_{ij}$ between the spins $\vec{S}_i$ and $\vec{S}_j$ [cf. Eq. (1.5)].

where $\vec{D}_{ij}$ is the DMI vector, which is perpendicular to both the asymmetry direction and the vector $\vec{r}_{ij}$ between the spins $\vec{S}_i$ and $\vec{S}_j$, and which scales with the DMI constant D. According to Eq. (1.4), the DMI energetically favors a nonhomogeneous spin configuration with a certain chirality[3] of the neighboring spins, thereby giving rise to chiral magnetic orders such as spin spirals and skyrmions [68–75].

The type of inversion symmetry breaking specifies the type of DMI [76]: A bulk DMI arises due to a lack of inversion symmetry in the lattice[4]. In this case, $\vec{D}_{ij}$ depends on the detailed symmetry of the lattice structure, and, for any in-plane direction $\vec{r}$, $\vec{D}(\vec{r}) \parallel \vec{r}$ applies. An interfacial DMI emerges from a lack of inversion symmetry at surfaces and interfaces. It can be particularly strong at the interface between a ferromagnet and a nonmagnetic heavy metal having a strong SOC [77]. In that case, the interfacial DMI can be modeled by a three-site indirect exchange mechanism, where two neighboring atomic spins $\vec{S}_i$ and $\vec{S}_j$ in the ferromagnetic layer interact with an adjacent atom in the heavy metal layer with the strong SOC [78] as sketched in Fig. 1.1. The corresponding DMI vector is given by [79, 80]

$$\vec{D}_{ij} = D \cdot (\vec{r}_{ij} \times \vec{n}) \ , \tag{1.5}$$

where $\vec{n}$ is the vector normal to the interface between the ferromagnetic and the nonmagnetic layer. $\vec{D}_{ij}$ points parallel to the interface [cf. Fig. 1.1].

The consequences of the presence of an interfacial DMI can only be observed in ultrathin/very thin ferromagnetic layers of thickness d since it is an interface effect, which scales with $1/d$. Moreover, in any trilayer structure, in which a very thin ferromagnetic layer is sandwiched between two nonmagnetic ones, where one of them exhibits a strong SOC while it is concurrently different from the other one, a net interfacial DMI occurs since the interfacial DMI originating at one interface is not fully compensated by the interfacial DMI arising at the other interface[5].

[3] The phrase "chirality" denotes the peculiarity that a certain handedness is preferred. If left- or right-handed is specified by the sign of D.

[4] The bulk DMI has been studied mostly for B20 structures such as MnSi [70], FeCoSi [69, 72], and FeGe [73, 75].

[5] When the ultrathin ferromagnetic films are prepared by sputtering, they consist of small grains exhibiting different lattice orientations, and therefore the contributions due to the bulk DMI tend to cancel, while the ones due to the interfacial DMI remain.

In the continuum approximation, for the geometry shown in Fig. 1.1, i.e., in case of a magnetic layer which is isotropic within the xz plane, the energy density of the interfacial DMI arising due to the inversion symmetry breaking along the y direction is given by [52, 81]

$$\varepsilon_{\mathrm{DMI}} = \frac{D}{M_{\mathrm{S}}^2}\left[M_y \mathrm{div}\vec{M} - \left(\vec{M}\cdot\vec{\nabla}\right)M_y\right] . \tag{1.6}$$

1.2.3 Zeeman Energy

The energy of a magnetic system in an external magnetic field $\vec{H}_0$ is given by the Zeeman energy. In the continuum limit, it is expressed by [66]

$$E_{\mathrm{Zeeman}} = \int_V \mathrm{d}V \varepsilon_{\mathrm{Zeeman}} \tag{1.7a}$$

$$\text{with} \qquad \varepsilon_{\mathrm{Zeeman}} = -\mu_0 \vec{M}\left(\vec{r}\right)\cdot\vec{H}_0\left(\vec{r}\right) , \tag{1.7b}$$

where $\varepsilon_{\mathrm{Zeeman}}$ is the corresponding energy density and $\mu_0 = 4\pi \times 10^{-7}\,\mathrm{A/m^2}$ is the vacuum permeability.

1.2.4 Magnetic Anisotropy Energies

The Hamiltonian of the Heisenberg model [cf. Eq. (1.2)] applies to an isotropic magnetic system, where the energy of the system depends only on the relative alignment of the individual spins, but the absolute directions do not play any role. Magnetic anisotropy expresses the peculiarity that the energy of a magnetic system depends on the (absolute) orientation of the magnetization with respect to certain specified directions of the system, which are determined both by intrinsic and extrinsic properties. There are different types of magnetic anisotropy. In the following, the focus is on the origin and characteristics of the magneto-crystalline anisotropy, the surface anisotropy, and the shape anisotropy.

Magneto-Crystalline Anisotropy

The origin of the magneto-crystalline anisotropy is the SOC: The electron orbits are linked to the crystallographic structure, and by their interaction with the electron spins they compel the spins to align along well-defined crystallographic axes. For this reason, there are specified directions in space along which it is easier to magnetize a given single crystalline system compared with other directions. The difference can be expressed as direction-dependent energy term. In general, it is given by [82]

$$E_{\mathrm{ani}} = \int_V \mathrm{d}V \varepsilon_{\mathrm{ani}} , \tag{1.8}$$

where the energy density $\varepsilon_{\mathrm{ani}}$ is approximated by a power series expansion in the direction cosines[6] α_i between the magnetization direction $\vec{M}$ and the respective crystallographic axes of high symmetry:

$$\varepsilon_{\mathrm{ani}} = \varepsilon_0 + \sum_{ij}\overline{\overline{b_{ij}}}\cdot\alpha_i\alpha_j + \sum_{ijkl}\overline{\overline{b_{ijkl}}}\cdot\alpha_i\alpha_j\alpha_k\alpha_l + \ldots . \tag{1.9}$$

[6] $\alpha_i = M_i/|\vec{M}| = M_i/M_{\mathrm{S}}$.

ε_0 is a constant and $\overline{\overline{b_{ij}}}$ and $\overline{\overline{b_{ijkl}}}$ are tensors of 2$^{\text{nd}}$ and 4$^{\text{th}}$ order, respectively. Due to the time inversion symmetry—which requires that the energy of the system does not change when the magnetization direction is reversed, i.e., $E_{\text{ani}}\left(\vec{M}\right) = E_{\text{ani}}\left(-\vec{M}\right)$—only even terms in α_i occur in Eq. (1.9). Furthermore, the magneto-crystalline anisotropy energy (density) needs to exhibit the symmetry properties of the crystal lattice.

In a crystalline system with one single axis of high symmetry, the magneto-crystalline anisotropy is referred to as a uniaxial magneto-crystalline anisotropy. For instance, when the y axis is considered to be the main symmetry axis of the crystal, the corresponding energy density up to the 4$^{\text{th}}$ order derived from Eq. (1.9) can be written as [82]

$$\varepsilon_{\text{ani}}^{\text{u}} = \underbrace{K_0}_{\text{constant}} - K_1^{(2)}\alpha_2^2 + K_2^{(4)}\alpha_2^4 + \dots , \tag{1.10}$$

where K_1 and K_2 are temperature-dependent anisotropy constants and α_2 is the direction cosine to the y axis. If K_1 is positive and if higher order terms are neglected, the magneto-crystalline anisotropy energy becomes minimal along the y axis. Hence, the magnetization favors to be aligned parallel to this axis, and therefore this axis is referred to as an easy axis. In contrast, if K_1 is negative and if higher order terms are neglected, the y direction is a hard axis. In this case, the magnetization prefers to be aligned at any direction within the easy xz plane, thereby minimizing the magneto-crystalline anisotropy energy.

In case of a crystalline system with cubic symmetry, the corresponding cubic magneto-crystalline anisotropy energy density up to the 6$^{\text{th}}$ order can be written as [82]

$$\varepsilon_{\text{ani}}^{\text{c}} = \underbrace{K_0}_{\text{constant}} + K_1^{(4)}\left(\alpha_1^2\alpha_2^2 + \alpha_2^2\alpha_3^2 + \alpha_1^2\alpha_3^2\right) + K_2^{(6)}\alpha_1^2\alpha_2^2\alpha_3^2 + \dots . \tag{1.11}$$

If K_1 is positive and if higher order terms are neglected once again, the magnetization favors an alignment along one of three main axes. If K_1 is negative and if higher order terms are neglected, the energetically favorable axes are oriented along $\langle 111 \rangle$ directions between the three main axes.

Surface Anisotropy

There are several contributions to this term. Following Néel the most important one arises due to a reduced symmetry at the surface of a ferromagnet: The spins at the surface have one nearest neighbor on one side, but none on the other. Consequently, the exchange interaction cannot be the same as in the bulk. A reduced symmetry is also present at the interface between a nonmagnetic metal and a ferromagnetic one or at the interface between two different ferromagnets. A reduction in symmetry implies that anisotropy terms of lower order [cf. Eq. (1.9)], which are forbidden in the bulk, might be allowed, which, in turn, result in additional contributions to the magnetic anisotropy energy. In most cases, for the description of a surface anisotropy, the 2$^{\text{nd}}$ order terms are sufficient as they contribute the most for all crystal structures. The corresponding

surface anisotropy energy density can be written as[7] [65]

$$\varepsilon_{\text{ani}}^{\text{surf}} = \frac{2k^{\text{surf}}}{d} \cdot \sin^2(\theta) = K_1^{\text{surf}} \cdot \sin^2(\theta) \,, \tag{1.12}$$

where θ is the angle between $\vec{M}$ and the surface normal of the magnetic layer, k^{surf} and K_1^{surf} are surface anisotropy constants in units of J/m^2 and J/m^3, respectively, and d is the thickness of the magnetic layer. For $\theta = 0°$, the system exhibits a perpendicular magnetic anisotropy (PMA)[8]. Since $\varepsilon_{\text{ani}}^{\text{surf}}$ scales with $1/d$, the surface anisotropy diverges for $d \to 0$, is dominant for very thin magnetic layers on the order of a few nanometers, and does not play a significant role in the case of thick layers, where the bulk magneto-crystalline anisotropy becomes dominant instead.

The combination of the bulk magneto-crystalline anisotropy and the magnetic surface anisotropy enables to define an effective magnetic anisotropy constant K_{eff} [65]:

$$K_{\text{eff}} := K_1^{\text{bulk}} + K_1^{\text{surf}} = K_1^{\text{bulk}} + \frac{2k^{\text{surf}}}{d} \,. \tag{1.13}$$

Shape Anisotropy

When the magnetization $\vec{M}$ inside a ferromagnetic medium meets the surface, it has to suddenly stop. Hence, there is a divergence of $\vec{M}$. Considering first the case where no external magnetic field $\vec{H}_0$ is applied, the magnetic induction is given by $\vec{B} = \mu_0 \left(\vec{M} + \vec{H}\right)$. Then, the Maxwell equation $\vec{\nabla}\vec{B} = 0$ yields

$$\vec{\nabla}\vec{H} = -\vec{\nabla}\vec{M} \,, \tag{1.14}$$

i.e., there is an equal, but opposite divergence of $\vec{H}$. The situation is as if magnetic charges are present inside the magnetic medium—denoted as magnetic volume charges—as well as on its surface(s)—which are called magnetic surface charges—as depicted in the schematic shown in Fig. 1.2. It is obvious that, overall, the magnetic volume charges cancel while the magnetic surface charges remain[9]. The latter ones are the source/sink of $\vec{M}$ thereby acting as the source of $\vec{H}$ [cf. Eq. (1.14)]. The resulting $\vec{H}$-field is referred to as demagnetizing

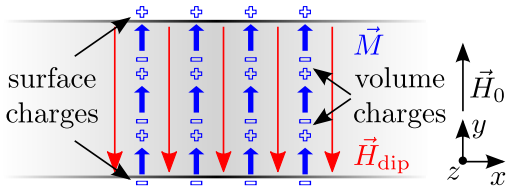

Figure 1.2. *H* Schematic of the origin of the demagnetization field.

[7] The factor 2 in Eq. (1.12) is included as the layer contains two surfaces.

[8] A very thin Co/Pt bilayer, for instance, exhibits a strong PMA, which arises due to the hybridization between the 3*d* electrons of the Co and the 5*d* electrons of the Pt at the Pt/Co interface [83].

[9] The magnetic surfaces charges act as positive and negative magnetic quasi-charges, which never appear isolated, but are always compensated by opposite charges [cf. Fig. 1.2].

field[10] $\vec{H}_{\mathrm{dip}}$. The term "demagnetizing field" expresses the fact that this field is oriented opposite to $\vec{M}$ [cf. Fig. 1.2]. Consequently, in the case where a magnetic bias field $\vec{H}_0$ is applied to the ferromagnetic medium, the total magnetic field inside the magnetic medium—referred to as internal magnetic field $\vec{H}_{\mathrm{i}}$—is given by $\vec{H}_0$ being reduced by the demagnetizing field[11].
In general, the demagnetizing field $\vec{H}_{\mathrm{dip}}$ can be calculated by [82]

$$\vec{H}_{\mathrm{dip}} = \int_V \mathrm{d}V \frac{(\vec{r}-\vec{r}\,')}{|\vec{r}-\vec{r}\,'|^3}\rho\,(\vec{r}\,') - \int_S \mathrm{d}S \frac{(\vec{r}-\vec{r}\,')}{|\vec{r}-\vec{r}\,'|^3}\sigma\,(\vec{r}\,')\ . \tag{1.15}$$

The first integral in Eq. (1.15) covers the magnetic volume charges $\rho = -\vec{\nabla}\vec{M}$ inside the volume V of the magnetic medium, while the second integral covers the magnetic surface charges $\sigma = \vec{n}\cdot\vec{M}$ on the surface S of the magnetic medium. In most cases, however, it is extremely complicated to calculate $\vec{H}_{\mathrm{dip}}$.
Alternatively to Eq. (1.15), $\vec{H}_{\mathrm{dip}}$ can be expressed by the demagnetizing tensor $\overline{\overline{N}}$ as

$$\vec{H}_{\mathrm{dip}} = -\overline{\overline{N}}\vec{M} \qquad \text{with} \qquad \begin{pmatrix} N_{xx} & N_{xy} & N_{xz} \\ N_{yx} & N_{yy} & N_{yz} \\ N_{zx} & N_{zy} & N_{zz} \end{pmatrix}, \tag{1.16}$$

where $\mathrm{tr}\left(\overline{\overline{N}}\right) = 1$. In this case, the difficulty is to calculate the quantities N_{ij}.

In the continuum limit, the energy arising due to the demagnetizing field is given by [65]

$$E_{\mathrm{dip}} = \int_V \mathrm{d}V \varepsilon_{\mathrm{dip}} \tag{1.17a}$$

$$\text{with} \qquad \varepsilon_{\mathrm{dip}} = -\frac{1}{2}\mu_0 \vec{M}\,(\vec{r}\,)\cdot\vec{H}_{\mathrm{dip}}\,(\vec{r}\,)\ , \tag{1.17b}$$

where $\varepsilon_{\mathrm{dip}}$ is the corresponding energy density of the demagnetizing field[12]. Alternatively, using Eq. (1.14), E_{dip} and $\varepsilon_{\mathrm{dip}}$ can also be written as[13]

$$E'_{\mathrm{dip}} = \int \mathrm{d}V \varepsilon'_{\mathrm{dip}} \tag{1.18a}$$

$$\text{with} \qquad \varepsilon'_{\mathrm{dip}} = \frac{1}{2}\mu_0 \vec{H}^2_{\mathrm{dip}}\,(\vec{r}\,)\,. \tag{1.18b}$$

Eq. (1.18b) implies that the magnetic stray field energy is always positive. As a consequence, the magnetic system tries to minimize it by limiting the stray fields to the sample volume. For this reason, this energy depends crucially on the shape

[10] The label "dip" denotes that the microscopic origin of the demagnetizing field is the weak but long-range dipole-dipole interaction: Every single magnetic moment interacts with the dipolar field generated by all other magnetic moments in the magnetic medium.

[11] The demagnetizing field is a space-dependent quantity, i.e., $\vec{H}_{\mathrm{dip}} = \vec{H}_{\mathrm{dip}}\,(\vec{r}\,)$, and thereby $\vec{H}_{\mathrm{i}}$ as well.

[12] The factor 1/2 needs to be included to avoid double counting of each volume element since the local magnetization itself also appears as a field source.

[13] In comparison to Eq. (1.17b), the integral in Eq. (1.18b) is not limited to the magnetic sample volume V anymore, but covers the whole space instead.

and dimensions of the magnetic sample as they specify certain "anisotropy" axes along which the magnetization favors to be aligned so that the magnetic stray field energy is minimal. Due to its shape dependence the magnetic stray field energy is also called "shape anisotropy". In general, a configuration, where the magnetization is aligned parallel to the sample boundaries, is energetically more favorable. Such a state can only be formed by an inhomogeneous magnetization configuration inside the magnetic sample which results in the formation of magnetic domains [65, 66].

1.2.5 Brown's Equations of Static Equilibrium

The total free energy density $\varepsilon_{\text{total}}$ at constant temperature is given by the sum of the various energy densities discussed above:

$$\varepsilon_{\text{total}} = \varepsilon_{\text{ex}} + \varepsilon_{\text{Zeeman}} + \varepsilon_{\text{ani}} + \varepsilon_{\text{dip}} \,. \tag{1.19}$$

It is minimized by the equilibrium magnetization distribution(s) $\vec{M}_{\text{eq}}(\vec{r})$. Thus, the variation of $\varepsilon_{\text{total}}$ with respect to the direction cosines α_i needs to vanish, i.e.,

$$\partial_{\alpha_i} \varepsilon_{\text{total}} \left(\vec{M}_{\text{eq}} \right) = 0 \,, \forall \alpha_i \,. \tag{1.20}$$

By solving these variational equations Brown derived two equations that enable the determination of $\vec{M}_{\text{eq}}(\vec{r})$ [64, 82]:

$$\vec{M} \times \vec{H}_{\text{eff}} = 0 \tag{1.21a}$$

$$\text{and} \qquad \vec{M} \times \partial_{\vec{n}} \vec{M} = 0 \,. \tag{1.21b}$$

The effective magnetic field $\vec{H}_{\text{eff}}$ in Eq. (1.21a) is given by [67]

$$\begin{aligned} \vec{H}_{\text{eff}} &= -\frac{1}{\mu_0} \frac{\partial \varepsilon_{\text{total}}}{\partial \vec{M}} \\ &= \vec{H}_0 + \frac{2A}{M_{\text{S}}^2} \vec{\nabla}^2 \vec{M} + \vec{H}_{\text{dip}} - \frac{1}{\mu_0} \frac{\partial \varepsilon_{\text{ani}}}{\partial \vec{M}} \,. \end{aligned} \tag{1.22}$$

Eq. (1.21a) has to be fulfilled everywhere inside the magnetic sample and implies a parallel alignment of the magnetization with respect to $\vec{H}_{\text{eff}}$. As indicated by the derivative along the surface normal $\partial_{\vec{n}}$, Eq. (1.21b) applies only to the surface of the magnetic sample. By solving this set of equations, in general, $\vec{M}_{\text{eq}}(\vec{r})$ of any magnetic structure can be determined.

1.3 Magnetization Dynamics—Equations of Motion

The magnetization configuration of a ferromagnetic structure can be manipulated for instance by applying a magnetic bias field or by the injection of a (spin-polarized) electric current. In the following, the underlying physical mechanisms of either method and the resulting equations of motion describing the temporal evolution of the magnetization and the resulting trajectories are discussed.

1.3.1 Field-Induced Magnetization Dynamics[14]

The effective magnetic field $\vec{H}_{\text{eff}}$ [cf. Eq. 1.22] exerts a torque on the magnetization $\vec{M}$ when $\vec{M}$ is not collinear with $\vec{H}_{\text{eff}}$, i.e., in the case where the excursion angle ψ between $\vec{H}_{\text{eff}}$ and is $\vec{M}$ finite. This torque is expressed by[15] [67]

$$\frac{\mathrm{d}\vec{M}}{\mathrm{d}t} = \underbrace{-\gamma\mu_0 \vec{M} \times \vec{H}_{\text{eff}}}_{\text{precession term}} , \tag{1.23}$$

where $\gamma = |\frac{ge}{2m_e}|$ is the gyromagnetic ratio, e and m_e are the charge and the mass of the electron, respectively, and g is the Landé factor. Eq. (1.23) is referred to as the precession term as this torque leads to a precessional motion of $\vec{M}$ around $\vec{H}_{\text{eff}}$ at the angular frequency ω [cf. Fig. 1.3(a)]. However, since $\vec{M} \times \vec{H}_{\text{eff}}$ remains constant, Eq. (1.23) does not comprise a change in energy, and consequently, it is not the appropriate equation of motion to describe the dynamics of a magnetic system on its way to equilibrium.
To account for dissipation associated with a change of energy analogous to mechanical friction, a second torque term—the damping term—is introduced which is proportional to the generalized velocity $\mathrm{d}\vec{M}/\mathrm{d}t$. The resulting equation of motion is called Landau-Lifshitz-Gilbert equation and reads as [84, 85]

$$\frac{\mathrm{d}\vec{M}}{\mathrm{d}t} = \underbrace{-\gamma\mu_0 \vec{M} \times \vec{H}_{\text{eff}}}_{\text{precession term}} + \underbrace{\frac{\alpha}{M_S} \vec{M} \times \frac{\mathrm{d}\vec{M}}{\mathrm{d}t}}_{\text{damping term}} , \tag{1.24}$$

where the strength of the damping is specified by a phenomenological damping parameter α, which is also referred to as Gilbert damping parameter. α specifies

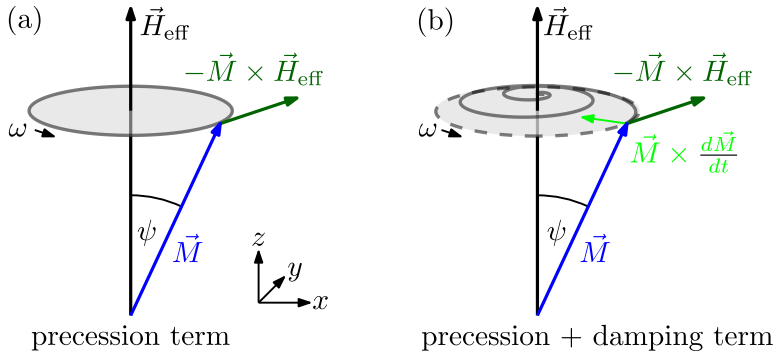

Figure 1.3. Schematic of the trajectory of the magnetization $\vec{M}$—which is deflected by the excursion angle ψ with respect to the direction of the effective magnetic field $\vec{H}_{\text{eff}}$—according to the two torque terms of the LLG equation [cf. Eq. (1.24)]. (a) The precession term describes the precessional motion of $\vec{M}$ around $\vec{H}_{\text{eff}}$ at the angular frequency ω. (b) The damping term itself represents a torque which forces $\vec{M}$ to align parallel to $\vec{H}_{\text{eff}}$. Thus, in combination with the precession term, the overall trajectory of $\vec{M}$ is a damped spiral motion around $\vec{H}_{\text{eff}}$ (assuming that $\vec{H}_{\text{eff}}$ is constant).

[14] For this discussion, $\vec{M} = M_x\vec{e}_x + M_y\vec{e}_y + M_z\vec{e}_z$, where $\vec{e}_x$, $\vec{e}_y$, $\vec{e}_z$ are unit vectors along the coordinate axes, and $\vec{H}_{\text{eff}} \parallel \vec{e}_z$.
[15] This description is valid for any ψ-value.

the intrinsic magnetic damping and is a material-dependent and dimensionless quantity. As illustrated in the schematic shown in Fig. 1.3(b), the damping torque forces $\vec{M}$ to align parallel to $\vec{H}_{\text{eff}}$. Consequently, the overall trajectory of $\vec{M}$ on its way to equilibrium—in case it is deflected from the $\vec{H}_{\text{eff}}$-direction—is a damped spiral motion around $\vec{H}_{\text{eff}}$, where the z component of $\vec{M}$ is continuously increasing while concurrently $|\vec{M}| = M_{\text{S}}$ is fulfilled [cf. Fig. 1.3(b)].

1.3.2 Current-Induced Magnetization Dynamics

When an electric current is injected across a metallic ferromagnetic structure, the spin-polarized conduction electrons[16] can interact with the local magnetization, thereby transferring their spin angular momentum. The resulting torque is referred to as spin-transfer torque (STT)[17]. It was theoretically predicted independently by Berger [17] and Slonczewski [18]. The occurrence of this torque enables the manipulation of the magnetization configuration of a ferromagnetic structure by a (spin-polarized) electric current without the assistance of a magnetic bias field. Hence, this physical mechanism is of particular interest for the realization of spintronic devices [54] such as the racetrack memory suggested by S. Parkin *et al.*, which employs the advantages of the field-free current-induced motion of domain walls (DWs) in narrow nanostripes [59].

As several experimental findings revealed, the spin-transfer cannot be modeled by a single torque term, but needs to be composed of two components [87–89]: the adiabatic STT term and the nonadiabatic STT term. Either torque term is discussed in detail below.

Adiabatic Spin-Transfer Torque

When a spin-polarized electric current flows across an inhomogeneous magnetization texture, the spins of the conduction electrons align with the local magnetization direction. If this process happens adiabatically, the orientation of the electron spin adjusts instantaneously to the (gradual) change(s) in the orientation of the local magnetization as sketched in Fig. 1.4. This re-orientation of the spin direction is associated with a change of angular momentum. As angular momentum is a conserved quantity, this process requires the transfer of angular momentum onto the local magnetization. The resulting torque leads to a rotation of the local magnetization, where the sense of rotation is opposite to the one of the electron spins. This adiabatic STT is expressed by [87, 90–95]

$$\left(\frac{\mathrm{d}\vec{M}}{\mathrm{d}t}\right)^{\text{STT}}_{\text{adiabatic}} = -\left(\vec{u}\cdot\vec{\nabla}\right)\vec{M}\,, \tag{1.25}$$

[16] The electric current is spin-polarized due to spin-dependent diffusive scattering, which arises as, in a ferromagnetic material, due to the exchange splitting, there are different densities of states of spin up and spin down (conduction) electrons at the Fermi energy [65]. In other words, the numbers of spin up and spin down conduction electrons differ.

[17] A profound tutorial to the physics of STTs in magnetic devices can be found in Ref. [86], where an elementary discussion of the mechanism of STT is provided and where the theoretical and experimental progress in this field is reviewed.

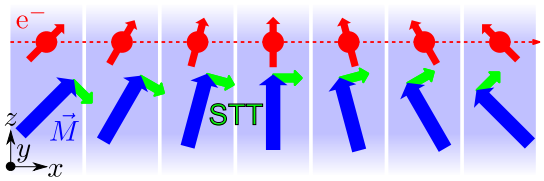

Figure 1.4. Action of a spin-polarized electric current flowing along the x direction across an inhomogeneous magnetization texture. The blue arrows represent the local orientation of the magnetization $\vec{M}$ inside the inhomogeneous magnetization texture. The red arrows on solid red circles denote the local orientation of the spins of the conduction electrons e^- while passing the inhomogeneous magnetization texture. The green arrows indicate the direction of action of the resulting adiabatic STT. In the situation depicted, it leads to a clockwise rotation of $\vec{M}$ while the sense of rotation of the electron spins is counter-clockwise due to the conservation of angular momentum.

where the generalized velocity $\vec{u}$—which is called spin-drift velocity—is a vector directed along the direction of the electron motion. It is given by [95]

$$\vec{u} = \frac{g\mu_\mathrm{B}}{2eM_\mathrm{S}} \cdot P \cdot \vec{j}\,, \tag{1.26}$$

where μ_B is the Bohr magneton, e is the charge of the electron, P is the spin polarization[18] of the electric current, and j is the current density. The magnitude of $\vec{u}$ is given by[19]

$$u = |\vec{u}| = \frac{g\mu_\mathrm{B}}{2|e|M_\mathrm{S}} \cdot P \cdot |\vec{j}|\,. \tag{1.27}$$

The adiabatic STT [cf. Eq. (1.25)] term alone is sufficient to reproduce experimental findings quantitatively—e.g., the characteristics of current-driven DW motion [59]—but it does not reveal a quantitative agreement. For this reason, modifications to the perfect adiabaticity and the pure local spin-transfer have to be to considered, which are modeled by phenomenologically introducing another STT term: the nonadiabatic STT term.

Nonadiabatic Spin-Transfer Torque

The nonadiabatic STT term is given by [95]

$$\left(\frac{\mathrm{d}\vec{M}}{\mathrm{d}t}\right)^{\mathrm{STT}}_{\mathrm{nonadiabatic}} = +\frac{\beta}{M_\mathrm{S}}\vec{M} \times \left[\left(\vec{u}\cdot\vec{\nabla}\right)\vec{M}\right]\,, \tag{1.28}$$

where the dimensionless parameter β is referred to as nonadiabatic parameter. It quantifies the ratio of the nonadiabatic STT to the adiabatic STT [89, 95].

The physical origin of this STT term is (still) discussed controversially. While

[18] The spin polarization is defined by $P = |\frac{n_\uparrow - n_\downarrow}{n_\uparrow - n_\downarrow}|$—where $n_\uparrow$ and $n_\downarrow$ are the respective densities of states at the Fermi energy—and is less than unity for elemental metallic ferromagnets: $P_\mathrm{Fe} = 0.44$, $P_\mathrm{Co} = 0.34$, and $P_\mathrm{Ni} = 0.11$ [65].

[19] u is positive for $P > 0$, i.e., in case of charge carriers, which are polarized along the majority spin direction [95].

some ascribe the nonadiabatic spin-transfer to a Larmor precession of the spins of the conduction electrons [96], it is more frequently related to the spatial mistracking of the spin orientation of the conduction electrons and the local magnetization[20] [97, 98]. The latter picture is usually discussed in an *s-d* model, which considers the exchange coupling between itinerant and local electrons. In this theory[21], the strength of the nonadiabatic STT is a result of the exchange coupling strength and of spin-flip relaxation processes [89]. Furthermore, it is also discussed if the Gilbert damping parameter α is related to β [99, 100].

In addition to its unclear physical origin, there is also some controversy concerning the numerical value of β. Estimates for β have been obtained from theory and experiments [101, 102]. Some studies suggest that β is equal to α [103, 104], while others predict the necessity of a difference between these parameters [105, 106].
Experiments evidencing the current-induced transformation of DW structures imply that α and β are not equal [107]. Measurements from various groups have reported significant differences for the ratio β/α as well as for the value of β, ranging from small—$\beta = \alpha = 0.02$ [108], $\beta = 2\alpha = 0.02$ [109], $\beta = 2\alpha$–$3\alpha = 0.02$ [49]—to intermediate—$\beta = 2\alpha = 0.04$ [101], $\beta = 8\alpha = 0.04$ [110]—and large values—$\beta = 0.15$ [111], $\beta = 1.45$ [112].

Eventually, the LLG equation extended by the two STT terms reads as [90, 92–95]

$$\frac{\mathrm{d}\vec{M}}{\mathrm{d}t} = \underbrace{-\gamma\mu_0 \vec{M} \times \vec{H}_{\mathrm{eff}}}_{\text{precession term}} + \underbrace{\frac{\alpha}{M_{\mathrm{S}}} \vec{M} \times \frac{\mathrm{d}\vec{M}}{\mathrm{d}t}}_{\text{damping term}} \underbrace{- \left(\vec{u} \cdot \vec{\nabla}\right) \vec{M}}_{\text{adiabatic STT term}} \underbrace{+ \frac{\beta}{M_{\mathrm{S}}} \vec{M} \times \left[\left(\vec{u} \cdot \vec{\nabla}\right) \vec{M}\right]}_{\text{nonadiabatic STT term}} . \tag{1.29}$$

Eq. (1.29) is the equation of motion, which describes the dynamics of a magnetic system under the influences of an effective magnetic field and a spin-polarized electric current.

1.4 Spin Waves

SWs are low energy collective spin excitations in a magnetically ordered body. Compared with a uniform excitation, where all magnetic moments/spins precess in phase, in case of a SW, there is a finite phase lag in the precession between neighboring magnetic moments/spins as depicted in the schematics shown in Fig. 1.5. Such an excitation is fully characterized by its dispersion $\omega\left(\vec{k}\right) = 2\pi f\left(\vec{k}\right)$, i.e., by the relation between the angular frequency ω—specifying the precession frequency of the magnetic moments forming the SW—and the wave

[20] For $\beta = 0$, the nonadiabatic STT vanishes, and, consequently, in this case, the electron spins align perfectly with the local orientation of the magnetization [cf. Fig. 1.4], i.e., there is no mistracking.

[21] $\beta = \left(\lambda_J/\lambda_{\mathrm{sf}}\right)^2 = \hbar/\left(J\tau_{\mathrm{sf}}\right)$, where J is the *s-d* exchange interaction energy, τ_{sf} is the spin-flip time, and λ_J and λ_{sf} are the associated diffusion lengths [95]. For instance, in the case of Permalloy ($Ni_{80}Fe_{20}$), $\lambda_J = 1\,\mathrm{nm}$ and $\lambda_{\mathrm{sf}} = 5\,\mathrm{nm}$, i.e., $\beta = 0.04$.

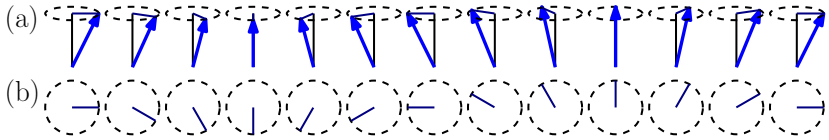

Figure 1.5. Schematic of a SW in a one-dimensional chain of exchange-coupled magnetic moments (blue arrows). (a) Side view. (b) Top view.

vector $\vec{k}$—specifying the SW propagation direction and the SW wave length $\lambda = 2\pi/|\vec{k}|$. Besides the dispersion, propagating SWs are further characterized by their attenuation length as it is a measure for their propagation distance which is finite due to magnetic damping [cf. Sec. 1.3.1].

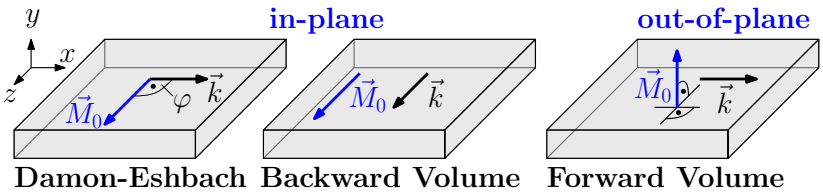

Figure 1.6. Schematic of the three different SW geometries—two in-plane configurations and one out-of-plane configuration—which differ in the relative orientation of the equilibrium magnetization direction $\vec{M}_0$ with respect to the wave vector $\vec{k}$ of the propagating SWs.

In a thin magnetic film, there are three different propagating SW geometries [2], which are illustrated in the schematics shown in Fig. 1.6. They differ in the relative orientation between the equilibrium magnetization direction $\vec{M}_0$ and the SW wave vector $\vec{k}$. In two of them, $\vec{M}_0$ lies in the plane of the film, while in the third one it is oriented out-of-plane. The latter configuration—where $\vec{k}$ can point along any in-plane direction—is referred to as *forward volume (FV)* geometry. It is characterized in that the SW propagation is isotropic within the xz plane. In contrast, the in-plane configurations are differentiated by the angle φ between $\vec{k}$ and $\vec{M}_0$. In the *backward volume (BV)* geometry, $\vec{M}_0$ is collinear with $\vec{k}$, i.e., $\varphi = 0°$, while in the *Damon-Eshbach (DE)* geometry [113], $\vec{M}_0 \perp \vec{k}$ applies, i.e., $\varphi = 90°$.

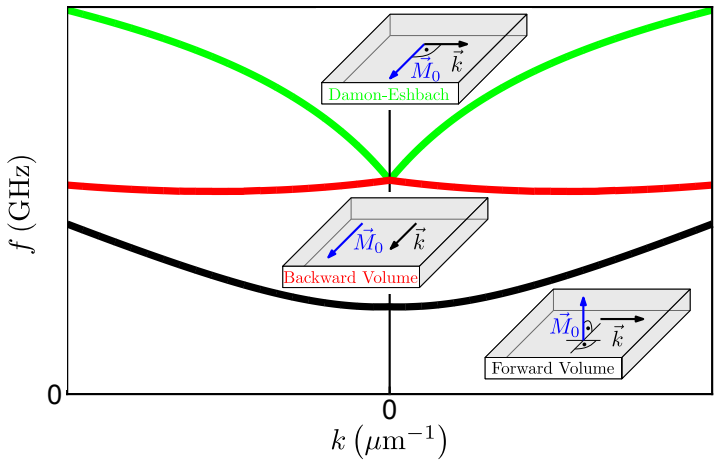

Figure 1.7. SW dispersions in the three propagation geometries sketched in the insets.

The main characteristics of propagating SWs—dispersion, group velocity[22] and attenuation length—are crucially dependent on the propagation geometry, as it can be seen in Fig. 1.7, where the SW dispersions corresponding to the respective geometries are displayed. The behaviors of the individual dispersions differ significantly.

In the following, only the in-plane SW geometries are considered, where the main focus is on the DE geometry since it is the characteristics of these SWs, which are investigated both qualitatively and quantitatively in the different SW propagation experiments presented in Ch. 3–6.

1.4.1 Spin Wave Dispersion and Spin Wave Attenuation

The derivation of expressions for the DE SW dispersion and DE SW attenuation length is based on Refs. [2, 52, 53, 114–116] and employs the thin film approximation, where it is assumed that the film thickness d is much smaller than its lateral dimensions. Moreover, to cover a more general case, the magnetic film additionally exhibits a uniaxial PMA.
For the derivation[23], the orientation of the Cartesian coordinate system is as depicted in Fig. 1.8:

- x denotes the DE SW propagation direction.
- The magnetic bias field with polarity p is applied along the z direction, i.e., $\vec{H}_0 = pH_0\vec{e}_z$. For $p = +1$ ($p = -1$), it is aligned along the $+z$ ($-z$) direction.
- The easy axis of the uniaxial PMA is oriented along the y direction, i.e., it is aligned parallel to the surface normal $\vec{n}$ of the thin magnetic film.

First, the DE SW dispersion $\omega(k) = 2\pi f(k)$ is derived and discussed in detail before focusing on the derivation of the expression for the DE SW attenuation length L_{att}.

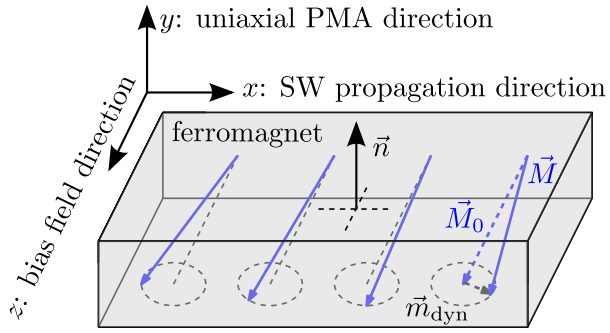

Figure 1.8. Orientation of the Cartesian coordinate system used for the derivation of the characteristics of propagating DE SWs.

[22] The group velocity is linked to the dispersion, as it is given by $\vec{v}_{\text{gr}} = \partial\omega\left(\vec{k}\right)/\partial\vec{k}$, and it quantifies the speed of propagation.

[23] If not otherwise stated explicitly, this orientation of the coordinate system is used in all subsequent derivations and discussions concerning the dispersion and attenuation length of propagating (DE) SWs.

Derivation of the Damon-Eshbach Spin Wave Dispersion

Neglecting magnetic damping in the first place, the spatial and temporal evolution of the magnetization $\vec{M}(x,t)$ of a DE SW propagating along the x direction under a magnetic bias field applied along the z direction can be divided into a static part and a dynamic part. The latter one can be expressed using a plane wave ansatz in the form of $e^{i(\omega t-kx)}$ [52, 53]. Then, $\vec{M}(x,t)$ is given by [52, 53]

$$\begin{aligned}\vec{M}(x,t) &= M_x(x,t)\,\vec{e}_x + M_y(x,t)\,\vec{e}_y + M_z\vec{e}_z \\ &= M_{\mathrm{S}} m_{x0} e^{i(\omega t-kx)}\vec{e}_x + M_{\mathrm{S}} m_{y0} e^{i(\omega t-kx)}\vec{e}_y + M_{\mathrm{S}} p\vec{e}_z \\ &= \underbrace{M_{\mathrm{S}}\left(m_{x0}e^{i(\omega t-kx)}\vec{e}_x + m_{y0}e^{i(\omega t-kx)}\vec{e}_y\right)}_{\vec{m}_{\mathrm{dyn}}(x,t)} + \underbrace{M_{\mathrm{S}} p\vec{e}_z}_{\vec{M}_0} \\ &= \vec{m}_{\mathrm{dyn}}(x,t) + \vec{M}_0\,, \end{aligned} \tag{1.30}$$

where $\vec{e}_x$, $\vec{e}_y$, $\vec{e}_z$ are unit vectors along the coordinate axes, and where m_{x0} and m_{y0} are dimensionless complex amplitudes. $\vec{m}_{\mathrm{dyn}}$ is the dynamic part of the magnetization while $\vec{M}_0$ denotes the equilibrium magnetization direction, which is parallel to the bias field direction $\vec{H}_0$. Moreover, since $|m_{x0}|, |m_{y0}| \ll 1$ applies, i.e., the excursion angle ψ between $\vec{M}_0$ and $\vec{M}$ is very small [cf. Figs. 1.3(a) and 1.8], a propagating DE SW represents a low-amplitude excitation of the magnetization.

In the DE geometry, the effective magnetic field is given by [cf. Eq. (1.22)]

$$\vec{H}_{\mathrm{eff}} = pH_0\vec{e}_z + \frac{J}{M_{\mathrm{S}}}\vec{\nabla}^2\vec{M} + \vec{H}_{\mathrm{dip}} + \vec{H}_{\mathrm{ani}} \tag{1.31}$$

with $J = 2A/(\mu_0 M_{\mathrm{S}})$. In case of a thin film, the dipolar field $\vec{H}_{\mathrm{dip}}$ arises only due to the dynamic part of the magnetization, i.e., $\vec{m}_{\mathrm{dyn}}$, and is given by[24] [52, 53, 114, 116]

$$\vec{H}_{\mathrm{dip}} = -M_x\xi(kd)\,\vec{e}_x - M_y\left[1-\xi(kd)\right]\vec{e}_y \tag{1.32}$$

with

$$\xi(kd) = 1 - \left[1-\exp(-|kd|)\right]/|kd|\,. \tag{1.33}$$

The uniaxial PMA field $\vec{H}_{\mathrm{ani}}$ is given by [cf. Eqs. (1.10) and (1.22)]

$$\vec{H}_{\mathrm{ani}} = \vec{H}_{\mathrm{u}}^{\perp} = \frac{2K_{\mathrm{u}}^{\perp}}{\mu_0 M_{\mathrm{S}}^2} M_y\vec{e}_y\,, \tag{1.34}$$

where $K_{\mathrm{u}}^{\perp}$ is the uniaxial PMA constant.

The resulting SW dynamics is described by the LLG equation [cf. Eq. (1.24)]. Inserting the expressions for $\vec{M}$ [cf. Eq. (1.30)] and $\vec{H}_{\mathrm{eff}}$ [cf. Eq. (1.31)] while

[24] The dipolar field is anisotropic owing to the inherent anisotropy of the dipolar interactions.

neglecting both the damping term as well as higher-order terms $\mathcal{O}\left(M_i^2\right)$, the linearized LLG equation yields the following system of equations:

$$i\omega M_x = -\gamma\mu_0 p\left[H_0 + Jk^2 + M_\mathrm{S}\left(1-\xi\right) - \frac{2K_\mathrm{u}^\perp}{\mu_0 M_\mathrm{S}}\right]\cdot M_y \tag{1.35a}$$

$$i\omega M_y = -\gamma\mu_0 p\left[-H_0 - Jk^2 - M_\mathrm{S}\xi\right]\cdot M_x\,. \tag{1.35b}$$

Rearranged it reads

$$\begin{pmatrix} 0 \\ 0 \end{pmatrix} = \underline{A}\begin{pmatrix} M_x \\ M_y \end{pmatrix} \tag{1.36}$$

with

$$\underline{A} := \begin{pmatrix} i\omega & \gamma\mu_0 p\left[H_0 + Jk^2 + M_\mathrm{S}\left(1-\xi\right) - H_\mathrm{u}^\perp\right] \\ -\gamma\mu_0 p\left[H_0 + Jk^2 + M_\mathrm{S}\xi\right] & i\omega \end{pmatrix}. \tag{1.37}$$

The solution to Eq. (1.36) at any angular frequency ω is given by the condition $\det\left(\underline{A}\right) \stackrel{!}{=} 0$, yielding

$$\begin{aligned}\omega\left(k\right) &= 2\pi f\left(k\right) \\ &= \gamma\mu_0\sqrt{\left[H_0 + Jk^2 + M_\mathrm{S}\xi\left(kd\right)\right]\left[H_0 + Jk^2 + M_\mathrm{S}\left(1-\xi\left(kd\right)\right) - H_\mathrm{u}^\perp\right]}\,.\end{aligned} \tag{1.38}$$

Eq. (1.38) is the dispersion of DE SWs propagating along the x direction in a thin magnetic film, where the static magnetization $\vec{M}_0$ is maintained along the z direction by the magnetic bias field, and which also exhibits a uniaxial PMA. The k-dependence arises both due to the exchange interactions [cf. terms highlighted in red in Eq. (1.38)] as well as due to the dipolar interactions [cf. terms highlighted in blue in Eq. (1.38)].
In Fig. 1.9(a) and (b), $f\left(k\right)$ is plotted in case of a thin Permalloy ($\mathrm{Ni_{80}Fe_{20}}$) film for different bias fields and different wave number ranges due to the fact that the DE SW dispersion can be divided into two different regimes depending on the magnitude of the exchange term Jk^2 in Eq. (1.38). This term can be rewritten in the form [2]

$$Jk^2 = M_\mathrm{S} l_\mathrm{ex}^2 k^2\,, \tag{1.39}$$

where $l_\mathrm{ex} = \sqrt{\frac{2A}{\mu_0 M_\mathrm{S}^2}}$ is the (magnetostatic) exchange length [117].
For small k, i.e., long-wavelength DE SWs, $l_\mathrm{ex}^2 k^2 \ll 1$ applies, which is synonymous to the statement that, in this case, the weak, but long-range magnetic dipolar interactions dominate the strong, short-range exchange interactions. Therefore, these DE SWs are called *dipolar-dominated* or *magnetostatic* DE SWs [cf. Fig. 1.9(b)].
As k increases, $l_\mathrm{ex}^2 k^2$ becomes large when compared with unity. In this case, the exchange interactions dominate the dipolar interactions, and therefore these short-wavelength DE SWs are referred to as *exchange-dominated* DE SWs. In this wave number range, the DE SW dispersion scales as k^2 [cf. Fig. 1.9(a)].

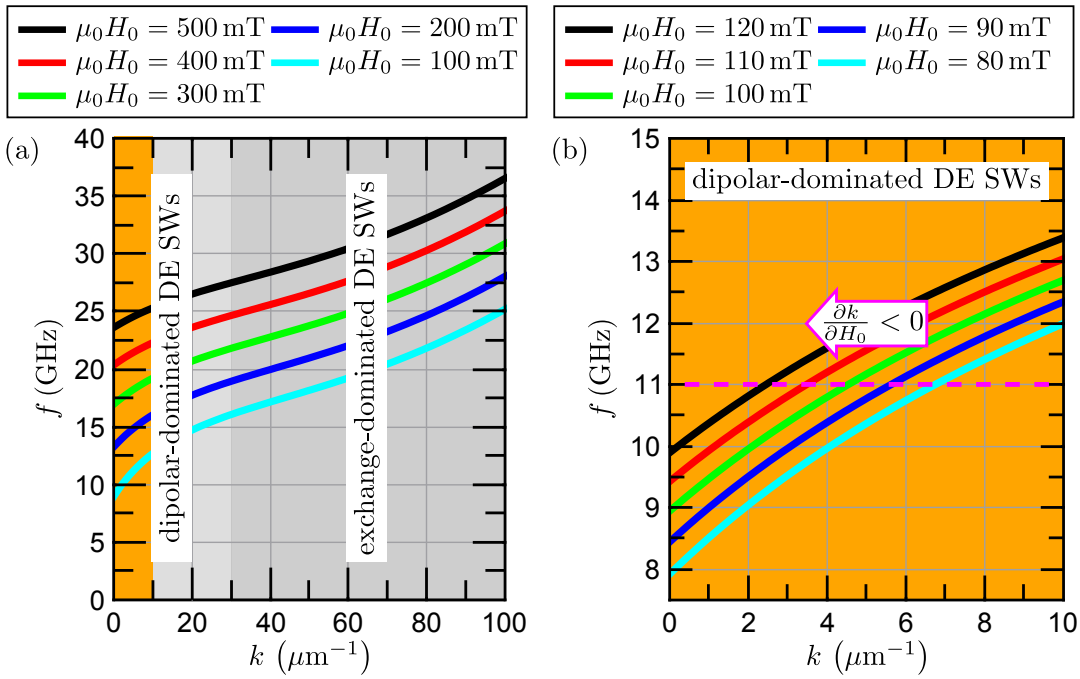

Figure 1.9. (a) DE SW dispersion[25] at different bias fields ranging from 100–500 mT. For small k, the DE SWs are called dipolar-dominated SWs, whereas they are denoted as exchange-dominated DE SWs for large k [cf. gray-shaded regions]. The k-range that can be accessed (magneto-)optically using time-resolved Kerr microscopy [cf. Ch. 2] is marked in orange. (b) DE SW dispersion in the dipolar-dominated regime at different bias fields ranging from 80–120 mT. As indicated, for any fixed (excitation) frequency—e.g., $f = 11\,\mathrm{GHz}$ (dashed magenta line)—k decreases as the bias field magnitude increases.

As DE SWs evolve continuously in character as k increases, in the wave number range, where both dipolar and exchange interactions are important, these DE SWs are called *dipolar-exchange* SWs [2].
Yet, only propagating *dipolar-dominated* DE SWs with wave numbers up to $\approx 10\,\mu\mathrm{m}^{-1}$—corresponding to SW wave lengths $\lambda = (2\pi)/|\vec{k}|$ on the order of $\approx 600\,\mathrm{nm}$—can be accessed experimentally using time-resolved Kerr microscopy since this magneto-optical technique utilizes visible light [cf. Ch. 2].

In general, for a fixed f, the wave number of propagating DE SWs can simply be increased (decreased) by decreasing (increasing) the bias field magnitude as elucidated by the dashed magenta line in Fig. 1.9(b).

The group velocity of propagating SWs, i.e., the speed of propagation, is given by

$$\vec{v}_{\mathrm{gr}} = \frac{\partial \omega}{\partial \vec{k}} = 2\pi \frac{\partial f}{\partial \vec{k}}\,. \tag{1.40}$$

Eq. (1.40) implies that, in general, the group velocity and the wave vector are not collinear. Yet, in the case of DE SWs, $\vec{v}_{\mathrm{gr}} \uparrow\uparrow \vec{k}$ applies, and hence, v_{gr} is

[25] $f(k)$ is calculated in case of a thin Permalloy film using the following material parameters: $\mu_0 M_{\mathrm{S}} = 0.92\,\mathrm{T}$, $\gamma = 176\times10^9\,\mathrm{rad/(Ts)}$, $A = 13\times10^{-12}\,\mathrm{J/m}$, $\mu_0 H_{\mathrm{u}}^{\perp} = 0.0\,\mathrm{T}$, and $d = 30\,\mathrm{nm}$.

simply given by the slope of the dispersion. As clearly visible in Fig. 1.9, it is always positive, and, for this reason, any kind of propagating DE SWs is referred to as a *forward wave*.

In the case of DE SWs, the angle φ between $\vec{k}$ and $\vec{H}_0$ is 90° [cf. Fig. 1.6], i.e., $\vec{k} = k_x\vec{e}_x \perp \vec{H}_0 = pH_0\vec{e}_z$. In contrast, in the case of BV SWs, $\varphi = 0°$, i.e., $\vec{k} = k_z\vec{e}_z \parallel \vec{H}_0 = pH_0\vec{e}_z$. The BV SW dispersion can be derived the same way as the DE SW dispersion when considering the different orientations of $\vec{m}_{\mathrm{dyn}}$ and $\vec{M}_0$ [cf. Eq. 1.30] with respect to $\vec{k}$ as well as the resulting modifications in the x, y and z components of the effective magnetic field [cf. Eq. 1.31]. It is given by [118]

$$\omega(k) = \gamma\mu_0\sqrt{[H_0 + Jk^2] \cdot [H_0 + Jk^2 + M_{\mathrm{S}}(1 - \xi(kd)) - H_{\mathrm{u}}^{\perp}]}\,, \tag{1.41}$$

and plotted in comparison to the DE SW dispersion for the same set of material and experimental parameters in Fig. 1.10. Either dispersion is symmetric in k, and, at $k = 0$, the DE and BV dispersion are degenerate. Moreover, in contrast to DE SWs, which always exhibit a positive v_{gr}, in the case of BV SWs, v_{gr} is initially negative, i.e., $\vec{v}_{\mathrm{gr}} \uparrow\downarrow \vec{k}$, so that $f(k > 0) < f(k = 0)$ applies for small k [cf. orange dashed line in Fig. 1.10]. But, it becomes and remains positive for larger k. Due to this characteristic this kind of propagating SW is referred to as a *backward wave*.

In the most general case, $\vec{H}_0 = pH_0\vec{e}_z$ and the in-plane SW wave vector is $\vec{k} = k_x\vec{e}_x + k_z\vec{e}_z$ with $|\vec{k}| = k = \sqrt{k_x^2 + k_z^2}$ with $0° \leq \varphi \leq 90°$. The corresponding in-plane SW dispersion is given by [114]

$$\omega(k, \varphi) = \gamma\mu_0\sqrt{[H_0 + Jk^2]\,[H_0 + Jk^2 + M_{\mathrm{S}} \cdot A(k, \varphi)]} \tag{1.42}$$

with

$$A(k, \varphi) := \xi(kd) + \left[1 - \xi(kd)\left(1 + \cos^2(\varphi)\right) + \frac{M_{\mathrm{S}}\xi(kd)\,(1 - \xi(kd))\sin^2(\varphi)}{(H_0 + Jk^2)}\right], \tag{1.43}$$

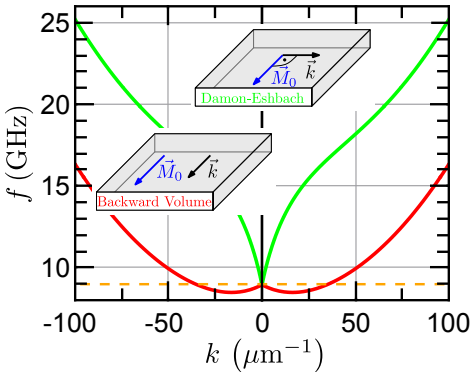

Figure 1.10. DE and BV SW dispersions[26]. The dashed orange line indicates $f(k = 0) = \omega(k = 0)/(2\pi)$, at which the two dispersions are degenerate. It is also a guide to the eye to elucidate that v_{gr} of BV SWs is negative for small k and positive for large k, while it is always positive in the case of DE SWs.

[26] Both dispersions are calculated at $\mu_0 H_0 = 0.1\,\mathrm{T}$ with that set of material parameters used for the calculation of the dispersions shown in Fig. 1.9.

in the case when no uniaxial PMA field is present. In contrast, when a uniaxial PMA field is present, it is given by [7, 118]

$$\omega\left(k,\varphi\right)=\gamma\mu_0\sqrt{B\left(k,\varphi\right)\cdot C\left(k\right)} \tag{1.44}$$

with

$$B\left(k,\varphi\right):=\left[H_0+Jk^2+M_\mathrm{S}\xi\left(kd\right)\sin^2\left(\varphi\right)\right] \tag{1.45a}$$

$$\text{and}\qquad C\left(k\right):=\left[H_0+Jk^2+M_\mathrm{S}\left(1-\xi\left(kd\right)\right)-H_\mathrm{u}^{\perp}\right], \tag{1.45b}$$

respectively, where φ can simply be expressed by the wave vector components as

$$\varphi=\frac{k_x}{\sqrt{k_x^2+k_z^2}}. \tag{1.46}$$

In Fig. 1.11(a), the in-plane SW dispersion—according to Eq. (1.42)—is displayed as a contour plot. The dashed (dotted) green (red) line denotes the DE (BV) configuration, i.e., $f\left(k\right)$ along each line agrees with the respective dispersion plotted in Fig. 1.10. The in-plane SW dispersion is anisotropic for small wave numbers $|\vec{k}|$ as it is clearly visible in the shape of the isofrequency curves depicted in Fig. 1.11(b). This anisotropy arises due to the dominating long-range dipolar interactions and results in anisotropic SW characteristics. For example, $\vec{v}_\mathrm{gr}$ and $\vec{k}$ are only collinear in the DE and BV geometries, while they are non-collinear for all other in-plane angles φ between $\vec{H}_0$ and $\vec{k}$. However, the larger $|\vec{k}|$ is, the less pronounced is the anisotropy. This behavior is due to the continuously increasing impact of the exchange contributions, and for very large $|\vec{k}|$, where the exchange interactions are dominating, the in-plane SW dispersion is quasi-isotropic as it scales with $|\vec{k}|^2$ [cf. Eq. (1.42)].

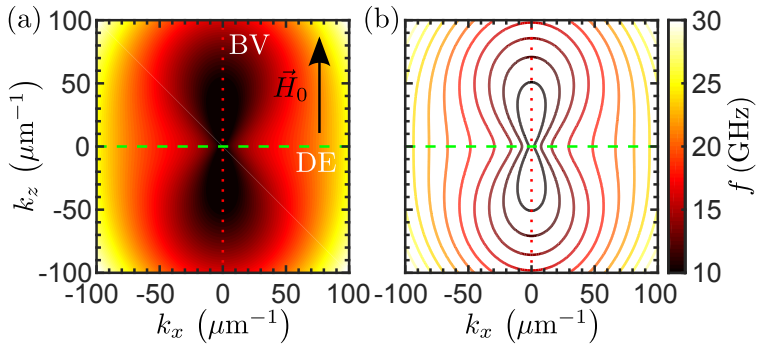

Figure 1.11. In-plane SW dispersion[27] for $\vec{k}=k_x\vec{e}_x+k_z\vec{e}_z$ and $\vec{H}_0$ applied along the z direction. The dashed (dotted) green (red) line indicates the DE (BV) configuration, i.e., $f\left(k_x\right)$ ($f\left(k_z\right)$). (a) Contour plot. (b) Selected isofrequency curves from (a) to elucidate the anisotropy of the in-plane SW dispersion for small $|\vec{k}|$, which becomes less pronounced the larger $|\vec{k}|$ is.

[27] $f\left(\vec{k}\right)$ is calculated at $\mu_0H_0=0.1\,\mathrm{T}$ with that set of material parameters used for the calculation of the individual dispersions shown in Fig. 1.9.

Finally, it is noted that, for $k = 0$—which corresponds to a SW with infinite wavelength—all magnetic moments precess uniformly in phase around $\vec{H}_{\text{eff}}$ at $\omega(k = 0)$ [cf. dashed orange line in Fig. 1.10]. This is the case of ferromagnetic resonance (FMR), and then, Eq. (1.38) simplifies to the Kittel formula [65, 119]

$$\omega(k) = \gamma\mu_0\sqrt{H_0\left(H_0 + M_{\text{S}} - H_{\text{u}}^{\perp}\right)} = \gamma\mu_0\sqrt{H_0\left(H_0 + M_{\text{eff}}\right)} \tag{1.47}$$

with the effective magnetization

$$M_{\text{eff}} := M_{\text{S}} - H_{\text{u}}^{\perp}\,. \tag{1.48}$$

When comparing Eqs. (1.38) and (1.47), it is obvious that, at a fixed bias field magnitude, the excitation of propagating DE SWs occurs at higher frequencies compared with the FMR mode [cf. green curve in Fig. 1.10], while at a fixed excitation frequency, the DE SW modes appear at lower bias fields than the FMR mode.

Derivation of the Damon-Eshbach Spin Wave Attenuation Length

When both the precession and the damping term are taken into consideration in the LLG equation, the system of equations given in Eq. (1.36) is modified as follows:

$$\begin{pmatrix} 0 \\ 0 \end{pmatrix} = \underbrace{\left[\underline{A} + \begin{pmatrix} 0 & i\alpha p\omega \\ -i\alpha p\omega & 0 \end{pmatrix}\right]}_{:=\underline{B}} \begin{pmatrix} M_x \\ M_y \end{pmatrix}. \tag{1.49}$$

The solution to Eq. (1.49) at any ω is given by the condition $\det(\underline{B}) \stackrel{!}{=} 0$. Neglecting higher-order terms $\mathcal{O}(\alpha^2)$ this condition yields a complex equation quadratic in ω:

$$-\omega^2 + i\alpha p\left(A_{12} - A_{21}\right)\omega - A_{12}A_{21} = 0\,. \tag{1.50}$$

The solution to Eq. (1.50) is a complex[28] $\underline{\omega}$, i.e.,

$$\underline{\omega} = \text{Re}\left(\underline{\omega}\right) + i \cdot \text{Im}\left(\underline{\omega}\right)\,, \tag{1.51}$$

where the real part is identical with DE SW dispersion, i.e., $\text{Re}\left(\underline{\omega}\right) = \omega(k)$ [cf. Eq. (1.38)], while the imaginary part

$$\text{Im}\left(\underline{\omega}\right) = \alpha\gamma\mu_0\left(H_0 + Jk^2 + \frac{M_{\text{S}}}{2} - \frac{H_{\text{u}}^{\perp}}{2}\right) \tag{1.52}$$

corresponds to a characteristic time scale τ defined as

$$\tau = \frac{1}{\text{Im}\left(\underline{\omega}\right)}\,. \tag{1.53}$$

When introducing a complex wave number $\underline{k} = \text{Re}\left(\underline{k}\right) + i \cdot \text{Im}\left(\underline{k}\right)$, where [6]

$$k = \text{Re}\left(\underline{k}\right) \tag{1.54}$$

$$\text{and} \qquad L_{\text{att}} = \frac{1}{\text{Im}\left(\underline{k}\right)}\,, \tag{1.55}$$

[28] Throughout this thesis, complex quantities are marked by underlining.

and since real and imaginary parts of $\underline{\omega}$ and $\underline{k}$ are linked via v_{gr}, the analogue to the characteristic time scale τ in space is the DE SW attenuation length, which is given by

$$L_{\mathrm{att}} = \frac{1}{\mathrm{Im}\left(\underline{k}\right)} = \frac{v_{\mathrm{gr}}}{\mathrm{Im}\left(\underline{\omega}\right)} = v_{\mathrm{gr}} \cdot \tau \overset{\text{Eq. (1.52)}}{=} \frac{v_{\mathrm{gr}}}{\alpha\gamma\mu_0 \left(H_0 + Jk^2 + \frac{M_{\mathrm{S}}}{2} - \frac{H_{\mathrm{u}}^{\perp}}{2}\right)} \,. \tag{1.56}$$

Using Eq. (1.56), the real spatio-temporal profile $\vec{M}\left(x,t\right)$ reads as[29] [52]

$$\vec{M}\left(x,t\right) = \vec{m}_{\mathrm{dyn}}\left(x,t\right) \cdot \exp\left(-x/L_{\mathrm{att}}\right) + \vec{M}_0 \,. \tag{1.57}$$

Eq. (1.57) clearly demonstrates that L_{att} is a characteristic length scale, since it specifies the propagation distance over which the DE SW amplitude decays to a factor $1/e$. Moreover, since $L_{\mathrm{att}} \sim v_{\mathrm{gr}} \sim d$ applies, for the same set of experimental parameters, the thicker the magnetic film, the further the DE SW propagate.

1.4.2 Nonreciprocity

The term "nonreciprocity" accounts for the peculiarity that SWs propagating in opposite directions do not exhibit the same characteristics [1, 2, 113]. In the case of DE SWs, depending both on the properties of the studied magnetic system as well as on the characteristics of the experiment, different types of nonreciprocity occur:

- modal profile nonreciprocity,
- frequency nonreciprocity, and
- amplitude nonreciprocity.

The frequency nonreciprocity arises due to the modal profile nonreciprocity in combination with an asymmetry of the magnetic film properties across the film thickness [120]—e.g., different anisotropies at the two film surfaces [121].

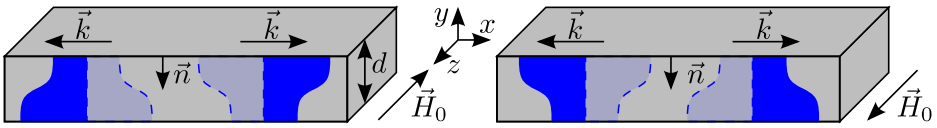

Figure 1.12. Schematic of the modal profile of DE SWs propagating along the x direction in a ferromagnetic film with thickness d, when the exchange interaction as well as the appropriate boundary conditions are taken into account. The width of the (shaded) blue regions[30] corresponds to the local precession amplitude across d. For a fixed propagation direction, depending on the orientation of the bias field, the DE mode is either localized at the top or at the bottom surface. In the case depicted, the signature of the modal profile asymmetry is in agreement with Eq. (1.58).

[29] For $x > 0$ ($x < 0$), $L_{\mathrm{att}} > 0$ ($L_{\mathrm{att}} < 0$) applies.

[30] Usually, for simplicity, only that half of the precession trajectory is plotted, where the larger precession amplitude is in line with the propagation direction.

The amplitude nonreciprocity is due to the excitation of propagating DE SWs using microwave antennas [44, 45, 122], and is addressed separately in detail in Sec. 1.4.5.

The modal profile nonreciprocity [2, 120, 121, 123] describes the characteristic that the DE SW mode is localized either at the bottom or top surface of the film depending both on the propagation direction $\vec{k}$ and the bias field direction $\vec{H}_0$. This behavior is illustrated in the schematics shown in Fig. 1.12. For this reason, DE SWs are also referred to as *surface modes*, in contrast to BV and FV SWs, which are *volume modes* [2]. Since this surface character is a fundamental intrinsic feature of DE SWs, its origin is discussed in detail below.

The origin is revealed when the spatial distribution of the dynamic dipolar field generated by the dynamic magnetization $\vec{m}_{\mathrm{dyn}}$ [cf. Eq. (1.30)] is investigated. In Fig. 1.13, for $k > 0$ and $\vec{M}_0 \uparrow\uparrow +\vec{e}_z$, the local orientation of $\vec{m}_{\mathrm{dyn}}$ is sketched across one SW wavelength. m^x_{dyn} [cf. open red arrows] and m^y_{dyn} [cf. solid blue arrows] create magnetic volume and surface charges, which, in turn, generate a dynamic dipolar field [cf. solid and dashed lines]. In the bottom half of the film, the contributions to the dipolar field arising from m^x_{dyn} and m^y_{dyn} add, while they partially compensate each other in the top half. Consequently, for $k > 0$, the total dipolar field is larger in the bottom half. The situation is reversed for $k < 0$ due to the different sense of rotation of $\vec{m}_{\mathrm{dyn}}$. This nonreciprocal asymmetry of the dynamic dipolar field is at the origin of the modal profile asymmetry. Because in order to establish a true SW eigenmode, $\vec{m}_{\mathrm{dyn}}$ tends to compensate this asymmetry by increasing its precession amplitude either in the bottom or top half of the film depending on the sign of k, and therefore the DE SW mode is localized in the vicinity of either surface. This mode localization also reverses when the direction of the equilibrium magnetization direction $\vec{M}_0$ is reversed by inverting the polarity of H_0 [cf. left and right graph in Fig. 1.12].
Fig. 1.13 is a simple graphic representation of the origin of the surface character of DE SWs resulting from the standard DE picture of magnetostatic SWs [113].

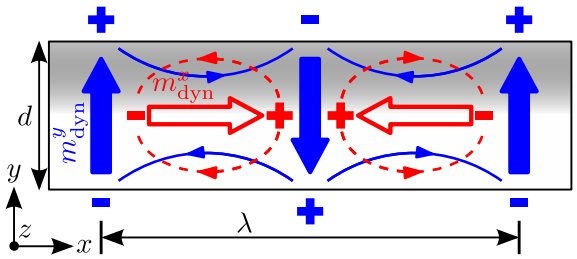

Figure 1.13. Schematic of the origin of the modal profile nonreciprocity of a DE SW propagating in a magnetic film with thickness d. Solid blue and open red arrows indicate the local orientation of the x and y components of the dynamic magnetization $\vec{m}_{\mathrm{dyn}}$ across one SW wavelength λ for $k > 0$ and $\vec{M}_0$ aligned along the $+z$ direction [cf. Fig. 1.8]. m^y_{dyn} generates magnetic charges on the y surfaces while m^x_{dyn} generates volume charges. The arrows on the blue solid and red dashed lines indicate the respective orientation of the resulting dipolar field lines. In the vicinity of the bottom (top) y surface, they point along the same (opposite) direction(s). (Figure is adapted from Ref. [121].)

Here, the exchange interaction is neglected, and due to the given boundary conditions at the film surfaces, the profile of $\vec{m}_{\mathrm{dyn}}$ across the film thickness needs to be a combination of two exponentials—$\exp(-ky)$ and $\exp(ky)$—with an asymmetry between the two components such that the amplitude of the magnetization precession is maximum at one of the film surfaces [2]. The surface, at which the SW precession amplitude is larger, is the one whose internal normal $\vec{n}$ along the film thickness verifies[31] [1, 123]

$$\frac{\vec{k}}{|\vec{k}|} = \vec{n} \times \frac{\vec{M}_0}{|\vec{M}_0|} \,. \tag{1.58}$$

Moreover, due to the exponential profile of the dynamic magnetization across the film thickness in the standard DE picture of magnetostatic SWs [2], in that case, a characteristic thickness d_{char} can be defined as follows:

$$\exp(-kd_{\mathrm{char}}) := 1/e \qquad \rightarrow \qquad d_{\mathrm{char}} = 1/k \,. \tag{1.59}$$

Eq. (1.59) can be used to roughly estimate whether the modal profile nonreciprocity becomes relevant for a given combination of DE SW wave number and magnetic film thickness[32].

Due to the fact that the exchange interaction is neglected, Eq. (1.58) contradicts certain experimental findings—e.g., the nonreciprocal Oersted field induced frequency shift [123]—which indicate a signature of the modal profile nonreciprocity, which is opposite to the one given by Eq. (1.58). This contradiction is removed, however, when the exchange interaction is taken into account as proven by Kostylev *et al.* [120], who revisited the theory of dipole-exchange SWs [114, 115] in combination with appropriate boundary conditions [124] to understand the modal profile nonreciprocity in thin ferromagnetic metallic films. In that case, the sign of the modal profile nonreciprocity is specified not only by the sign of k [cf. Eq. (1.58)], but also by the magnitude of k [120]. Their findings enable the determination of the correct shape and signature of the modal profile in a broad range of wave numbers.

Considering the exchange interaction along with the appropriate boundary conditions at either surface of the thin magnetic film reveals realistic modal profiles across the film thickness for propagating DE SWs. These are the ones sketched in Fig. 1.12. They clearly differ from the exponential profile in the classical DE picture [2].

[31] Eq. (1.58) also considers the inversion in signature of the modal profile nonreciprocity, when either the bias field direction or the propagation direction is reversed.

[32] The different SW propagation experiments presented in Ch. 3–6 are performed on magnetic structures with thicknesses on the order of a few tens of nanometers. Moreover, the DE SWs that can be accessed magneto-optically [cf. Ch. 2] exhibit wave numbers on the order of 1–10 $\mu\mathrm{m}^{-1}$. Inserting these values into Eq. (1.59) reveals d_{char}-values on the order of 1–0.1 μm. These values are (much) larger than the thicknesses of the individual magnetic structures. For this reason, the modal profile nonreciprocity is expected to be of minor or no relevance in these experiments.

1.4.3 Spin Waves Propagating Under an Applied Electric Current

As discussed in Sec. 1.4.1, propagating DE SWs are entirely characterized by their dispersion $\omega\left(\vec{k}\right)$ and attenuation length L_{att}. When these SWs are subjected to a spin-polarized electric current, a spin-transfer occurs [90, 93] that leads to modifications in the DE SW characteristics, which are discussed in detail below.

Conceptually, the interaction between a spin-polarized electric current and a propagating DE SW can be divided into the effect arising from the adiabatic STT and the one due to the nonadiabatic STT [11, 49, 125].

Effect of the Adiabatic Spin-Transfer Torque

The effect of the adiabatic STT on the characteristic of a propagating SW is discussed for the situation sketched in Fig. 1.14. Here, a DE SW with wave vector $\vec{k}$ propagates along the $+x$ direction while an electrical dc current I_{dc} is applied along the $-x$ direction, i.e., the direction of flow of the electrons—e^-—is identical to the DE SW propagation direction, i.e., $\vec{u} \uparrow\uparrow \vec{k}$ applies [cf. Eq. (1.27)]. The solid red arrows denote the local orientation of the electron spin—in case of a spin polarization $P > 0$—at two positions, which are separated by a fraction of a SW wavelength. Since the electron spin follows adiabatically the local orientation of $\vec{M}$ as it passes the DE SW, and due to the conservation of angular momentum, the adiabatic STT arises acting on $\vec{M}$ [cf. Sec. 1.3.2]. The direction of action of the adiabatic STT is indicated by the solid green arrow. This torque is clearly collinear with the precession torque, thus leading to an increase of ω. Conversely, when the current direction is reversed, i.e., $\vec{u} \uparrow\downarrow \vec{k}$ applies, the adiabatic STT causes a decrease of ω [93, 125].

A quantitative expression for the shift in the DE SW frequency due to the

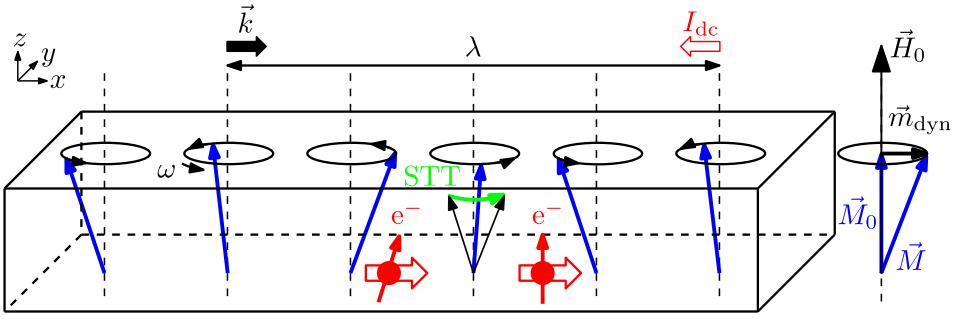

Figure 1.14. Sketch of the action of the adiabatic STT arising when an electric dc current I_{dc} with a spin polarization $P > 0$ passes a propagating DE SW, which is characterized by its wave vector $\vec{k}$/wavelength λ and its angular frequency ω. In the situation depicted, the DE SW propagates along the $+x$ direction against I_{dc}, i.e., along the direction of motion of the electrons e^-. The blue arrows represent the local orientation of the magnetization $\vec{M}$, the solid red arrows represent the current orientation of the electron spin as it passes the DE SW, and the solid green arrow indicates the direction of the resulting adiabatic STT. (Figure is adapted from Ref. [11].)

adiabatic STT can be derived by inserting the expression for the magnetization $\vec{M}(x,t)$ of a DE SW propagating along the $+x$ direction [cf. Eq. (1.30)] into the extended LLG equation [cf. Eq. (1.29)] while neglecting the nonadiabatic STT term. This procedure yields:

$$\begin{aligned} i\omega\vec{m}_{\mathrm{dyn}} &= -\gamma\mu_0\vec{M}\times\vec{H}_{\mathrm{eff}} + i\omega\frac{\alpha}{M_{\mathrm{S}}}\vec{M}_0\times\vec{m}_{\mathrm{dyn}} + iuk\vec{m}_{\mathrm{dyn}} \\ \rightarrow i\left(\omega-uk\right)\vec{m}_{\mathrm{dyn}} &= -\gamma\mu_0\vec{M}\times\vec{H}_{\mathrm{eff}} + i\omega\frac{\alpha}{M_{\mathrm{S}}}\vec{M}_0\times\vec{m}_{\mathrm{dyn}}\,. \end{aligned} \tag{1.60}$$

It is obvious that the impact of the adiabatic STT term in Eq. (1.60) is entirely accounted for by the substitution $\omega\rightarrow\omega+\Delta\omega_{\mathrm{STT}}$[33] with

$$\Delta\omega_{\mathrm{STT}} = uk\,, \tag{1.61a}$$

$$\text{or, in general form,} \qquad \Delta\omega_{\mathrm{STT}} = \vec{u}\cdot\vec{k}\,. \tag{1.61b}$$

Eq. (1.61b) states that "what happens at ω in the absence of an adiabatic STT, happens at $\omega+\Delta\omega_{\mathrm{STT}}$ in the presence of an adiabatic STT".
As already suggested by Lederer and Mills more than 50 years ago [126], this current-induced frequency shift can be formally identified as a Doppler shift that would emerge if the full electron system were simply moving with respect to the lab frame with the spin-drift velocity u. For this reason, the shift in frequency according to Eq. (1.61b) is called SW Doppler shift[34].

Effect of the Nonadiabatic Spin-Transfer Torque

A quantitative expression for the effect of the nonadiabatic STT on the characteristic of a propagating DE SW can be deduced by inserting $\vec{M}(x,t)$ [cf. Eq. (1.30)] into the extended LLG equation [cf. Eq. (1.29)] while neglecting the adiabatic STT term. This procedure yields:

$$\begin{aligned} i\omega\vec{m}_{\mathrm{dyn}} &= -\gamma\mu_0\vec{M}\times\vec{H}_{\mathrm{eff}} + i\omega\frac{\alpha}{M_{\mathrm{S}}}\vec{M}_0\times\vec{m}_{\mathrm{dyn}} \\ &\quad + iuk\frac{\beta}{M_{\mathrm{S}}}\left(\vec{M}_0\times\vec{m}_{\mathrm{dyn}}\right) \\ \rightarrow i\omega\vec{m}_{\mathrm{dyn}} &= -\gamma\mu_0\vec{M}\times\vec{H}_{\mathrm{eff}} + \frac{i\omega}{M_{\mathrm{S}}}\left(\alpha+\beta\frac{uk}{\omega}\right)\vec{M}_0\times\vec{m}_{\mathrm{dyn}}\,. \end{aligned} \tag{1.62}$$

It is obvious that the effect of the nonadiabatic STT term in Eq. (1.62) is entirely accounted for by the substitution $\alpha\rightarrow\alpha+\Delta\alpha_{\mathrm{STT}}$[35] with

$$\Delta\alpha_{\mathrm{STT}} = -\beta\frac{uk}{\omega}\,, \tag{1.63a}$$

$$\text{or, in general form,} \qquad \Delta\alpha_{\mathrm{STT}} = -\beta\frac{\vec{u}\cdot\vec{k}}{\omega}\,. \tag{1.63b}$$

[33] This substitution is reasonable since, for typical values of u—on the order of a few m/s—and k—on the order of 1–10 $\mu\mathrm{m}^{-1}$—$\Delta\omega_{\mathrm{STT}}$ is on the order of a few tens of MHz, which is much smaller than ω—which is on the order of a few GHz—and, therefore, $\Delta\omega_{\mathrm{STT}}\ll\omega$ applies. Moreover, as typical values for the Gilbert damping parameter α in metallic systems are on the order of 10^{-3}–10^{-2}, the factor $\alpha\omega$ in the second term on the right hand side in Eq. (1.60) does not considerably change for $\omega\rightarrow\omega+\Delta\omega_{\mathrm{STT}}$.

[34] It should not be confused with a true Doppler shift [127], which occurs, for example, when a detector is moved along the ferromagnet in which the SW propagates [128].

[35] This substitution is reasonable since $\alpha\omega$ and $\Delta\omega_{\mathrm{STT}}=\vec{u}\cdot\vec{k}$ are small compared with ω.

Eq. (1.63a) states that the nonadiabatic STT results in a modification of the Gilbert damping parameter α, which scales with the nonadiabatic parameter β. In turn, this α-modification manifests as a variation in the DE SW attenuation length [cf. Eq. (1.56)].

1.4.4 Spin Waves Propagating in the Presence of an Interfacial Dzyaloshinskii-Moriya Interaction

When DE SWs are propagating in a bi-/multi-layer system exhibiting an interfacial DMI [cf. Sec. 1.2.2], their characteristics—dispersion and attenuation length—are different compared to the situation where no interfacial DMI is present [52].

In the following, the occurring changes are discussed and derived on the basis of the bilayer system sketched in Fig. 1.15. It consists of a very thin ferromagnetic layer of thickness d on top of a nonmagnetic layer[36] with strong SOC [cf. Sec. 1.2.2]. Besides the interfacial DMI that arises at the interface between both layers as the inversion symmetry of this system is broken along the y direction [cf. Sec. 1.2.2] the system additionally exhibits a (strong) uniaxial PMA with an easy axis that is collinear with the y direction[37].

In the DE geometry, the interfacial DMI energy density [cf. Eq. (1.6)] is given by [52, 81]

$$\varepsilon_{\mathrm{DMI}} = \frac{D}{M_{\mathrm{S}}^2}\left(M_y\frac{\partial M_x}{\partial x} - M_x\frac{\partial M_y}{\partial x} + M_y\frac{\partial M_z}{\partial z} - M_z\frac{\partial M_y}{\partial z}\right), \tag{1.64}$$

where D is the DMI constant, and M_i is the i-th-component of the magnetization $\vec{M}(x,t)$ [cf. Eq. (1.30)]. Since $\partial M_z/\partial z = \partial M_y/\partial z = 0$ applies, the

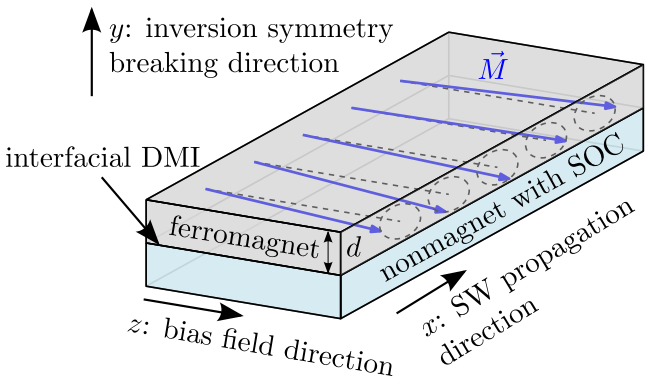

Figure 1.15. Orientation of the Cartesian coordinate system used for the derivation of the characteristics of DE SWs propagating in the presence of an interfacial DMI arising due to the inversion symmetry breaking in a bilayer system consisting of a ferromagnet of thickness d on top of a nonmagnet with strong SOC. (Figure is adapted from Ref. [52].)

[36] Typically, this nonmagnetic layer is a heavy metal. In most of the experiments investigating different aspects of the propagation of DE SWs in the presence of an interfacial DMI, the heavy metal used is Pt [53, 129–131].

[37] In case of a very thin Pt/Co bilayer, for instance, a strong PMA arises at the interface between both layers due to the hybridization between the $3d$ electrons of the Co and the $5d$ electrons of the Pt [83].

corresponding effective magnetic field is [52, 53, 116]

$$\begin{aligned}\vec{H}_{\mathrm{DMI}} &= -\frac{1}{\mu_0}\frac{\partial \varepsilon_{\mathrm{DMI}}}{\partial \vec{M}} = \frac{2D}{\mu_0 M_{\mathrm{S}}^2}\left(\frac{\partial \vec{M}}{\partial x}\times\vec{e}_z\right) \\ &= \frac{2D}{\mu_0 M_{\mathrm{S}}^2}\left(\frac{\partial M_y}{\partial x}\vec{e}_x - \frac{\partial M_x}{\partial x}\vec{e}_y\right) \overset{\text{Eq. (1.30)}}{=} \frac{2D}{\mu_0 M_{\mathrm{S}}^2}\left(\frac{\partial \vec{m}_{\mathrm{dyn}}}{\partial x}\times\vec{e}_z\right). \end{aligned} \tag{1.65}$$

For simplicity, assuming that the precession of $\vec{M}$ is circular, i.e., $m_{x0} = m_{y0} = m_0$ applies [cf. Eq. (1.30)], $\vec{m}_{\mathrm{dyn}}(x,t)$ of a DE SW propagating along the $+x$ direction reads as

$$\vec{m}_{\mathrm{dyn}} = M_{\mathrm{S}}\left[m_0 \sin(\omega t - kx)\,\vec{e}_x + m_0 \cos(\omega t - kx)\,\vec{e}_y\right]. \tag{1.66}$$

In this case, Eq. (1.65) can be rewritten as

$$\vec{H}_{\mathrm{DMI}} = \frac{D^*}{M_{\mathrm{S}}} k \vec{m}_{\mathrm{dyn}} \tag{1.67}$$

with[38] $D^* = \frac{2D}{\mu_0 M_{\mathrm{S}}}$. $\vec{H}_{\mathrm{DMI}}$ is a dynamic quantity, which is proportional to k and oriented either parallel or anti-parallel to $\vec{m}_{\mathrm{dyn}}$ depending on the sign of k. It modifies the expression for the (total) effective magnetic field [cf. Eq. (1.31)]:

$$\vec{H}'_{\mathrm{eff}} = \vec{H}_{\mathrm{eff}} + \vec{H}_{\mathrm{DMI}}. \tag{1.68}$$

Consequently, it is obvious, that in the presence of an interfacial DMI, the characteristics of propagating DE SWs—dispersion and attenuation length—will be different compared with the situation where no interfacial DMI is present as discussed in detail below.

Derivation of the Damon-Eshbach Spin Wave Dispersion in the Presence of an Interfacial Dzyaloshinskii-Moriya Interaction

The steps in the derivation[39] of the DE SW dispersion in the presence of an interfacial DMI are the same as in the case where no interfacial DMI is present [cf. Sec. 1.4.1]. However, due to the modified effective magnetic field $\vec{H}'_{\mathrm{eff}}$, the linearized LLG equation—where the damping term is neglected in the first place—yields an altered system of equations, namely

$$\begin{pmatrix} 0 \\ 0 \end{pmatrix} = \underline{A}' \begin{pmatrix} M_x \\ M_y \end{pmatrix} \tag{1.69}$$

with

$$\underline{A}' := \begin{pmatrix} i(\omega - p\gamma\mu_0 D^* k) & \gamma\mu_0 p\left[H_0 + Jk^2 + M_{\mathrm{S}}(1-\xi) - H_{\mathrm{u}}^{\perp}\right] \\ -\gamma\mu_0 p\left[H_0 + Jk^2 + M_{\mathrm{S}}\xi\right] & i(\omega - p\gamma\mu_0 D^* k) \end{pmatrix}. \tag{1.70}$$

[38] This definition reveals the analogy between $D^* = \frac{2D}{\mu_0 M_{\mathrm{S}}}$ and $J = \frac{2A}{\mu_0 M_{\mathrm{S}}}$, but it should be noted that D is given in J/m^2 while A is given in J/m. Nonetheless, the magnitude of both quantities can be compared when D^* is multiplied by the thickness d of the ferromagnetic layer.

[39] For the derivation, the thin film approximation is employed once again [cf. Sec. 1.4.1].

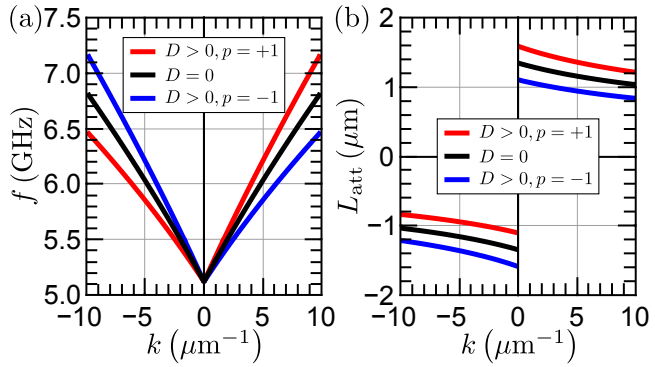

Figure 1.16. Asymmetric DE SW propagation induced by an interfacial DMI[40]. (a) Dispersion. (b) Attenuation length as a function of the DE SW wave number.

The solution to Eq. (1.69) is given by the condition $\det(\underline{A}') \stackrel{!}{=} 0$, thereby revealing the dispersion of DE SWs propagating in the presence of an interfacial DMI [53, 116]

$$\begin{aligned}\omega(k) &= \omega_0(k) + \omega_{\mathrm{iDMI}}(k) = 2\pi\left[f_0(k) + f_{\mathrm{iDMI}}(k)\right] \\ &= \gamma\mu_0\sqrt{\left[H_0 + Jk^2 + M_{\mathrm{S}}\xi(kd)\right]\left[H_0 + Jk^2 + M_{\mathrm{S}}\left(1 - \xi(kd)\right) - H_{\mathrm{u}}^{\perp}\right]} \\ &\quad + \gamma\mu_0 D^* pk\,.\end{aligned} \tag{1.71}$$

In Eq. (1.71), the first term ω_0 is the standard DE SW dispersion [cf. Eq. (1.38)], while the second term ω_{iDMI} arises due to the presence of an interfacial DMI. ω_{iDMI} is a frequency shift in the dispersion of propagating DE SWs, which is linear in k, and its sign depends on the polarity p of the magnetic bias field. Consequently, as depicted in Fig. 1.16(a), for a fixed p, in the presence of an interfacial DMI, the dispersion of counterpropagating DE SWs becomes asymmetric, while it is symmetric in the absence of an interfacial DMI. The signature of this asymmetry—which can also be referred to as another type of nonreciprocity [cf. Sec. 1.4.2]—reverses upon switching the bias field polarity. In general, for $k \cdot p > 0$, the frequency shift is positive, while it is negative when $k \cdot p < 0$. Qualitatively, this DMI-induced frequency shift and its asymmetry can be simply understood by examining the precession term in the LLG equation [cf. Eq. (1.24)]. In the presence of an interfacial DMI it is given by

$$\frac{\mathrm{d}\vec{M}}{\mathrm{d}t} = -\gamma\mu_0\vec{H}'_{\mathrm{eff}} = -\gamma\mu_0\vec{M} \times \left(\vec{H}_{\mathrm{eff}} + \vec{H}_{\mathrm{DMI}}\right). \tag{1.72}$$

As sketched in Fig. 1.17, Eq. (1.72) describes the precessional motion of the magnetization $\vec{M}$ under the influence of $\vec{H}'_{\mathrm{eff}}$. The precession frequency ω is specified by the magnitude of $\vec{M} \times \left(\vec{H}_{\mathrm{eff}} + \vec{H}_{\mathrm{DMI}}\right)$. In case of a DE SW propagating along the $-x$ direction, i.e., $k < 0$, $-\vec{M} \times \vec{H}_{\mathrm{DMI}}$ is oriented anti-parallel to $-\vec{M} \times \vec{H}_{\mathrm{eff}}$ [cf. Fig. 1.17(a)] due to $\vec{H}_{\mathrm{DMI}} \nparallel \vec{m}_{\mathrm{dyn}}$ [cf. Eq. (1.67)], and therefore ω will be lower compared with the case where no interfacial DMI is present. In contrast, for a DE SW propagating along the $+x$ direction, i.e., $k > 0$, $-\vec{M} \times \vec{H}_{\mathrm{DMI}}$ is collinear with $-\vec{M} \times \vec{H}_{\mathrm{eff}}$ [cf. Fig. 1.17(b)] resulting in a larger ω. Moreover, since $|\vec{H}_{\mathrm{DMI}}|$ is proportional to k [cf. Eq. (1.67)], the respective shift in ω towards lower or higher frequencies will increase with increasing DE SW wave number.

[40] The individual dispersions and the wave number dependence of the attenuation length are calculated using the following material and experimental parameters: $|\mu_0 H_0| = 43\,\mathrm{mT}$, $d = 5.4\,\mathrm{nm}$, $\mu_0 M_{\mathrm{S}} = 1.3\,\mathrm{T}$, $\mu_0 H_{\mathrm{u}}^{\perp} = 0.6\,\mathrm{T}$, $\gamma = 180 \times 10^9\,\mathrm{rad/(Ts)}$, $A = 13 \times 10^{-12}\,\mathrm{J/m}$, $D = 0.64\,\mathrm{mJ/m^2}$, and $\alpha = 0.013$.

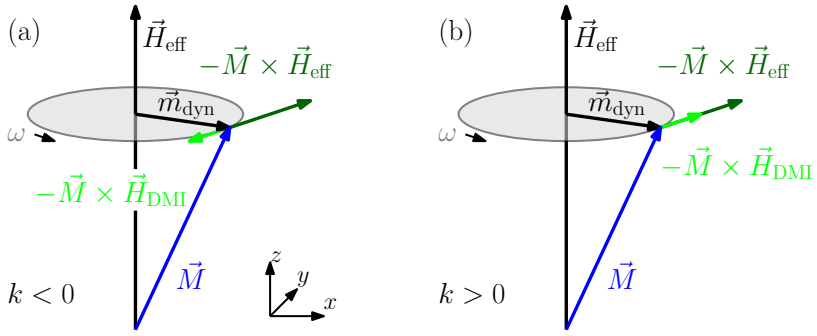

Figure 1.17. Schematic of the origin of the frequency shift in the dispersion of DE SWs propagating in presence of an interfacial DMI. For $k < 0$, the torques arising from $\vec{H}_{\mathrm{eff}}$ and $\vec{H}_{\mathrm{DMI}}$ act in opposite directions, thereby leading to a decrease in ω, while, for $k > 0$, both torques are collinear, thereby causing an increase in ω. (Figure is adapted from Ref. [116].)

Derivation of the Damon-Eshbach Spin Wave Attenuation Length in the Presence of an Interfacial Dzyaloshinskii-Moriya Interaction

For the derivation of the DE SW attenuation length in the presence of an interfacial DMI, both the precession term and the damping term in the LLG equation need to be taken into account. Then, Eq. (1.69) is modified as follows:

$$\begin{pmatrix} 0 \\ 0 \end{pmatrix} = \underbrace{\left[\underline{A}' + \begin{pmatrix} 0 & i\alpha p\omega \\ -i\alpha p\omega & 0 \end{pmatrix}\right]}_{:=\underline{B}'} \begin{pmatrix} M_x \\ M_y \end{pmatrix} . \tag{1.73}$$

Neglecting high-order terms[41] $\mathcal{O}(\alpha^2)$ the solution to this system of equations is a complex ω. Its real part $\mathrm{Re}(\underline{\omega})$ is identical to the DE SW dispersion in the presence of an interfacial DMI [cf. Eq. (1.71)], while its imaginary part is given by

$$\mathrm{Im}(\underline{\omega})^{p=\pm 1} = \alpha\gamma\mu_0 \left(H_0 + Jk^2 - \frac{H_{\mathrm{u}}^{\perp}}{2} + \frac{M_{\mathrm{S}}}{2}\right) \cdot \left(1 + \frac{\omega_{\mathrm{iDMI}}^{p=\pm 1}}{\omega_0}\right) . \tag{1.74}$$

Finally—according to the relation between $\mathrm{Im}(\underline{\omega})$ and L_{att} given in Eq. (1.56)—the DE SW attenuation length in the presence of an interfacial DMI is given by[42]

$$L_{\mathrm{att}}^{p=\pm 1} = \frac{1}{\mathrm{Im}(\underline{\omega})^{p=\pm 1}} \cdot v_{\mathrm{gr}}^{p=\pm 1} . \tag{1.75}$$

According to Eq. (1.75), the presence of an interfacial DMI also induces an asymmetry in the attenuation length of counterpropagating DE SWs as seen in Fig. 1.16(b). As in the case of the asymmetry in the DE SW dispersion, the signature of the asymmetry in L_{att} reverses when the magnetic bias field is

[41] Additionally, since $(A_{12} - A_{21}) \ll A_{12}A_{21}$ applies, $\sqrt{1+x} \approx 1 + \frac{1}{2}x$ (in case of small x) can be applied.

[42] In the presence of an interfacial DMI, the dispersion of propagating DE SWs $\omega(k)$ also depends on p [cf. Eq. (1.71)]. For this reason, the group velocity—$v_{\mathrm{gr}} = \partial\omega/\partial k$—is also dependent on p.

switched[43]. In general, for $k \cdot p > 0$, the absolute value of L_{att} is larger compared to case where no interfacial DMI is present, while it is smaller when $k \cdot p < 0$.

1.4.5 Spin Wave Excitation Using Microwave Antennas

In metallic ferromagnetic systems, propagating magnetostatic DE SWs, which can be detected magneto-optically [cf. Ch. 2], are characterized by excitation frequencies in the low GHz-range and wave numbers ranging from $\approx$1–10 $\mu\mathrm{m}^{-1}$ [cf. Fig. 1.9(b)]. These k-values correspond to SW wave lengths λ in the range from $\approx$6 μm down to $\approx$600 nm. Most commonly these DE SWs are excited by microwave antennas [7, 11, 13, 121, 132–135] whose their lateral dimensions need to be on the same length scale as λ [1]. Typical shapes of microwave antennas utilized in SW propagation experiments are (shorted) coplanar waveguide (CPW) structures [7, 132–135], or even more complicated periodic/meander-shaped antenna structures [11, 13, 121]. It is beneficial to employ the latter type in PSWS experiments [12, 13, 136], where propagating SWs are both excited and detected by inductive microwave antennas, as it exhibits a narrow excitation spectrum around a central wave number [137], while the former type exhibits a broad excitation spectrum [138], which is advantageous in experiments, where it is essential to investigate the SW dispersion over a much wider wave number or frequency range [132, 133, 135].
In the various SW propagation experiments presented in Ch. 3–6, microwave antennas in the shape of shorted CPW structures are employed to excite propagating magnetostatic DE SWs. For this reason, this antenna type and its characteristics as well as the SW excitation process itself along with its peculiarities are discussed in detail below.

A schematic of a microwave antenna in the shape of a shorted CPW structure is shown in Fig. 1.18. It consists of a signal line of width w_{s}, which is separated from the two ground lines of width w_{gr}, by a gap of width w_{g}. The actual figure of merit is the signal-to-ground distance $d_{\mathrm{s,gr}}$—defined as the center-to-center distance—as it specifies the dominant wave number in the corresponding excitation spectrum [1]. Typical values for the widths of the individual CPW constituents are[44]: $w_{\mathrm{s}} = 600\,\mathrm{nm}$, $w_{\mathrm{gr}} = 300\,\mathrm{nm}$, and $w_{\mathrm{g}} = 300\,\mathrm{nm}$, i.e., $d_{\mathrm{s,gr}} = 750\,\mathrm{nm}$.
To excite propagating DE SWs in a metallic ferromagnetic layer, such a microwave antenna is placed on top of this layer while it is concurrently electrically decoupled from it by a thin insulting layer as depicted in Fig. 1.18(b).
By supplying an radio-frequency (rf) current $I_{\mathrm{rf}}(\omega)$ to the microwave antenna a dynamic, spatially inhomogeneous Oersted field $\vec{h}_{\mathrm{dyn}}(\vec{r},t) = \vec{h}^{\,0}_{\mathrm{dyn}}(\vec{r})\, e^{i\omega t}$ is generated around it as sketched in Fig. 1.18(b). It couples inductively to the magnetization of the ferromagnetic layer beneath [1], thereby exciting propagating DE SWs at the same frequency ω when a magnetic bias field is concurrently

[43] The signature of the asymmetry in L_{att} with respect to k and p is opposite to the one in $\mathrm{Im}(\underline{\omega})$—which is the quantity corresponding to L_{att} in BLS measurements [53]—since $\mathrm{Im}(\underline{\omega})$ and $L_{\mathrm{att}} = 1/\mathrm{Im}(\underline{k})$ are linked via v_{gr}.

[44] The smallest possible feature size of the CPW, which is at the edge of feasibility using current common state-of-the-art nano-fabrication techniques, is on the order of about 100 nm. However, a reproducible fabrication of such narrow structures requires a lot of efforts and time.

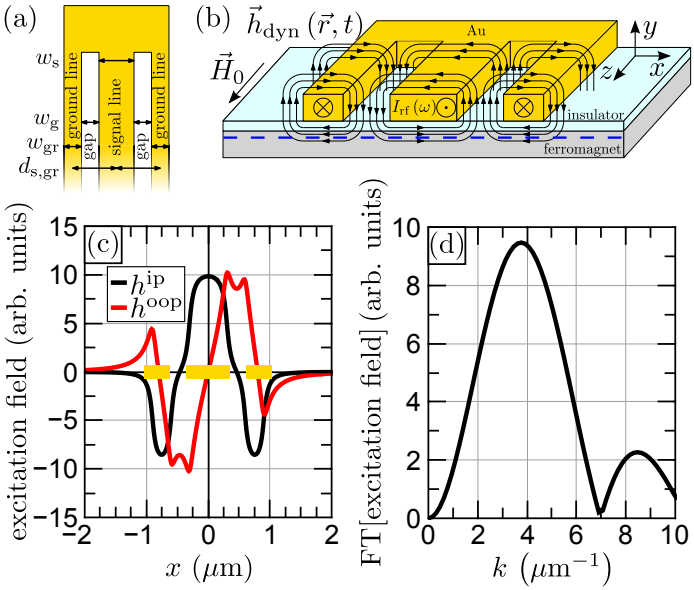

Figure 1.18. (a) Schematic of a microwave antenna in the shape of a shorted CPW. The dimensions of its constituents are labeled as follows: signal line width w_s, ground line width w_{gr}, gap w_{gap}, and signal-to-ground distance $d_{s,gr}$. (b) Schematic of the local orientation of the microwave field $\vec{h}_{dyn}(\vec{r},t)$ generated by a microwave current $I_{rf}(\omega)$ running across an Au microwave antenna which is separated from the ferromagnetic layer beneath by an insulating layer. (c) Spatial profiles along the x direction of the in-plane and out-of-plane components of the excitation field, i.e., $\vec{h}_{dyn}(x) = h^{ip}(x)\,\vec{e}_x + h^{oop}(x)\,\vec{e}_y$, extracted at a fixed distance beneath the microwave antenna inside the ferromagnetic layer [cf. dashed blue line in (b)]. The yellow boxes mark the extends and position of the constituents of the microwave antenna. (d) Excitation spectrum of this antenna, i.e., the Fourier transform of the spatial profile(s) shown in (c).

applied along the z direction, i.e., parallel to the long axis of the microwave antenna[45].
$\vec{h}^0_{dyn}(\vec{r})$ can be calculated numerically using the two-dimensional Biot-Savart law when assuming that the current distribution within the CPW structure is uniform. Due to the spatial symmetry of the microwave antenna along the z direction, $\vec{h}^0_{dyn}(\vec{r},t) = \vec{h}^0_{dyn}(x,y,t)$ holds, and, consequently, it can be decomposed into its in-plane and out-of-plane components:

$$\begin{aligned}\vec{h}_{dyn}(\vec{r},t) &= \vec{h}^0_{dyn}(x,y)\,e^{i\omega t}\\ &= \left(h^{ip}(x,y)\,\vec{e}_x + h^{oop}(x,y)\,\vec{e}_y\right)e^{i\omega t}.\end{aligned} \tag{1.76}$$

For a fixed y coordinate inside the ferromagnetic layer [cf. dashed blue line in Fig. 1.18(b)], the spatial profiles of $h^{ip}(x)$ and $h^{oop}(x)$ are shown in Fig. 1.18(c). $h^{ip}(x)$ is symmetric in x [cf. black curve in Fig. 1.18(c)] while $h^{oop}(x)$ is antisymmetric in x [cf. red curve in Fig. 1.18(c)]. The Fourier transform of the spatial profile(s) of the excitation field(s) yields the excitation spectrum of the microwave antenna as depicted in Fig. 1.18(d). It is a measure for the excitation efficiency of the individual DE SW wave numbers. Since the shape of the

[45] The resulting SW dynamics can be derived by solving the linearized LLG equation using $\vec{M} = \vec{M}_0 + \vec{m}_{dyn}$ in combination with the substitution $\vec{H}^{(\prime)}_{eff} \to \vec{H}^{(\prime)}_{eff} + \vec{h}_{dyn}$ [cf. Eqs. (1.31), (1.68) and (1.30)]. The procedure is very similar to the one presented in Sec. 1.4.1.

spectrum[46] is directly linked to the spatial dimensions of the constituents of the microwave antenna—w_s, w_g, and w_{gr}—it can be tailored to specific needs by modifying the respective dimensions appropriately [cf. Ch. 6].

Finally, the peculiarities of the DE SW excitation process using a microwave antenna are addressed. For a better understanding, this discussion refers to the

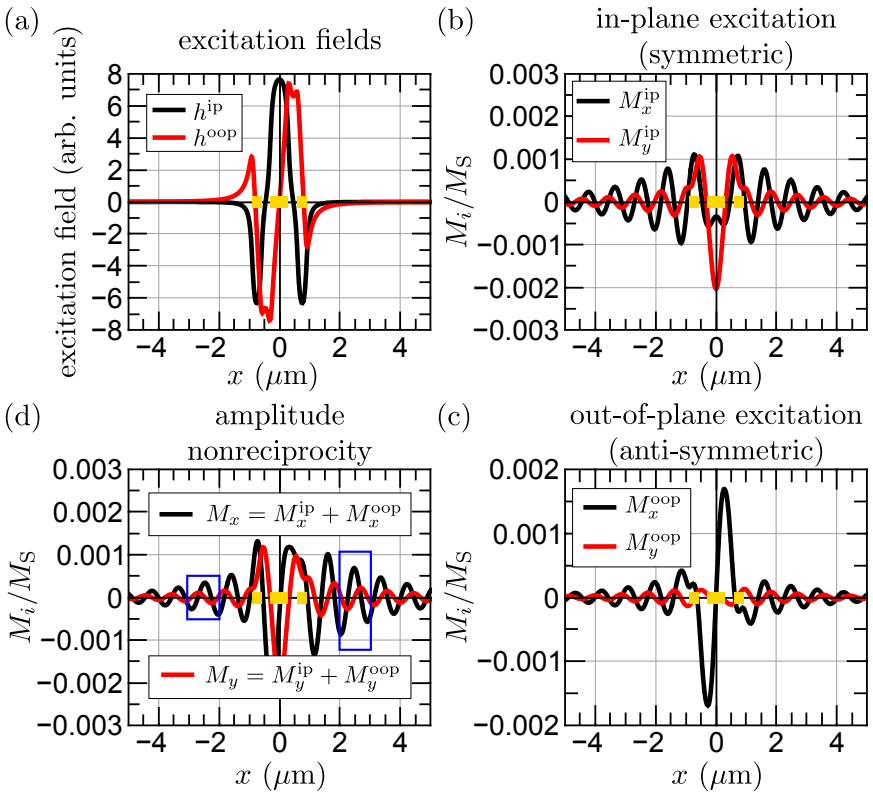

Figure 1.19. Micromagnetic study of the DE SW excitation process in an extended ferromagnetic layer by the in-plane and out-of-plane components of the dynamic excitation field $\vec{h}_{dyn}$ of a microwave antenna[47]. (a) Spatial profiles—along the x direction—of the in-plane and out-of-plane excitation fields generated by the microwave antenna whose position as well as the lateral dimension of its constituents are indicated by the yellow boxes [cf. Fig. 1.18(c)]. h^{ip} is symmetric in x while the out-of-plane field h^{oop} is anti-symmetric in x. (b) Spatial profiles of the in-plane and out-of-plane dynamic magnetization excited only by h^{ip}. (c) Spatial profiles of the in-plane and out-of-plane dynamic magnetization excited only by h^{oop}. (d) Spatial profiles of the in-plane and out-of-plane dynamic magnetization excited by both components of $\vec{h}_{dyn}$. The blue boxes are a guide to the eye to facilitate the observation of the amplitude nonreciprocity. (Figure is adapted from Ref. [139].)

[46] The excitation spectrum is symmetric in k, i.e., it applies to the excitation of DE SWs propagating along either x direction. The wave number of the first maximum in the excitation spectrum does not agree with that one, which is expected due to the signal-to-ground-distance—$k_{exp} = (2\pi)/d_{s,gr}$—since the shorted CPW structure is a non-periodic structure in real space.

[47] These data are extracted from a micromagnetic simulation on a Permalloy ($Ni_{80}Fe_{20}$) film. The material and experimental parameters used are: $f = 10\,\mathrm{GHz}$, $\mu_0 H_0 = -70\,\mathrm{mT}$, $d = 15\,\mathrm{nm}$, $\mu_0 M_S = 0.92\,\mathrm{T}$, $\gamma = 187\times10^9\,\mathrm{rad/(Ts)}$, and $\alpha = 0.0075$. The lateral dimensions of the microwave antenna are: $w_s = 600\,\mathrm{nm}$, and $w_{gr} = w_g = 300\,\mathrm{nm}$.

results shown in Fig. 1.19, which are extracted from a micromagnetic simulation on this excitation process using the micromagnetic simulation program MuMax3 [cf. Appendix B.1].
Both h^{ip} and h^{oop} contribute to the DE SW excitation. The M_x- and M_y-components of the dynamic magnetization resulting from h^{ip} are symmetric in x [cf. black and red curves in Fig. 1.19(b)] while the ones arising due to h^{oop} are anti-symmetric in x [cf. black and red curves in Fig. 1.19(c)]. Consequently, since both dynamic microwave field components contribute to the overall SW excitation, on one side of the microwave antenna, they add resulting in a stronger excitation of $\vec{M}$ on that side [cf. the $x > 0$-range in Fig. 1.19(d)] while, in contrast, on the other side of the antenna, they partially cancel each other, thereby resulting in a weaker excitation of $\vec{M}$ [cf. the $x < 0$-range in Fig. 1.19(d)]. This amplitude asymmetry becomes clearly obvious in Fig. 1.19(d) when comparing the amplitudes of M_x and M_y within the blue boxes on either side of the microwave antenna, whose distance to the edges of the microwave antenna is identical.
This amplitude asymmetry is referred to as amplitude nonreciprocity. In contrast to the modal profile nonreciprocity [cf. Sec. 1.4.2], it is not an intrinsic characteristic of DE SWs, but arises due to the excitation method[48]. The amplitude nonreciprocity reverses upon switching the bias field direction. Despite the amplitude nonreciprocity, DE SWs propagating along the x and $-x$ direction are in-phase. This feature can be clearly seen when comparing the local profiles of M_x and M_y within the blue boxes in Fig. 1.19(d).
Fig. 1.19(d) also reveals, that, in reality, the amplitude of the out-of-plane component of the dynamic magnetization of a propagating DE SW M_y is smaller than that one of the in-plane component M_x. This characteristic arises due to the different demagnetizing fields along the x and y directions. Consequently, as the M_x- and M_y-amplitudes differ [cf. Eq. (1.30)], the precessional motion of $\vec{M}$ around $\vec{H}_{\mathrm{eff}}^{(\prime)}$ is not circular—as sketched in Fig. 1.3—but elliptical.

1.4.6 Lateral Confinement and Spin Wave Mode Coupling

Eq. (1.44) is the in-plane SW dispersion in case of a plain ferromagnetic film with thickness d. In contrast, in case of a nanostructured thin stripe, the width of the stripe w is finite while its length l is quasi infinite, i.e., $l \gg w \gg d$ applies. This lateral confinement yields two significant consequences, which are discussed in the following in terms of propagating DE SWs.

First, the internal magnetic field H_{i} changes considerably. When both static and dynamic contributions are taken into account, its calculation is quite cumbersome [140]. Yet, it simplifies, when the dynamic contributions are neglected and the following assumption is made: The bias field is strong enough to align the magnetization along the z direction, i.e., transverse to the stripe's long axis, everywhere within the stripe except for the very narrow regions close to its ed-

[48] For a ferromagnetic layer with a thickness on the order of a few tens of nanometers, the amplitude nonreciprocity due the excitation of propagating DE SWs using microwave antennas is dominant compared with the modal profile nonreciprocity.

ges. In this case, in those regions, where $\vec{M} \uparrow\uparrow \vec{H}_0$ applies, H_i coincides with the static effective magnetic field, and hence it can simply be modeled[49] as a spatially homogeneous magnetic field [65, 82, 141]:

$$H_\mathrm{i} = H_0 - N_{zz} M_\mathrm{S} \,, \tag{1.77}$$

where N_{zz} is the demagnetizing factor along the z direction, which can be calculated based on the static demagnetizing field(s) [82].

Secondly, the wave vector component in the direction perpendicular to the propagation direction, i.e., k_z, becomes restricted to specific values [142], which can be reasonably estimated by the quantization condition [6]

$$k_z^\mathrm{quant} = n \frac{\pi}{w} \,, \tag{1.78}$$

where $n \in \mathbb{N}^+ \setminus \{0\}$ indicates the respective transverse mode number. When assuming that the dynamic magnetization is totally pinned at either edge of the stripe, the corresponding mode profiles across the width of the stripe, i.e., $m_x\,(z)$, can be modeled as (co-)sine functions with $n-1$ nodes as it is depicted in the top row of Fig. 1.20 for $n = 1$–4 in the case of a 1 μm-wide stripe. More realistic, however, is the assumption that the dynamic magnetization is only partially pinned at the edges. When additionally the inhomogeneity of the internal magnetic

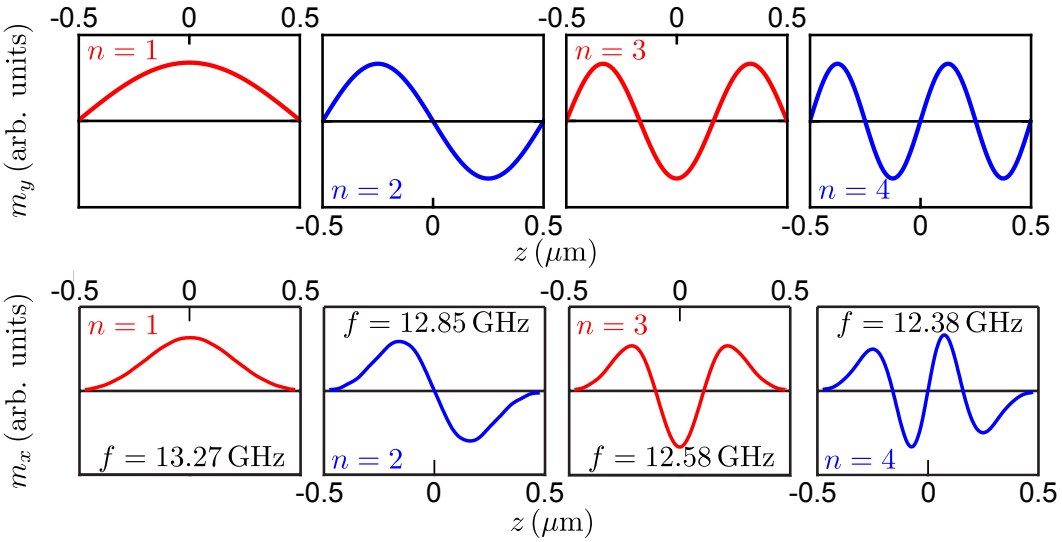

Figure 1.20. Top row: Transverse mode profiles across a stripe of finite width $w = 1\,\mu$m for quantized wave numbers $k_z = n\frac{\pi}{w}$ when the inhomogeneous internal magnetic field is neglected and assuming that the dynamic magnetization is totally pinned at the edges of the stripe. n is the mode number, and odd (even) modes are indicated in red (blue). Bottom row: More realistic transverse mode profiles[50] at the given frequencies when the inhomogeneous internal magnetic field is taken into account and assuming that the dynamic magnetization is only partially pinned at the edges of the stripe. (Figure is partially adapted from Ref. [141].)

[49] Eq. (1.77) does not apply to edge domains and the corresponding edge modes [141].

[50] These profiles are calculated numerically in case of a 33 nm-thick Permalloy ($Ni_{80}Fe_{20}$) stripe while a magnetic bias field of 200 mT is applied along the z direction, i.e., perpendicularly to the stripe's long axis.

field is considered in this situation, also more realistic shapes of the transverse mode profiles can be derived numerically as done by Bayer *et al.* [141]. In this case, they are quasi cosinusoidal modes, which are localized near the center of the stripe as shown in the bottom row of Fig. 1.20, which also covers the modes from $n = 1$–4 in the case of a $1\,\mu$m-wide stripe for the ease of emphasizing the differences with respect to the top row[51].

Due to these two consequences, strictly speaking, Eq. (1.38) only specifies the dispersion of DE SWs propagating in a plain film. For this reason, in the case of a narrow stripe, the DE SW dispersion is usually discussed in terms of a simple model known as the effective stripe model [6]. This model comprises the dispersion of a plain film and a quantized wave vector component perpendicular to the propagation direction [cf. Eq. (1.78)]. This situation is depicted in the in-plane SW dispersion $f\,(k_x, k_z)$ shown in Fig. 1.21(a).

For $k_x = 0$, the SW corresponds to a BV SW propagating in a plain film, i.e., $\vec{k} \parallel \vec{H}_0$ [cf. Eq. 1.41]. First, for small wave numbers k_z, the resonance frequency decreases before increasing again for larger wave numbers [cf. red curve in Fig. 1.7]. Consequently, depending on the (quantized) transverse wave number k_z, the dispersion $f\,(k_x)$ of a DE SW propagating in a stripe starts either below or above the dispersion of the $n = 1$ SW mode. In the latter case, in the regions marked by the orange circles in Fig. 1.21(b), the dispersion branch

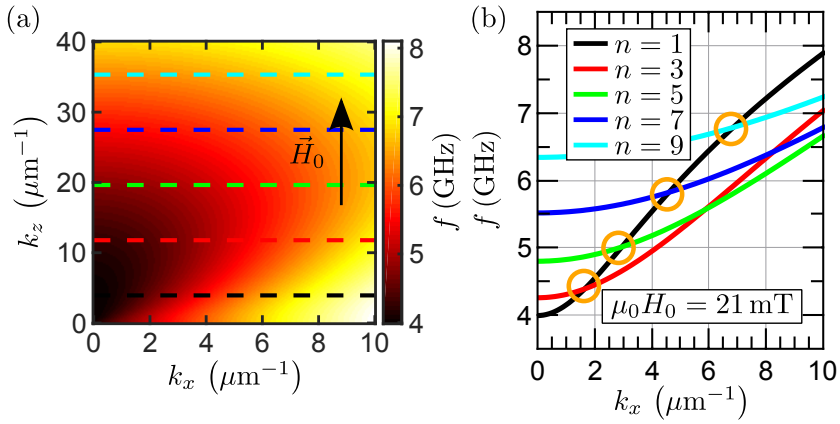

Figure 1.21. Lateral confinement and SW mode coupling in a stripe of finite width w in the effective stripe model[52]. (a) In-plane SW dispersion $f\,(k_x, k_z)$ in case of a thin film at a bias field of 21 mT applied along the z direction [cf. Eq. (1.42)]. The differently-colored dashed horizontal lines indicate those quantized transverse wave numbers $k_z^{\text{quant}} = n\frac{\pi}{w}$, which can be excited when using a microwave antenna, i.e., only the ones with odd n. (b) SW dispersion $f\,(k_x, k_z^{\text{quant}})$. The orange circles indicate crossings of the main propagating SW mode with $n = 1$ with branches of higher order modes. In case of a stripe of finite width, these crossings become anticrossings. (Figure is adapted from Ref. [6].)

[51] The spatial distribution $m_y\,(z)$ is similar in shape, but one order of magnitude smaller [141] due to the ellipticity of the precession [cf. Fig. 1.19(d)].

[52] The respective SW dispersions are calculated in case of a 800 nm-wide and 15 nm-thin Permalloy ($Ni_{80}Fe_{20}$) stripe using the following material parameters: $\mu_0 M_S = 0.95$ T, $\gamma = 176 \times 10^9$ rad/(Ts), and $A = 13 \times 10^{-12}$ J/m.

corresponding to the $n = 1$ SW mode [cf. black line in Fig. 1.21(b)] crosses the branches of the (other) lowest transverse modes.
For a plain film, where SWs are the eigenmodes of the system, which do not interact with each other, the (individual) dispersion branches cross each other without repulsion [cf. Fig. 1.21(b)]. In reality, however, these eigenmodes do not represent the eigenmodes for a stripe of finite width as the mode profile across the stripe width considerably changes since the contribution of the dipolar interaction is significantly modified [cf. Fig. 1.20]. Hence, the modes interact with each other. Usually, this interaction is the strongest, when the frequencies of two branches (nearly) coincide, and results in a repulsion of the (individual) dispersion branches. This repulsion is referred to as an anticrossing. Such anticrossings occur for specific k_x at a given bias field magnitude [cf. Fig. 1.21(b)], and are observed in the case of thin and narrow stripes, while for wider and thicker stripes only a co-propagation of the different transverse modes is observed [143].

When a microwave antenna is utilized to excite propagating DE SWs in a stripe, the excitation field across the width of the stripe is homogeneous [cf. Sec. 1.4.5], and consequently, since odd and even transverse modes exhibit different symmetries [cf. red and blue curves in Fig. 1.20], only modes with odd n are excited at all [cf. dashed lines in Fig. 1.21(a)]. For this reason, anticrossings only occur when two almost degenerate modes of the same symmetry interact[53] [cf. Fig. 1.21(b)].

Anticrossings have a severe impact on the propagation characteristics of the main propagating mode, which is the one with the largest group velocity. As v_{gr} decreases in the vicinity of an anticrossing, and since L_{att} scales with v_{gr} [cf. Eq. (1.56)], an anticrossing manifests as a significant decrease in L_{att}, which can be detected experimentally [6].

1.5 Magneto-Optical Kerr Effect

The magneto-optical Kerr effect (MOKE) occurs when linearly polarized light is reflected from the surface of a magnetic sample resulting either in a change in the state of polarization or in a change in intensity depending on the experimental geometry. There are three different geometries, which are illustrated schematically in Fig. 1.22(a) [65, 119]:

- In the case of the polar MOKE (PMOKE), the magnetization $\vec{M}$ is oriented perpendicular to the sample surface and lies in the plane of incidence of the light. Consequently, this geometry is suited for the investigation of magnetic samples with an out-of-plane magnetization (component). The PMOKE is characterized by a Kerr rotation and a Kerr ellipticity [cf. Fig.1.22(b)].

[53] In general, the different SW modes can interact, but the excitation efficiency of the individual transverse modes scales with $1/n$ [144]. Consequently, it is the $n = 1$ and $n = 3$ modes that are the ones most likely to be excited and to occur.

- In the case of the longitudinal MOKE (LMOKE), $\vec{M}$ is oriented parallel both to the sample surface and to the plane of incidence of the light. Consequently, this geometry is suited for the investigation of magnetic samples with an in-plane magnetization (component). The LMOKE is also characterized by a Kerr rotation and a Kerr ellipticity [cf. Fig.1.22(b)].

- In the case of the transverse MOKE (TMOKE), $\vec{M}$ is parallel to sample surface, but perpendicular to the plane of incidence of the light. Consequently, this geometry is suited as well for the investigation of magnetic samples with an in-plane magnetization (component). However, in contrast to the LMOKE and PMOKE, the TRMOKE is not characterized by a Kerr rotation and a Kerr ellipticity, but only by a change in intensity of the reflected light.

Furthermore, one differentiates whether the incident light is polarized parallel (s) or perpendicular (p) to the plane of incidence. The magnitude of the MOKE depends on the incident angle θ_0 of the light with respect to the surface normal of the magnetic sample [cf. Fig. 1.22(a)] as well as on whether the light is s- or p-polarized. In general, the TMOKE is the weakest MOKE while, in turn, the PMOKE is one order of magnitude more pronounced than the LMOKE.
In case of the LMOKE and PMOKE, the characteristics of the effect—the Kerr rotation and the Kerr ellipticity—can be expressed as a complex Kerr angle

$$\Theta_{\text{Kerr}} = \theta_{\text{Kerr}} + i\eta\,, \tag{1.79}$$

where θ_{Kerr} accounts for the rotation of the plane of polarization while η quantifies the ellipticity, i.e., the ratio between minimum and maximum, as it is depicted schematically in Fig. 1.22(b). Both the Kerr rotation and the Kerr ellipticity reverse sign when the magnetization direction $\vec{M}$ is switched, and Θ_{Kerr} is proportional to M [66, 119].
Microscopically, in a ferromagnetic material, the MOKE arises from the simultaneous occurrence of exchange splitting and SOC [145]. Macroscopically, the MOKE is discussed in terms of the off-diagonal terms in the dielectric tensor $\overline{\overline{\varepsilon}}$,

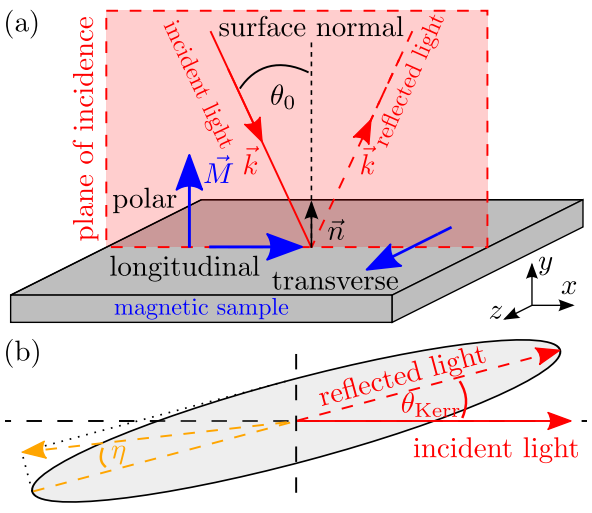

Figure 1.22. (a) Schematic of the orientation of the magnetization $\vec{M}$ with respect to the sample surface and with respect to the plane of incidence of the light in case of the polar, longitudinal and transverse MOKE geometry. (b) The polar and longitudinal MOKE are characterized by a complex rotation of the plane of polarization of initially linearly polarized light upon reflection from the surface of a magnetized sample. The plane of polarization is rotated with respect to the initial one by the Kerr angle θ_{Kerr} while the ellipticity is quantified by the angle η.

which specifies the (magneto-)optical properties of the medium [65, 119, 146–148]. The off-diagonal terms are a consequence of the time-reversal symmetry breaking due to the magnetization $\vec{M}$. In the polar and longitudinal configuration, $\overline{\overline{\varepsilon}}$ is given by [65, 119, 146, 147]

$$\overline{\overline{\varepsilon}} = N^2 \begin{pmatrix} 1 & iQ & 0 \\ -iQ & 1 & 0 \\ 0 & 0 & 1 \end{pmatrix} \text{(polar)} \qquad \text{and} \tag{1.80}$$

$$\overline{\overline{\varepsilon}} = N^2 \begin{pmatrix} 1 & 0 & -iQ \\ 0 & 1 & 0 \\ iQ & 0 & 1 \end{pmatrix} \text{(longitudinal)}\,, \tag{1.81}$$

respectively, where N and Q are the refractive index of the magnetic medium and the magneto-optical parameter or Voigt constant [65, 146, 147], respectively. Both quantities are material-dependent and complex numbers, i.e., they have a real and an imaginary part [119].
Each tensor [cf. Eqs. (1.80) and (1.81)] leads to two normal modes—denoted as σ^- and σ^+—which correspond to left- and right-handed circularly polarized light. To the two modes different refraction indices n, where $n = \sqrt{\varepsilon}$, are assigned, namely [119, 146, 147]

$$n^{\sigma^+,\sigma^-} = N\left(1 \pm \frac{1}{2}\vec{\alpha}_{\vec{k},\vec{M}}Q\right) \qquad \left(n^{\sigma^+,\sigma^-} \in \mathbb{C}\right)\,, \tag{1.82}$$

where $\vec{\alpha}_{\vec{k},\vec{M}}$ is the direction cosine between the magnetization $\vec{M}$ and the propagation vector of the light $\vec{k}$ (inside the magnetic medium) [146]. The real part of n [cf. Eq. (1.82)] specifies the propagation velocity of the respective mode within the medium while the imaginary part quantifies its attenuation [149, 150]. Consequently, initially linearly polarized light—which can be considered as the superposition of left- and right-handed circularly polarized light—decomposes into these two modes upon entering the magnetic medium. Then, the two circular modes propagate with different velocities and attenuate differently inside the magnetic medium. Upon emerging from the magnetic medium in reflection, the two modified modes recombine yielding a rotation in the plane of polarization and an ellipticity.

Whenever the magnetization $\vec{M}$ is oriented along an arbitrary direction and whenever there is a finite angle between the wave vector $\vec{k}$ of the incident (linearly polarized) light and the surface normal of the sample, i.e., $\theta_0 \neq 0°$ holds [cf. Fig. 1.22], the overall MOKE is a combination of the contributions arising from TMOKE, LMOKE and PMOKE.
Furthermore, θ_{Kerr} is a material-dependent quantity which exhibits a significant dependence on the wavelength λ of the incident light. For the common $3d$ ferromagnets—Fe, Co and Ni—θ_{Kerr} shows a maximum at $\lambda \approx 800\,\text{nm}$ [119].

Although the penetration depth of visible light into metals is on the order of a few tens of nanometers[54], the MOKE is a surface-sensitive effect deriving its

[54] In case of Permalloy ($Ni_{80}Fe_{20}$), the penetration depth is about 15 nm at a wavelength of 400 nm [151].

surface sensitivity from the limited thickness of the magnetic structure under investigation, which can be as thin as one atomic layer [148]. Hence, measurements of the MOKE are well suited for example for the investigation of various aspects of SW dynamics in thin magnetic layers [5–7, 132, 133, 135], the characterization of (ultra)thin magnetic films and nanostructures [152], and domain imaging [153].

In the following chapter, the time-resolved Kerr microscopy setup utilized in the different SW propagation experiments [cf. Ch. 3-6] is presented. It is operated in the PMOKE geometry, and hence it is sensitive to the out-of-plane component of the dynamic magnetization of the (DE) SWs [cf. Fig. 1.8] propagating in the magnetic nanostructures.

Chapter 2

Experimental Technique: Time-Resolved Magneto-Optical Kerr Microscopy

Contents

In the magnetic nanostructures, SW dynamics is accessed by time-resolved magneto-optical Kerr microscopy (TRMOKE) performed in the polar geometry using a femtosecond laser system. This technique provides both the required sensitivity and the required spatial and temporal resolution [148, 152]. In the following, the components and the functional principle of the TRMOKE setup used[55] as well as its modes of operation are explained in detail.

2.1 Components and Functional Principle of the Time-Resolved Kerr Microscope

A schematic of the setup is shown in Fig. 2.1. Each sample is mounted in a modified *Cryovac* helium-flow cryostat which, in principle, enables to perform measurements at temperatures ranging from about 5 K up to room temperature[56]. The cryostat is equipped with input connections for microwaves as well as for an electric DC current. It is mounted on a *xyz PI P500* piezo stage which enables to move the sample within the xz plane with a resolution on the order of a few nanometers as well as to fine tune the sample position along the y direction with respect to the focus plane of the objective lens. For a coarse alignment of the sample position within the xz plane the piezo stage is mounted on a mechanical micrometer positioning stage, while for the coarse alignment of the focus plane the objective lens is mounted as well on a micrometer positioning stage.
A 360°-rotatable, computer-controlled electromagnet with an iron yoke in the shape of a horseshoe enables to apply a static magnetic field at any desired angle within the xz plane of the sample. Its magnitude is measured by a Hall probe attached to one of the pole shoes, and the maximum possible field magnitude at the position of the sample, i.e., in the middle of the gap between the pole shoes, is about 250 mT. The error in field is about 0.1 mT.

To be able to optically detect and resolve SW dynamics at GHz frequencies requires a pulsed light source where the probing pulse width is much shorter than one SW oscillation period [cf. Eq. (1.38)]. For this reason, a femtosecond laser system is employed. As illustrated in Fig. 2.1, it consists of a pulsed *Coherent Mira 900* titanium:sapphire (Ti:Sa) laser—2 W output power in CW mode—which is pumped by a *Laser Quantum Finesse* neodymium-doped yttrium aluminum garnet (Nd:YAG) laser at a wavelength of 532 nm with a nominal output power of 10 W. The Ti:Sa laser is tunable within a small range of central wavelength λ_c and pulse width τ_w. Typical values for either quantity are: $\lambda_\mathrm{c} \approx 800\,\mathrm{nm}$, and $\tau_\mathrm{w} \approx 200\,\mathrm{fs}$. The red laser pulses are emitted with a repetition rate f_rep of 80 MHz, i.e., the duration between individual pulses Δt is 12.5 ns, and consequently the dynamic magnetization is probed at certain times $\tilde{t}_n$, which are defined as

$$\tilde{t}_n = n \cdot \Delta t + t_0 \qquad \left(n \in \mathbb{N}^+\right), \tag{2.1}$$

[55] The TRMOKE setup was originally set up by Frank Hoffmann [154] and further improved and modified by Jean-Yves Chauleau and Johannes Stigloher throughout the past years.
[56] All experiments presented in Ch. 3–6 are conducted at room temperature.

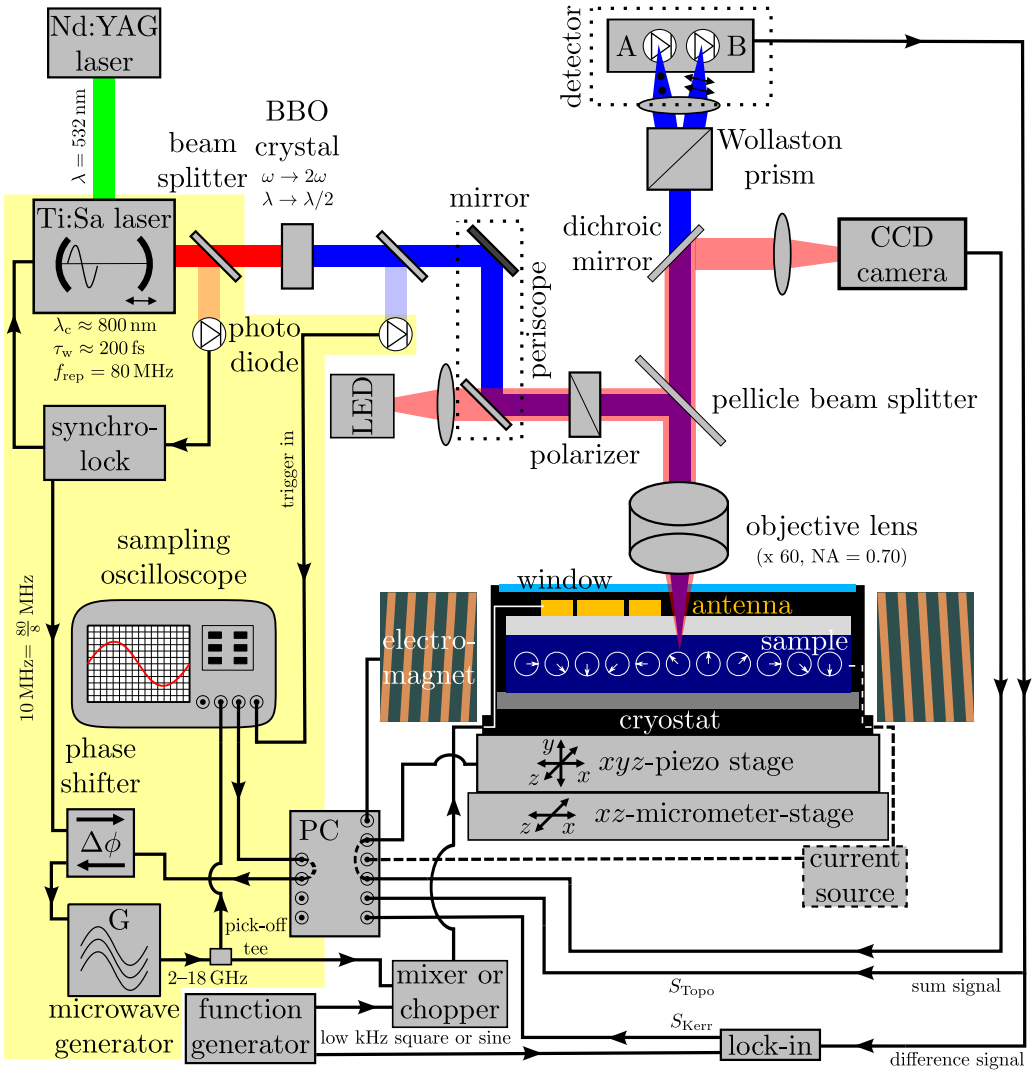

Figure 2.1. Schematic of the TRMOKE setup. A BBO crystal doubles the frequency of the laser pulses that are emitted with a repetition rate of 80 MHz by the Ti:Sa laser, which is pumped by the Nd:YAG laser. The resulting blue light is used for the detection of the dynamic out-of-plane component of the SWs propagating in the magnetic sample. The yellow shaded area covers all components of the setup enabling the phase-locking of the probing laser pulses to the microwave excitation. The red light emitted by the LED is required for the image stabilization. The current source is optional[57]. Further details are provided in the text.

where t_0 is an arbitrary offset in time. It is mandatory, that at each $\tilde{t}_n$ the same state of the dynamic out-of-plane magnetization is probed as it is depicted schematically in Fig. 2.2. In order to achieve this, two conditions must be fulfilled:

(i) The propagating SWs need to be excited at a frequency which is an integer multiple of 80 MHz.

(ii) The phase between the excitation and the detection needs to be constant, i.e., the probing laser pulses have to be phase-locked to the microwave excitation.

[57] It is only used in experiments where an electric dc current needs to be injected across the magnetic sample [cf. Ch. 3].

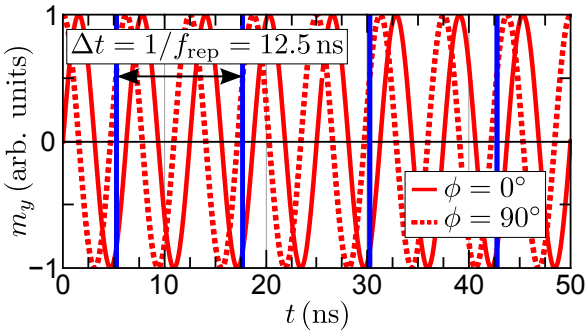

Figure 2.2. Schematic of the principle of phase-locking essential for the detection of the dynamic out-of-plane component of the dynamic magnetization (red) of the propagating SWs. When these SWs are excited at a frequency f which represents an integer multiple of the repetition rate of the probing laser pulses (blue)—$f_{\mathrm{rep}} = 80\,\mathrm{MHz}$—every probe pulse detects the same m_y-value independent of the phase ϕ between excitation and detection.

This phase-locking is realized by using the components of the TRMOKE setup, which are highlighted in yellow in Fig. 2.1, as follows:

The repetition rate of the laser pulses emitted by the Ti:Sa laser is stabilized by the *Coherent Synchrolock 900*. Basically, it is a computer-assisted device, which records the current repetition rate of the pulses via an optical fiber connected to an internal photo-diode, compares it with an internal reference frequency of 80 MHz—which represents the master frequency—and, if required, it adjusts the length of the Ti:Sa laser cavity accordingly by moving a mirror, which is mounted on a piezo tube. Moreover, the *Synchrolock* also sends a 10 MHz (= 80/8 MHz) reference signal via an electronic phase shifter to a *HP8672A* synthesized signal generator providing microwaves at frequencies ranging from 2–18 GHz at nominal output powers in the range from -120 dBm to +8 dBm with a frequency resolution of 1 kHz, 2 kHz, and 3 kHz, respectively, for frequencies ranging from 2.0–6.4 GHz, 6.2–12.4 GHz, and 12.4–18.0 GHz, respectively.
The phase shifter is controlled by a computer, and it is mandatory to be able to change and stabilize the relative phase between the microwave excitation and the optical detection. The term "relative" accounts for the fact that the absolute phase is unknown since arbitrary phases are introduced by every single component of the rf circuit, i.e., by each device and each cable. Yet, they can be regarded as constant. Consequently, an additional arbitrary, but known phase ϕ between excitation and detection can be added using the phase shifter. But, in reverse, ϕ must be stabilized. For this purpose, the microwave excitation is continuously monitored by a *HP54120* digitizing sampling oscilloscope, which is triggered by the signal generated when a portion of the (blue) laser beam hits another fast photo-diode [cf. Fig. 2.1]. The computer processes the oscilloscope signal, fits it to a sine function to determine the current ϕ-value, compares it with the desired ϕ-value and, if required, it instructs the phase shifter to adjust the phase accordingly, thereby stabilizing ϕ. As a result, the probing laser pulses are phase-locked to the microwave excitation. The error in time resulting from this active feedback loop is ≈1 ps which is much less than the period of the microwave excitation. For example, an excitation frequency of 10 GHz corresponds

to a period of 100 ps, and consequently the error in phase is $\approx\pm 3.6°$ which is sufficient to accurately probe SW dynamics.

The function principle of the actual Kerr microscope, which enables to spatially resolve and detect SW dynamics in magnetic nanostructures optically in the first place, is explained in the following:

The red laser pulses emitted by the Ti:Sa laser cross a barium borate (BBO) crystal which leads to a doubling in frequency due to second harmonic generation [149, 150]. The resulting blue laser pulses have a power of about 100 mW and enter the microscope via the periscope, which enables a proper alignment of the laser beam. After passing the linear polarizer the beam hits the pellicle beam splitter at an angle of 45°. Since the nominal splitting ratio between transmission and reflection of the uncoated pellicle beam splitter is 92:8, 8% of the beam intensity is reflected towards the objective lens with a numerical aperture of NA = 0.70 and a magnification of 60. Theoretically, its spatial resolution is given by $d_{\mathrm{min}} = \lambda/(2 \cdot \mathrm{NA}) \approx 270\,\mathrm{nm}$, i.e., it is on the order of the Abbe diffraction limit [149], while, in reality, it is rather in the range between d_{min} and λ. The laser beam hits the objective lens at normal incidence and is focused on the sample. It enters the cryostat via a polarization-conserving window, and becomes elliptically polarized only upon reflection from the surface of the magnetic parts of the sample due to the MOKE [cf. Sec. 1.5].
This experimental measurement geometry corresponds to the polar MOKE geometry [cf. Fig. 1.22(a)] since the laser beam is in fact only sensitive to the out-of-plane component of the propagating SWs, i.e., the y component of the dynamic magnetization [cf. Fig. 2.1]. This fact can be explained as follows: The focused laser beam consists of several partial beams which hit the sample surface at different incidence angles θ_0 which do not correspond to a normal incidence [cf. Fig. 1.22(a)]. Hence, their respective wave vector $\vec{k}$ can be decomposed into components parallel and perpendicular to the sample surface, i.e., $k_{\parallel}$ and $k_{\perp}$, respectively. Consequently—assuming a radial symmetry of the focused laser beam with respect to the sample normal—for each partial beam i there is another partial beam j with $k_{\parallel}^{i} = -k_{\parallel}^{j}$, but $k_{\perp}^{i} = k_{\perp}^{j}$; and therefore the contributions from the longitudinal and transverse MOKE arising due to the in-plane components of the static and dynamic magnetization eventually cancel upon detection, while those due to the polar MOKE remain.
The reflected beam, which contains the magnetic information, passes the pellicle beam splitter—but this time 92% of its intensity are transmitted—and crosses the dichroic mirror before passing the Wollaston prism, where it is split into its two orthogonal polarization components [150]. The resulting (linearly) polarized beams are focused onto the detector unit consisting of two photo diodes—A and B—and a built-in amplifier.
The detector unit outputs the sum signal as well as the difference signal of the two diodes. The former one is proportional to the local reflectivity of the sample surface. As this quantity is material-dependent, different materials on the sample can be distinguished, and consequently a "topography" image of the sample can be acquired when the sample is scanned by the laser beam. For this reason, the sum signal is also denoted as S_{Topo}. The difference signal contains

the magnetic information, i.e., the information about the local magnitude of the out-of-plane component of the dynamic magnetization at a given phase ϕ, since it is proportional to the Kerr angle θ_{Kerr} [cf. Sec. 1.5]. For this reason, it is also denoted as S_{Kerr}.
S_{Kerr} is detected by a *SR830* lock-in amplifier while exploiting the advantage of phase-modulation. For this reason, an *Agilent 33220A* function generator is employed. It ensures that the phase of the microwave excitation is changed by 180° at a low kHz-frequency when passing the mixer (or the chopper) while concurrently acting as the reference for the lock-in amplifier. The alternation in phase can be regarded as quasi-static compared with microwave excitation frequencies in the GHz-range as well as with the 80 MHz repetition rate of the laser pulses. As a result[58], as illustrated in Fig. 2.3, the laser pulses either probe m_y or $-m_y$, and consequently the output signal of the lock-in amplifier processed by the computer is twice as large compared to the case where the microwave excitation would be only switched on and off. Typical lock-in integration times are on the order of hundreds of milliseconds, thereby covering several thousand SW oscillations.

Since drifts in the x, y and z position of the sample can never be excluded and since depending on the mode of operation of the TRMOKE setup [cf. Sec. 2.2], it is mandatory either

(i) to maintain the laser beam on a fixed position on the sample to be able to locally probe the dynamic magnetization [cf. Sec. 2.2.1] or

(ii) to scan the very same section of the sample several times when investigating the spatial distribution of the dynamic magnetization as a function of different experimental parameters [cf. Sec. 2.2.2],

the focus and/or the position of the sample need to be stabilized either during or in between individual measurements. This is achieved by a procedure called

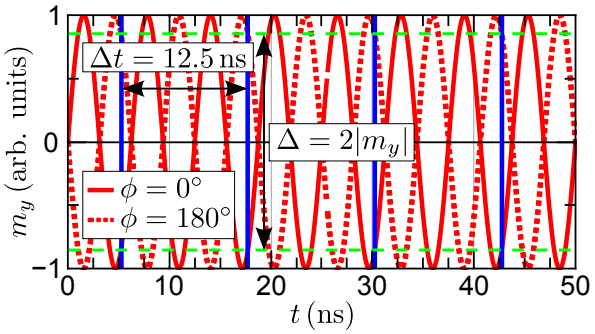

Figure 2.3. Schematic of the principle of phase-modulation. As the phase ϕ between the microwave excitation and the probing laser pulses (blue) is continuously switched by 180° at a low kHz-frequency—while it is concurrently still locked in between—the laser pulses either probe m_y or $-m_y$ (red), and consequently the overall detected signal by the lock-in amplifier Δ is twice as large compared with the case where the microwave excitation would be only switched on and off.

[58] For simplicity, a circular precessional motion of the magnetization around its equilibrium position is assumed.

"image stabilization". For this purpose, as shown in the schematic in Fig. 2.1, a large section of the sample—a circle with a diameter of ≈50 μm—is illuminated by the red light emitted by a LED. The path of the red light inside the microscope is identical with the one of the blue light up to the dichroic mirror where the blue light is transmitted while the red light is reflected, and then focused onto a CCD camera. The camera is connected to the computer where the current red light image is compared with a red light reference image—recorded prior to the beginning of the actual measurement—by a software in order to detect drifts in the focus as well as in the position of the sample within the xz plane. Whenever required, the software moves the xyz piezo stage to compensate for either drift, thereby moving the sample back to its "initial" local and focal position.

2.2 Modes of Operation

For the detection of propagating DE SWs [cf. Sec. 1.4.1] the TRMOKE setup can be operated in two modes, which provide complementary information: the SW spectroscopy mode, or the SW imaging mode. Each mode as well as the analysis and interpretation of the resulting data are explained in detail below.

2.2.1 Spin Wave Spectroscopy

In the spectroscopy mode, the microwave excitation frequency f, the microwave power and the phase ϕ are fixed while the laser beam is continuously kept on a given position $(x_{\text{fixed}}, z_{\text{fixed}})$ on the magnetic structure using the image stabilization routine. This position is usually some micrometer away from the edge of the microwave antenna so that the actual measurement is not affected by its dynamic Oersted fields [cf. Sec. 1.4.5]. Then, the magnitude of the magnetic bias field H_0 applied along the z direction is swept while concurrently recording the corresponding Kerr signal S_{Kerr}. The resulting $S_{\text{Kerr}}(H_0)$ curve is called SW resonance spectrum. An example is shown in Fig. 2.4.
The shape of the SW resonance spectrum is given by the convolution of the

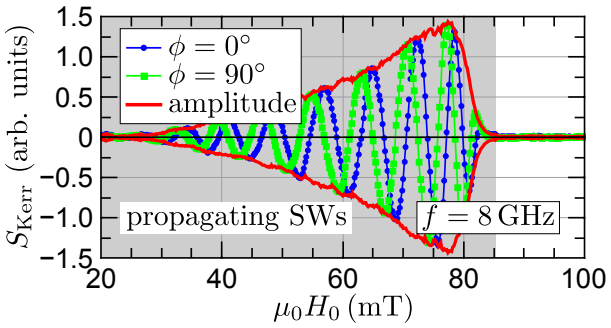

Figure 2.4. Example of the result when operating the TRMOKE setup in the SW spectroscopy mode: The blue and green curves are DE SW resonance spectra recorded at 8 GHz at two different phases ϕ (on a 15 nm-thin, micrometer-wide $Ni_{80}Fe_{20}$ stripe and some micrometer away from the edge of the microwave antenna). The absolute local DE SW amplitude (red curves) results from the combination of both spectra according to Eq. (2.2). The field range, where propagating DE SWs occur, is marked in grey.

excitation spectrum of the microwave antenna [cf. Fig. 1.18(d)] with the respective DE SW dispersion curve [cf. Eq. 1.38]. Several resonances occur since the laser beam locally probes the magnitude of the out-of-plane component of the dynamic magnetization. The value of this quantity changes continuously since the SW wave number k (SW wavelength $\lambda = 2\pi/|\vec{k}|$) decreases (increases) as the magnitude of the applied bias field increases. Moreover, since $S_{\mathrm{Kerr}}(x_{\mathrm{fixed}}, z_{\mathrm{fixed}}) \sim m_y(x_{\mathrm{fixed}}, z_{\mathrm{fixed}})$, it does not represent the absolute SW amplitude, but only the "relative" SW amplitude at the given fixed phase [cf. Fig. 2.2]. The absolute SW amplitude at $(x_{\mathrm{fixed}}, z_{\mathrm{fixed}})$ and its bias field dependence [cf. red curve in Fig. 2.4] can be accessed easily by recording SW resonance spectra at two different phases ϕ_i and ϕ_j [cf. blue and green curves in Fig. 2.4], which need to be separated from each other by 90°, and by combining them as follows [cf. Fig. 2.2]:

$$\text{abs. SW amplitude}(H_0) \sim \sqrt{S_{\mathrm{Kerr}}(H_0, \phi = 0°)^2 + S_{\mathrm{Kerr}}(H_0, \phi = 90°)^2}\,. \quad (2.2)$$

The grey shaded area in Fig. 2.4 marks the bias field range where propagating DE SWs can be observed. In case of a magnetic structure where the thin film approximation is applicable, the threshold value of the bias field magnitude at which the Kerr signal vanishes can be specified. In this case, it corresponds to the FMR resonance field at the given excitation frequency f [cf. Eq. (1.47)].

It is noted that distinct changes in the characteristics of the SW resonance spectrum occur when the nominal microwave power set at the microwave generator is so intense that the DE SW excitation process becomes nonlinear [1, 2, 138]. However, in the different SW propagation experiments presented in Ch. 3–6, a linear DE SW excitation by the dynamic in-plane and out-of-plane microwave fields of the microwave antenna [cf. Sec. 1.4.5] is observed at nominal microwave output powers ranging from 0 to +8 dBm.

2.2.2 Spin Wave Imaging

In the imaging mode, the magnetic bias field H_0, the excitation frequency f, the microwave power, and the phase ϕ are fixed. Then, using the piezo stage the sample is moved within the xz plane on a given grid beneath the laser beam while concurrently $S_{\mathrm{Topo}}(x, z)$ and $S_{\mathrm{Kerr}}(x, z)$ are recorded, thereby acquiring two images, whose resolution, i.e., the pixel size of the image, is prescribed by the spatial resolution of the Kerr microscope.
The topography image [cf. top graph in Fig. 2.5(a)] visualizing the local reflectivity of the sample is used as the reference image to determine the position and the orientation of the microwave antenna as well as of the magnetic structure(s) in the corresponding Kerr image [cf. bottom graph in Fig. 2.5(a)]. Since $S_{\mathrm{Kerr}}(x, z) \sim m_y(x, z)$, the Kerr image reveals the spatial distribution of the magnitude of the dynamic out-of-plane magnetization, i.e., it displays the spatial profile of the excited DE SWs propagating in the magnetic structure. Usually, the recorded Kerr images cover DE SWs propagating on either side of the microwave antenna.
From such an image, on either side of the microwave antenna, line scans are extracted along the propagation direction of the SWs in the magnetic structure

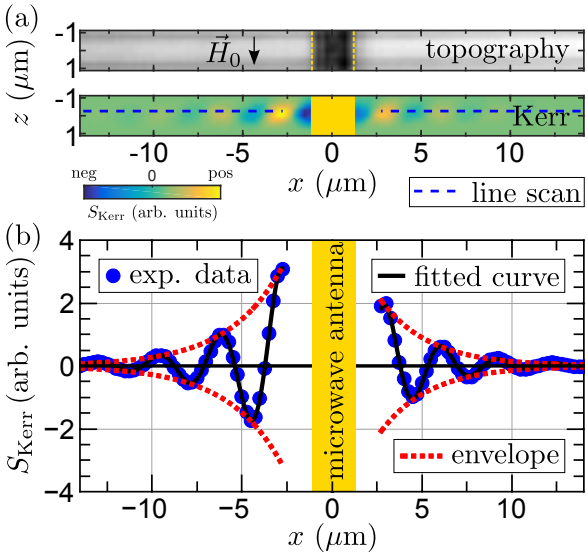

Figure 2.5. Example of the result when operating the TRMOKE setup in the SW imaging mode (on a 15 nm-thin, micrometer-wide $Ni_{80}Fe_{20}$ stripe at $f = 8\,\mathrm{GHz}$, $\phi = 0°$, and $\mu_0 H_0 = +75\,\mathrm{mT}$): (a) The topography image (top) displays the local reflectivity of the sample and is used to determine both the position of the microwave antenna (yellow) and the magnetic stripe in the corresponding simultaneously acquired Kerr image (bottom). (b) Line scans extracted along the blue dashed lines marked in the Kerr image on either side of the microwave antenna $\approx 1\,\mu$m away from its edges. The line scans are fitted to Eq. (2.3). The amplitude nonreciprocity is clearly visible when comparing the envelopes on either side of the microwave antenna.

as denoted by the dashed blue lines in the bottom graph in Fig. 2.5(a). These line scans are either one-dimensional or two-dimensional, i.e., the former ones are simply extracted at a fixed z coordinate, i.e., $S_{\mathrm{Kerr}}(x, z_{\mathrm{fixed}})$, while the latter ones initially cover several neighboring lines with different z coordinates, which are then averaged along the z direction, i.e., $S_{\mathrm{Kerr}}(x) = \sum_i^j S_{\mathrm{Kerr}}(x, z_i)/(j-i)$ with $i, j \in \mathbb{N}$, thereby also yielding one-dimensional line scans. In either case, they start $\approx 1\,\mu$m away from the edge of the microwave antenna in order to exclude those sections of the magnetic structure, where the detected Kerr signal arises indeed due to the dynamic out-of-plane magnetization of the propagating DE SWs, but where it might also be affected by the dynamic Oersted field of the microwave antenna [cf. Sec. 1.4.5].

To determine the two fundamental quantities characterizing propagating DE SWs—the wave number k and the attenuation length L_{att} [cf. Sec. 1.4.1]—each one-dimensional line scan $S_{\mathrm{Kerr}}(x)$ is fitted to an exponentially decaying sine function given by

$$S_{\mathrm{Kerr}}(x) = \tilde{S}_{\mathrm{Kerr}} \cdot \sin(k \cdot x + \varphi_0) \cdot \exp\left(-\frac{x}{L_{\mathrm{att}}}\right) + S_{\mathrm{Kerr}}^{\mathrm{off}}, \tag{2.3}$$

as shown exemplarily in Fig. 2.5(b). $\tilde{S}_{\mathrm{Kerr}}$, φ_0 and $S_{\mathrm{Kerr}}^{\mathrm{off}}$ represent the three other mandatory independent fit parameters besides k and L_{att}. Unless otherwise stated, positive (negative) k- and L_{att}-values correspond to DE SWs propagating along the $+x$ ($-x$) direction.

Using the values of the resulting fit parameters the envelope

$$\text{envelope}[S_{\text{Kerr}}(x)] = \pm\tilde{S}_{\text{Kerr}} \cdot \exp\left(-\frac{x}{L_{\text{att}}}\right) + S_{\text{Kerr}}^{\text{off}} \tag{2.4}$$

can be calculated and plotted for either SW propagation direction with respect to the microwave antenna as depicted by the dashed red lines in Fig. 2.5(b). This representation is beneficial for example for the visualization of the amplitude nonreciprocity [cf. Sec. 1.4.2]. Moreover, since the envelope represents the absolute SW amplitude at a fixed x position, it can also be imaged directly. For this purpose, two Kerr images $S_{\text{Kerr}}^{i}(x,z)$ and $S_{\text{Kerr}}^{j}(x,z)$ are recorded at different phases ϕ_i and ϕ_j, which are separated from each other by 90°. Then, these images are combined as prescribed by Eq. (2.2).

Chapter 3

Determination of the Key Spin-Transfer Torque Parameters for $Ni_{80}Fe_{20}$ from Spin Wave Doppler Experiments

The results presented in this chapter are published in [132]:

J.-Y. Chauleau, H. G. Bauer, **H. S. Körner**, J. Stigloher, M. Haertinger, G. Woltersdorf, and C. H. Back.
Self-consistent determination of the key spin-transfer torque parameters from spin-wave Doppler experiments.
Phys. Rev. B **89**, 020403(R) (2014).

Contents

3.1 Motivation and Goal

Spin-transfer torques (STT) arise when an electric current interacts with a non-homogeneous region of magnetic texture. The action of the STT on a continuous magnetization distribution is theoretically well modeled by the Landau-Lifshitz-Gilbert equation extended by the adiabatic and nonadiabatic STT terms, which reads as follows [cf. Eq. (1.29)]:

$$\frac{\mathrm{d}\vec{M}}{\mathrm{d}t} = -\gamma\mu_0\vec{M}\times\vec{H}_{\mathrm{eff}} + \frac{\alpha}{M_{\mathrm{S}}}\vec{M}\times\frac{\mathrm{d}\vec{M}}{\mathrm{d}t} \underbrace{-\left(\vec{u}\cdot\vec{\nabla}\right)\vec{M}}_{\text{adiabatic STT term}} \underbrace{+\frac{\beta}{M_{\mathrm{S}}}\vec{M}\times\left[\left(\vec{u}\cdot\vec{\nabla}\right)\vec{M}\right]}_{\text{nonadiabatic STT term}} . \tag{3.1}$$

This equation of motion is parameterized by three main quantities, which are highlighted in red: the intrinsic Gilbert damping parameter α, the spin-drift velocity $\vec{u}$, and the nonadiabatic parameter β. $\vec{u}$ is related to the spin polarization P of the electric current as follows [cf. Eq. (1.27)]:

$$\vec{u} = \frac{g\mu_{\mathrm{B}}}{2eM_{\mathrm{S}}}\cdot P\cdot\vec{j}\,. \tag{3.2}$$

Although Eq. (3.1) is well established, there is no consensus on the exact values of these parameters for a given magnetic texture and sample geometry even for the prototypical material Permalloy ($Ni_{80}Fe_{20}$). The discrepancies are the largest for the nonadiabatic parameter β. Theoretical studies have revealed that the value of β is dominated by the electronic band structure and details of the magnetic texture [97, 100, 106]. However, the lack of consistency prevents a clear experimental verification.
So far, all experimental studies have been performed using three different kinds of inhomogeneous magnetic textures: DWs, vortex cores (VCs), and SWs.

Studies of the behavior of DWs and VCs subjected to an electric current have provided tremendous breakthroughs in terms of current-induced magnetization dynamics [111, 155–157]. However, their respective magnetic texture are fairly complex, they are subjected to pinning and transformations, and their STT-induced dynamics is a consequence of a subtle combination of α, $\vec{u}$, and β, thereby preventing an independent access to each of these three key parameters.

On the other side, SW propagation experiments have proven to be of great relevance for the determination of P in the pioneering work on the current-induced SW Doppler shift by Vlaminck and Bailleul [11] as well as in the work of Zhu *et al.* [48], both of them using inductive detection techniques. Conceptually, the action of the STT arising upon the interaction of a spin-polarized electric current with a propagating SW can be divided into two main effects [cf. Sec. 1.4.3 for details]:

(i) The adiabatic STT leads to a shift in the SW frequency [cf. Eq. (1.61b)]:

$$\omega \to \omega + \Delta\omega_{\mathrm{STT}} = \omega + \vec{u}\cdot\vec{k}\,. \tag{3.3}$$

At a fixed excitation frequency, this shift in the SW frequency is equivalent to a shift in the SW wave number k [cf. Appendix A].

(ii) The nonadiabatic STT causes a change of the absolute value of the magnetic damping parameter [cf. Eq. (1.63a)]:

$$\alpha \rightarrow \alpha + \Delta\alpha_{\mathrm{STT}} = \alpha - \beta \frac{\vec{u} \cdot \vec{k}}{\omega} \,. \tag{3.4}$$

A change in the magnetic damping parameter manifests as a variation in the SW attenuation length L_{att} [cf. Eq. (1.56)].

Upon highlighting the key parameters of current-induced magnetization dynamics in Eqs. (3.3) and (3.4) in red once again, it becomes immediately clear that a study of the action of a spin-polarized electric current on propagating SWs enables in fact an independent determination of all three parameters in one single experiment. Yet, to achieve a consensus especially on the value of β, it is mandatory to access all parameters from the identical structure, since even small changes in the sample structure may result in significantly different values for each parameter—e.g., as reported in a study on the thickness dependence of P [12]—and since the precise evaluation of α in nanostructured elements—e.g., disks, squares, and stripes—remains a delicate issue [158, 159].

A first step towards the successful realization of this goal has been reported by Sekiguchi *et al.* [49]. They performed real-time measurements of the current-induced SW Doppler shift(s) using an inductive technique on a series of $Ni_{80}Fe_{20}$ films, which actually allowed them to evaluate the values of the three key STT parameters, but they still had to resort to the results of micromagnetic simulations.

The goal of this study is to demonstrate the applicability of an alternative approach, which enables a direct, self-consistent, and fully experimental assessment (of the values) of the key STT parameters for $Ni_{80}Fe_{20}$ without resorting to micromagnetic simulations. This approach employs DE SWs propagating in a submicron $Ni_{80}Fe_{20}$ stripe and is based on a detailed optical and simultaneous detection of the complete set of SW parameters and their current-induced changes using TRMOKE, where the main quantities of interest are k and L_{att}, which can be regarded as the real and imaginary parts of a complex wave number $\underline{k}$. The key advantage of TRMOKE is that it enables to detect $\underline{k}$ and its current-induced changes simultaneously, thereby allowing to apply in the first place these analytical expressions for the evaluation of the individual STT parameters, which result from an analytical model that was implemented in this case by Hans Bauer [138]. The key features of these expressions are a disentanglement of the individual STT parameters and the fact that all occurring quantities can be determined experimentally on the very same magnetic structure.

3.2 Samples: Layout, Fabrication and Characterization

The layout of the sample(s) used for this study is illustrated in the SEM image shown in Fig. 3.1(a). These samples are fabricated in several steps:

In the first step, 70 μm-long stripes having $35 \times 15\,\mu m^2$ large rectangles attached at either end are patterned by electron beam lithography (EBL), thermal evaporation of $Ni_{80}Fe_{20}$(15 nm)/Al(3 nm) and liftoff on a GaAs substrate. The layer stack is illustrated in the schematic shown in Fig. 3.1(b). The Al layer oxidizes at ambient conditions and preserves the magnetic layer against oxidation. The nominal width of the stripes is varied between 800 nm and 5 μm. For the injection of an electric current across the stripe, in the next step, on top of each $Ni_{80}Fe_{20}$ rectangle, an additional pad of similar size along with two large current leads attached to it is defined by optical lithography, thermal evaporation of Cr(10 nm)/Au(60 nm) and liftoff. Prior to the evaporation of Cr/Au the insulating, oxidized Al layer is removed both by wet etching and Ar^+-ion pre-sputtering to ensure a good ohmic contact between the metallic layers. In the last step, as shown in Fig. 3.1(c), a microwave antenna in the shape of a shorted CPW is patterned across the stripe by EBL, thermal evaporation of Cr(10 nm)/Au(60 nm) and liftoff. It is electrically decoupled from the magnetic stripe by a 50 nm-thick insulating layer of Al_2O_3 grown beforehand by atomic layer deposition (ALD). The nominal width of the signal line is 600 nm while the nominal width of the ground lines and the gaps is 300 nm. The excitation spectrum of this microwave antenna [cf. Sec. 1.4.5] is fairly broad, which enables an efficient excitation of propagating (DE) SWs in the $Ni_{80}Fe_{20}$ stripe covering a continuum of SW wave numbers k in the wave number range of interest, i.e., $k \approx 1$–$9\,\mu m^{-1}$.

A $Ni_{80}Fe_{20}$ layer grown under the same conditions as the patterned stripes is

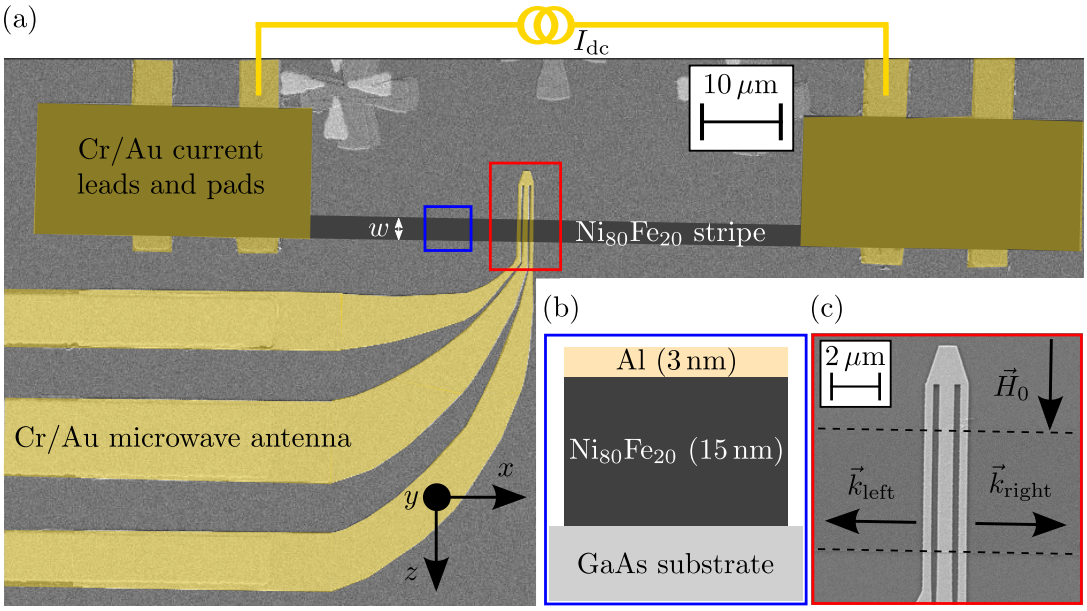

Figure 3.1. (a) SEM image of one of the fabricated samples. The microwave antenna in the shape of a shorted CPW, the current leads/pads and the magnetic stripe are highlighted. An electric dc current I_{dc} can be injected across the $Ni_{80}Fe_{20}$ stripe of width w via the current leads/pads attached to its either ends. (b) Schematic of the stripe layer stack [cf. blue box in (a)]. (c) Close-up SEM image of the microwave antenna [cf. red box in (a)] illustrating the DE measurement geometry.

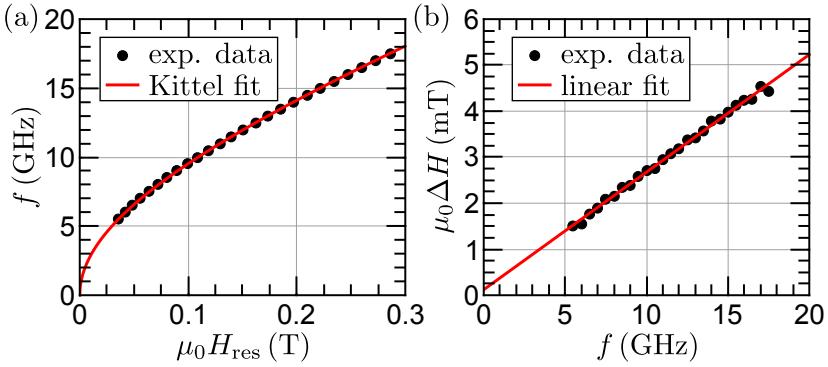

Figure 3.2. In-plane FMR characterization of a $Ni_{80}Fe_{20}$ full film. (a) Frequency dependence of the resonance field. (b) Frequency dependence of the linewidth.

characterized both by in-plane FMR measurements[59] performed at room temperature and superconducting quantum interference device (SQUID) measurements in the range from 270–330 K. At room temperature[60] the latter one reveals the saturation magnetization: $\mu_0 M_S = 0.92\,\mathrm{T}$. The results of the in-plane FMR measurements are shown in Fig. 3.2. The Kittel fit to the frequency dependence of the resonance field H_{res} [cf. Fig. 3.2(a)] yields the gyromagnetic ratio: $\gamma = (187 \pm 7) \times 10^9\,\mathrm{rad/(Ts)}$. The intrinsic Gilbert damping parameter is deduced from the slope of the linear fit to the frequency dependence of the in-plane FMR linewidth [cf. Fig. 3.2(b)]: $\alpha = (0.0076 \pm 0.0001)$.

3.3 Implementation of the Experiment and Data Analysis

The study is performed in the DE geometry: As illustrated in Fig. 3.1(c), DE SWs are excited by the microwave antenna and propagate along the x direction on either side in the $Ni_{80}Fe_{20}$ stripe, whose static magnetization is maintained transverse to its long axis by a magnetic bias field $\vec{H}_0$ applied along the z direction. To distinguish either propagation direction, the labeling and sign convention is as follows: DE SWs propagating along the $+x$ ($-x$) direction, i.e., on the right (left) side of the microwave antenna, have the wave vector $\vec{k}_{\mathrm{right}} = k_{\mathrm{right}}\vec{e}_x$ ($\vec{k}_{\mathrm{left}} = k_{\mathrm{left}}\vec{e}_x$) with the wave number $k_{\mathrm{right}} > 0$ ($k_{\mathrm{left}} < 0$). If not stated otherwise, the microwave excitation frequency f is set to 10.00 GHz.
For those measurements, where an electric dc current is injected across the $Ni_{80}Fe_{20}$ stripe, the following sign convention applies: For a positive (negative) current, i.e., $I > 0$ ($I < 0$), the corresponding current density $\vec{j}$ is oriented along the negative (positive) x direction, i.e., it is oriented opposite to the direction of flow of the electrons.

SW dynamics in the $Ni_{80}Fe_{20}$ stripe is accessed magneto-optically by TRMOKE [cf. Ch. 2]. The setup is operated in either mode to obtain complementary infor-

[59] The FMR measurements were performed and analyzed by Markus Härtinger.
[60] Here, room temperature stands for $T = 300\,\mathrm{K}$, as this was the average temperature in the lab during this SW propagation experiment.

mation. If not stated otherwise, the phase ϕ between the microwave excitation and the probing laser pulses is set to 0°. In the spectroscopy mode [cf. Sec. 2.2.1], the laser spot is maintained on a fixed position on the $Ni_{80}Fe_{20}$ stripe—≈3 μm away from the center of the microwave antenna on either side—and by sweeping the bias field magnitude at fixed f, SW resonance spectra are recorded. In the imaging mode [cf. Sec. 2.2.2], at a fixed bias field, at fixed ϕ, and at fixed f, the sample is scanned in the xz plane, thereby acquiring a spatial mapping of the local sample reflectivity and the local magnetic signal(s). Typically, the Kerr (and topography) images cover both sides of the $Ni_{80}Fe_{20}$ stripe with respect to the microwave antenna, thereby enabling the simultaneous study of the DE SW characteristics for either propagation direction at a given set of experimental parameters.

In the Kerr images, first, the position of the microwave antenna is ascertained from the corresponding topography image. Then, line scans along the x direction are extracted in the middle of the stripe starting ≈3 μm from the center of the microwave antenna on either side. These line scans are fitted to an exponentially decaying sine function to deduce the two main quantities of interest for this study: k and L_{att}. Whenever reasonable for the ease of the representation of the experimental data, these two quantities are expressed by a complex wave number $\underline{k} = \mathrm{Re}\,(\underline{k}) + i \cdot \mathrm{Im}\,(\underline{k})$, where they represent the real part and the inverse of the imaginary part, respectively [cf. Sec. 1.4.1].

The experimental approach of this study is composed of three steps, thereby enabling an independent and self-consistent determination of the key STT parameters:

1. In the case, where no electric current is applied, i.e., $I = 0$, the DE SW characteristics are precisely investigated by magnetic imaging.

2. An electric current is applied, i.e., $I \neq 0$, and the current-induced changes in DE SW characteristics are analyzed both qualitatively and quantitatively.

3. The key parameters of current-induced magnetization dynamics—α, u, P, and β—are deduced.

All experimental results presented and discussed below are obtained from DE SW propagation experiments performed on one single 855 nm-wide $Ni_{80}Fe_{20}$ stripe[61].

3.4 Experimental Results and Discussion

In the following, the results of each step of the experimental approach are presented and discussed, starting with the DE SW characteristics in the absence of an electric current [cf. Sec. 3.4.1], followed by the current-induced changes in DE SW characteristics [cf. Sec. 3.4.2] and the determination of the key STT parameters [cf. Sec. 3.4.3].

[61] Its width is determined from a SEM image of the sample.

3.4.1 Spin Wave Characteristics without an Applied Electric Current

The first step of the study is the detailed characterization of the excited propagating DE SW modes by magnetic imaging. Based on the individual Kerr images, first, the bias field dependencies of the quantities of interest—k, L_{att}, and v_{gr}—are determined, before verifying the equivalence of both propagation directions.

Characterization of Spin Wave Modes—Determination of the Bias Field Dependencies of the Quantities of Interest

By recording Kerr images at 10.00 GHz at different bias fields [cf. Fig. 3.3(a)] and analyzing them according to the procedure described in Sec. 3.3, the bias field dependencies of k and L_{att} are assessed. In the field range covered, k decreases linearly with increasing bias field from $\approx 6\,\mu\mathrm{m}^{-1}$ to $\approx 1\,\mu\mathrm{m}^{-1}$ [cf. black symbols in Fig. 3.3(b)], which, in turn, corresponds to an increase in the SW wavelength—given by $\lambda = 2\pi/|\vec{k}|$—which is clearly visible in the selection of Kerr images shown in Fig. 3.3(a). $L_{\mathrm{att}}(H_0)$ reveals that L_{att} is on the order of $\approx 2\,\mu\mathrm{m}$ up to $\approx 115\,\mathrm{mT}$, and, for larger bias fields, it slightly decreases to $\approx 1.5\,\mu\mathrm{m}$.
To determine the group velocity of the propagating DE SWs, these measurements are repeated at excitation frequencies 80 MHz above and below 10 GHz [cf. red and blue symbols in Fig. 3.3(b)]. From the three frequency-dependent $k(H_0)$-curves the bias field dependence of v_{gr} [cf. Fig. 3.3(e)] is deduced from the slope of a linear fit to $v_{\mathrm{gr}}(H_0) = 2\pi\left(\partial k(H_0)/\partial f\right)^{-1}$ at fixed H_0. v_{gr} is on the order of about 1.5 km/s.

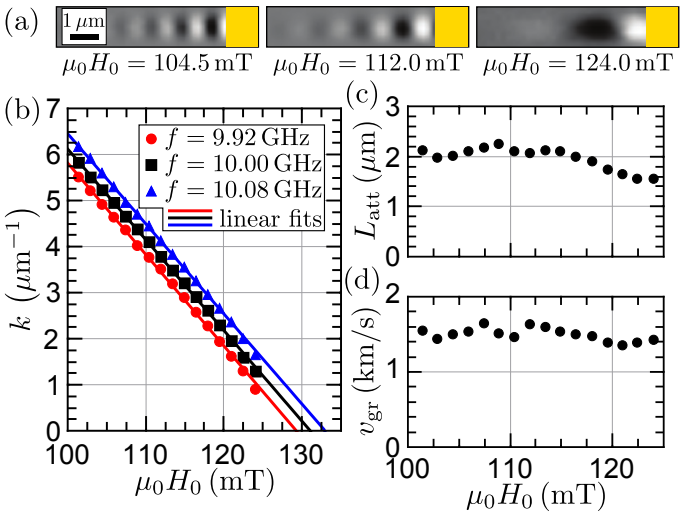

Figure 3.3. Characterization of DE SW modes[62]. (a) Selection of Kerr images at different bias fields of DE SWs propagating on the left side of the microwave antenna (yellow). (b) Bias field dependence of k at different excitation frequencies. (c) Bias field dependence of L_{att} at 10.00 GHz. (d) Bias field dependence of v_{gr} at 10.00 GHz.

Verifying the Equivalence of Both Propagation Directions

The central point of the quantitative analysis of the current-induced changes in the DE SW characteristics, i.e., the shifts in k and L_{att}, respectively, is the

[62] In Fig. 3.3(b)-(d), the error bars are smaller than the symbol size and are therefore not shown in the individual graphs.

direct comparison of these changes for DE SWs propagating on either side of the microwave antenna. Taking advantage of symmetry arguments this approach enables the elimination of all contributions to the shift in either quantity except for those arising from the STT. Hence, and since STT-induced SW dynamics is usually a subtle effect, it is mandatory to verify the equivalence between the two sides.

First of all, it is checked whether the modal profile nonreciprocity inherently present when working in the DE geometry needs to be taken into account since DE SWs are surface modes, which are localized either on the top or the bottom surface of the magnetic layer depending both on their propagation direction $\vec{k}$ and the orientation of the bias field H_0 [cf. Sec. 1.4.2]. However, in this study, the DE modal profile is negligible considering that, in the classical DE picture of magnetostatic waves[63], the modal profile decays (exponentially) on a characteristic length scale that is equal to the wavelength λ of the corresponding mode [cf. Eq. (1.59)]. Here, they range from $\lambda \approx 0.9$–$6.3\,\mu$m [cf. Fig. 3.3(b)], and, therefore, they are much larger than the thickness d of the $Ni_{80}Fe_{20}$ layer, which is only 15 nm. Consequently, all occurring modes can be considered as bulk modes.

Secondly, for a quantitative comparison of the DE modes propagating on either side of the microwave antenna, Kerr images are recorded at $\mu_0 H_0 = \pm 106\,\mathrm{mT}$.

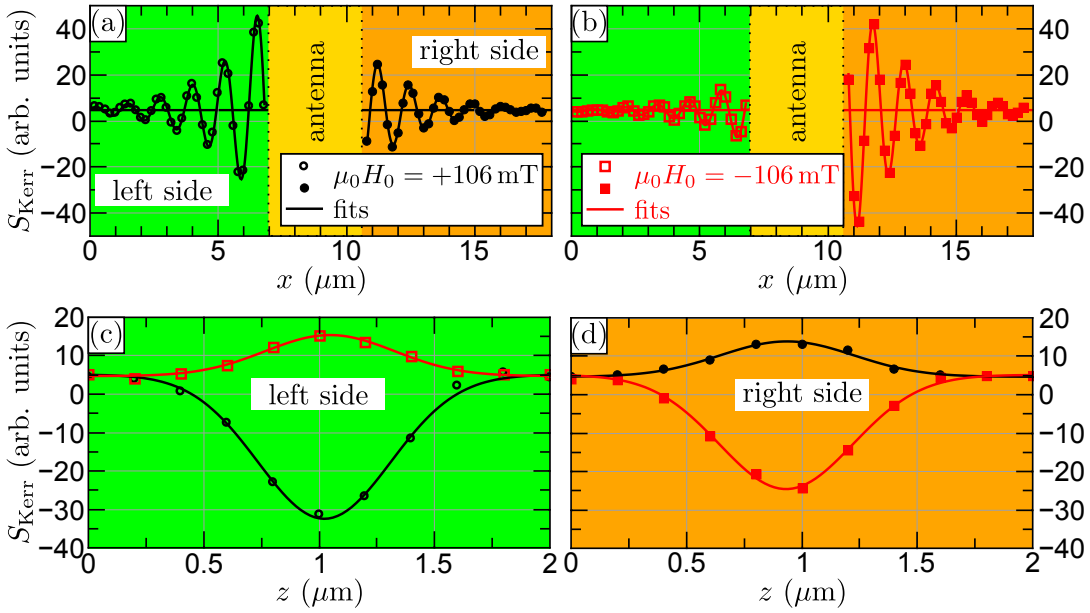

Figure 3.4. Characterization of DE SW modes in the case, where no electric current is applied. (a)-(b) Examples of line scans extracted along the stripe on the left (green) and right (orange) side of the microwave antenna (yellow) from Kerr images recorded at 10 GHz at either orientation of the bias field. The solid lines indicate fits to an exponentially decaying sine function. (c)-(d) Examples of SW amplitude profiles across the width of the stripe extracted both on the left and right side $\approx 2\,\mu$m away from the center of the microwave antenna from the same Kerr images as in (a)-(b). Here, the solid lines denote fits to a Gaussian function.

[63] In this picture, the exchange interaction is neglected [2, 113].

From these images line scans are extracted both along [cf. Figs. 3.4(a) and (b)] and across [cf. Figs. 3.4(c) and (d)] the $Ni_{80}Fe_{20}$ stripe on the left and right side. The former ones start $\approx 2\mu$m away from the center of the antenna, and they fit perfectly to an exponentially decaying sine function as illustrated in Figs. 3.4(a) and (b). These graphs also clearly reveal that DE SWs propagating on the left and right side are in phase despite a small phase shift visible, which is not real yet, as it arises due to a sub-pixel error in the determination of the center of the microwave antenna in the corresponding topography image. This error is $\approx 100\,\text{nm}$ ($\approx 180\,\text{nm}$) at $+106\,\text{mT}$ ($-106\,\text{mT}$). The phase, however, does not play any role in the analysis of the current-induced changes in SW in k and L_{att}, which are—besides the phase—two more out of the five independent parameters of the fits to an exponentially decaying sine function to the line scans along the magnetic stripe [cf. Eq. (2.3)].
The line scans across the stripe are extracted $\approx 2\,\mu$m away from the center of the microwave antenna. As shown in Figs. 3.4(c) and (d), they reveal a clear Gaussian profile, which is mainly due to the convolution with the Gaussian profile of the laser spot, with a characteristic width of $(573 \pm 20)\,\text{nm}$. In contrast, the line scans across the stripe extracted from the corresponding topography images reveal as well a Gaussian shape, but with a larger characteristic width of $(853 \pm 20)\,\text{nm}$. This value is in perfect agreement with the actual width of the stripe: $w = 855\,\text{nm}$. This finding indicates that the propagating DE SW modes are slightly localized in the middle of the stripe as expected for the first transversal mode imposed by the stripe geometry [cf. Sec. 1.4.6].
Moreover, as clearly visible in Figs. 3.4(a)/(b) and Figs. 3.4(c)/(d), respectively, an asymmetry in the amplitude of SWs propagating on the left and right side is observed, which is inverted upon reversal of the direction of the bias field.The signature of the asymmetry agrees with the one expected due to the amplitude nonreciprocity arising due the excitation of propagating DE SWs by microwave antennas [cf. Sec. 1.4.5]. Figures 3.4(c) and (d) enable a direct comparison of the SW amplitude at the same distance away from the microwave antenna at

left side	$\mu_0 H_0 < 0$	$\mu_0 H_0 > 0$
$\lvert k_{\text{left}} \rvert\,[\mu\text{m}^{-1}]$	5.09 ± 0.01	5.01 ± 0.01
$\lvert v_{\text{gr}}^{\text{left}} \rvert\,[\text{km/s}]$	1.53 ± 0.04	1.53 ± 0.02
$\lvert L_{\text{att}}^{\text{left}} \rvert\,[\mu\text{m}]$	2.02 ± 0.02	1.95 ± 0.01
α_{left}	0.0073 ± 0.0003	0.0076 ± 0.0003
right side	$\mu_0 H_0 < 0$	$\mu_0 H_0 > 0$
$k_{\text{right}}\,[\mu\text{m}^{-1}]$	5.18 ± 0.01	5.13 ± 0.01
$v_{\text{gr}}^{\text{right}}\,[\text{km/s}]$	1.52 ± 0.02	1.54 ± 0.02
$L_{\text{att}}^{\text{right}}\,[\mu\text{m}]$	1.99 ± 0.01	1.98 ± 0.01
α_{right}	0.0074 ± 0.0003	0.0075 ± 0.0003

Table 3.1. Comparison of the relevant SW parameters[64] of DE SWs propagating on the left and right side of the microwave antenna, at 300 K, 10 GHz and $\pm 106\,\text{mT}$ in the case, where no electric current is applied.

[64] The values given are the mean values of five individual measurements.

$\pm 106\,\mathrm{mT}$. It differs by a factor of 2–3.
Besides the amplitude difference—which also does not need to be considered any further—the SW modes on the left and right side are equivalent for either orientation of the bias field. This fact is confirmed as well by the values of the relevant SW parameters listed in Table 3.1. A small difference in k on the order of $\approx 0.1\,\mu\mathrm{m}^{-1}$ is observed between the left and the right side, whereas both sides are equivalent in terms of the group velocity, the attenuation length and the Gilbert damping parameter.
Based on these findings, it can be stated that the comparison of the two DE SW propagation directions at a given orientation of the bias field is justified when investigating and analyzing the changes in the DE SW characteristics due to the injection of an electric current across the $Ni_{80}Fe_{20}$ stripe.

3.4.2 Spin Wave Characteristics with an Applied Electric Current

In the second step of the study, an electric dc current is injected across the $Ni_{80}Fe_{20}$ stripe. Subsequent to the investigation of the impact of Joule heating due to the electric current on the DE SW characteristics, the current-induced changes in the DE SW characteristics due to the STT(s) are evidenced and analyzed both qualitatively and quantitatively, thereby providing the basis for the determination of the key STT parameters.
In case of $Ni_{80}Fe_{20}$, in order to be able to detect and resolve the STT-induced changes in the DE SW characteristics—which scale with j [cf. Sec. 1.4.3]—typically, current densities on the order of $\approx 10^{11}$–$10^{12}\,\mathrm{A/m^2}$ are required. Here, the small cross section of the $Ni_{80}Fe_{20}$ stripe—$855 \times 15\,\mathrm{nm^2}$—is beneficial as the desired current density can be achieved by a relatively small dc current. For the measurements presented below, I is set to 1.2 mA, which corresponds to a current density j of $0.935 \times 10^{11}\,\mathrm{A/m^2}$.

Impact of Joule Heating

Although the current (density) is relatively low, the impact of Joule heating on the DE SW characteristics is already noticeable. As shown in Fig. 3.5(a), the bias field dependence of k is shifted by ≈ 1.0–$1.1\,\mathrm{mT}$ towards higher fields compared with the case, where no electric current is applied [cf. Fig. 3.3(b)]. The displayed shift in k is in fact the one arising only due to Joule heating since, for a fixed propagation direction of the DE SWs, it can be separated from the STT-induced changes in k by taking advantage of the symmetry of either effect with respect to the current direction. The shift due to Joule heating—$\Delta k^{\mathrm{Joule}}$—is the same for either current direction, while the shift due to the STT—Δk^{STT}—switches sign upon reversal of the current direction [cf. Sec. 1.4.3]. Hence[65],

$$k\,(I > 0) = k\,(I = 0) + \Delta k^{\mathrm{Joule}} + \Delta k^{\mathrm{STT}} \tag{3.5a}$$

$$k\,(I < 0) = k\,(I = 0) + \Delta k^{\mathrm{Joule}} - \Delta k^{\mathrm{STT}}\,. \tag{3.5b}$$

[65] The contribution arising from the Oersted field associated with the electric current is not taken into account in Eqs. (3.5a)–(3.5b) since it is expected to be two orders of magnitude smaller compared with the shift due to Joule heating and one order of magnitude smaller than the current-induced shift(s).

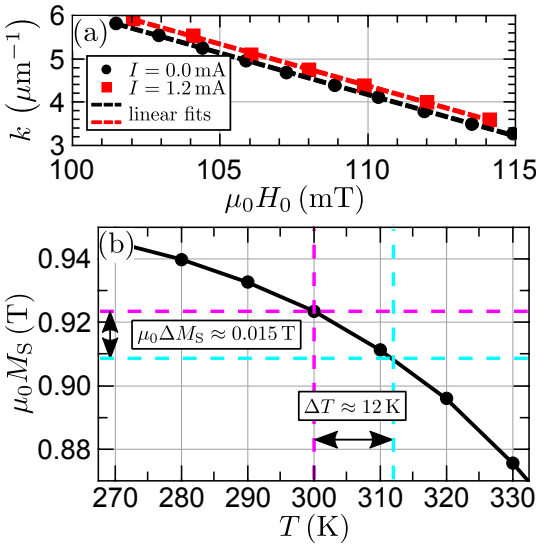

Figure 3.5. (a) Bias field dependence of k at $I = 0.0\,\mathrm{mA}$ and $I = 1.2\,\mathrm{mA}$, respectively, at 10 GHz. (b) Temperature dependence of the saturation magnetization in the range from 270 to 330 K obtained from SQUID measurements on the $Ni_{80}Fe_{20}$ full film [cf. Sec. 3.2]. The colored dashed lines denote how the shift in k [cf. (a)] corresponding to a reduction in M_S is translated to a change in temperature inside the $Ni_{80}Fe_{20}$ stripe.

Consequently, $k\,(I \neq 0)$ [cf. red curve in Fig. 3.5(a)] can be deduced from the combination of the results obtained at positive and negative current as follows:

$$k\,(I \neq 0) = [k\,(I > 0) + k\,(I < 0)]\,/2\,. \tag{3.6}$$

The shift in k due to Joule heating arises since it causes a change in the saturation magnetization. The given value—$\Delta k \approx 1.0{-}1.1\,\mathrm{mT}$—corresponds to a reduction of $\approx$15 mT [cf. Eq. (1.38)]. As illustrated in Fig. 3.5(b), this reduction $\mu_0 \Delta M_S$ can be translated to an increase in temperature within the $Ni_{80}Fe_{20}$ stripe when referring to the temperature dependence of the saturation magnetization in the range from 270 to 330 K, which is measured by SQUID on the $Ni_{80}Fe_{20}$ full film grown under the same conditions as the stripe. Here, the shift in k corresponds to $\Delta T \approx 12\,\mathrm{K}$.
Since the impact of the slightly elevated stripe temperature upon injection of the electric dc current cannot be neglected, another (detailed) SW characterization is performed, yielding the bias field dependencies of k, L_{att} and v_{gr} under the applied electric current[66].

Qualitative Analysis of the Impact of the Spin-Transfer Torque—Spin Wave Resonance Spectra Under an Applied Electric Current

From a qualitative point of view, STT-induced changes[67] in the DE SW characteristics can be simply evidenced by the observation of a (Doppler) shift between the SW resonance spectra recorded at a positive and negative applied electric current, where sign of the shift of either spectrum in comparison to the case, where no current is applied, is consistent with the action of the STT [cf. Eq. (3.3)]. For this purpose, at 10 GHz and at positive bias fields, SW resonance spectra are recorded on the left side as well as on the right side of the

[66] The results of this SW characterization are not shown as they only become relevant when evaluating the values of the key STT parameters [cf. Sec. 3.4.3].

[67] Strictly speaking, by recording SW resonance spectra, it is only possible to detect the impact of the adiabatic STT as it is not possible to resolve a tiny change in the local precession amplitude due a small variation in the absolute value of the magnetic damping parameter that is induced by the nonadiabatic STT [cf. Eq. (3.4)].

microwave antenna at a distance of $\approx 3\,\mu$m from its center while concurrently a positive or negative electric dc current is injected across the $Ni_{80}Fe_{20}$ stripe. At either side, the SW resonance spectra for opposite current polarities are recorded "concurrently" in an alternating fashion: Instead of sweeping the bias field while its polarity is fixed—which represents the standard way for recording a SW resonance spectrum [cf. Sec. 2.2.1]—the bias field is still swept, but, at each field step, the corresponding Kerr signal is recorded at either polarity. This approach is beneficial for the detection of small shifts between the respective SW resonance spectra as it minimizes the impact of drifts during the measurement.

For the four different configurations of SW propagation and current direction—right side: $(k > 0, I > 0)$ and $(k > 0, I < 0)$, left side: $(k < 0, I > 0)$ and $(k < 0, I < 0)$—the corresponding SW resonance spectra are shown in Fig. 3.6(a). At either propagation direction, a shift in field between the traces at positive and negative current occurs, which is more clearly visible in the selected, magnified regions of the SW resonance spectra shown in Figs. 3.6(b) and (c). In the left-sided spectra [cf. Fig. 3.6(b)], this SW Doppler shift in field between the two traces is reversed compared with the one observed in the right-sided spectra

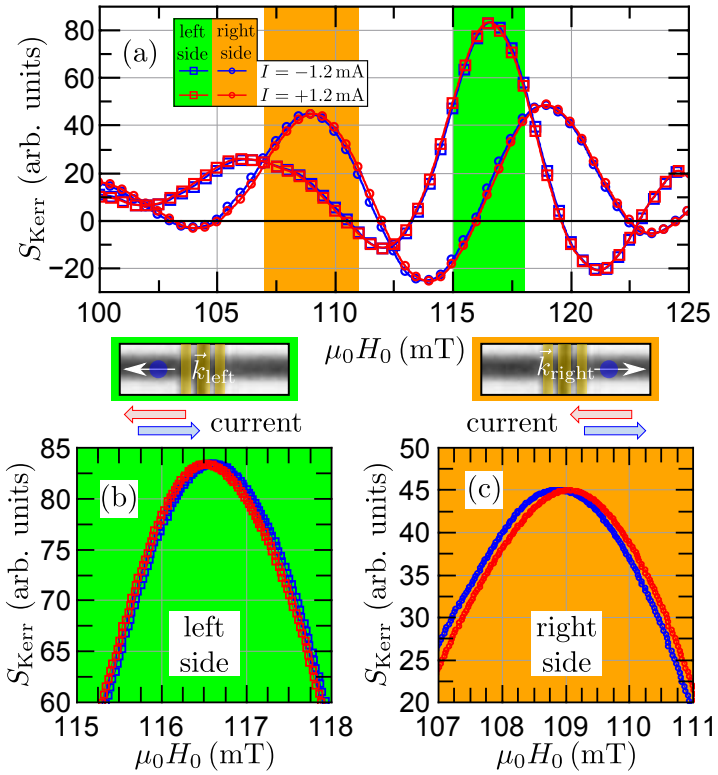

Figure 3.6. (a) SW resonance spectra recorded at 10 GHz on the left (squares) and right side (circles) $\approx 3\,\mu$m away from the center of the microwave antenna while a positive (red symbols)/negative (blue symbols) electric dc current is injected across the $Ni_{80}Fe_{20}$ stripe. (b)-(c) Selected regions of the SW resonance spectra (highlighted by the green and orange areas in (a)). The colored topography image above each graph visualizes the respective configuration of current direction and SW propagation direction on the left and right side of the microwave antenna (yellow). The blue circle marks the position of the laser spot on the $Ni_{80}Fe_{20}$ stripe while recording the spectra.

[cf. Fig. 3.6(c)]: For $k > 0$, the SW resonance spectrum recorded at $I > 0$ is shifted towards higher fields compared with the one recorded at $I < 0$, whereas, for $k < 0$, it is the opposite.
These observations are in fact consistent with the expected changes in the DE SW characteristics due to the action of the (adiabatic) STT: For $\vec{u} \cdot \vec{k} > 0$, the corresponding spectrum is shifted towards larger fields, while it is shifted towards lower fields for $\vec{u} \cdot \vec{k} < 0$ [cf. Sec. 1.4.3].
Defining the shift in field between the SW resonance spectra recorded at opposite current polarities as

$$\mu_0 \Delta H_0 = \mu_0 \left[H_0 \left(I > 0 \right) - H_0 \left(I < 0 \right) \right] \tag{3.7}$$

its bias field dependence can be analyzed on either side of the stripe[68]. The result is shown in Fig. 3.7. At first glance, on either side, ΔH_0 decreases as the bias field increases. In fact, when fitting each data set to a linear function, it becomes much clearer that the decrease is linear in H_0, thus presenting another observation which is also consistent with the action of the (adiabatic) STT: Considering that the electric current is kept constant—which implies that the spin-drift velocity is constant as well [cf. Eq. (3.2)]—and considering as well that k decreases linearly with increasing bias field [cf. Fig. 3.4], ΔH_0 needs to exhibit a linear dependency on H_0 as well. Moreover, the extrapolated, linear fits to $\Delta H_0 \left(H_0 \right)$ for either side [cf. dashed orange and green lines in Fig. 3.7]—which have similar slopes—intersect at $(128 \pm 7)\,\mathrm{mT}$. This field value agrees well with the one, at which k becomes zero [cf. solid black line in Fig. 3.3], i.e., where the magnetization gradient vanishes. This case occurs at $\approx$131 mT. The intercept of the linear fit curves also reveals that there is a slight asymmetry between both sides and enables as well the quantification of the asymmetry [cf. dotted lines in Fig. 3.7]. It is $\approx$0.03 mT, i.e., it is about one order of magnitude smaller than the STT-induced shift in field [cf. Fig. 3.7], and even two orders of magnitude smaller than the shift in field in the bias field dependence of k due to Joule heating [cf. Fig. 3.5]. The origin of this very weak asymmetry is attributed[69] to be the result of a slightly asymmetric distribution of the Oersted field due to a nonuniform distribution of the current flowing across the $Ni_{80}Fe_{20}$ stripe in combination with the amplitude nonreciprocity inherently present when exciting propagating DE

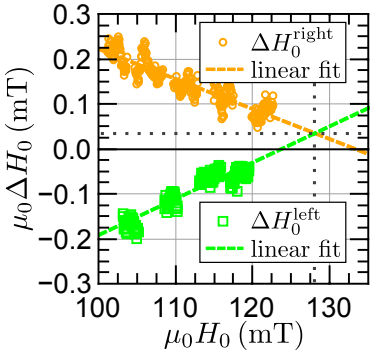

Figure 3.7. Shift in field between the SW resonance spectra recorded at positive and negative currents on the left and right side of the microwave antenna [cf. Fig. 3.6]. The colored dashed lines denote linear fits to the data. At their intercept, the dotted lines are a guide to the eye to determine both the corresponding bias field value and the shift in field value.

[68] According to the definition given [cf. Eq. (3.7)], the shift in field is negative (positive) on the left (right) side of the microwave antenna [cf. Figs. 3.6(b) and (c)]. Moreover, it is only reasonable to analyze it at those bias fields, where neither of the SW resonance spectra exhibits either a maximum or minimum.

[69] This explanation is confirmed by the findings from micromagnetic simulations [139].

SWs by microwave antennas [cf. Sec. 1.4.5]. The asymmetry is canceled when averaging the shifts in field detected on either side of the microwave antenna.

Quantitative Analysis of the Impact of the Spin-Transfer Torque—Imaging Damon-Eshbach Spin Waves Propagating Under an Applied Electric Current

The detailed analysis of the SW resonance spectra recorded under an applied electric current enabled a qualitative view on the impact of the (adiabatic) STT on the DE SW characteristics. However, in order to reach the required quantitative precision and to detect both the changes due to the adiabatic STT and the ones due to the nonadiabatic STT, magnetic imaging is essential since it enables (direct) access to the STT-induced changes in the complex wave number $\underline{k}$:

- The action of the adiabatic STT manifests as a change in the real part $\mathrm{Re}\left(\Delta\underline{k}^{\mathrm{STT}}\right)$—corresponding to a change in the SW wave number, while
- the action of the nonadiabatic STT manifests as a change in the imaginary part $\mathrm{Im}\left(\Delta\underline{k}^{\mathrm{STT}}\right)$—corresponding to a change in the SW attenuation length [cf. Sec. 1.4.3].

Quantifying these changes precisely is the basis for an accurate determination of the values of the key STT parameters for $Ni_{80}Fe_{20}$.

In order to achieve the required accuracy, the following approach is chosen, which allows both statistics and error reduction in the measured quantities:
As illustrated schematically in Fig. 3.8, at $f = 10\,\mathrm{GHz}$, 100 individual Kerr images of the DE SWs propagating on the left and right side of the microwave antenna are acquired for either polarity of the injected dc current[70]. The current is set to $I = 1.2\,\mathrm{mA}$, while the bias field is set[71] to -105 mT, and either quantity is kept constant. The Kerr images are analyzed as before to analyze the complex wave numbers $\underline{k}_{\mathrm{left/right}}$ ($I = +1.2\,\mathrm{mA}$) and $\underline{k}_{\mathrm{left/right}}$ ($I = -1.2\,\mathrm{mA}$), respectively.

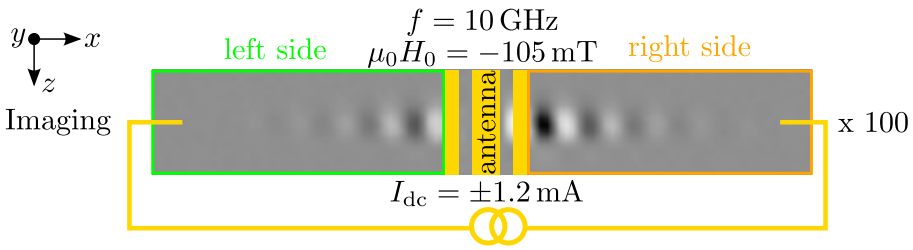

Figure 3.8. Schematic of the approach chosen for the quantitative determination of the STT-induced shifts in the real and imaginary part of the complex wave number. At fixed f and fixed H_0, the DE SWs propagating on the left and right side of the microwave antenna are imaged 100 times for either polarity of the injected dc current.

[70] The Kerr images for opposite current polarities are acquired one after the other in an alternating fashion, i.e., $I > 0$, $I < 0$, $I > 0$, ...

[71] This field value is chosen as the STT-induced changes in the DE SW characteristics scale both with j and k, and, as j is fixed, the larger k is [cf. Fig. 3.3], the larger are the resulting shifts in the real and imaginary parts of $\underline{k}$ and the easier they can be detected and resolved.

For either propagation direction, $\underline{k}_{\mathrm{left/right}}\,(I \neq 0)$, $\mathrm{Re}\left(\Delta\underline{k}^{\mathrm{STT}}\right)$ and $\mathrm{Im}\left(\Delta\underline{k}^{\mathrm{STT}}\right)$ are deduced by taking advantage of the symmetry of the changes in the DE SW characteristics due to the adiabatic and nonadiabatic STT with respect to the current direction. These expressions apply:

$$\mathrm{Re}\left(\underline{k}\,(I>0)\right) = \mathrm{Re}\left(\underline{k}\,(I=0)\right) + \mathrm{Re}\left(\Delta\underline{k}^{\mathrm{Joule}}\right) + \mathrm{Re}\left(\Delta\underline{k}^{\mathrm{STT}}\right) \tag{3.8a}$$

$$\mathrm{Re}\left(\underline{k}\,(I<0)\right) = \mathrm{Re}\left(\underline{k}\,(I=0)\right) + \mathrm{Re}\left(\Delta\underline{k}^{\mathrm{Joule}}\right) - \mathrm{Re}\left(\Delta\underline{k}^{\mathrm{STT}}\right) \tag{3.8b}$$

$$\mathrm{Im}\left(\underline{k}\,(I>0)\right) = \mathrm{Im}\left(\underline{k}\,(I=0)\right) + \mathrm{Im}\left(\Delta\underline{k}^{\mathrm{Joule}}\right) + \mathrm{Im}\left(\Delta\underline{k}^{\mathrm{STT}}\right) \tag{3.8c}$$

$$\mathrm{Im}\left(\underline{k}\,(I<0)\right) = \mathrm{Im}\left(\underline{k}\,(I=0)\right) + \mathrm{Im}\left(\Delta\underline{k}^{\mathrm{Joule}}\right) - \mathrm{Im}\left(\Delta\underline{k}^{\mathrm{STT}}\right)\,. \tag{3.8d}$$

The real and the imaginary part of $\underline{k}\,(I \neq 0)$ result when adding Eqs. (3.8a) and (3.8b), and Eqs. (3.8c) and (3.8d), respectively:

$$\mathrm{Re}\left(\underline{k}\,(I\neq 0)\right) = \left[\mathrm{Re}\left(\underline{k}\,(I>0)\right) + \mathrm{Re}\left(\underline{k}\,(I<0)\right)\right]/2 \tag{3.9}$$

$$\mathrm{Im}\left(\underline{k}\,(I\neq 0)\right) = \left[\mathrm{Im}\left(\underline{k}\,(I>0)\right) + \mathrm{Im}\left(\underline{k}\,(I<0)\right)\right]/2\,. \tag{3.10}$$

The STT-induced changes in either quantity result when subtracting Eqs. (3.8a) and (3.8b), and Eqs. (3.8c) and (3.8d), respectively:

$$\mathrm{Re}\left(\Delta\underline{k}^{\mathrm{STT}}\right) = \left[\mathrm{Re}\left(\underline{k}\,(I>0)\right) - \mathrm{Re}\left(\underline{k}\,(I<0)\right)\right]/2 \tag{3.11}$$

$$\mathrm{Im}\left(\Delta\underline{k}^{\mathrm{STT}}\right) = \left[\mathrm{Im}\left(\underline{k}\,(I>0)\right) - \mathrm{Im}\left(\underline{k}\,(I<0)\right)\right]/2\,. \tag{3.12}$$

In the following the label "STT" is dropped when referring to shifts evaluated by Eqs. (3.11) and (3.12) as they are the actual quantities of interest.

First, the complex wave number $\underline{k}\,(I \neq 0)$ is analyzed using Eqs. (3.9) and (3.10). It is[72] $\underline{k} = [(5.33 + i \cdot 0.502) \pm (0.0017 + i \cdot 0.0011)]\,\mu\mathrm{m}^{-1}$. $\mathrm{Re}\left(\underline{k}\,(I \neq 0)\right)$ specifies the SW wave number, which is $5.33\,\mu\mathrm{m}^{-1}$. This value agrees perfectly with

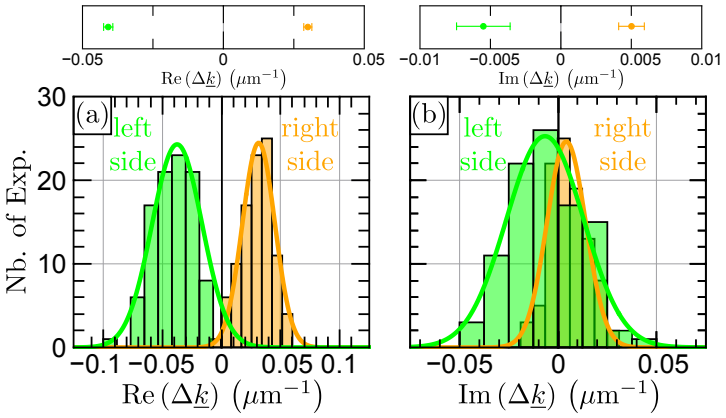

Figure 3.9. Histograms of the measured current-induced shifts in the (a) real and (b) imaginary part of the complex wave number $\Delta\underline{k}$ for DE SWs propagating on the left (green) and right (orange) side of the microwave antenna at -105 mT and at 10 GHz [cf. Fig. 3.8]. The graphs above the histograms emphasize the measured shifts in either quantity given as arithmetic mean with standard error [cf. Eqs. (3.13a)-(3.14b)].

[72] The specified value is averaged over both propagation directions, and the error bars are considerably reduced due to statistics.

the corresponding value derived from the red linear fit curve in Fig. 3.5. Then, $\mathrm{Re}\left(\Delta\underline{k}_{\mathrm{left/right}}\right)$ is analyzed. Figure 3.9(a) displays the statistical histograms of $\mathrm{Re}\left(\Delta\underline{k}\right)$ for either propagation direction. The distribution of each histogram reveals a Gaussian shape, thereby verifying the independence of the individual measurements. The measured shifts[73] are

$$\mathrm{Re}\left(\Delta\underline{k}_{\mathrm{right}}\right) = (0.0299 \pm 0.0013)\ \mu\mathrm{m}^{-1} \tag{3.13a}$$

$$\mathrm{Re}\left(\Delta\underline{k}_{\mathrm{left}}\right) = (-0.0408 \pm 0.0017)\ \mu\mathrm{m}^{-1}\,. \tag{3.13b}$$

Finally, $\mathrm{Im}\left(\Delta\underline{k}_{\mathrm{left/right}}\right)$ is analyzed. This shift results from a subtle combination of a change in $\mathrm{Re}\left(\underline{k}\right)$ and the nonadiabatic STT [cf. Appendix A]. Figure 3.9(b) displays the statistical histograms of $\mathrm{Im}\left(\Delta\underline{k}\right)$ for either propagation direction. Similarly to the histograms of $\mathrm{Re}\left(\Delta\underline{k}\right)$ [cf. Fig. 3.9(a)], these histograms also show a Gaussian profile, but with larger deviations. The measured shifts[74] are

$$\mathrm{Im}\left(\Delta\underline{k}_{\mathrm{right}}\right) = (0.0050 \pm 0.0009)\ \mu\mathrm{m}^{-1} \tag{3.14a}$$

$$\mathrm{Im}\left(\Delta\underline{k}_{\mathrm{left}}\right) = (-0.0055 \pm 0.0018)\ \mu\mathrm{m}^{-1}\,. \tag{3.14b}$$

They are one order of magnitude smaller than the measured shifts in $\mathrm{Re}\left(\Delta\underline{k}\right)$ [cf. Eqs. (3.13a) and (3.13b)].

The measured values of the individual quantities given above are the basis for the determination of the values of the key parameters of current-induced magnetization dynamics.

3.4.3 Determination of the Key Spin-Transfer Torque Parameters

The final step of this study is the quantitative analysis of the key STT parameters for $Ni_{80}Fe_{20}$: α, u, P, and β. The expressions employed for the determination of u and β are those resulting from an analytical model, which was developed and validated by micromagnetic simulations by Hans Bauer [138]. In this model, the extended LLG equation [cf. Eq. 3.1] is solved in the framework of the DE geometry in stripes [cf. Appendix A]. The key feature of the derived expressions is the fact that all appearing quantities can be accessed experimentally. In other words, the value of each STT parameter can be determined based solely on the values of various quantities—all of which can be measured—without any need to resort to micromagnetic simulations at all.

Gilbert damping parameter α

The value of the Gilbert damping parameter α is calculated using the following expression[75]:

$$\alpha = (2 \cdot v_{\mathrm{gr}}) / [L_{\mathrm{att}} \gamma \mu_0 (2 \cdot H_{\mathrm{eff}} + M_{\mathrm{S}})]\,. \tag{3.15}$$

[73] They are given as arithmetic mean with standard error. The error bars are considerably reduced due to statistics.

[74] They are given as arithmetic mean with standard error.

[75] This expression is very similar to Eq. (1.56), when neglecting both the uniaxial PMA field term and the exchange term while concurrently substituting the magnetic bias field with the effective magnetic field.

In Eq. (3.15), the finite width of the stripe is taken into account[76] by including the demagnetizing factor N along the z direction [160] in the effective magnetic field [cf. Sec. 1.4.6]: $H_{\mathrm{eff}} = H_0 - NM_{\mathrm{S}}$. The validity of this approximation is corroborated by micromagnetic simulations using mumax2 [161], which reveal errors of less than 3% for bias fields lower than 113 mT [139]. For the given dimensions of the $Ni_{80}Fe_{20}$ stripe, N is 0.031. Eventually, using $\mu_0 M_{\mathrm{S}} = 0.92\,\mathrm{T}$—measured by SQUID at $T = 300\,\mathrm{K}$ [cf. Fig. 3.5(b)]—along with the v_{gr}- and L_{att}-values deduced from the detailed DE SW characterization in the case, where no electric current was applied [cf. Sec. 3.4.1], yields $\alpha = 0.0075 \pm 0.0003$. This value[77] is in very good agreement with the one resulting from the analysis of the in-plane FMR measurements on the $Ni_{80}Fe_{20}$ full film [cf. Fig. 3.2].

Spin-Drift Velocity u and Spin Polarization P

The spin-drift velocity u is directly linked to the shift in the real part of the wave number [cf. Fig. 3.9(a)] as follows[cf. Appendix A]:

$$u \approx \mathrm{Re}\left(\frac{\Delta \underline{k}}{\underline{k}}\right) v_{\mathrm{gr}}\,. \tag{3.16}$$

This expression stresses the importance of an experimental access to the group velocity, the complex wave number and the shift(s) in the complex wave number[78] to be able to evaluate the spin-drift velocity accurately. Using the v_{gr}-value at $I = 0.0\,\mathrm{mA}$—which is justified as the change in this quantity due to an increased stripe temperature induced by the electric current is negligible—yields $u = (5.1 \pm 0.2)\,\mathrm{m/s}$.
Based on this u-value, the degree of spin polarization P is calculated according to the following expression [cf. Eq. (3.2)]:

$$P = \frac{2eM_{\mathrm{S}}}{g\mu_{\mathrm{B}}} \cdot \frac{u}{j} = \frac{2eM_{\mathrm{S}}}{g\mu_{\mathrm{B}}} \cdot \frac{u \cdot w \cdot d}{I}\,. \tag{3.17}$$

Using $\mu_0 M_{\mathrm{S}} = 0.91\,\mathrm{T}$—the value of the saturation magnetization in the case, where the electric dc current is applied [cf. Fig. 3.5(b)]—yields[79] $P = 0.64 \pm 0.03$. This value is in good agreement with the room temperature value reported by Zhu *et al.*—$P = 0.60 \pm 0.02$ [48][80]—and slightly larger than the one reported by Vlaminck *et al.*—$P = 0.50 \pm 0.05$ [11]—who both also performed SW Doppler experiments on $Ni_{80}Fe_{20}$.

[76] As the bias field is applied parallel to the short axis of a stripe of finite width, the inhomogeneous demagnetizing field along the z direction has to be taken into account, which is well modeled by the averaged demagnetizing field $-NM_{\mathrm{S}}$.

[77] It is also in good agreement with the value needed to reproduce the experimentally observed DE SW characteristics in micromagnetic simulations: $\alpha = 0.0077$ [139].

[78] The key advantage of magnetic imaging by TRMOKE is the ability to probe simultaneously $\underline{k}$ and $\Delta\underline{k}$.

[79] The specified value is averaged over both propagation directions to exclude experimental asymmetries.

[80] In this reference, a summary of published values of P in $Ni_{80}Fe_{20}$ is given along with the respective measurement method. Yet, most of the P-values are extracted at $T = 4.2\,\mathrm{K}$. Hence, it is not reasonable to compare the P-value deduced in this study with those P-values.

Nonadiabatic Parameter β

The nonadiabatic parameter β is analyzed using the following expression [cf. Appendix A]:

$$\beta = \frac{-1}{v_{\mathrm{gr}} \cdot \mathrm{Re}\left(\frac{\partial \underline{k}}{\gamma\mu_0 \partial H}\right)} \left[\frac{\mathrm{Im}\left(\frac{\Delta \underline{k}}{\underline{k}}\right)}{\mathrm{Re}\left(\frac{\Delta \underline{k}}{\underline{k}}\right)} - \frac{\mathrm{Im}\left(\underline{k}\right) d}{1 - \mathrm{Re}\left(\underline{k}\right) d}\right] + \alpha\,. \tag{3.18}$$

Inserting all measured quantities—where the α- and v_{gr}-values at $I = 0.0\,\mathrm{mA}$ are used since the change in either quantity at an elevated stripe temperature due to the electric current is negligible—yields[81] $\beta = (0.035 \pm 0.011)$. This value corresponds to $\beta \approx 4.6\alpha$.

For $Ni_{80}Fe_{20}$, the β-value deduced in this study—$\beta \approx 0.035$—is slightly larger than the β-values reported either for the real-time measurement of the STT-induced SW Doppler shifts—$\beta_{\mathrm{SW}} \approx 0.020$ [49]—or for current-induced DW motion experiments—$\beta_{\mathrm{DW}} \approx 0.026$ [162], but it is much smaller than the β-value extracted from the fit of the elliptical trajectory of VCs subjected to a spin-polarized electric current—$\beta_{\mathrm{VC}} \approx 0.140$ [111]. Nonetheless, a direct comparison of the different reported β-values must be treated with care not only since the inhomogeneous magnetic textures utilized in the individual studies—SWs, DWs, and VCs—significantly differ from each other, but also since the growth of $Ni_{80}Fe_{20}$ under different conditions—e.g., thermal evaporation [132], sputtering [11], or e-beam evaporation [48]—may result in deviations in the values of β, α, P and u.

3.5 Conclusion

In this study, DE SWs propagating in a submicron $Ni_{80}Fe_{20}$ stripe were subjected to an electric dc current of either polarity. The optical and simultaneous detection of the complete set of SW parameters and their current-induced changes enabled the determination of the values of the key STT parameters for $Ni_{80}Fe_{20}$ in a self-consistent and independent way: $\alpha = 0.0075$, $u = 5.1\,\mathrm{m/s}$—corresponding to $P = 0.64$—and $\beta = 0.035$.

The characteristic features of this study were an experimental determination of these parameters, which was direct and performed on the same single $Ni_{80}Fe_{20}$ stripe, and the fact that all quantities occurring in the expressions for β and u could be accessed independently. Even though the validity of the expressions employed for the evaluation of u and β—which resulted from the analytical model developed by Hans Bauer [138]—as well as the validity of all approximations made were verified by micromagnetic simulations, the assessment of the various quantities was achieved fully experimentally and did not resort to micromagnetic or one-dimensional model fitting procedures.

Finally, it is emphasized that the ability to measure α, u and β independently from each other on the same magnetic structure represents the only reasonable starting point toward a microscopic understanding of current-induced magneti-

[81] The specified β-value is averaged over both propagation directions to exclude experimental asymmetries.

zation dynamics, where the link between the Gilbert damping parameter and the nonadiabatic parameter is still a matter of particular interest [99, 100].

Chapter 4

Interfacial Dzyaloshinskii-Moriya Interaction in Thin Pt/Co/Py/MgO Stripes

The results presented in this chapter are published in [133]:

H. S. Körner, J. Stigloher, H. G. Bauer, H. Hata, T. Taniguchi, T. Moriyama, T. Ono, and C. H. Back.
Interfacial Dzyaloshinskii-Moriya interaction studied by time-resolved scanning Kerr microscopy.
Phys. Rev. B **92**, 220413(R) (2015).

Contents

4.1 Motivation and Goal

The antisymmetric component of the magnetic exchange interaction—the Dzyaloshinskii-Moriya interaction (DMI) [25, 26]—has triggered significant interest recently as its exploitation is beneficial for the operation of future spintronic devices [62, 63, 76]. An interfacial DMI arises from the inversion symmetry breaking at surfaces or at interfaces between a ferromagnetic layer and a nonmagnetic one having a strong spin-orbit coupling (SOC) due to the three-site indirect exchange mechanism [76, 78] [cf. Sec. 1.2.2].
One appropriate approach to prove the occurrence of an interfacial DMI in ultrathin, multi-layered material stacks such as Pt/Co/Ni [53], Pt/Co [130, 163], or Pt/Py [129, 131] is to study its impact on the propagation of DE SWs. An interfacial DMI leads to asymmetries in the dispersion and attenuation length of counterpropagating DE SWs [cf. Sec. 1.4.4]. Evaluating these asymmetries enables the investigation of different properties of the interfacial DMI. It is possible, for example, to quantify the strength of the interfacial DMI, analyze its thickness [131, 163] and angular dependence [164], and determine its relation to the Heisenberg exchange interaction [129]. So far, all of the experimental studies were performed on thermally excited DE SWs in full film samples using BLS [53, 116, 129–131].
The goal of this study is to prove the occurrence an interfacial DMI in thin, patterned, several tens of micrometers wide Pt/Co/Py/MgO stripes as well as to quantify its strength. For this purpose, the characteristics of counterpropagating DE SWs excited by a microwave antenna are investigated by magnetic imaging using TRMOKE since this detection method enables direct access to the dispersion and the attenuation length [cf. Sec. 2.2.2].

4.2 Samples: Design, Fabrication and Characterization[82]

First, as illustrated in the schematic in Fig. 4.1(a), a multi-layered full film consisting of Ta(2 nm)/Pt(2 nm)/Co(0.4 nm)/Py(5 nm)/MgO(5 nm) is grown on a Si substrate by sputter deposition. Since the ferromagnetic layers Co and Py ($Ni_{80}Fe_{20}$) are sandwiched between two nonmagnetic layers, where the bottom one is the heavy metal Pt exhibiting a strong SOC, which is different from the top MgO layer, the inversion symmetry across the thickness of the multi-layered stack is broken. Hence, an interfacial DMI is expected to arise at the Pt/Co interface [cf. Sec. 1.4.4].
The additional Py layer is strongly exchange-coupled to the Co layer. It is inserted as it facilitates the propagation of DE SWs as well as their optical detection using TRMOKE due to an enhanced Kerr signal. Its thickness d_{Py} is carefully chosen to be as thin as possible, since the strength of the interfacial DMI scales with $1/d$ [165], while concurrently being thick enough to enable the propagation of DE SWs, since their group velocity as well as their attenuation length scale

[82] The samples were designed and fabricated by Hiroshi Hata, Takuya Taniguchi, and Takahiro Moriyama from the group of Prof. Dr. Teruo Ono at Kyoto University, Japan. They also performed the FMR and SQUID measurements.

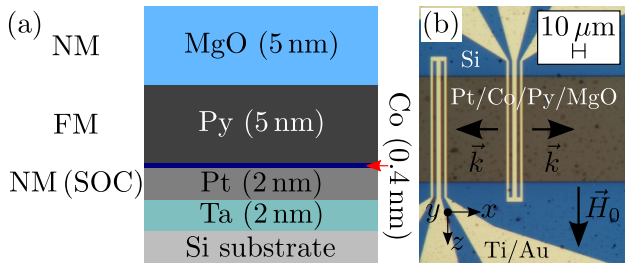

Figure 4.1. (a) Schematic of the full film layer stack grown. The ferromagnetic (FM) layers are sandwiched between two nonmagnetic (NM) layers, where the bottom one is a heavy metal with strong SOC. (b) Optical microscopy image of a patterned sample where the characteristics of SWs propagating in the DE geometry [cf. Fig. 1.6] are investigated.

with d [cf. Sec. 1.4.1]. MgO is selected as the top layer as it is transparent for wavelengths in the visible spectrum, which is beneficial for an optical detection of the SWs propagating in the ferromagnetic layer(s) beneath using TRMOKE.

Secondly, the major part of the full film is patterned into multiple 500 μm-long and 70 μm-wide stripes by EBL, chemically assisted ion beam etching using Ar^+-ions and liftoff. Next, on each stripe, two microwave antennas in the shape of shorted CPWs are fabricated by EBL, thermal evaporation of Ti(5 nm)/Au(100 nm) and liftoff. They are separated from each other by 20–50 μm and electrically decoupled from the stripes by an additional 30 nm-thick insulating layer of SiO_2 grown by ALD. Microwave antennas with different dimensions are fabricated, but the ratio "*signal line width : signal to ground line gap : ground line width*" is always 7 : 5 : 4. The final sample design is displayed in the optical microscopy image shown in Fig. 4.1(b).

The unpatterned piece of the full film is characterized by SQUID and in-plane FMR measurements at room temperature. The former ones reveal an in-plane hysteresis and an effective saturation magnetization $\mu_0 M_S^{\text{eff}} = (1.30 \pm 0.03)$ T. It is called effective as the Co/Py bilayer is considered as one effective uniform medium [166, 167], since the Co and Py layers are coupled by strong exchange

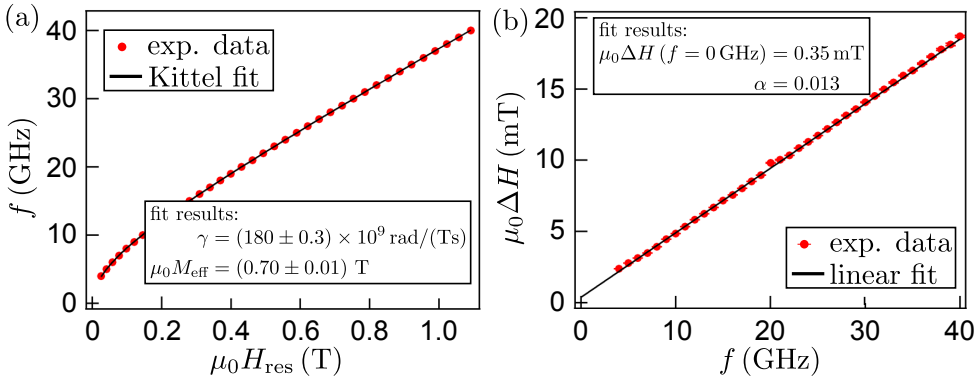

Figure 4.2. Full film in-plane FMR characterization. (a) Frequency dependence of the resonance field H_{res} along with the results from the Kittel fit. (b) Frequency dependence of the linewidth along with the results obtained from the linear fit to it.

interactions. For this reason, for the evaluation of M_S^{eff}, the total magnetic moment measured by SQUID is simply divided by the total thickness d of the ferromagnetic layers, i.e., $d = d_{\text{Py}} + d_{\text{Co}} = 5.4\,\text{nm}$.
The Kittel fit to the frequency dependence of the resonance field H_{res} shown in Fig. 4.2(a) yields a gyromagnetic ratio $\gamma = (180 \pm 0.3) \times 10^9\,\text{rad/(Ts)}$ and an effective magnetization $\mu_0 M_{\text{eff}} = \mu_0 \left(M_S - H_u^{\perp}\right) = (0.70 \pm 0.01)\,\text{T}$. Consequently, $\mu_0 H_u^{\perp} = (0.60 \pm 0.04)\,\text{T}$ is the strength of the uniaxial PMA field [cf. Eq. (1.48)]. The intrinsic Gilbert damping parameter α is extracted from the slope of a linear fit to the frequency dependence of the linewidth[83] shown in Fig. 4.2(b). It is 0.013. The zero-frequency linewidth offset ΔH ($f = 0\,\text{GHz}$) is very small, and, therefore, negligible.

4.3 Implementation of the Experiment and Data Analysis

The experiment is performed in the DE geometry. As illustrated in Fig. 4.1(b), in the stripe, SWs with wave vector $\vec{k}$ are excited by the dynamic driving fields of the microwave antenna and propagate along the x direction on either side of the antenna while the static magnetization direction is maintained transverse to the stripe's long axis by applying a bias field $\vec{H}_0$ along the z direction. Its

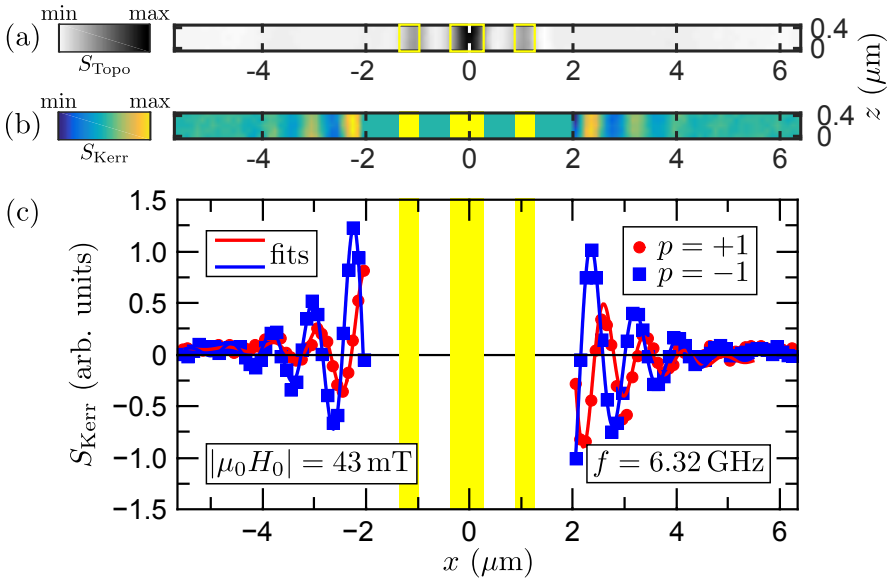

Figure 4.3. (a) Topography image used as a reference image to determine the position of the microwave antenna (yellow-framed region) in (b). (b) Corresponding Kerr image recorded at $f = 6.32\,\text{GHz}$ and $\mu_0 H_0 = -43\,\text{mT}$ showing counterpropagating DE SWs on either side of the microwave antenna. The Kerr signal is only displayed and enhanced in the region where the DE SW propagation is analyzed. (c) Line scans (solid symbols) extracted from the Kerr images taken at $f = 6.32\,\text{GHz}$ at either polarity of the bias field with a magnitude of 43 mT. The solid lines denote the individual fits to an exponentially decaying sine function.

[83] half width at half maximum

polarity is +1, when it is oriented along the positive z direction, and −1, respectively, when it points in the opposite direction. The bias field magnitude is set to 43 mT, which is sufficient to align the static magnetization homogeneously along the z direction everywhere within the 70 μm-wide stripe apart from the regions close to the edges. According to the dispersion[84] [cf. Eq. (1.38)], at this bias field, propagating DE SWs having wave numbers in the range from ≈1–9 $\mu\mathrm{m}^{-1}$—which can be accessed magneto-optically—occur at excitation frequencies f ranging from ≈5.40–6.60 GHz.

For the verification of an interfacial DMI arising at the Pt/Co interface in the fabricated Pt/Co/Py/MgO stripes, in the first place, it is essential to observe asymmetries in the dispersion $f(k)$ as well as in the attenuation length L_{att} of counterpropagating DE SWs [cf. Sec. 1.4.4]. Moreover, for a given (known) sign of the effective DMI constant D_{eff}, the signature of the asymmetries needs to agree with the one that is characteristic to the presence of an interfacial DMI. As the second term in DE SW dispersion in the presence of an interfacial DMI given by [cf. Eq. (1.71)]

$$\begin{aligned}\omega(k) &= \omega_0(k) + \omega_{\mathrm{iDMI}}(k) \\ &= \gamma\mu_0\sqrt{\left[H_0 + Jk^2 + M_{\mathrm{S}}\xi(kd)\right]\left[H_0 + Jk^2 + M_{\mathrm{S}}\left(1-\xi(kd)\right) - H_{\mathrm{u}}^{\perp}\right]} \\ &\quad + \frac{2\gamma}{M_{\mathrm{S}}}D_{\mathrm{eff}}pk\,.\end{aligned} \tag{4.1}$$

is proportional to pk it is not decisive whether the asymmetries are evidenced (i) for counterpropagating DE SWs at a fixed bias field polarity p, or (ii) for DE SWs propagating along the same direction, but at opposite orientations of the bias field. The same argument also applies to the attenuation length [cf. Eq. (1.75)].

To access the four different dispersions—$f(k>0, p=+1)$, $f(k>0, p=-1)$, $f(k<0, p=+1)$, and $f(k<0, p=-1)$—and the corresponding frequency dependencies of the attenuation length at $|\mu_0 H_0| = 43$ mT directly, f is swept in the range from 5.52 to 6.48 GHz in steps of 80 MHz for either p-value, while concurrently imaging the propagating DE SWs by TRMOKE [cf. Sec. 2.2.2]. The Kerr images cover a 400 nm-wide and 12 μm-long section in the center of the stripe, where the microwave antenna is close to the center of each image with respect to the x direction. Hence, as shown exemplarily in Fig. 4.3(b), each Kerr image covers counterpropagating DE SWs at a given combination of f and p. The topography image recorded at the same time [cf. Fig. 4.3(a)] serves as the reference image to determine the position of the microwave antenna in the Kerr image. Then, line scans are extracted from the Kerr images starting ≈1 μm away from either side of the microwave antenna. They are fitted to an exponentially decaying sine function [cf. Fig. 4.3(c)] to deduce the two quantities characterizing propagating DE SWs: the wave number k and the attenuation length. In general, positive (negative) k- and L_{att}-values denote DE SWs propagating along the positive (negative) x direction.

[84] The dispersion is calculated using the sample parameters resulting from the full film characterization [cf. Sec. 4.2].

4.4 Experimental Results and Discussion

In the following, first, the experimental findings on the dispersion [cf. Sec. 4.4.1] and attenuation length [cf. Sec. 4.4.2] of counterpropagating DE SWs in the Pt/Co/Py/MgO stripes are presented and discussed. Based on these results, the strength of the interfacial DMI is determined [cf. 4.4.3], where two different approaches are utilized. Finally, in Sec. 4.4.4, it is discussed, why the origin of the observed asymmetries in the quantities characterizing DE SWs is indeed an interfacial DMI arising at the Pt/Co interface.

4.4.1 Findings on the Dispersion of Counterpropagating Damon-Eshbach SWs

The four measured dispersions are shown in Fig. 4.4. The most prominent feature is the asymmetry: At fixed f and at a fixed propagation direction along the x direction, the wave numbers of DE SWs propagating at $p = +1$ and $p = -1$, respectively, differ. For example, for $k > 0$, the SW wave number is larger for $p = -1$ (squares) than for $p = +1$ (circles). This asymmetry reverses when the propagation direction is inverted to $k < 0$. As it can be assumed that D_{eff} is positive in case of a Pt/Co interface [53, 130], the signature of the observed asymmetry is in agreement with the expected one according to Eq. (4.1). Hence, at first glance, this asymmetry is attributed to be caused by the occurrence of an interfacial DMI at the Pt/Co interface.

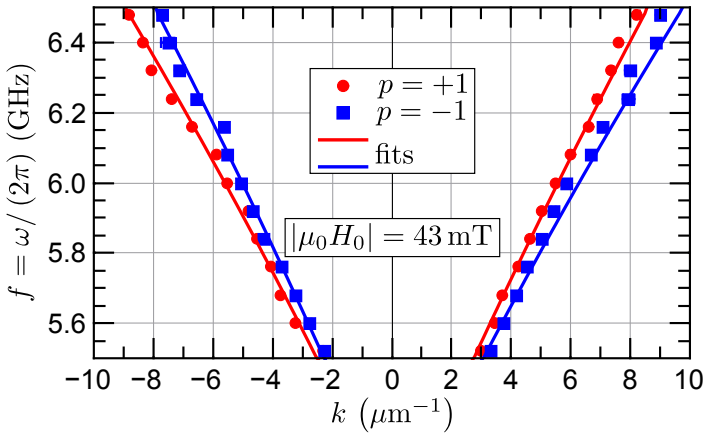

Figure 4.4. Dispersions of counterpropagating DE SWs at $|\mu_0 H_0| = 43\,\text{mT}$ at either polarity of the bias field. Circles and squares denote measurement data, where the error bars, which are smaller than symbol size, are those obtained from the line scan fits. The solid lines indicate fits to Eq. (4.1) for any combination of k and p.

4.4.2 Findings on the Attenuation Length of Counterpropagating Damon-Eshbach SWs

In contrast to the clearly visible asymmetry in the measured dispersions [cf. Sec. 4.4.1] such an asymmetry can be barely observed in the corresponding frequency dependencies of the attenuation length shown in Fig. 4.5. For SWs propagating along the $+x$ direction L_{att} is slightly larger for $p = +1$ than for $p = -1$. This observation itself is consistent with the signature of the asymmetry expected in case an interfacial DMI arises at the Pt/Co [cf. Eq. (1.75)]. Yet, in the opposite propagation direction, there seems to be only a very small or

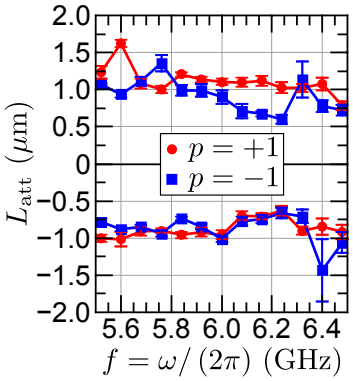

Figure 4.5. Frequency dependencies of the attenuation length at either bias field polarity and at either propagation direction. The error bars are those obtained from the line scan fits.

nonexistent difference between the L_{att}-values at $p = +1$ and $p = -1$, respectively. Hence, the question arises why—firmly assuming that an interfacial DMI is present at the Pt/Co interface—an asymmetry is observed in the dispersions, which does not appear as clear/at all in $L_{\mathrm{att}}(f, p)$. The reason for this finding can be revealed once the strength of the interfacial DMI is quantified. It should be already mentioned here that it does not contradict the statement that an interfacial DMI arises at the Pt/Co interface.

4.4.3 Quantifying the Strength of the Interfacial Dzyaloshinskii-Moriya Interaction and its Implications

Quantification of the Strength of the Interfacial Dzyaloshinskii-Moriya Interaction

For the quantification of the strength of the interfacial DMI arising at the Pt/Co interface, i.e., for the determination of the value of D_{eff}, two different approaches are utilized.

In the first approach, the dispersions measured for the same propagation direction, but at opposite orientation of the bias field are simultaneously fitted to Eq. (4.1)[85]. The discrimination between the '$k > 0$'-case and the '$k < 0$'-case takes into account that, in the fabricated Pt/Co/Py/MgO stripes, the magnetic properties might be slightly different on both sides of the microwave antenna. In this case, it is more reasonable to evaluate the effect of the interfacial DMI on DE SWs propagating on the same side of the microwave antenna. D_{eff} and $H_{\mathrm{u}}^{\perp}$ are chosen as the independent fit parameters. This choice is appropriate since $H_{\mathrm{u}}^{\perp}$ determines the cutoff frequency $\omega(k = 0)$, which is identical with the FMR frequency [cf. Eq. (1.47)] and which also specifies the absolute shift of either dispersion curve along the frequency axis, while D_{eff} quantifies the splitting between the dispersions for $p = +1$ and $p = -1$ at a fixed propagation direction. In Table 4.1, the resulting individual fit parameter values are listed and the corresponding fit curves are depicted as solid red and blue lines in Fig. 4.4. The small deviation between the $H_{\mathrm{u}}^{\perp}$-values for $k > 0$ and $k < 0$ is attributed to be due to little local magnetic inhomogeneities within the Pt/Co/Py/MgO stripes. In con-

[85] Here, the Jk^2-terms arising due to the exchange interaction are neglected as their strength is much weaker compared with the other terms. Moreover, the γ- and M_{S}-values used are those obtained from the full film characterization [cf. Sec. 4.2].

	$D_{\text{eff}}\,[\text{mJ/m}^2]$	$\mu_0 H_{\text{u}}^{\perp}\,[\text{T}]$
$k > 0$	(0.17 ± 0.03)	(0.642 ± 0.002)
$k < 0$	(0.16 ± 0.03)	(0.619 ± 0.002)

Table 4.1. Fit parameter values obtained from fitting the measured DE SW dispersions to Eq. (4.1). Details are given in the text.

trast, the D_{eff}-values are in agreement within the error bars. As these values are "effective" ones, i.e., they are averaged across the total thickness d of the Co/Py bilayer, they cannot be directly compared to the values reported by other groups. Yet, when assuming the DMI to be of purely interfacial nature, a variation with thickness according to $D_{\text{eff}}(d) = D_{\text{int}}/d$ is expected [130, 165], where the quantity D_{int} is independent of the uncertainty in the thickness of the ferromagnetic bilayer. Here, $D_{\text{int}} = (0.89 \pm 0.16)\,\text{pJ/m}$ is the average value. This value is on the same order of magnitude as the ones reported by other groups[86] for layer stacks, which have similar layer thicknesses and also comprise a Pt/Co interface, e.g., $D_{\text{int}} \approx 1.4\,\text{pJ/m}$ in the case of Pt(4 nm)/Co(1.6 nm)/Ni(1.6 nm) [53], or $D_{\text{int}} \approx 1.6$–$1.9\,\text{pJ/m}$ in the case of Pt/Co/Al_2O_3 multi-layers with varying Co thickness [130].

The second approach can be utilized only under certain conditions and, in addition, it enables only a reasonable estimation for D_{eff} and D_{int}, respectively. Here, the idea is to take advantage of the fact that, at the given bias field, the individual DE SW dispersions $f(k,p)$ are almost linear within the frequency range studied [cf. Fig. 4.4]. Consequently, the respective group velocities $v_{\text{gr}} = 2\pi\partial f(k,p)/\partial k$ are almost constant. Moreover, $\max(kd) \approx 0.05 \ll 1$ holds[87]. For this reason, neglecting the Jk^2-terms while concurrently expanding the $\xi(kd)$-term, where only the lowest order terms in k are retained, the first term in Eq. (4.1) can be modified in such a way that it becomes linear in k as well [52]. Finally, an expression for the group velocities can be deduced, which depends only on p:

$$v_{\text{gr}}^{\pm}(p) = v_{\text{gr}}^{0} \pm p\frac{2\gamma}{M_{\text{S}}}D_{\text{eff}}\,. \tag{4.2}$$

In Eq. (4.2), the positive sign (negative sign) refers to DE SWs propagating along the $+x$ ($-x$ direction). According to Eq. (4.2), D_{eff} can be gauged by deducing the difference in the group velocities of DE SWs propagating along the same direction, but at opposite orientations of the bias field[88]. Yet, the actual advantage of the fact of this approach is the fact that it does not require any knowledge about the behavior of the first term in Eq. (4.1) since this term only contributes to the constant v_{gr}^{0} in Eq. (4.2).
Due to this independence from $\omega_0(k)$, this approach can also be used to estimate D_{eff} when investigating the propagation of DE SWs in the presence of an interfacial DMI in much narrower stripes on the order of less than a few micrometer rather than in several tens of micrometer wide stripes or in full films given

[86] They also performed SW propagation experiments, but used BLS for the optical detection.
[87] The total thickness d of the ferromagnetic bilayer is 5.4 nm, while the largest detected SW wave number k_{max} is $\approx 9\,\mu\text{m}^{-1}$ [cf. Fig. 4.4].
[88] When the dispersion is quasi-linear within the frequency range studied, the group velocity can simply be deduced from a linear fit to the measured dispersion data as is specifies the slope of the dispersion.

that the dispersion is quasi-linear in the frequency range studied. Applying it to the measured SW dispersions yields[89] the estimated, effective DMI constant $D_{\text{eff}}^{\text{estimate}} = (0.15 \pm 0.02)\ \frac{\text{mJ}}{\text{m}^2}$. Within the error bars, it agrees with the D_{eff}-values listed in Table 4.1.

Implications

(i) Due to plotting the individual fit curves along with the respective measured dispersions in Fig. 4.4 the splitting between the dispersions measured at a fixed propagation direction at $p = +1$ and $p = -1$ becomes clearly visible. Moreover, based on these fit curves, a proper analysis of the frequency dependence of the splitting is possible in the first place. Here, the figure of merit is the difference in wave numbers Δk between both curves at fixed f. It is defined as follows:

$$\begin{aligned} k < 0: &\qquad \Delta k = k^{p=+1} - k^{p=-1} &&\text{(i.e.,}\Delta k < 0\text{)} \\ k > 0: &\qquad \Delta k = k^{p=-1} - k^{p=+1} &&\text{(i.e.,}\Delta k > 0\text{)}\,. \end{aligned}$$

When considering Δk deduced directly from the measured k-values, it is difficult to make a plain statement about its frequency dependence since the individual values depicted by the orange symbols in Fig. 4.6 fluctuate noticeably. Yet, it should be pointed out that variations in Δk can be expected in advance due to the definition of Δk itself: Since Δk quantifies the difference between two independently determined k-values, the corresponding Δk-value can be either larger or smaller than the actual Δk-value depending on whether the individual k-value resulting from the line scan fit is larger or smaller than the actual k-value. For this reason, for a quantitative analysis of $\Delta k\,(f)$, the Δk-values deduced from difference between the respective fit curves are considered. They are denoted as gray lines in Fig. 4.4. Δk increases monotonically as f is increased: at $f = 6.48\,\text{GHz}$, for $k > 0$, $\Delta k \approx 1.2\,\mu\text{m}^{-1}$, and, for $k < 0$, $\Delta k \approx -1.0\,\mu\text{m}^{-1}$, respectively. This finding can be regarded as another proof for an interfacial DMI arising at the Pt/Co interface since, in this case, at a fixed propagation direction, the splitting needs to increase monotonically the larger f becomes [cf. Eq. (4.1) or Fig. 1.16]. The difference between both Δk-values at $f = 6.48\,\text{GHz}$ results from the different values of the fit parameters D_{eff} and $H_{\text{u}}^{\perp}$ for $k > 0$ and $k < 0$, respectively. For $k > 0$, $H_{\text{u}}^{\perp}$ is stronger than for $k < 0$ resulting in a lower cutoff frequency [cf. Eq. (4.1)]. As a consequence, at fixed f, the wave

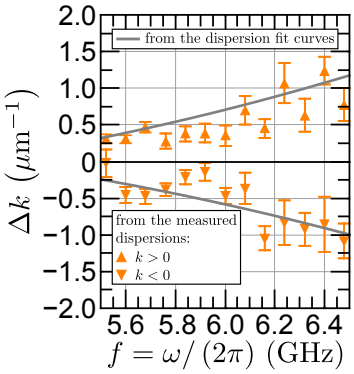

Figure 4.6. Difference Δk between the wave numbers of DE SWs propagating along the same direction, but at opposite orientations of the bias field. The orange up/down triangles denote values determined from the measured dispersions [cf. red and blue symbols in Fig. 4.4], while the gray lines mark the difference between the respective fit curves at a fixed propagation direction [cf. red and blue lines in Fig. 4.4].

[89] The value given is averaged over both propagation directions.

numbers of DE SWs propagating along the $+x$ direction are always larger than those of DE SWs propagating along the opposite direction. Additionally, D_{eff} is also larger for $k > 0$ than for $k < 0$. In combination, these two features result in Δk-values, which are larger for $k > 0$ than for $k < 0$.

(ii) The reason, why a clear asymmetry is observed in the dispersions, while it seems as if it does not occur as clear/at all in the corresponding frequency dependencies of the attenuation length, is revealed by calculating the respective frequency dependencies of the attenuation length according to [cf. Eq. (1.75)]

$$L_{\text{att}}(\omega, p) = \frac{v_{\text{gr}}(p)}{\text{Im}[\omega(p)]} = \frac{\partial\omega/\partial k(p)}{\text{Im}[\omega(p)]} \qquad (\omega = 2\pi f) \tag{4.3}$$

using the average values of the fit parameters D_{eff} and $H_{\text{u}}^{\perp}$ [cf. Table 4.1]. In Fig. 4.7, the four different frequency dependencies of L_{att} are shown. For comparison, the frequency dependence for $D_{\text{eff}} = 0$ is plotted as well, which is symmetric both in p and k. At first glance, at a fixed propagation direction, a distinct difference between the curves for $p = +1$ and $p = -1$ is visible. More importantly, however, is not the occurrence of this difference, but its absolute value as a function of frequency, which is defined as $\Delta L_{\text{att}}(f) = |L_{\text{att}}^{p=+1}(f) - L_{\text{att}}^{p=-1}(f)|$. In the frequency range study it is only on the order of ≈100–150 nm, i.e., it is tiny, which implies, in turn, that it is challenging to resolve it magneto-optically. Using single magnetic imaging $L_{\text{att}}(f, p)$ and $\Delta L_{\text{att}}(f)$, respectively, can indeed not be resolved properly given the facts (i) that L_{att} is derived from fitting line scans extracted from the Kerr images to an exponentially decaying sine function [cf. Eq. (2.3)], where k and L_{att} are two out of the five required independent fit parameters, and (ii) that, in contrast to k, the fit value for L_{att} can be crucially affected even by small deviations from an almost perfect exponentially decaying shape in the detected local SW amplitude. For this reason, from a qualitative point of view, the observed differences in L_{att} [cf. Fig. 4.5] are barely sufficient to be used to confirm the occurrence of an interfacial DMI arising at the Pt/Co interface.
At this point, it is worth noting that the asymmetry in $\Delta L_{\text{att}}(f)$ might be resolved using a statistical approach instead, where counterpropagating SWs are imaged several tens/hundreds/thousand times for the same set of experimental parameters[90]. This approach is very time-consuming. Nonetheless, it was

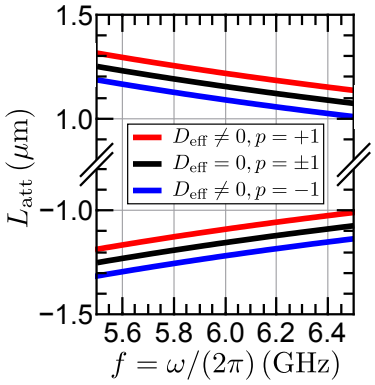

Figure 4.7. Frequency dependencies of the attenuation length at either bias field polarity and at either propagation direction calculated according to Eq. (4.3) using the average values of the fit parameter values for D_{eff} and $H_{\text{u}}^{\perp}$ [cf. Table 4.1]. For comparison, in the case, where no interfacial DMI is present, i.e., $D_{\text{eff}} = 0$, the corresponding curve is plotted as well.

[90] Such an approach was chosen for the determination of the key STT parameters [cf. Ch. 3].

conducted, e.g., by Di *et al.*, who demonstrated by BLS measurements that the presence of an interfacial DMI can also be proven by an asymmetry in the lifetime[91] of thermally excited SWs [53].

4.4.4 Discussion about the Signature of the Observed Asymmetry

In the following it needs to be discussed, why the signature of the asymmetry as well as the asymmetry itself observed in the dispersions of counterpropagating DE SWs [cf. Fig. 4.4] is indeed due to an interfacial DMI arising at the Pt/Co interface in the fabricated Pt/Co/Py/MgO stripes, and, why it is not simply an effect that is related to the characteristic modal-profile nonreciprocity of the DE SWs [cf. Sec. 1.4.2].

As DE SWs are surface SWs, they are localized either on the bottom interface or on the top interface of the ferromagnetic layer depending both on their propagation direction and the bias field polarity [cf. Sec. 1.4.2]. Hence, in principle, in any SW propagation experiment, they can probe asymmetric distributions of magnetic parameters across the thickness of the studied magnetic system, thus representing a circumstance, which needs to be addressed carefully especially when studying interface-induced effects.
In case of the fabricated Pt/Co/Py/MgO stripes, in the standard Damon-Eshbach picture[92] of magnetostatic waves [2, 113], the characteristic length scale d_{char} of the classical exponential DE modal profile is given by Eq. (1.59). Using $k_{\mathrm{max}} \approx 10\,\mu\mathrm{m}^{-1}$ d_{char} is about 100 nm, i.e., it is much larger than the total thickness of the Co/Py bilayer, which is only 5.4 nm. Therefore, the modal profile of the propagating DE SWs is almost uniform across the thickness of the magnetic layer as illustrated in the schematics shown in Fig. 4.8. It resembles very much those of bulk modes. The amplitude difference[93] between both interfaces is about 5%. Even such a small difference might be sufficient so that any asymmetric distribution in a magnetic parameter is probed differently by propagating DE SWs localized at the top surface compared with those localized

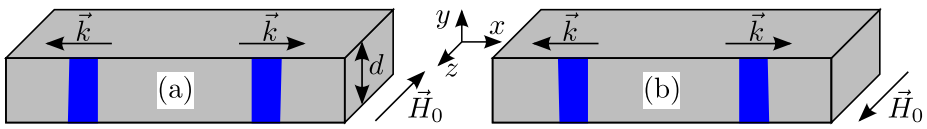

Figure 4.8. Modal profiles in the classical picture of DE SWs propagating along the $+x$ and $-x$ direction, respectively, when the bias field is applied either (a) along the $-z$ or (b) along the $+z$ direction. The profiles are calculated for $d = 5.4\,\mathrm{nm}$ and $k_{\mathrm{max}} = 10\,\mu\mathrm{m}^{-1}$, respectively. At these k- and d-values, they are almost uniform across the thickness of the layer.

[91] The SW lifetime is the measurement parameter in BLS experiments corresponding to L_{att} in TRMOKE measurements. The reversed signature of the asymmetry in the SW lifetime compared with the one in L_{att} is due to the fact that real and imaginary parts of ω and k are linked via v_{gr}.
[92] In this picture, the exchange interaction is neglected.
[93] When taking into account the exchange interactions as well as the appropriate boundary conditions, this amplitude difference is larger [cf. Sec. 1.4.2].

at the bottom surface. In case of the fabricated multi-layered stripes, there are three asymmetric distributions of magnetic parameters:

1. The saturation magnetization M_S is asymmetric as the ferromagnetic layer, which is sandwiched between the Pt and MgO layers, is in fact a bilayer of Co(0.4 nm) and Py(5 nm), which have different saturation magnetizations: $\mu_0 M_S^{Co} = 1.8\,T$ vs. $\mu_0 M_S^{Py} \approx 1.0\,T$.

2. There is an asymmetry arising from the proximity-induced magnetic moment in the Pt layer [168–172].

3. The uniaxial PMA field $H_u^{\perp}$ is asymmetric as it originates from the Pt/Co interface.

It is assumed that the impact of either of the first two asymmetries is not sufficiently strong enough to give rise to such a distinct asymmetry in the dispersions of counterpropagating DE SWs [cf. Fig. 4.4], although it can not be verified experimentally on the fabricated Pt(2 nm)/Co(0.4 nm)/Py(5 nm)/MgO(5 nm) stripes. The validity of this assumption is supported by the findings reported by Di *et al.* [53], who also performed SW propagation experiments to prove the presence of an interfacial DMI on a very similar layer stack, where a ferromagnetic bilayer is sandwiched as well between Pt and MgO layers: Pt(4 nm)/Co(1.6 nm)/Ni(1.6 nm)/MgO(2 nm). They proved by measurements on "control samples" (i) that the contribution of the asymmetric distribution in M_S to the asymmetry in the SW dispersion is not relevant at all[94] as well as (ii) that the contribution arising from the proximity-induced magnetic moment in the Pt layer is even weaker[95] than the one arising from the asymmetry in M_S.

In contrast, the asymmetry in the strength of the uniaxial PMA field across the thickness of the ferromagnetic layer might be strong enough to manifest as a distinct asymmetry in the DE SW dispersion. The uniaxial PMA field originates from the Pt/Co interface, and, therefore, it is stronger in the vicinity of that interface than in the vicinity of the Py/MgO interface. In this case, however, according to Eq. (4.1), at fixed f and at a fixed propagation direction, the wave number of propagating DE SWs localized at the Pt/Co interface would be larger than of those localized on the Py/MgO interface, i.e., the signature of the asymmetry with respect to the bias field polarity would be inverted compared with the one observed in the experimental data [cf. Fig. 4.4].
This finding implies two logical consequences:

(i) An interfacial DMI arises in fact at the Pt/Co interface.

(ii) As the impact of this interfacial DMI is superimposed by impact of the uniaxial PMA field acting in the opposite direction and as, in addition to that, the signature of the asymmetry observed in the DE SW dispersions is different to the one expected in the case, where no interfacial DMI is

[94] This finding reveals the justification to consider the Co/Ni bilayer as an effective medium.
[95] This finding is reasonable since the induced magnetic moment in the Pt is highly localized within the first few atomic layers adjacent to the Pt/Co interface, and it is much weaker than the magnetic moments of Co and Ni [171].

present, the question arises, whether the D_{eff}-value deduced from the experimental data specifies in fact only a lower boundary to the (absolute) strength of the interfacial DMI.

Experimentally, it is impossible to disentangle both contributions to the asymmetry in the DE SW dispersion since the interfacial DMI and the uniaxial PMA field originate from the Pt/Co interface. For this reason, micromagnetic simulations using MuMax3 [173] need to be performed enabling the investigation and quantification of either contribution as well as an interpretation of the meaningfulness of the experimentally deduced D_{eff}-value.

4.5 Implementation of the Micromagnetic Simulations

The fabricated Pt/Co/Py/MgO stripes are modeled as illustrated in the schematic shown in Fig. 4.9: Retaining the layer order along the y direction, the Co/Py bilayer is considered as an effective medium called "ferromagnet", which is sandwiched between the Pt layer at the bottom and the MgO layer at the top. To be able to account for interface-related effects in the simulations in the first place, the ferromagnet is divided into N_y layers along the y direction [cf. Fig. 4.9], thereby enabling to assign different material parameter values to the individual ferromagnetic layers[96]. The material parameters[97] used are listed Table 4.2.
To access the dispersions of counterpropagating DE SWs, in agreement with the

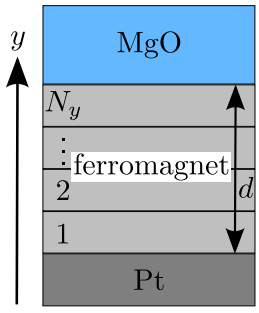

Figure 4.9. Schematic of the multilayered stack, in which the propagation of DE SWs is simulated. The ferromagnet is subdivided into N_y layers across its thickness d. The layer order along the y direction is the same as in case of the fabricated Pt/Co/Py/MgO stripes.

quantity	value
$\mu_0 M_{\text{S}}^{(\text{eff})}$ [T]	1.23
A [J/m]	13×10^{-12}
γ [rad/(Ts)]	180×10^9
K_{u1} [J/m^3]	2.6×10^5
$\mu_0 H_{\text{u}}^{\perp} = 2K_{\text{u1}}/M_{\text{S}}$ [T]	0.53
$D_{\text{eff}}^{\text{sim}}$ [mJ/m^2]	0.00–0.30
d [nm]	5.7
α	0.013

Table 4.2. Material parameters used for the various simulations.

[96] At the time the micromagnetic simulations were performed, it was only possible to assign different values for K_{u1} to individual layers, but not for $D_{\text{eff}}^{\text{sim}}$.

[97] They are very similar to the ones deduced in case of the fabricated Pt/Co/Py/MgO stripes. The small deviations only result in negligible changes since the dominating factor in the DE SW dispersion [cf. Eq. (4.1)] is the effective magnetization $M_{\text{eff}} = M_{\text{S}}^{(\text{eff})} - H_{\text{u}}^{\perp}$ [cf. Eq. (1.48)], and the M_{eff}-values are the same.

experiment [cf. Sec. 4.3], at either bias field polarity, the propagation of DE SWs is simulated at a bias field magnitude of 43 mT, while sweeping the excitation frequency from 5.28 GHz to 6.48 GHz in steps of 80 MHz. The resulting simulation data are analyzed almost the same way as the Kerr images [cf. Sec. 4.3]. Additional details about the general implementation and the analysis of the simulation data are given in Appendix B.2.

Three different scenarios are simulated enabling to investigate and quantify the impact of a (localized) uniaxial PMA field on the dispersion of propagating DE SWs when the (interfacial) DMI is either present or not.

Scenario A The DMI and the uniaxial PMA field (anisotropy axis along the y direction) are uniform across the thickness of the ferromagnet. For this purpose, in each layer, the value of the first order first order uniaxial PMA constant K_{u1} is set to the value listed in Table 4.2, while the value of the effective DMI constant $D_{\mathrm{eff}}^{\mathrm{sim}}$ is either set to $0\,\mathrm{mJ/m^2}$, i.e., no interfacial DMI is present, or to[98] $0.176\,\mathrm{mJ/m^2}$, i.e., an interfacial DMI is present.

Scenario B An interfacial DMI is not present, i.e., $D_{\mathrm{eff}}^{\mathrm{sim}} = 0\,\mathrm{mJ/m^2}$, while the uniaxial PMA field is present, but it is only effective in that ferromagnetic layer, which is adjacent to the Pt layer. For this purpose, K_{u1} is only assigned to the cells in layer[99] "1". Moreover, in this scenario, the magnitude of the uniaxial PMA field can be varied by introducing a scaling factor s ($s \geq 0$) enabling to assign an effective first order uniaxial PMA constant $K_{\mathrm{u1}}^{\mathrm{eff}} = s \times K_{\mathrm{u1}}$ to the cells in that particular layer[100], thereby enabling the modification of the cutoff frequency $\omega\,(k = 0) = 2\pi f\,(k = 0)$.

Scenario C This scenario is a mixture of scenarios A and B. The uniaxial PMA field is only effective in that layer of the ferromagnet, which is adjacent to the Pt layer, i.e., layer "1", while the DMI is uniform across the thickness of the ferromagnet. Moreover, in this scenario, the scaling factor is fixed, i.e., $s = s_{\mathrm{fix}}$, while the strength of the DMI is varied by sweeping the $D_{\mathrm{eff}}^{\mathrm{sim}}$-value in the range from 0.10–$0.30\,\mathrm{mJ/m^2}$.

4.6 Simulation Results and Discussion

In the following, the findings concerning the simulations of the different scenarios A, B, and C are presented and discussed in Sec. 4.6.1, 4.6.2 and 4.6.3, respectively.

[98] The difference between this $D_{\mathrm{eff}}^{\mathrm{sim}}$-value and the experimentally determined one [average value, cf. Table 4.1] is negligible, as it is only about 6%.

[99] The bottommost layer of cells in the xz plane—labeled "1"—is the one next to the Pt layer, while the uppermost layer of cells in the xz plane—labeled "N_y"—is adjacent to the MgO layer [cf. Fig. 4.9].

[100] Related to the bottommost layer of the ferromagnet only, this is equivalent to an interfacial-like effective first order uniaxial PMA constant $K_{\mathrm{u1}}^{\mathrm{eff,int}} = K_{\mathrm{u1}}^{\mathrm{eff}} \times \frac{d}{N_y}$ ($\widehat{=} \frac{s}{N_y} \times 1.5\,\mathrm{mJ/m^2}$).

4.6.1 Scenario A: Uniform Perpendicular Magnetic Anisotropy Field and Uniform Dzyaloshinskii-Moriya Interaction

In scenario A, the uniaxial PMA field and the DMI are both uniform across the thickness of the ferromagnet. This case is assumed when the strength of the interfacial DMI is deduced from fits of the measured DE SW dispersions to Eq. (4.1) [cf. Sec. 4.4.3]. The corresponding DE SW dispersions simulated with $D_{\mathrm{eff}}^{\mathrm{sim}} = 0.176\,\mathrm{mJ/m^2}$ are shown in Fig. 4.10. Symbols denote simulation data while solid lines indicate the DE SW dispersions resulting from Eq. (4.1) when inserting the sample parameters listed in Table 4.2. For ease of comparison with the experimental data, the symbol and color code is identical with the one used in Fig. 4.4.
At first glance, the scenario A simulations seem to reproduce all the essential experimental findings:

(i) The dispersions of counterpropagating DE SWs are asymmetric with respect to the bias field polarity, and the signature of the asymmetry is identical with the one observed in the experiment [cf. Fig. 4.4]. For comparison, the additionally simulated and calculated dispersions for $D_{\mathrm{eff}}^{\mathrm{sim}} = 0\,\mathrm{mJ/m^2}$ are plotted as well, which are symmetric. As clearly visible in Fig. 4.4, all simulated dispersions agree perfectly with the calculated ones.

(ii) At a fixed propagation and at $f = 6.48\,\mathrm{GHz}$, the maximum difference in wave numbers Δk at opposite orientation of the bias field is $\approx 1\,\mu\mathrm{m}^{-1}$. This Δk-value coincides well with the experimental one(s).

(iii) The cutoff frequency $f\,(k = 0)$ of each dispersion branch is $\approx 5.12\,\mathrm{GHz}$[101]. This value is in good agreement with the FMR frequency at 43 mT [cf. 4.2].

Yet, despite all these matches, the assumption that the uniaxial PMA field is uniform across the thickness of the ferromagnet is not very realistic as, in the fabricated Pt/Co/Py/MgO stripes, the uniaxial PMA field originates from

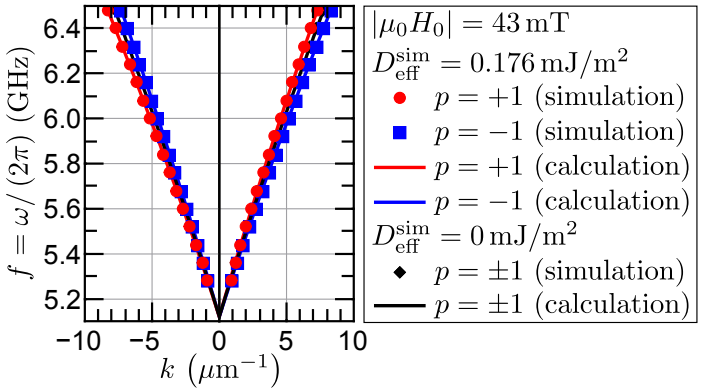

Figure 4.10. Dispersions of counterpropagating DE SWs in scenario A. Symbols denote simulation data while solid lines indicate the DE SW dispersions calculated using Eq. (4.1).

[101] As the simulated and the calculated dispersions agree perfectly, the value given is the one resulting from Eq. (4.1) when inserting the material parameters used in the simulations [cf. Table 4.2] at $k = 0$.

the Pt/Co interface, in whose vicinity it is the strongest. This characteristic is accounted for in the scenario B simulations.

4.6.2 Scenario B: Localized Perpendicular Magnetic Anisotropy Field with Varying Strength and no Dyzaloshinskii-Moriya Interaction

In scenario B, it is assumed that no interfacial DMI is present while concurrently a uniaxial PMA occurs, which is strongly localized near the Pt/ferromagnet interface.

First of all, in agreement with the expectation, in general, the scenario B simulations reveal that the cutoff frequency can be simply tuned by modifying the strength of the effective first order uniaxial anisotropy constant $K_{\mathrm{u1}}^{\mathrm{eff}}$ assigned only to the cells in layer "1": the smaller the $K_{\mathrm{u1}}^{\mathrm{eff}}$-value given, i.e., the weaker the strength of the uniaxial PMA field arising at the Pt/ferromagnet interface, the larger the cutoff frequency, and, consequently, the smaller the wave number(s) of propagating DE SWs excited at any frequency in the range from 5.28–6.48 GHz, as $k \sim f$ applies [cf. Sec. 1.4.1].

For the comparison of the simulations results of the individual scenarios from a quantitative point of view, a common starting point needs to be defined. One appropriate choice is the cutoff frequency, which should be identical with the FMR frequency deduced from the full film characterization [cf. Sec. 4.2] independent of the scenario simulated since $f_{\mathrm{FMR}} = \lim_{k\to 0} f(k)$ applies [cf. Eq. (1.47)]. In the scenario B simulations, the closest match with respect to the cutoff frequency in scenario A—which can be calculated using Eq. (4.1)—is found for $s = 3.5$. The corresponding simulated DE SW dispersions are shown in Fig. 4.11 in comparison with the dispersion calculated for scenario A with $D_{\mathrm{eff}}^{\mathrm{sim}} = 0\,\mathrm{mJ/m^2}$, as this dispersion corresponds to the case, where no interfacial DMI is present while concurrently the uniaxial PMA field is homogeneous across the thickness of the ferromagnet.
Either scenario B dispersion is shifted towards smaller wave numbers compared with the scenario A dispersion with $D_{\mathrm{eff}}^{\mathrm{sim}} = 0\,\mathrm{mJ/m^2}$ [cf. red and blue symbols vs. black lines in Fig. 4.11]. More prominent, however, is the signature of the

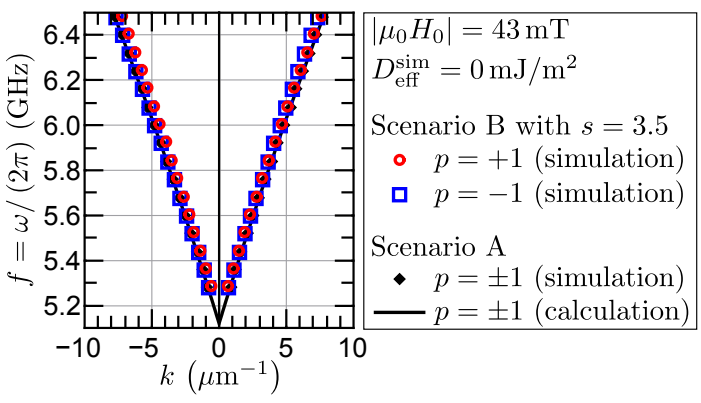

Figure 4.11. Dispersions of counterpropagating DE SWs in scenario B with $s = 3.5$ and $D_{\mathrm{eff}}^{\mathrm{sim}} = 0\,\mathrm{mJ/m^2}$ in comparison with scenario A with $D_{\mathrm{eff}}^{\mathrm{sim}} = 0\,\mathrm{mJ/m^2}$. Symbols denote simulation data while solid lines indicate the DE SW dispersion corresponding to this particular scenario A calculated using Eq. (4.1).

asymmetry in the DE SW dispersions occurring in this scenario B simulation/all scenario B simulations: It is reversed compared with the one observed in the experiment [cf. Fig. 4.4] as well as with the one revealed by the scenario A simulations with finite $D_{\mathrm{eff}}^{\mathrm{sim}}$ [cf. Fig. 4.10]. Moreover—for $s = 3.5$—Δk at 6.48 GHz is only $\approx 0.4\,\mu\mathrm{m}^{-1}$, which is much smaller than the Δk-value deduced from the experimental data.

These findings confirm

(i) that—in agreement with the findings reported by other groups [53, 131]—in the absence of an interfacial DMI, an asymmetric distribution of the uniaxial PMA field across the thickness of the ferromagnet alone induces in fact an asymmetry in the DE SW dispersions, but its signature is opposite to the one emerging due to the presence of an interfacial DMI, as well as

(ii) that the asymmetry in the DE SW dispersions observed in the experiment can only be explained by the co-occurrence of an interfacial DMI originating from the Pt/Co interface.

Consequently, these statements imply

(i) that the interfacial DMI acts contrary to the uniaxial PMA field and that it is much stronger than it[102], as well as

(ii) that the D_{eff}-value resulting from the fits of the measured DE SW dispersions to Eq. (4.1) does not quantify the actual strength of the interfacial DMI, but only specifies a lower boundary to it.

Either implication is addressed by the scenario C simulations.

4.6.3 Scenario C: Localized Perpendicular Magnetic Anisotropy Field with Fixed Strength and Uniform Dzyaloshinskii-Moriya Interaction with Varying Magnitude

In scenario C, only in the cells of layer "1", $K_{\mathrm{u1}}^{\mathrm{eff}}$ is now set to a fixed value, namely $s_{\mathrm{fix}} \times K_{\mathrm{u1}}$ with $s_{\mathrm{fix}} = 3.5$, thereby ensuring that the cutoff frequency is identical both with the one in the scenario A simulations and with the one in the scenario B simulation with $s = 3.5$. Concurrently, the $D_{\mathrm{eff}}^{\mathrm{sim}}$-value is varied

Table 4.3. Δk for different $D_{\mathrm{eff}}^{\mathrm{sim}}$-values deduced from the respective scenario C simulations.

$D_{\mathrm{eff}}^{\mathrm{sim}}$ [mJ/m^2]	0.10	0.176	0.25	0.30
Δk [μm^{-1}]	≈0.16	≈0.57	≈0.97	≈1.35

[102] Only when the strength of the interfacial DMI is larger than the strength of the asymmetrically distributed uniaxial PMA field, the signature of the asymmetry in the DE SW dispersion becomes opposite to the one induced by the uniaxial PMA field alone.

in the range from 0.10 to 0.30 mJ/m^2. For a quantitative comparison with the experimental results, Δk is evaluated once again at 6.48 GHz. The results are listed in Table 4.3 while the corresponding simulated DE SW dispersions are shown in Fig. 4.12.
The scenario C simulations reveal two features:

(i) When a strong enough interfacial DMI is present at the Pt/ferromagnet interface along with a uniaxial PMA field, which is (mainly) localized at the same interface, the signature of the asymmetry in the simulated DE SW dispersions coincides with the one observed in the experiment. It is even possible to specify a threshold value $D_{\mathrm{eff}}^{\mathrm{thres}}$. Here, it is defined as the $D_{\mathrm{eff}}^{\mathrm{sim}}$-value, at which the signature of the asymmetry changes from the case, where the uniaxial PMA field dominates, to the case, where the interfacial DMI dominates. For the multi-layer system studied, $D_{\mathrm{eff}}^{\mathrm{thres}}$ is slightly smaller than $\approx$0.10 mJ/m^2 [cf. Fig. 4.12(a)].

(ii) Δk—evaluated at 6.48 GHz—increases monotonically from $\approx$0.16 μm^{-1} up to $\approx$1.35 μm^{-1} when $D_{\mathrm{eff}}^{\mathrm{sim}}$ is increased from 0.10 mJ/m^2 to 0.30 mJ/m^2 [cf. Table 4.3 and Figs. 4.12(a)-(d)]. For $D_{\mathrm{eff}}^{\mathrm{sim}} = 0.176$ mJ/m^2—the value closest to the one determined from the experimental data—Δk is $\approx$0.57 μm^{-1}. However, this Δk-value is much smaller than the Δk-value of about 1 μm^{-1} deduced from the experimental data. The experimentally deduced Δk-value ensues when $D_{\mathrm{eff}}^{\mathrm{sim}}$ is set[103] to 0.25 mJ/m^2.

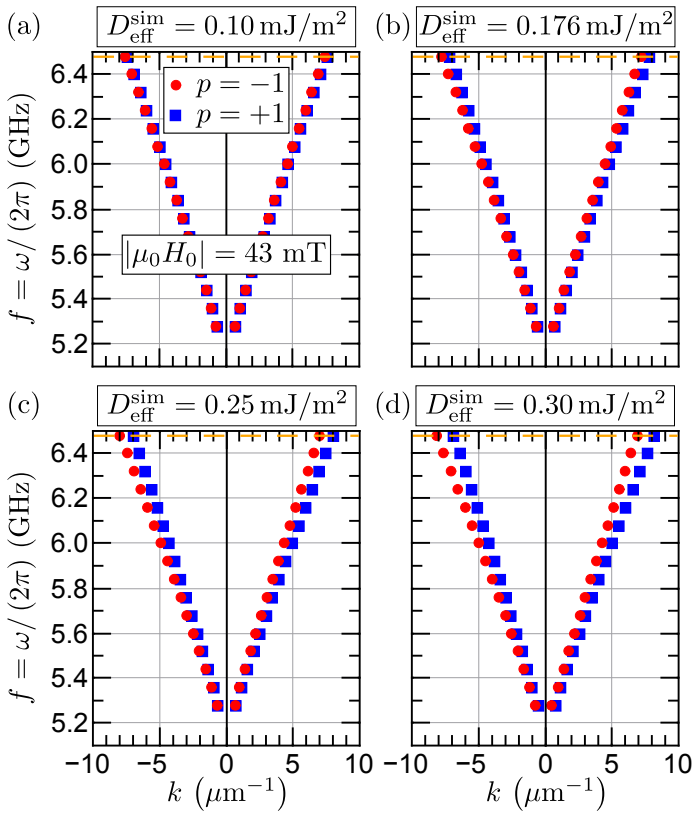

Figure 4.12. Dispersions of counterpropagating DE SWs in scenario C with $s_{\mathrm{fix}} = 3.5$ and $D_{\mathrm{eff}}^{\mathrm{sim}}$ in the range from 0.10–0.30 mJ/m^2. The dashed orange lines mark the excitation frequency $f = 6.48$ GHz, at which Δk is evaluated [cf. Table 4.3].

[103] In this case, the absolute values of the respective DE SW wave numbers are about 1 μm^{-1} smaller than the experimental ones. This feature is attributed to the way the (localized) uniaxial PMA field and the interfacial DMI are modeled in the micromagnetic simulations.

Based on these findings, it can be stated that the D_{eff}-value—evaluated from fits of the measured DE SW dispersions to Eq. (1.71) assuming that the uniaxial PMA field arising at the Pt/ferromagnet interface is uniform across the thickness of the ferromagnet—underestimates the impact of the interfacial DMI (concurrently) emerging at the Pt/ferromagnet interface by up to 40% assuming that the uniaxial PMA field is strongly localized at the Pt/ferromagnet interface. In other words, the D_{eff}-value deduced from the experimental data only specifies a lower boundary to the strength of the interfacial DMI occurring in the fabricated Pt/Co/Py/MgO stripes.

4.7 Conclusion

In conclusion, it was demonstrated that TRMOKE on propagating DE SWs is in fact a sensitive tool to prove the existence of an interfacial DMI arising at the Pt/Co interface in the fabricated Pt(2 nm)/Co(0.4 nm)/Py(5 nm)/MgO(5 nm) stripes. It manifested itself in a distinct asymmetry in the dispersions of DE SWs propagating in the same direction, but at opposite orientations of the magnetic bias field. This asymmetry could not yet be observed in the attenuation length as well since the corresponding differences were too small to be resolved by single magnetic imaging. Micromagnetic simulations confirmed that the observed signature of the asymmetry along with the observed differences in the respective DE SW wave numbers can not be solely caused by the uniaxial PMA field originating from the Pt/Co interface as well, but are consistent with the co-occurrence of an interfacial DMI at this interface, which acts contrary to the uniaxial PMA field and which is much stronger than it. The simulations additionally revealed that the approach used to evaluate the strength of the interfacial DMI from the asymmetry in experimentally acquired DE SW dispersions underestimates its actual strength by up to 40%, thereby only yielding a lower boundary to it.

Chapter 5

Magnetic Damping in Poly-Crystalline $Co_{25}Fe_{75}$—Ferromagnetic Resonance vs. Spin Wave Propagation Experiments

The results presented in this chapter are published in [135]:

H. S. Körner, M. A. W. Schoen, T. Mayer, M. M. Decker, J. Stigloher, T. Weindler, T. N. G. Meier, M. Kronseder, and C. H. Back.
Magnetic damping in poly-crystalline $Co_{25}Fe_{75}$: Ferromagnetic resonance vs. spin wave propagation experiments.
Appl. Phys. Lett. **111**, 132406 (2017).

Contents

5.1 Motivation and Goal

Further advances in the field of magnonics, where SWs will be utilized as information carriers, essentially depend on magnetic films in which SWs can propagate over large distances, i.e., on the order of several tens of micrometers up to millimeters [3]. The corresponding figure of merit is the SW attenuation length L_{att} defined as the distance over which the SW amplitude decays to a factor of $1/e$ [cf. Sec. 1.4]. It strongly depends on the parameters and magnetic properties of the film—the saturation magnetization M_{S}, the presence and orientation of magneto-crystalline anisotropies, and the thickness—as well as on the magnetization precession losses [1, 2]. The latter ones enter the effective magnetic SW damping parameter $\alpha_{\mathrm{eff}}^{\mathrm{SW}}$ which scales with $1/L_{\mathrm{att}}$ [cf. Eq. 1.56]. Hence, one branch in the field of magnonics focuses on the fabrication and study of magnetic materials with low magnetic damping parameters. From this perspective, within the last decade, various different materials have been thoroughly investigated.

The ferrimagnetic insulator yttrium iron garnet (YIG)—$Y_3Fe_5O_{12}$—exhibits extremely low magnetic damping parameters α—on the order of 10^{-5}–10^{-4} [174, 175]—but its low saturation magnetization—about 0.2 T—results in relatively low group velocities [176]. Moreover, it requires delicate growth techniques and its integration into micrometer scale magnonic devices remains challenging.
Ferromagnetic metal films are considered as promising alternatives since the disadvantage of much larger magnetic damping parameter values—on the order of 2–8$\times10^{-3}$—is compensated by a much larger saturation magnetization—on the order of 1–2 T—and by an easier deposition and integration into magnonic elements. So far, various metals have been explored, e.g., the ferromagnetic metals Permalloy—$Ni_{80}Fe_{20}$, $\alpha \approx 6$–8×10^{-3}, $\mu_0 M_{\mathrm{S}} \approx 1\,\mathrm{T}$ [11, 49, 132]—and Fe—$\alpha \approx 2\times10^{-3}$, $\mu_0 M_{\mathrm{S}} \approx 2.2\,\mathrm{T}$ [13]— half-metallic Heusler alloys [177, 178], and CoFeB alloys [179], where the fabrication of the latter two with low damping parameters still remains a delicate issue.
Just recently, a very low magnetic damping was theoretically predicted by Mankovsky *et al.* [180] and experimentally verified by Schoen *et al.* [181, 182] for the ferromagnetic binary $3d$ transition metal alloy Co_xFe_{1-x} revealing pure intrinsic damping parameters as low as 5×10^{-4} for the composition $Co_{25}Fe_{75}$. In combination with its large saturation magnetization—about 2.4 T at room temperature—and its relatively easy deposition, $Co_{25}Fe_{75}$ offers several benefits to become a very promising ferromagnetic metal to be employed in future magnonic devices.

Up to now and despite its many promising properties, an experimental investigation of the propagation and attenuation of SWs in $Co_{25}Fe_{75}$ is still lacking. Hence, the goal of this study is to assess the magnetic damping in 10 nm-thin, poly-crystalline $Co_{25}Fe_{75}$ (CoFe) grown by molecular beam epitaxy (MBE) by in-plane FMR measurements on a full film sample as well as by SW propagation experiments performed by TRMOKE on micrometer-wide stripes patterned from the very same CoFe full film since stripes are a more realistic geometry to be utilized in magnonic devices. The FMR measurements are used to prove that the CoFe grown exhibits indeed a low intrinsic Gilbert damping parame-

ter $\alpha_{\mathrm{int}}^{\mathrm{FMR}}$ [cf. Ref. [182]], which should be reflected in SW attenuation lengths on the order of several tens of micrometer[104]. The thorough evaluation of the attenuation length enables access to the effective magnetic SW damping parameter $\alpha_{\mathrm{eff}}^{\mathrm{SW}}$, which is then compared with $\alpha_{\mathrm{int}}^{\mathrm{FMR}}$ to eventually make a statement about whether poly-crystalline CoFe is actually a suitable metallic material for magnonic devices.

5.2 Samples: Design, Fabrication and Characterization

The full film sample is grown in a multi-step process by MBE[105]. First, a GaAs(001) substrate is degassed at 250 °C prior to the growth of a 5 nm-thin MgO seed layer. Then a 10 nm-thin $Co_{25}Fe_{75}$ layer is grown by the co-deposition from Co and Fe sources. Finally, a MgO(5 nm)/Al_2O_3(7 nm) bilayer capping is added to prevent the magnetic layer from oxidation. The final full film layer stack is illustrated in the schematic in Fig. 5.1(a).
The composition of the CoFe layer is verified by X-ray photoelectron spectroscopy (XPS) measurements[106] with an error of less than 3%. Its quality is checked by SQUID measurements conducted at $T = 290\,\mathrm{K}$ revealing a saturation magnetization of $\mu_0 M_{\mathrm{S}} = (2.4 \pm 0.1)\,\mathrm{T}$, which is in good agreement with the value reported by Schoen *et al.* [181]. The full film is further characterized in detail by in-plane FMR measurements[107]. [cf. Sec. 5.4.1].
Later on, for the SW propagation experiments [cf. Sec. 5.4.2], a piece of the full film is patterned into eight 500 μm-long and 1.15 μm-wide stripes by EBL, chemically assisted ion beam etching (CAIBE) with Ar^+ ions and liftoff. As shown in Fig. 5.1(b), the long axis of the stripes is oriented perpendicular to the easy axis of the weak uniaxial in-plane anisotropy of the CoFe layer [cf. Fig. 5.2(a) in Sec. 5.4.1]. Then, an additional 80 nm-thick insulating Al_2O_3 layer is grown by ALD. It ensures that the CoFe stripes are electrically decoupled

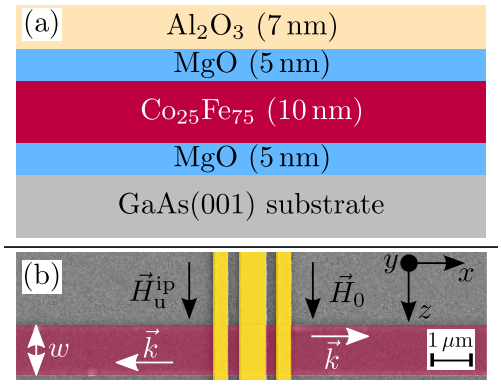

Figure 5.1. (a) Schematic of the full film multi-layer stack grown by MBE. (b) Colored SEM image of one CoFe stripe sample fabricated from this stack for the SW propagation experiments. In the CoFe stripe of width $w = 1.15\,\mu\mathrm{m}$ (red), propagating DE SWs with wave vector $\vec{k}$ are excited by the microwave antenna (yellow) while the magnetic bias field $\vec{H}_0$ is applied along the z direction. The stripe's long axis is oriented perpendicular to the easy axis of the uniaxial in-plane anisotropy field $\vec{H}_{\mathrm{u}}^{\mathrm{ip}}$.

[104] These values result from Eq. (1.56) when using the aforementioned CoFe material parameters.
[105] The full film sample was grown by Matthias Kronseder.
[106] The XPS measurements were performed and analyzed by Thomas Meier.
[107] The FMR measurements were performed and evaluated by Martin Schön and Thomas Mayer.

from the microwave antennas in the shape of shorted CPWs, which are subsequently patterned on top by EBL, thermal evaporation of Cr(10 nm)/Au(60 nm) and liftoff as depicted in Fig. 5.1(b).

5.3 Implementation of the Experiment and Data Analysis

The experiment is divided into two steps:

1. The full film sample is characterized by in-plane FMR measurements and the intrinsic magnetic damping parameter $\alpha_{\mathrm{int}}^{\mathrm{FMR}}$ is evaluated.

2. In micrometer-wide stripes patterned from this full film, the propagation of DE SWs is investigated magneto-optically by TRMOKE. Here, the main focus is on the determination of the SW attenuation length L_{att} as access to this quantity enables the determination of the effective magnetic SW damping parameter $\alpha_{\mathrm{eff}}^{\mathrm{SW}}$ and its comparison with $\alpha_{\mathrm{int}}^{\mathrm{FMR}}$.

The waveguide-based FMR measurements are performed at room temperature in the in-plane geometry utilizing a Schottky diode detector and lock-in amplification of the field-modulated signal [182]. Frequencies up to 40 GHz and fields up to 2 T are applied at in-plane angles ranging from 0 to 360°. The FMR data are fitted by the method described in Ref. [183] to extract the frequency dependence of both the resonance field H_{res} and the linewidth[108] ΔH.

The SW propagation experiments are performed as well at room temperature in the DE geometry, i.e., as illustrated in Fig. 5.1(b), SWs with wave vector $\vec{k}$ are excited by the microwave antenna and propagate along the x direction in the CoFe stripe while its static magnetization is maintained perpendicular to its long axis by a magnetic bias field $\vec{H}_0$ applied along the z direction. SW dynamics in the CoFe stripes is accessed magneto-optically by TRMOKE. The setup is operated in the spectroscopy mode [cf. Sec. 2.2.1] as well as in the imaging mode [cf. Sec. 2.2.2]. SW resonance spectra are recorded at different excitation frequencies f approximately 2 μm away from the edges of the microwave antenna at a fixed phase—$\phi = 0°$—between the microwave excitation and the laser pulses. From these spectra the field ranges are extracted, in which propagating DE SWs can be detected optically at fixed f. Kerr images of the propagating DE SWs are recorded at different combinations of f and H_0 at the same phase ϕ. They are analyzed as follows:
First, two-dimensional arrays—xz plane—covering the stripe are cropped from the Kerr images starting some micrometer away from the edges of the microwave antenna, and then they averaged along the z direction [cf. Sec. 2.2.2]. Due to the amplitude nonreciprocity inherently present when exciting DE SWs by a microwave antenna [cf. Sec. 1.4.5] the analysis focuses on that side of the CoFe stripe where the Kerr signal/the SW amplitude is larger at a fixed polarity of

[108] full width at half maximum

the magnetic bias field. The resulting one-dimensional line scans are fitted to an exponentially decaying sine function to extract the SW wave number k and the attenuation length L_{att} [cf. Eq. (2.3)]. At this point, it should be noted that, in contrast to k, the fit results for L_{att} depend crucially on both the starting point of the fit as well as on noise on the Kerr signal amplitude. Furthermore, fits to Eq. (2.3) reveal reasonable results for L_{att} only when applied to line scans extracted from regions of the CoFe stripe, where the exponentially decaying character of the SW amplitude is still significantly pronounced, i.e., not too far away from the microwave antenna, and where the actual SW amplitude is not superimposed by the Oersted field of the microwave antenna, i.e., not too close to the microwave antenna. Due to these peculiarities a proper and careful analysis of L_{att} is essential for a precise determination of $\alpha_{\mathrm{eff}}^{\mathrm{SW}}$. For this purpose, from the Kerr images different regions of the CoFe stripe are cropped. All resulting one-dimensional line scans cover 7.5 μm in total along the x direction, and their starting point is shifted from $\approx$1 μm away from the edges of the microwave antenna to 8.5 μm in steps of 250 nm[109]. Hence, from each Kerr image approximately 30 different line scans are extracted and fitted, thereby enabling statistics on both k and L_{att}.
Moreover, during the SW data analysis, it is also checked, whether averaging the cropped, two-dimensional arrays along the z direction is justified. This needs to be done since the DE SW propagation is investigated in micrometer-wide CoFe stripes, where the impact of the lateral confinement on the SW propagation [cf. Sec. 1.4.6] might need to be taken into consideration. However, the respective fits do not reveal discernable different fits results compared with fits to one-dimensional line scans extracted from the center of the stripe.

5.4 Experimental Results and Discussion

In this section, the experimental findings on the FMR characterization on the CoFe full film sample are presented and discussed in Sec. 5.4.1, while those on the investigation of the DE SW propagation in micrometer-wide CoFe stripes are addressed in Sec. 5.4.2.

5.4.1 Ferromagnetic Resonance Measurements on the $Co_{25}Fe_{75}$ Full Film

The results of the in-plane FMR measurements are compiled in Fig. 5.2. The Kittel fit to the frequency dependence of the in-plane resonance field—extracted from the measurements performed at 12 GHz—yields a gyromagnetic ratio γ of 185×10^9 rad/ (Ts) and an effective magnetization [cf. Eq. 1.47] $\mu_0 M_{\mathrm{eff}} = \left(\mu_0 M_{\mathrm{S}} - \mu_0 H_{\mathrm{u}}^{\perp}\right) = (1.91 \pm 0.02)$ T. Consequently, using the M_{S}-value obtained from SQUID measurements [cf. Sec. 5.2], $\mu_0 H_{\mathrm{u}}^{\perp} = (0.49 \pm 0.10)$ T is the strength of the uniaxial PMA field. The angular dependence of the in-plane resonance field [cf. Fig. 5.2(a)] reveals that the CoFe full film is almost magnetically isotropic as the uniaxial in-plane anisotropy field $H_{\mathrm{u}}^{\mathrm{ip}}$ is not clearly pronounced:

[109] The step size is given by the number of pixels and the size of the Kerr images.

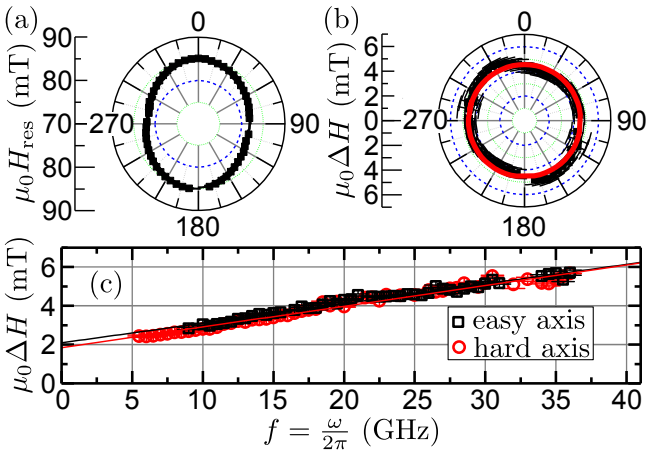

Figure 5.2. Full film in-plane FMR characterization. (a) Angular dependence of the in-plane resonance field H_{res} at $f = 12\,\mathrm{GHz}$. (b) Corresponding angular dependence of the in-plane linewidth ΔH. The red circle visualizes the isotropy of this quantity. (c) Frequency dependence of ΔH extracted from measurements performed with the bias field applied along the hard axis, i.e., along 0° in (a), as well as along the easy axis, i.e., along 90° in (a). Solid lines denote linear fits to the data.

$\mu_0 H_u^{ip} = (1.7 \pm 0.2)\,\mathrm{mT}$, i.e., it is two orders of magnitude weaker than the uniaxial PMA field. The easy axis of the uniaxial in-plane anisotropy is oriented along the (110) direction of the GaAs substrate, which corresponds to an in-plane angle of 90° in Fig. 5.2(a). In contrast to the four-fold symmetry, which is characteristic for a crystalline grown *bcc* CoFe [184], the presence of this uniaxial in-plane anisotropy indicates the poly-crystalline growth of the CoFe layer. This kind of growth is most likely induced by the poly-crystalline or amorphous growth of the MgO seed layer on the native oxide layer on top of the GaAs(001) substrate, which was not removed upon preparation of the substrate [cf. Sec. 5.2]. In contrast to H_{res}, the corresponding linewidth ΔH does not display any discernable dependence on the in-plane angle of the magnetic bias field within the error bars as indicated by the red circle in Fig. 5.2(b). For the determination of the intrinsic Gilbert damping parameter α_{int}^{FMR} the frequency dependence of ΔH is measured for $f \approx 5$–$36\,\mathrm{GHz}$ with the bias field applied at different in-plane angles between 0° and 90°, which correspond to the hard and easy axis of the uniaxial in-plane anisotropy. The results for 0° and 90° shown in Fig. 5.2(c) reveal no discernable angular dependence within the error bars.

The standard procedure to deduce α_{int}^{FMR} as well as the extrinsic contributions to the magnetic damping—indicated by a finite zero-frequency linewidth offset $\Delta H\,(\omega = 0)$—is to fit the frequency dependence of ΔH to [185, 186]

$$\Delta H\,(\omega) = \frac{2\alpha_{int}^{FMR}\omega}{\mu_0\gamma} + \Delta H\,(\omega = 0) \qquad (\omega = 2\pi f)\ . \tag{5.1}$$

The fits yield $\alpha_{int}^{FMR} = (1.5 \pm 0.1)\times 10^{-3}$ and $\mu_0 \Delta H\,(\omega = 0) = (2.0 \pm 0.1)\,\mathrm{mT}$, respectively. At this point, it should be noted that the values given are the average of the values for 0° and 90°, and that the contribution to the intrinsic magnetic damping arising from radiative damping inherently present when performing waveguide-based FMR measurements [187] is already subtracted. This α_{int}^{FMR}-value is indeed three times larger than the one reported by Schoen *et al.* [181] in the case of sputtered $Co_{25}Fe_{75}$ full films, but still very low for a metallic system. However, more remarkable is the fact that the inhomogeneous linewidth

broadening $\Delta H(\omega = 0)$ is not negligible small, but significant thereby indicating a distinct impact of the extrinsic contributions such as inhomogeneities and two-magnon scattering on the magnetic damping [186].

5.4.2 Spin Wave Propagation in Micrometer-Wide $Co_{25}Fe_{75}$ Stripes

In the micrometer-wide CoFe stripes, the propagation of DE SWs is demonstrated both by SW resonance spectra and by magnetic imaging. In Fig. 5.3(a), a selection of SW resonance spectra recorded at different frequencies is displayed. Clear SW resonances are observed for $f = 10$–$18\,\mathrm{GHz}$ at bias field magnitudes ranging from 30 to 180 mT. In the top panel of Fig. 5.3(b), an example Kerr image is shown, whereas the corresponding line scans—extracted on either side of the microwave antenna—are depicted in the bottom panel. The amplitude nonreciprocity is clearly visible.

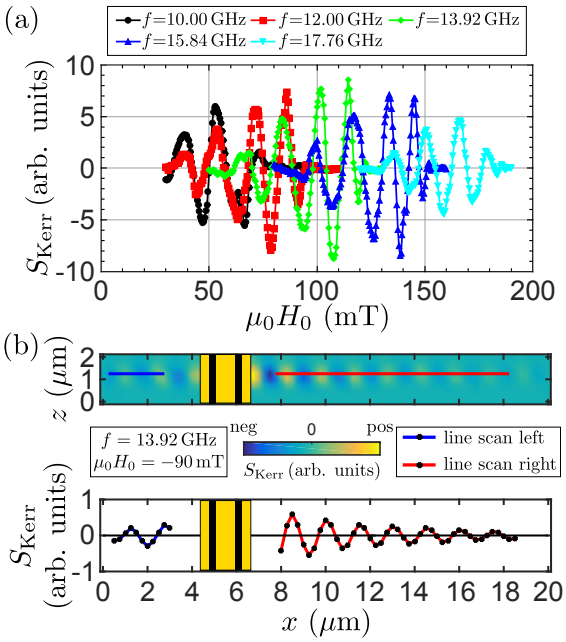

Figure 5.3. DE SW propagation in micrometer-wide CoFe stripes demonstrated by (a) SW resonance spectra and (b) magnetic imaging. From the Kerr image (top panel in (b)) one-dimensional line scans (bottom panel in (b)) are extracted along the red and blue lines on either side of the microwave antenna (yellow) and fitted to an exponentially decaying sine function.

Based on the SW resonance data, for the investigation of L_{att} and the determination of $\alpha_{\mathrm{eff}}^{\mathrm{SW}}$, Kerr images are recorded at bias fields ranging from 75 to 100 mT at a center frequency of 13.92 GHz as well as at frequencies 240 MHz above and below[110] 13.92 GHz. The evaluation of these images acquired for the different combinations of f and H_0 reveals $k(H_0, f)$ and $L_{\mathrm{att}}(H_0, f)$ as displayed in Fig 5.4(a) and (b), respectively. For each fixed f, as expected, k decreases linearly with increasing bias field. Since $k(f, H_0)$ is recorded for three different f, the group velocity of the propagating DE SWs—given by $v_{\mathrm{gr}} = 2\pi\,(\partial f/\partial k)$ [cf. Sec. 1.4.1]—can be easily deduced from linear fits to $f(k)$ at fixed H_0. In the field range studied, v_{gr} is in the range between 3.8–4.5 km/s, which is—at first glace—significantly larger or similar to the values reported for other metallic ferromagnetic systems, e.g., $v_{\mathrm{gr}} \approx 1.5\,\mathrm{km/s}$ in case of 15 nm-thick, micrometer-wide $Ni_{80}Fe_{20}$ stripes [132], or $v_{\mathrm{gr}} \approx 4.0\,\mathrm{km/s}$ in case of 20 nm-thick

[110] $\Delta f = 240\,\mathrm{MHz}$ is the smallest possible frequency step, which is both a multiple of the 80 MHz repetition rate of the probing laser pulses and can be generated by the microwave generator in case of frequencies above 12.4 GHz [cf. Sec. 2.1].

single crystal Fe films [13]. However, such a comparison must be treated with care since v_{gr} is indeed related to the slope of the DE SW dispersion, which, in fact, scales with the thickness of the magnetic layer, but can also vary significantly depending on the frequency and bias field range the investigation is performed at.

In contrast, $L_{att}(H_0, f)$ reveals no clear trend. The L_{att}-values scatter with average values in the range from ≈5–8 μm. Moreover, preliminary assuming that α_{int}^{FMR} also represents the value of the magnetic damping parameter in the case of propagating DE SWs, these values are much lower than the L_{att}-values in the range from ≈13-15 μm resulting when inserting all known and measured quantities into Eq. (1.56)[111]. This finding indicates that the effective magnetic SW damping parameter α_{eff}^{SW} is different compared with α_{int}^{FMR}. α_{eff}^{SW} itself is evaluated using the following expression [2, 132]:

$$\alpha_{eff}^{SW} = \frac{v_{gr}}{L_{att}} \cdot \frac{2}{\gamma\mu_0 \left(2\left[H_0 - N_z M_S\right] + M_S - H_u^{\perp}\right)} . \tag{5.2}$$

In contrast to Eq. (1.56), Eq. (5.2) also takes into account the static demagnetizing field arising as the static magnetization in the CoFe stripe of finite width is maintained perpendicular to its long axis by the magnetic bias field [cf. Fig. 5.1(b)]. The simplest (and most common) way[112] to model it reasonably is

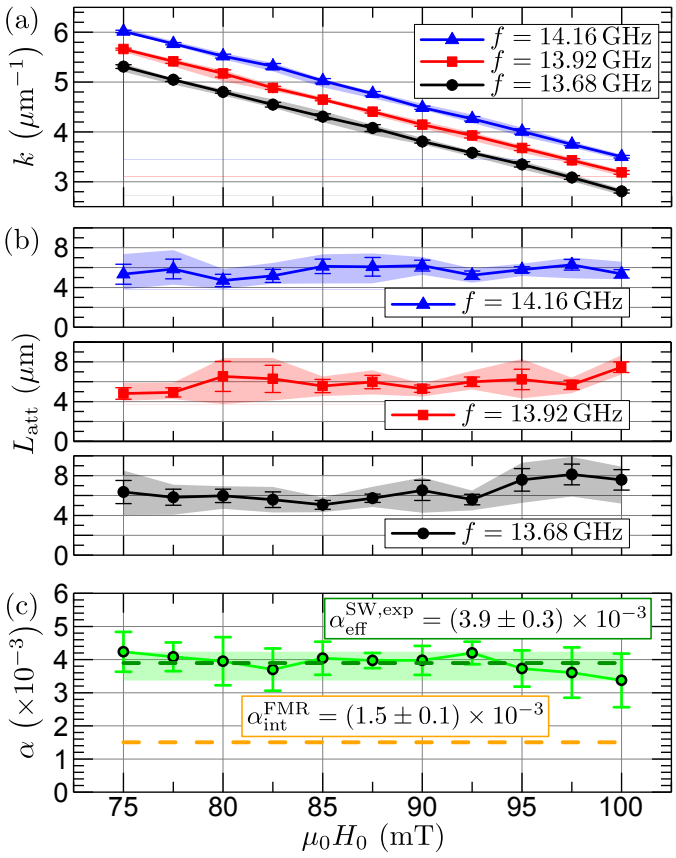

Figure 5.4. Field dependence of (a) k and (b) L_{att}, respectively, at different f. (c) Field dependence of $\alpha_{eff}^{SW,exp}$ derived from (a) and (b) using Eq. (5.2) in comparison with α_{int}^{FMR}. Symbols denote average values. Error bars indicate the corresponding standard deviation. Color-shaded areas mark the range of values of each quantity between the minimum and maximum values. The colored horizontal dashed lines in (c) denote the average value of either damping parameter.

[111] Using this expression to estimate the expected L_{att}-value is reasonable, although it does neither take into account the demagnetizing field arising due to the lateral confinement nor the uniaxial in-plane anisotropy, since the contribution of either quantity can be neglected.

[112] A proper derivation of an expression for the static (and dynamic) demagnetizing fields is quite cumbersome due to their inhomogeneity [140].

by modifying the bias field in the denominator of Eq. (5.2) by the term $-N_z M_S$ [cf. Eq. (1.77)]. The magnitude[113] of this term corresponds to the value of the static demagnetizing field averaged across the stripe width [cf. Sec. 1.4.6]. Based on the dimensions of the fabricated CoFe stripe, the demagnetizing factor along the z direction is calculated using the analytical expression given in Ref. [160]: $N_z = 0.0172$.
At this point, it should be noted that, strictly speaking, Eq. (1.56) (as well as its modified version Eq. (5.2)) is an appropriate analytical expression for $\alpha_{\mathrm{eff}}^{\mathrm{SW}}$ only in case of a magnetic system exhibiting no uniaxial in-plane anisotropy [cf. Sec. 1.4.1]. Yet, in the presence of a uniaxial in-plane anisotropy, it is impossible to derive such an analytical expression for $\alpha_{\mathrm{eff}}^{\mathrm{SW}}$. Despite this fact, it is justified to employ Eq. (5.2) for the evaluation of $\alpha_{\mathrm{eff}}^{\mathrm{SW}}$ as it is still a proper approximation, since, in the CoFe grown, the uniaxial in-plane anisotropy is very weak [cf. Sec. 5.4.1], and since both v_{gr} and L_{att} are accessed experimentally, i.e., in fact, the impact of the uniaxial in-plane anisotropy on the SW characteristics is incorporated in the measured value of either quantity. Moreover, as the in-plane anisotropy is very weak, it is justified to assume that the absolute value of the "correct" scaling factor of the $v_{\mathrm{gr}}/L_{\mathrm{att}}$-ratio is not discernably different to the one of the scaling factor in Eq. (5.2).
Figure 5.4(c) displays the evaluated $\alpha_{\mathrm{eff}}^{\mathrm{SW,exp}}$-values in the field range studied in comparison with the intrinsic Gilbert damping parameter $\alpha_{\mathrm{int}}^{\mathrm{FMR}}$ deduced from the FMR measurements. It is clearly obvious that the average value $\alpha_{\mathrm{eff}}^{\mathrm{SW,exp}} = (3.9 \pm 0.3) \times 10^{-3}$ does not coincide with the $\alpha_{\mathrm{int}}^{\mathrm{FMR}}$-value. In fact, it is 2.6 times larger, thus revealing a distinct difference between both experimentally determined magnetic damping parameters. To cross-check this $\alpha_{\mathrm{eff}}^{\mathrm{SW,exp}}$-value, the SW propagation experiment is repeated on three other CoFe stripes, but the evaluation of the individual data set reveals quantitatively the same results.

There are different possible reasons, why the $\alpha_{\mathrm{eff}}^{\mathrm{SW,exp}}$-value deduced from SW propagation experiments performed on the micrometer-wide CoFe stripes is significantly different compared to the $\alpha_{\mathrm{int}}^{\mathrm{FMR}}$-value obtained from in-plane FMR measurements performed on the CoFe full film:

1) Patterning the stripes from the full film might have caused noticeable changes in the quality of the CoFe layer and/or in the strength of the in-plane and out-of-plane anisotropies due to increased temperatures during the fabrication process, which are up to 150 °C during the bake out of the EBL resist poly-methyl-methacrylate.

2) The propagation of DE SWs in a thin plain film is different compared with the one in a thin narrow stripe, not only due to the static inhomogeneous demagnetizing field arising due to the lateral confinement, but also since the lowest order transverse modes might

[113] Nonetheless, the contribution of this term is small compared with the strength of the other field(-like) terms in the denominator of Eq. (5.2). At a fixed bias field, i.e., for a fixed $v_{\mathrm{gr}}/L_{\mathrm{att}}$-ratio, using the known CoFe parameters, neglecting this term changes the resulting $\alpha_{\mathrm{eff}}^{\mathrm{SW}}$-value only by about 2-3% for bias fields ranging from 70–100 mT. This variation is negligible.

interact with the main propagating mode [45, 188] [cf. Sec. 1.4.6]. As a result, so called anticrossings appear, which manifest as steps in the DE SW dispersion curve. These steps are associated with a significant decrease in L_{att}, however, only for particular combinations of f and H_0 [6]. In this case, consequential, the evaluation of $\alpha_{\mathrm{eff}}^{\mathrm{SW}}$ using Eq. (5.2) would reveal a (larger) magnetic damping parameter value, which does not coincide with the actual one.

3) Based on the findings on the frequency dependence of the in-plane linewidth in the FMR measurements, it could be attributed to the presence of the extrinsic contributions to the magnetic losses: inhomogeneities and two-magnon scattering. They can lead to an effective magnetic SW damping, which is significantly enhanced, thereby resulting in much shorter SW attenuation lengths compared with those expected solely based on determination of the strength of the intrinsic Gilbert damping parameter $\alpha_{\mathrm{int}}^{\mathrm{FMR}}$.

In order to exclude high temperatures during the fabrication process of the stripes as the origin of a distinct enhancement of the magnetic damping, additional in-plane FMR measurements are performed on a separate piece of the CoFe full film, which has been annealed for several hours at temperatures up to 200 °C. They yield no discernable changes in the quantities of interest [189], especially not in $\alpha_{\mathrm{int}}^{\mathrm{FMR}}$. Moreover, the patterning process of the stripes only affects the roughness of their edges, but this quantity does not have any discernable effect on the SW propagation itself [132].

In order to investigate whether anti-crossings due to a coupling of SW modes in the CoFe stripe of finite width w occur in the frequency and bias field ranges chosen for this SW propagation experiment, the dispersions of the various mo-

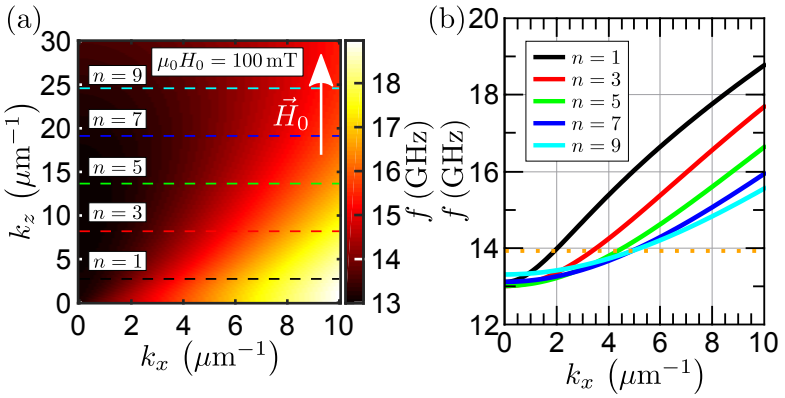

Figure 5.5. (a) Contour plot of the in-plane SW dispersion $f\,(k_x, k_z)$ at 100 mT in case of the CoFe plain film. In case of the CoFe stripe with width w, the transverse wave number is quantized, i.e., $k_z^{\mathrm{quant}} = n\frac{\pi}{w}$, as denoted by the horizontal dashed colored lines, and only odd n are allowed. (b) SW dispersions $f\,(k_x, k_z^{\mathrm{quant}})$. The dispersion branch with the largest group velocity/slope is the main propagating mode with $n = 1$. This branch does not cross other dispersion branches at frequencies close to 13.92 GHz (dotted orange line).

des are calculated[114]. The contour plot in Fig. 5.5(a) visualizes the in-plane SW dispersion in case of the CoFe plain film, i.e., $f(k_x, k_z)$ at a magnetic bias field of 100 mT applied along the z direction. In contrast to the full film, in case of the CoFe stripe of finite width w, k_z is no longer continuous, but quantized, i.e., $k_z^{\mathrm{quant}} = n\frac{\pi}{w}$, where n is the transverse mode number [cf. Sec. 1.4.6], but only odd modes with odd n can be excited by the microwave antenna due to the different symmetries of odd and even transverse modes [cf. Fig. 1.20]. These "allowed" k_z^{quant} are marked by the horizontal dashed lines in Fig. 5.5(a). For each k_z^{quant}, the corresponding (DE) SW dispersion $f(k_x, k_z^{\mathrm{quant}})$ is shown in Fig. 5.5(b). The main propagating mode exhibits the largest group velocity, i.e., the largest slope $\partial f(k_x, k_z^{\mathrm{quant}})/\partial k_x$. As expected, it is the $n = 1$ mode, which is localized in the center of the stripe [cf. Fig. 1.20]. More importantly, however, is the fact, that the $n = 1$-dispersion branch does not cross the branches of the higher order modes at frequencies around 13.92 GHz. This behavior is observed at all bias field ranging from 75 to 100 mT. Consequently, a coupling of SW modes in the stripe can also be excluded to be the origin of an enhanced magnetic SW damping.

The impact of inhomogeneities in the CoFe layer on the attenuation length of propagating DE SWs is investigated by micromagnetic simulations using MuMax3 [173]. Apart from this, micromagnetic simulations are utilized to revise the experimental findings. Moreover, they are also suited to confirm a posteriori that evaluating $\alpha_{\mathrm{eff}}^{\mathrm{SW,exp}}$ using Eq. (5.2) is justified even in the presence of a weak uniaxial in-plane anisotropy. The corresponding findings are presented below.

5.5 Implementation and Analysis of the Micromagnetic Simulations

The propagation of DE SWs is simulated in 80 μm-long, 1.15 μm-wide and 10 nm-thin CoFe stripes, and, for comparison, as well in 10 nm-thin CoFe full films (in the same bias field and frequency ranges as chosen for the SW propagation experiments [cf. Fig. 5.3(a)]). The sample parameters used correspond to the experimentally determined ones. The weak uniaxial in-plane anisotropy is both included and neglected to study its influence on the characteristics of the DE SW propagation. Inhomogeneities are modeled by local variations in the saturation magnetization. The simulation Gilbert damping parameter α_{sim} is either set to 1.5×10^{-3}, i.e., to $\alpha_{\mathrm{int}}^{\mathrm{FMR}}$, or to 4.0×10^{-3}, i.e., to $\approx\alpha_{\mathrm{eff}}^{\mathrm{SW,exp}}$. For the evaluation of $f(k, H_0)$, $L_{\mathrm{att}}(f, H_0)$, and $v_{\mathrm{gr}}(H_0)$, the simulation data resulting from field sweeps at fixed f/frequency sweeps at fixed H_0 are analyzed in a similar way as the recorded Kerr images [cf. Sec. 5.3]. Based on these data, in analogy to $\alpha_{\mathrm{eff}}^{\mathrm{SW,exp}}$, the quantity $\alpha_{\mathrm{eff}}^{\mathrm{SW,sim}}$ is deduced using Eq. (5.2). Further details about the implementation and the analysis of the simulation data are provided in Appendix B.3.

[114] The dispersions are calculated using Eq. (1.44) along with the respective sample and experimental parameters. The presence of a weak uniaxial in-plane anisotropy is not included in Eq. (1.44).

5.6 Simulation Results and Discussion

In the following, first, in Sec. 5.6.1, the findings on the impact of the uniaxial in-plane anisotropy on the SW propagation in $Co_{25}Fe_{75}$ stripes and full films are presented and discussed. In Sec. 5.6.2, the simulation results are compared with the respective experimental findings, thereby revealing the physical origin of the observed distinct difference between $\alpha_{\mathrm{int}}^{\mathrm{FMR}}$ and $\alpha_{\mathrm{eff}}^{\mathrm{SW,exp}}$. Moreover, in Sec. 5.6.3, based on the experimental and simulations findings, a definition of an alternative effective magnetic damping parameter is suggested, which seems to be capable of appropriately quantifying $\alpha_{\mathrm{eff}}^{\mathrm{SW,exp}}$ based on the frequency dependence of the in-plane FMR linewidth.

5.6.1 Impact of the Uniaxial In-Plane Anisotropy on the Spin Wave Propagation in $Co_{25}Fe_{75}$ Stripes and Full Films

First, the effective impact of the uniaxial in-plane anisotropy on the dispersion and attenuation of propagating DE SWs is investigated in case of a CoFe stripe, and, for comparison, as well in case of a CoFe full film. For this purpose, micromagnetic simulations are performed, where the in-plane anisotropy is either neglected or included. In the latter case, the orientation of the easy axis is either along the x or the z direction.

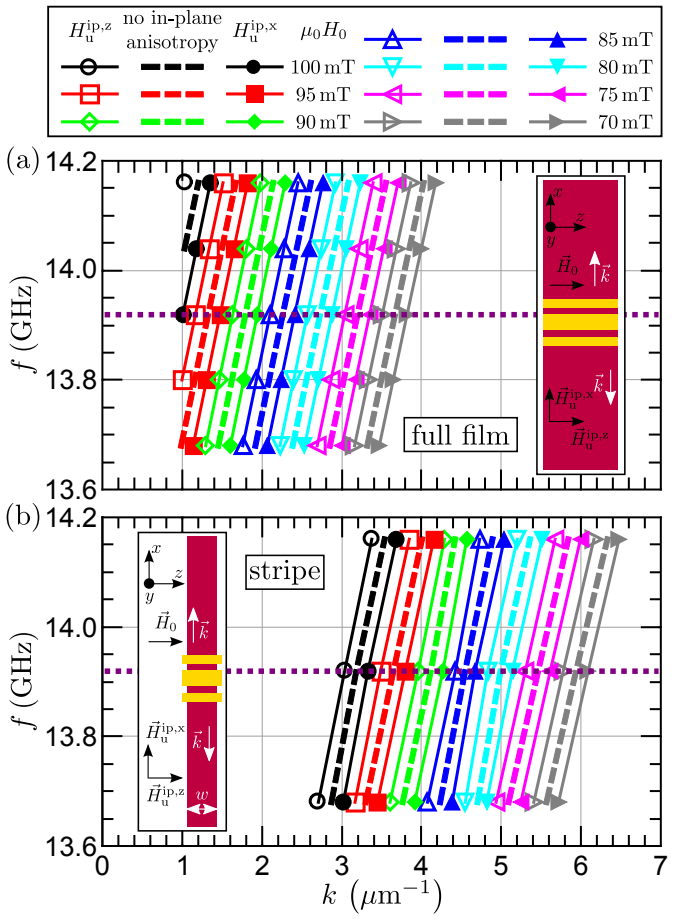

Figure 5.6. Simulated DE SW dispersions at different bias fields at frequencies around 13.92 GHz (dotted purple line) (a) in case of the CoFe full film and (b) in case of the CoFe stripe, respectively. The uniaxial in-plane anisotropy is either not present (dashed lines) or its easy axis is oriented either along the z direction (open symbols) or along the x direction (solid symbols). The insets in (a) and (b) illustrate the possible orientations of the uniaxial in-plane anisotropy with respect to the sample geometry.

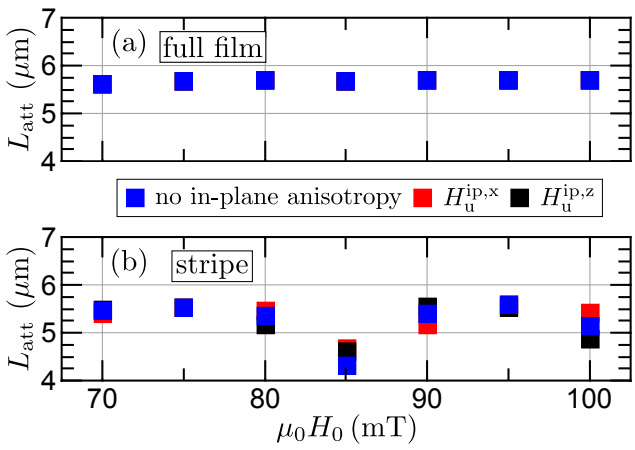

Figure 5.7. Bias field dependence of L_{att} of DE SWs propagating (a) in the CoFe full film and (b) in the CoFe stripe, respectively. These data are extracted from simulations performed at 13.92 GHz with $\alpha_{sim} = 0.0040$, where the uniaxial in-plane anisotropy is either not present (blue symbols) or its easy axis is oriented either along the z direction (black) or along the x direction (red).

When the easy axis of the uniaxial in-plane anisotropy is oriented along the x direction (z direction), at fixed f, the wave numbers are larger (smaller) compared with the case where no uniaxial in-plane anisotropy is present as clearly visible in the individual dispersions for full films and stripes[115] shown in Fig. 5.6(a) and (b), respectively. The shift in wave number Δk is about $0.2\,\mu\text{m}^{-1}$. More importantly, however, is the finding that the slope of the dispersion, i.e., the group velocity, is not noticeably affected by the in-plane anisotropy.
The field dependence of L_{att} is shown in Fig. 5.7. In the case of the full film [cf. Fig. 5.7(a)], there is no difference between the L_{att}-values resulting from the simulations performed without the in-plane anisotropy and those including it. In the field range studied, it remains constant at about $5.6\,\mu$m. In contrast, in the case of the stripe [cf. Fig. 5.7(b)], the L_{att}-values scatter in the range of 4–$6\,\mu$m, and differ slightly between simulations including or neglecting the in-plane anisotropy.

On the one hand, these findings on the dispersion and attenuation length clearly reveal that the very weak uniaxial in-plane anisotropy indeed modifies the characteristics of propagating DE SWs, but the changes in the quantities of interest—v_{gr} and L_{att}—are not substantial. On the other hand, they justify using Eq. (5.2) for the evaluation of $\alpha_{eff}^{SW,exp}$ in the presence of a uniaxial in-plane anisotropy when its impact is negligible.

5.6.2 Validation of the Experimental Observations

Next, the focus is on the validation of the experimental observations by comparing the experimental results for $f(k)$, v_{gr}, L_{att} and $\alpha_{eff}^{SW,exp}$ with the corresponding results from different stripe simulations. These simulations are performed without the in-plane anisotropy as well as with a simulation Gilbert damping parameter α_{sim}, which is set both to 0.0015 and 0.0040.

[115] At fixed f and fixed H_0, the wave number of a DE SW propagating in a full film is always smaller compared with the wave number of a DE SW propagating in a stripe of finite width. This characteristic is due to the arising demagnetizing field in the stripe, which reduces the magnitude of the internal magnetic field [cf. Eq. (1.77)], and the weaker the internal magnetic field, the larger the resulting DE SW wave number [cf. Sec. 1.4].

In Fig. 5.8(a), the dispersion data are shown, while the resulting field dependence of the group velocity is plotted in Fig. 5.8(b). For either quantity—$f(k, H_0)$ and $v_{gr}(H_0)$—the experimental and simulation data are in qualitatively good agreement. At first glance, due to the scaling of the v_{gr}-axis, it seems as if the variations in this quantity would be pronounced. Yet, they are actually less than 15%.

Since L_{att} is inversely proportional to the magnetic damping parameter [cf. Eq. (5.2)], in Fig. 5.8(c), the experimentally determined field dependence of L_{att} is compared with $L_{att}(H_0)$ resulting from the simulations performed with the two different simulation Gilbert damping parameters. The simulations with $\alpha_{sim} = 0.0015 = \alpha_{int}^{FMR}$ reveal L_{att}-values, which are about 2.5 times larger than those observed in the experiment, while, in contrast, good agreement between experiment and simulation is found when $\alpha_{sim} = 0.0040 \approx \alpha_{eff}^{SW,exp}$. This finding strongly indicates that α_{int}^{FMR} does not represent the correct magnetic damping parameter to quantify the SW attenuation. It is supported by the result of a

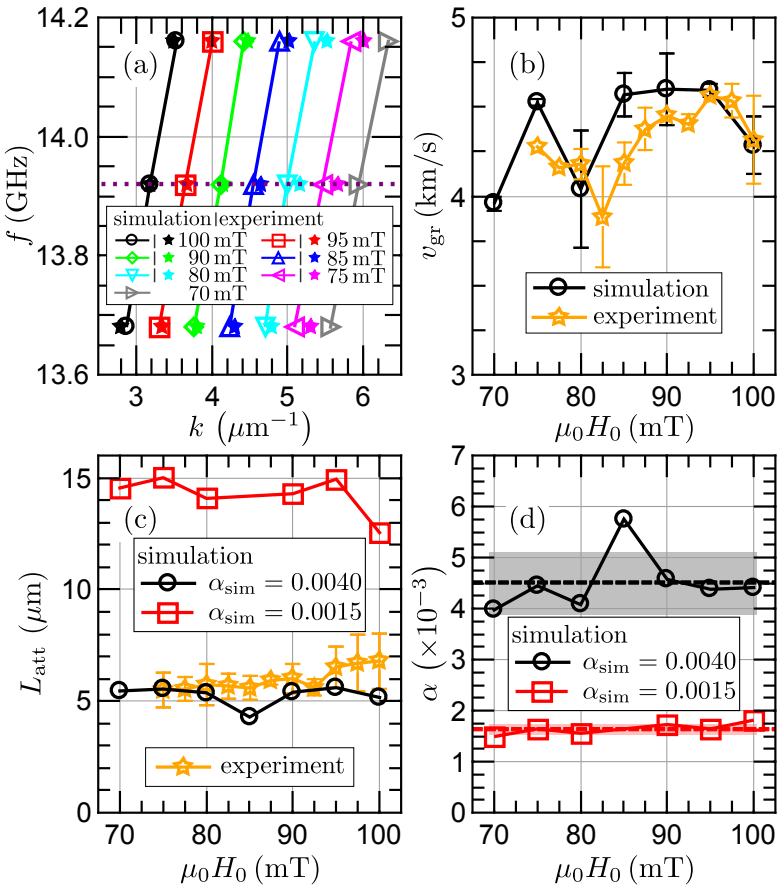

Figure 5.8. Comparison of simulation and experimental results on the CoFe stripe. The simulation data are obtained from simulations performed without the in-plane anisotropy. (a) DE SW dispersion at different bias fields at frequencies around 13.92 GHz. (b) Field dependence of v_{gr} at 13.92 GHz [cf. dotted line in (a)]. (c) Field dependence of L_{att} at 13.92 GHz. These data are extracted from simulations performed with $\alpha_{sim} = 0.0015 = \alpha_{int}^{FMR}$ and $\alpha_{sim} = 0.0040 \approx \alpha_{eff}^{SW,exp}$, respectively. (d) Comparison of the deduced $\alpha_{eff}^{SW,sim}$-values with α_{sim}. Dashed lines indicate mean values while color-shaded areas denote the corresponding error range.

self-consistency check of the simulation data analysis procedure. For this purpose, $\alpha_{\mathrm{eff}}^{\mathrm{SW,sim}}$ is evaluated according to Eq. (5.2) using the simulation results for v_{gr} and L_{att}, and then compared with the input values. As clearly visible in Fig. 5.8(d), $\alpha_{\mathrm{eff}}^{\mathrm{SW,sim}}$ and α_{sim} agree within the error bars, and since the mean value of $\alpha_{\mathrm{eff}}^{\mathrm{SW,sim}}$ is indeed larger than α_{sim}, but by not more than 15%, the self-consistency is verified.

The finding that the L_{att}- and $\alpha_{\mathrm{eff}}^{\mathrm{SW,sim}}$-values obtained from the simulations agree well with the experimental results when the simulation Gilbert damping parameter is set to 0.0040, but do not coincide when it is set to the $\alpha_{\mathrm{int}}^{\mathrm{FMR}}$, clearly suggests the assumption that the physical origin of the observed distinct difference in the magnetic damping parameters $\alpha_{\mathrm{eff}}^{\mathrm{SW,exp}}$ and $\alpha_{\mathrm{int}}^{\mathrm{FMR}}$ is the following:
In case of the poly-crystalline grown CoFe, the attenuation of propagating SWs is not solely predetermined by the strength of the intrinsic magnetic Gilbert damping parameter, but is significantly enhanced due to the extrinsic contributions to the magnetic losses such as two-magnon scattering and inhomogeneities [185, 186], which manifest as a distinct inhomogeneous broadening of the in-plane FMR linewidth $\Delta H\,(\omega)$ [cf. Fig. 5.2(c)].
From a qualitative point of view, the validity of this statement is confirmed by micromagnetic simulations, where α_{sim} is set to $\alpha_{\mathrm{int}}^{\mathrm{FMR}}$, and where inhomogeneities are integrated to the CoFe layer. Compared with the simulations performed without inhomogeneities, the more pronounced they are, the shorter the SW attenuation length. Consequently, the corresponding $\alpha_{\mathrm{eff}}^{\mathrm{SW,sim}}$-value is always larger than the input value, i.e., larger than $\alpha_{\mathrm{int}}^{\mathrm{FMR}}$. Additionally, these simulations reveal that the presence of inhomogeneities leads to noticeable changes in the SW dispersion and group velocity when compared with experimental data as well as with the simulations performed with $\alpha_{\mathrm{sim}} = \alpha_{\mathrm{eff}}^{\mathrm{SW,exp}}$. The latter finding, and the circumstance that it is not possible to study the impact of inhomogeneities from a quantitative point of view, is attributed to the fact that there is no unambiguous way on how to accurately model extrinsic contributions to the magnetic losses in micromagnetic simulations in general[116].

5.6.3 Defining an Alternative Effective Magnetic Damping Parameter

From a theoretical point of view, in case of a magnetic system exhibiting significant extrinsic contributions to the magnetic losses, there does not exist any model, which provides a description on how to transfer the intrinsic Gilbert damping parameter α—deduced from the slope of the frequency dependence of the FMR linewidth—and the extrinsic contributions—manifested as a zero-frequency linewidth offset—into an effective magnetic damping parameter α_{eff}, which is capable to accurately quantify the attenuation of propagating SWs in such a system. This is most likely due to the fact that there is no obvious way on how to achieve that since the derivations of the FMR linewidth and the

[116] Inhomogeneities, for instance, can be implemented as local variations in the saturation magnetization or in the strength of the uniaxial PMA field, by the incorporation of grains, which can be associated with a modification of the exchange interaction between the individual grains, or by a combination of all of them.

characteristics of propagating SWs [cf. Sec. 1.4.1] are based on the LLG equation, where only the intrinsic magnetic damping is considered, whose strength is quantified by the Gilbert damping parameter [cf. Eq. (1.24)]. Moreover, in those magnetic materials, where a vast number of SW propagation experiments is performed—YIG and Permalloy—the extrinsic contributions are typically very small [132, 176] with the result that no discernable difference between $\alpha_{\mathrm{int}}^{\mathrm{FMR}}$ and $\alpha_{\mathrm{eff}}^{\mathrm{SW,exp}}$ is observed.
Despite this fact, as the simulations reveal a good agreement with the experimental data when the simulation Gilbert damping parameter is simply set to $\alpha_{\mathrm{eff}}^{\mathrm{SW,exp}}$, the following definition for α_{eff} is suggested:
Instead of fitting the frequency dependence of the FMR linewidth $\Delta H(\omega)$ to Eq. (5.1) to determine the (frequency-independent) intrinsic magnetic Gilbert damping parameter $\alpha_{\mathrm{int}}^{\mathrm{FMR}}$, for each single frequency $\tilde{\omega}$, a corresponding (frequency-dependent) $\alpha_{\mathrm{eff}}(\tilde{\omega})$ is specified by the slope of a straight line between the origin and $\tilde{\omega}$, i.e.,

$$\mu_0 \Delta H(\tilde{\omega}) = \frac{2\alpha_{\mathrm{eff}}(\tilde{\omega})\,\tilde{\omega}}{\gamma} \qquad \left(\tilde{\omega} = 2\pi\tilde{f}\right). \tag{5.3}$$

At first glance, this definition seems to be reasonable since α_{eff} approaches $\alpha_{\mathrm{int}}^{\mathrm{FMR}}$ when the extrinsic contributions to the FMR linewidth are not pronounced, i.e., $\Delta H(\omega = 0) \ll \Delta H(\omega)$.
Applying Eq. (5.3) to the experimental data—$\mu_0 \Delta H(2\pi \cdot 13.92\,\mathrm{GHz}) = 3.49\,\mathrm{mT}$ [cf. linear fit to the easy axis data in Fig. 5.2(c)]—yields $\alpha_{\mathrm{eff}}(2\pi \cdot 13.92\,\mathrm{GHz}) \approx 3.8 \times 10^{-3}$. This value is in excellent agreement with $\alpha_{\mathrm{eff}}^{\mathrm{SW,exp}} = (3.9 \pm 0.3) \times 10^{-3}$.
Repeating this procedure for $f = 10$–$18\,\mathrm{GHz}$—the frequency range, where propagating DE SWs are observed [cf. Fig. 5.3(a)]—reveals α_{eff}-values in the range from $\approx 4.3 \times 10^{-3}$–$3.4 \times 10^{-3}$. $\alpha_{\mathrm{eff}} \gg \alpha_{\mathrm{int}}^{\mathrm{FMR}}$ applies for all f, thereby indicating that DE SWs propagating in the fabricated, poly-crystalline grown CoFe stripes always suffer more attenuation due to the presence of "strong" extrinsic contributions than expected based solely on the assessment of a low $\alpha_{\mathrm{int}}^{\mathrm{FMR}}$-value. The experimental verification of the validity of the α_{eff}-definition given by repeating the SW propagation experiments at other frequencies goes beyond the scope of this work.

5.7 Conclusion

In summary, the magnetic damping of 10 nm poly-crystalline $Co_{25}Fe_{75}$ grown by MBE was experimentally investigated both by in-plane FMR measurements on a full film sample and by the optical detection of the characteristics of DE SWs propagating in micrometer-wide stripes patterned from the full film using TRMOKE. The FMR measurements reveal an intrinsic magnetic Gilbert damping parameter $\alpha_{\mathrm{int}}^{\mathrm{FMR}} = (1.5 \pm 0.1) \times 10^{-3}$. In contrast, the DE SW attenuation length was only about 6 μm corresponding to an effective magnetic SW damping parameter $\alpha_{\mathrm{eff}}^{\mathrm{SW,exp}} = (3.9 \pm 0.3) \times 10^{-3}$. Based on the findings from micromagnetic simulations, this distinct difference between the magnitude of both damping parameters is attributed to arise from the significant extrinsic contributions to the magnetic losses present in the grown $Co_{25}Fe_{75}$. They cause a much stronger

SW attenuation than expected due to the sole assessment of the low intrinsic magnetic Gilbert damping parameter. Moreover, the definition of an alternative effective magnetic damping parameter was introduced, which seems to be capable to quantify the attenuation of propagating SWs in a magnetic system, where the extrinsic contributions to the magnetic losses need to be considered.
Nonetheless, overall, the experimental findings clearly demonstrate that the binary $3d$ transition metal alloy $Co_{25}Fe_{75}$—exhibiting the lowest intrinsic magnetic Gilbert damping reported for a metallic system so far [181]—can become a promising material for magnonic devices, where the attenuation length of propagating SWs is one essential figure of merit, especially when the extrinsic contributions to the magnetic damping can be reduced as much as possible. Most likely, this can be achieved by optimizing the growth (conditions) of the $Co_{25}Fe_{75}$ as well as by the choice and preparation of the substrate and the seed layer [189].

Chapter 6

Excitation and Tailoring of Diffractive Spin Wave Beams in NiFe Using Nonuniform Microwave Antennas

The results presented in this chapter are published in [134]:

H. S. Körner, J. Stigloher, and C. H. Back.
Excitation and tailoring of diffractive spin-wave beams in NiFe using nonuniform microwave antennas.
Phys. Rev. B **96**, 100401(R) (2017).

Contents

6.1 Motivation and Goal

Within the field of magnonics, the implementation of concepts originating from optics has become an active field of research. So-called SW nano-optics [143] require the generation and manipulation of SW beams in the microwave frequency range and enable the realization of devices like SW fibers [190, 191] or the exploitation of refraction and reflection effects [7, 192, 193]. Within the last few years, various approaches to generate SW beams were proposed and investigated.

(i) Caustic SW beams occur in anisotropic media since here the group velocity $\vec{v}_{\mathrm{gr}} = 2\pi \left(\partial f / \partial \vec{k}\right)$ [cf. Eq. (1.40)] indicating the direction of the energy propagation does not, in general, coincide with the direction of the wave vector $\vec{k}$. Consequently, when the anisotropy of the in-plane SW dispersion is sufficiently strong [cf. Fig. 1.11], the direction of the group velocity of the SW beam may become independent of the wave vectors forming the beam in the vicinity of a certain carrier wave vector. Hence, wave packets excited with a broad angular spectrum of wave vectors may be channeled along this direction. SW caustics present practically quasi-nondiffractive beams as they maintain their transverse aperture over large propagation distances (on the order of several millimeters) [38]. Experimentally the creation and occurrence of these type of SW beams was observed when SWs propagate from a microwaveguide into a continuous film [38, 194], being emitted from edge modes [195], or when using single antidots [47] while unidirectional SW caustics were recently examined theoretically in ultrathin ferromagnets with DMI [196, 197].

(ii) SW propagation in antidot lattices [198, 199] and the efficient SW propagation occurring in confined narrow channels [200, 201] can also be regarded as a kind of SW beam thus representing possible other mechanisms to generate SW beams.

(iii) Moreover, recently, Gruszecki *et al.* presented another approach enabling the generation of multiple narrow SW beams in the exchange-dominated regime of the DE SW dispersion [cf. Fig. 1.9] in magnetic full films such as YIG or NiFe [202]. Here, the desired beam type behavior can be achieved with the aid of a properly designed CPW generating a nonuniform magnetic microwave field. In contrast to the micromagnetic simulations they performed, there are two crucial constraints for the experimental verification of this approach. First, the exchange-dominated regime cannot be accessed by magneto-optical techniques such as TRMOKE or BLS since the corresponding SW wavelengths are below the optical detection limit [10, 153]. Secondly, the dimensions of the constituents of microwave antennas enabling the generation of SWs belonging to this regime need to be on the order of about 100 nm which is at the edge of feasibility using current common state-of-the-art nanofabrication techniques.

Inspired by the work by Gruszecki *et al.* [202], for this study, their approach is adapted to the dipolar-dominated regime of the DE SW dispersion [cf. Fig. 1.9]. For this purpose, proper nonuniform microwave antennas composed of differently sized CPW segments with feature sizes down to ≈300 nm are fabricated on top of

a thin NiFe film. The primary goal is to experimentally demonstrate by magnetic imaging using TRMOKE the possibility to locally excite multiple SW beams in an unpatterned magnetic film using one single of these nonuniform microwave antennas. The additional goals are to investigate whether the characteristics of the occurring SW beams can be tailored or manipulated and whether the SW beams can be steered.

6.2 Samples: Design, Characteristics and Fabrication

The generation of SW beams is investigated in NiFe ($Ni_{80}Fe_{20}$) films. In contrast to the ferrimagnetic insulator YIG, in metallic NiFe, the attenuation length L_{att} of DE SWs is much smaller due to a much larger magnetic damping: $\alpha_{YIG} \approx 5 \times 10^{-4}$ [174, 175] $\ll \alpha_{NiFe} \approx 6\text{–}8 \times 10^{-3}$ [11, 49, 132]. Hence, in order to be able to observe the propagation of SW beams over large distances at all, one takes advantage of the fact that L_{att} scales with the film thickness d. In this study, $d_{NiFe} = 50\text{–}60\,\text{nm}$ is chosen resulting in L_{att}-values on the order of several micrometers. The films are modeled as $240\,\mu\text{m} \times 240\,\mu\text{m}$-wide NiFe($d$)/Al(3 nm) pads, which are patterned by EBL, thermal evaporation and liftoff on a $5 \times 5\,\text{mm}^2$ GaAs substrate. The Al layer oxidizes under ambient conditions and prevents the NiFe pads from oxidation. The quality of the NiFe films is checked by FMR and SQUID measurements at room temperature which reveal γ- and M_S-values that are typical for NiFe. They vary slightly between individual samples since they are grown at different times, but under similar conditions. On top of the NiFe pads, differently shaped nonuniform microwave antennas in the shape of shorted CPWs are patterned by EBL, thermal evaporation of Cr(10 nm)/Au(80–100 nm) and liftoff. The smallest possible feature size of the microwave antenna is given by the fabrication process and is on the order of 300 nm. The microwave antennas are electrically decoupled from the metallic NiFe film by an additional 80 nm-thick[117] insulating Al_2O_3 layer grown by ALD.

In general, a microwave antenna excites a broad range of wave vectors. Its excitation spectrum indicating how efficiently each wave number can be excited—i.e., nonvanishing excitation efficiency—or not excited at all—i.e., vanishing excitation efficiency—is inherently determined by the dimensions of its constituents [cf. Sec. 1.4.5]. Consequently, for the generation of propagating SW beams, which are locally excited in a full film using a nonuniform microwave antenna, it is mandatory that the excitation spectra of the individual, differently sized CPW segments such an antenna is composed of are significantly different.
The nonuniform microwave antennas fabricated for this study are composed of three different CPW building blocks denoted as $CPW_{1\text{–}3}$ which differ in the widths of their signal and ground lines as depicted in the schematics in Fig. 6.1. The width of the gap w_g is the same for all of them. In the sections labeled as CPW_2 and CPW_3, respectively, the width of the signal line w_s is half the size as for CPW_1, whereas the width of the ground line w_{gr} is either halved as well

[117] Its thickness is tuned to maximize the sample reflectivity for the wavelength of the probing laser pulses using TRMOKE, which is around 400 nm [cf. Ch. 2].

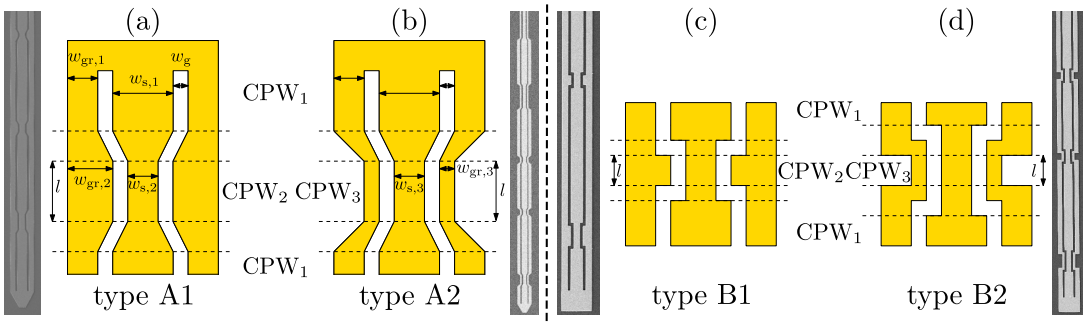

Figure 6.1. SEM images of the four different types of nonuniform microwave antennas fabricated along with the corresponding schematics, where the dimensions of the individual constituents are labeled. (a)-(b) Nonuniform microwave antennas with slanted transitions between segments CPW_1 and CPW_2 (type A1) or between segments CPW_1 and CPW_3 (type A2), respectively. (c)-(d) Nonuniform microwave antennas with sharp edged transitions between segments CPW_1 and CPW_2 (type B1) or between segments CPW_1 and CPW_3 (type B2), respectively.

(CPW_3) [cf. Figs. 6.1(b) and (d)] or widened in order to keep the total width of the nonuniform microwave antenna constant (CPW_2) [cf. Figs. 6.1(a) and (c)]. The dimensions—nominal width in micrometers—of signal line, ground line, and gap are chosen to be 1.2/0.6/0.3 (CPW_1), 0.6/0.9/0.3 (CPW_2), and 0.6/0.3/0.3 (CPW_3), respectively.

Based on these dimensions and assuming a uniform current density within each CPW segment, the corresponding spatial profiles of the in-plane and out-of-plane microwave fields generated by each CPW segment can be calculated using the two-dimensional Biot-Savart. The Fourier transform of these profiles yields the individual excitation spectra [cf. Sec. 1.4.5]. For wave numbers up to $10\,\mu\mathrm{m}^{-1}$, i.e., only considering those wave numbers in the dipolar-dominated regime of the DE SW dispersion, which can be detected magneto-optically by TRMOKE [cf. Fig. 1.9(b) and Ch. 2], they are shown in Fig. 6.2 along with several DE SW dispersions $f(k)$ calculated for different bias field magnitudes H_0 [cf. Eq. (1.38)] in case of a 60 nm-thick NiFe film with $\gamma = 193\times10^9\,\mathrm{rad/(Ts)}$ and $\mu_0 M_S = 0.95\,\mathrm{T}$. They are significantly different as indicated by the dashed orange lines, which mark distinct wave numbers $\tilde{k}$ that cannot be excited by a CPW_1 segment, but by either a CPW_2 or CPW_3 segment. Hence, using a nonuniform microwave antenna, which is composed of a series of CPW_1 and CPW_2/CPW_3 segments with the specified dimensions, should, in principle, enable the local, simultaneous excitation of multiple SW beams, where any intersection between the dashed lines and the dispersions in Fig. 6.2 denotes a certain set of values ($\tilde{f}$,$\tilde{H}_0$) for which a SW beam with wave number $\tilde{k}$ is expected to occur.

Furthermore, in order to be able to investigate as well whether the initial width of the SW beams excited by one of the fabricated nonuniform microwave antennas can simply be tailored by the length l of the CPW_2 (CPW_3) sections, l is varied[118] from 500 nm up to $10\,\mu$m, while keeping the length of the neighboring CPW_1 sections much larger. Several of these differently long CPW_2

[118] The values given are nominal values.

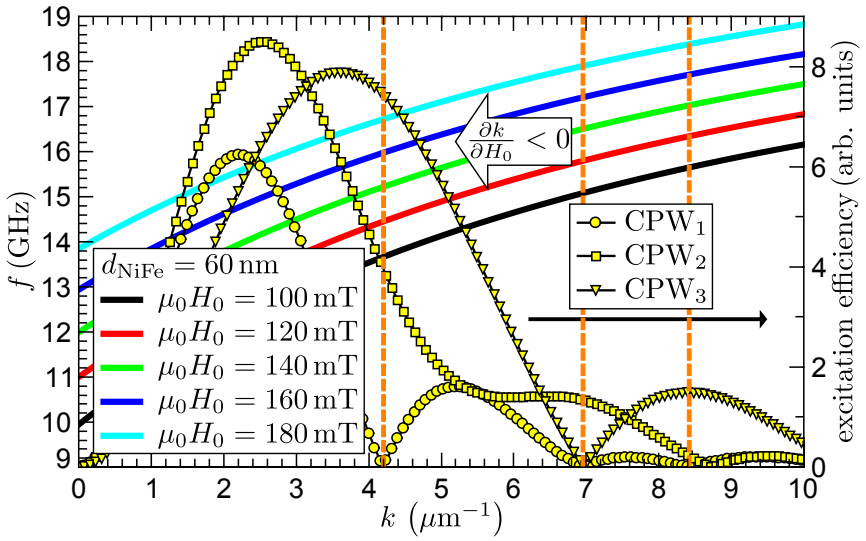

Figure 6.2. Calculated excitation spectra of the individual CPW segments along with DE SW dispersions for different H_0 in case of a 60 nm-thick NiFe film. The vertical dashed orange lines indicate distinct wave numbers which cannot be excited by the CPW$_1$ segment, but by either of the other two CPW segments. Any intercept of these lines with the dispersions denotes a pair of values ($\tilde{f}$,$\tilde{H}_0$), for which locally excited SW beams with wave number $\tilde{k}$ are expected to occur.

(CPW$_3$) segments are integrated into one single nonuniform microwave antenna as shown in the SEM images in Fig. 6.1. The transitions between the CPW$_1$ and CPW$_2$ (CPW$_3$) segments are either designed sharp edged—types B1 and B2 [cf. Fig. 6.1(c) and (d)]—or slanted—types A1 and A2 [cf. Fig. 6.1(a) and (b)]—thereby enabling to study the effect of the shape of the nonuniformity on the SW beam characteristics as well.

6.3 Implementation of the Experiment and Data Analysis

The study is performed in the DE geometry, i.e., as illustrated in the SEM image in Fig. 6.3, SWs/SW beams with wave vector $\vec{k}$ excited by the different sections of the nonuniform microwave antenna propagate along the x direction while the bias field $\vec{H}_0$ is applied along the z direction. SW dynamics in the NiFe films is accessed magneto-optically by TRMOKE [cf. Ch. 2]. The setup is operated in both the spectroscopy mode [cf. Sec. 2.2.1] and the imaging mode [cf. Sec. 2.2.2]. From the SW resonance spectra, which are recorded for ϕ=0° and 90° ≈3–4 μm away from the microwave antenna, the appropriate

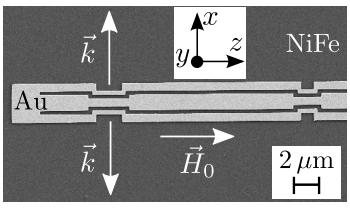

Figure 6.3. Visualization of the DE SW geometry employed in the study by means of a SEM image of a type B2 antenna. SWs/SW beams with wave vector $\vec{k}$ are excited in the NiFe film by the nonuniform Au microwave antenna and propagate along the x direction while the magnetic bias field $\vec{H}_0$ is applied along the z direction.

bias field range is extracted in which SW propagation can be detected at a fixed excitation frequency. In agreement with the DE SW dispersions shown in Fig. 6.2, appropriate f are in the range from 12 to 18 GHz for H_0 in the range from 20 to 180 mT. Then, for different H_0, Kerr images of the excited propagating SWs/SW beams are acquired. They cover at least one or more CPW_2/CPW_3 sections of the nonuniform microwave antenna and, due to the amplitude and modal profile nonreciprocity [cf. Sec. 1.4.2 and Sec. 1.4.5], only that side of the microwave antenna where the SW amplitude is larger at a given polarity of H_0. In the Kerr images, the position of the nonuniform microwave antenna is determined by superimposing the simultaneously acquired topography image onto them, thus allowing to identify those CPW segments which enable or suppress the excitation of SWs/SW beams at a given set of (f, H_0). If not otherwise stated, all Kerr images shown and discussed below are acquired at $f = 16.08$ GHz.

6.4 Experimental Results and Discussion

In this section, the experimental results on the excitation [cf. Sec. 6.4.1], tailoring [cf. Sec. 6.4.2] and steering [cf. Sec. 6.4.3] of SW beams using the different types of nonuniform microwave antennas are presented and discussed.

6.4.1 Exciting Diffractive Spin Wave Beams

First of all, it needs to be demonstrated that the fabricated nonuniform microwave antennas actually enable the excitation of SW beams, thus confirming that the approach suggested by Gruszecki *et al.* [202] can indeed be employed for the generation of locally excited SW beams in an unpatterned magnetic film. As explained before, for this purpose, that combinations of (f,H_0) need to be determined, for which SW excitation is enabled by one type of CPW segment while it is concurrently suppressed by the other(s). Hence, several Kerr images are recorded as the bias field magnitude is swept from 100 to 180 mT, thereby scanning the DE dispersions and the individual excitation spectra from large towards small wave numbers [cf. Fig. 6.2].

To begin with, a type A2 antenna is used. SW beams propagating along the x direction are observed at 109 mT as clearly visible in the Kerr image shown in Fig. 6.4(a). Here, they are excited by the two 1 μm-long CPW_3 segments since, at that particular bias field value, the excitation efficiency of the CPW_3 segment is finite while it vanishes for the CPW_1 segment. This bias field value is in reasonable agreement with the right vertical dashed orange line in Fig. 6.2 since it has to be taken into account that the excitation spectra shown in this figure are calculated for CPW segments with well-known dimensions, whereas the local dimensions of the constituents of the fabricated nonuniform microwave antennas can differ from the nominal ones by up to 50 nm as shown exemplarily in the SEM image of a type A2 antenna in Fig. 6.5. Consequently, the shape of the actual excitation spectrum of each CPW building block—especially the position of the zero points, i.e., the $\tilde{k}$-values—can be slightly different. Note

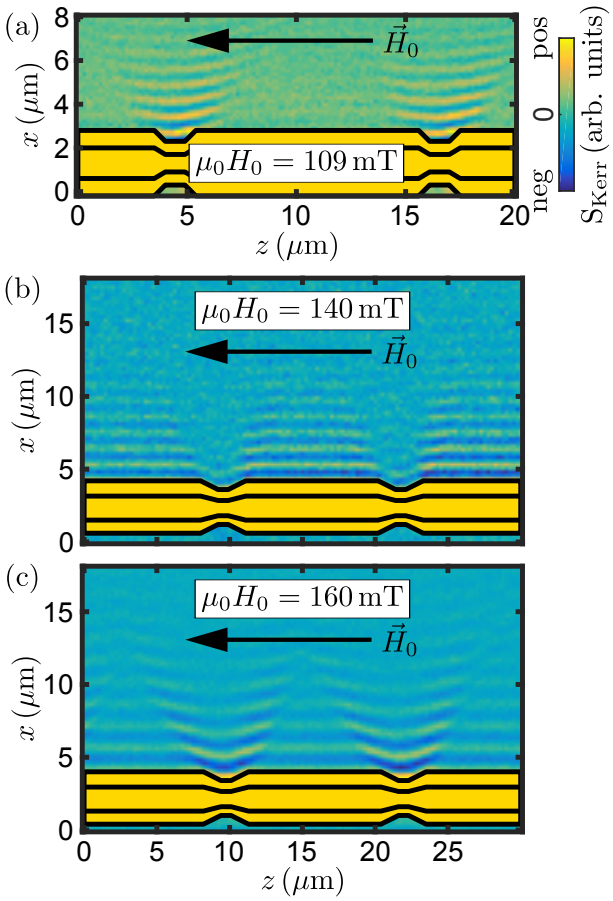

Figure 6.4. Selection of Kerr images obtained at 16.08 GHz. (a) Two diffractive SW beams propagating along the x direction are simultaneously excited at 109 mT by the 1 μm-long CPW_3 segments of a type A2 antenna[119] which is illustrated schematically in yellow. (b) Opposite situation as in (a) at 140 mT. Now, diffractive SW beams are excited by the much longer CPW_1 sections. (c) At 160 mT, SWs are excited by all CPW segments. On top of that, an enhanced Kerr signal occurs along distinct directions within the xz plane.

that the Kerr signal is rather weak since the excitation efficiency of the CPW_3 segment is low for wave numbers close to 9 $\mu\mathrm{m}^{-1}$ [cf. Fig. 6.2].

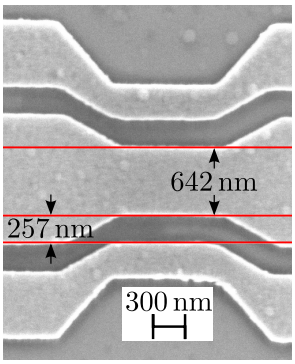

Figure 6.5. SEM image of a type A2 antenna revealing that the actual dimensions of the constituents of the fabricated CPW building blocks can differ from the nominal ones by up to 50 nm.

Moreover, Fig. 6.4(a) also proves that one single nonuniform microwave antenna is suitable to locally excite multiple SW beams simultaneously, where the number of occurring beams is given by the number of nonuniformities integrated into it.

The occurring SW beams are clearly diffractive, i.e., their width increases from ≈4 μm right next to the antenna to about 7 μm for a propagation distance of about 5 μm, and it seems as if the initial width of the SW beam is not related to the length of the CPW_3 segment since it is much shorter.

In contrast to quasi-nondiffractive caustic SW beams, for which there is a solid definition for the width of the beam [38], here, in the case of diffractive SW beams, this expression is used to describe the width of the beam wavefront at a certain distance away from the nonuniform microwave antenna. It quantifies the width of the region in the Kerr images where still a finite SW amplitude can be detected. Note that, here, this quantity is only discussed in terms of quality, but not in terms of quantity.

[119] The values given for the length of the individual CPW_3 segments are the nominal ones.

At 140 mT, SW beams occur again. Now, however, the situation is opposite compared to the one at 109 mT. As shown in Fig. 6.4(b), propagating SWs cannot be excited by the CPW_3 segments, but only by the CPW_1 segments. Although these segments are originally designed to be much longer than the CPW_3 (CPW_2) sections—here, 10 μm vs. 1 μm—the occurring propagating SWs can be regarded as much wider SW beams since they are clearly separated from each other by regions where no SWs propagate. Nonetheless, these beams are also diffractive. Yet, now, their width decreases the further they propagate away from the microwave antenna. This characteristic is attributed to the slanted transitions between the neighboring CPW segments of the type A2 antenna.

Finally, at 160 mT, propagating SWs are excited by all CPW segments of the nonuniform microwave antenna as shown in Fig. 6.4(c). i.e., no SW beams can be identified anymore. Yet, an enhanced Kerr signal is observed along distinct directions within the xz plane which decreases with increasing distance to the nonuniform microwave antenna. This feature becomes even more clearly visible when the phase-resolved Kerr images recorded at $\phi = 0°$ and $\phi = 90°$, respectively, are combined into one image visualizing the absolute SW amplitude within the xz plane [cf. Sec. 2.2.2]. Such an image is shown in Fig. 6.6, where a type A1 antenna is employed to demonstrate that this enhancement of the SW amplitude along distinct directions is observed for either type A antenna. It is attributed to the superposition of SWs with different in-plane wave vectors $\vec{k}$ where the ones, which do not match the characteristic of the DE geometry, i.e., $\vec{k} \not\perp \vec{H}_0$, are most likely excited at the slanted transitions between neighboring CPW sections of the type A antenna. However, owing to the relatively short attenuation length in NiFe [11, 49, 132] compared with the one in thick YIG [174, 175], it is not possible to unambiguously clarify whether this feature is an interference effect or due to the onset of the formation of SW caustics [38]. The latter scenario might also be possible since according to the in-plane SW dispersion, i.e., $f\left(\vec{k}\right) = f\left(k_x, k_z\right)$ [cf. Sec. 1.4.1], at this bias field magnitude, the direction of the group velocity denoting the direction of energy flow becomes independent of the direction of the corresponding wave vector, i.e., $\vec{v}_{\mathrm{gr}}\left(\vec{k}\right) = 2\pi\left(\partial f/\partial \vec{k}\right) = \vec{v}_{\mathrm{gr}}$.

So far, it is demonstrated that type A antennas enable the excitation of SW beams for particular combinations ($\tilde{f}$,$\tilde{H}_0$). However, the clearly visible diffractive behavior of the SW beam is unfavorable. Consequently, the question arises whet-

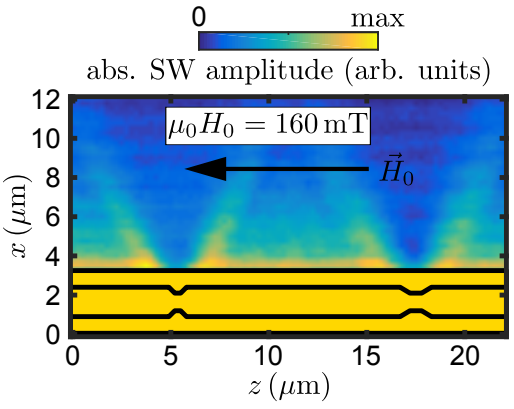

Figure 6.6. Absolute SW amplitude image obtained at 160 mT from the combination of Kerr images acquired at $\phi = 0°$ and $\phi = 90°$, respectively, visualizing the occurrence of an enhanced SW amplitude along distinct directions within the xz plane. Here, a type A1 antenna is used, which is illustrated schematically in yellow.

her this behavior can potentially be tailored by the shape of the nonuniformities integrated into the microwave antenna, in particular, by the shape of the transitions between neighboring CPW sections. Moreover, it is also of great interest to check whether it is possible to set the initial width of the SW beam by the length of the individual CPW segments which would be beneficial in combination with a "less" diffractive SW beam. Additionally, it has to be to proven that the SW beam excitation frequency can be tuned as well since this feature becomes essential from the application point of view.

6.4.2 Tailoring Diffractive Spin Wave Beams

Now, SW beams excited by a type B2 antenna are investigated. The only difference between the type A2 and the type B2 antenna is the shape of the transitions while the nominal dimensions of the individual CPW segments are the same. Consequently, based on the previous findings for the type A2 antenna, SW beams are expected to occur for similar combinations of f and H_0 as in the case of the type A2 antenna. They are only similar as the type B antennas are fabricated on top of another NiFe film having a different thickness and slightly different material parameter resulting in slightly modified DE SW dispersions at any given H_0.

At 150 mT, SW beams are excited by the CPW_3 segments of the type B2 antenna as shown exemplarily in the Kerr image in Fig. 6.7(a) covering a $\approx$10 μm-long CPW_3 segment. They manifest as a significantly enhanced Kerr signal above this segment compared with the surrounding regions. Note that propagating SWs with a much smaller amplitude are excited by the CPW_1 segments only be-

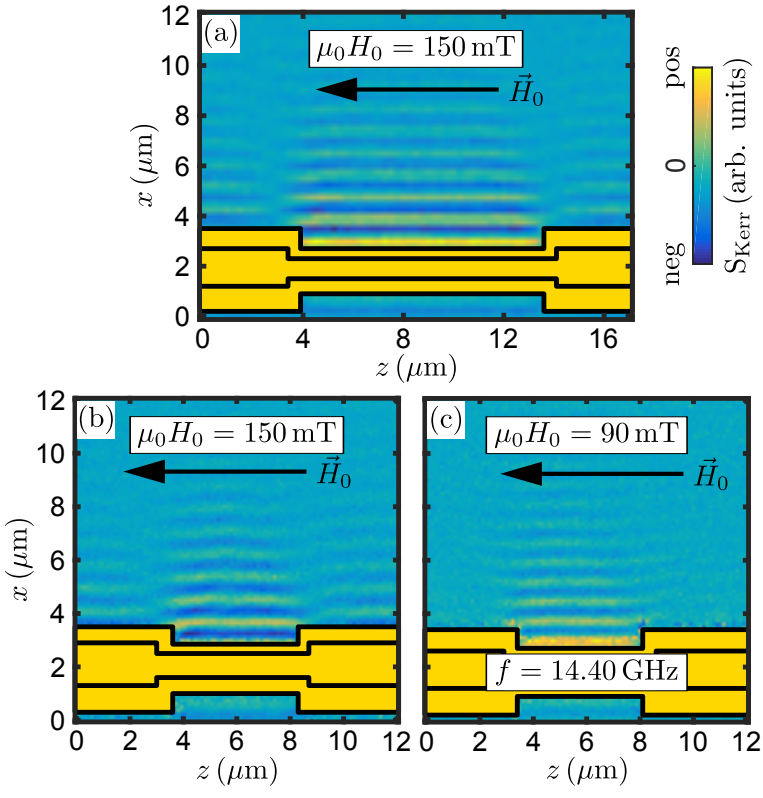

Figure 6.7. Selection of Kerr images showing "less" diffractive SW beams excited by a type B2 antenna[120] marked schematically in yellow. (a) A diffractive SW beam is excited by a 10 μm-long CPW_3 segment. (b) Same situation as in (a), but now only a 5 μm-long CPW_3 segment is displayed. (c) Same situation as in (b), now at $f = 14.40$ GHz and 90 mT.

[120] The values given for the length of the individual CPW_3 segments are the nominal ones.

cause the bias field magnitude is not perfectly tuned to match the wave number for which the excitation efficiency of the CPW_1 segment vanishes. Hence, it is finite, but very weak. More importantly, the width of the beam does not change considerably within the detectable propagation distance compared with the SW beams excited by a type A2 antenna [cf. Fig. 6.6(a)]. Yet, it still changes, i.e., the SW beams are still diffractive, but "less" diffractive since after $\Delta x \approx 5\,\mu$m the SW beam width is almost the same as its initial width. Moreover, it seems to be possible to set the initial beam width by the length of the CPW_3 segment since the same beam characteristic is observed in case of a $\approx 5\,\mu$m-long CPW_3 segment as displayed in Fig. 6.7(b).
The "less" diffractive behavior is attributed to the sharp edged shape of the transitions between neighboring CPW elements of the type B2 antenna. While the building blocks of either type of nonuniform microwave antenna, i.e., the $CPW_{1–3}$ segments, dominantly favor the excitation of DE SWs when $\vec{H}_0$ is oriented along the z direction, i.e., propagating SWs for which $\vec{k} \perp \vec{H}_0$ applies, the slanted transitions of the type A antennas very likely facilitate the additional excitation of wave components having different in-plane wave vectors for which $\vec{k} \perp \vec{H}_0$ does not apply, whereas it is very unlikely that such SWs are excited by the sharp edged transitions of the type B antennas which can be regarded as infinitely slanted transitions. Consequently, the width of the SW beam as it propagates can be more easily tailored and controlled when a type B antenna is used.

In order to prove the possibility to tune the excitation frequency of the ("less") diffractive SW beams, f is reduced from 16.08 GHz to 14.40 GHz. In case of the type B2 antenna, now propagating SW beams excited by the CPW_3 segments occur when the bias field magnitude is simultaneously lowered to ≈ 90 mT as shown in Fig. 6.7(c). This bias field value is in agreement with the corresponding DE SW dispersion. Additionally, it is worth pointing out that it matches the wave number very well for which the excitation efficiency of the CPW_1 segment vanishes.

Since SW beams can be (locally) excited in a magnetic full film using nonuniform microwave antennas and since it is possible to tailor their diffractive behavior, set their initial width and tune their frequency, from the application point of view, it would be also advantageous that the propagation direction of these SW beams can be manipulated.

6.4.3 Steering Diffractive Spin Wave Beams

This part of the study is only carried out in the case of the type A antennas to prove only qualitatively that SW beam steering is possible. For this purpose, the in-plane direction of the bias field is simply rotated counter-clockwise with respect to the z direction. Now, as clearly visible in the Kerr image shown in Fig. 6.8, the propagation direction of the two diffractive SW beams is no longer parallel to the x direction, but rotated counter-clockwise towards the z direction. It is noted that, here, a type A1 antenna is used. Hence, in agreement with the expectation according to Fig. 6.2 [cf. the middle dashed orange line], the bias field value, at which diffractive SW beams are excited by the CPW_2 segments, is

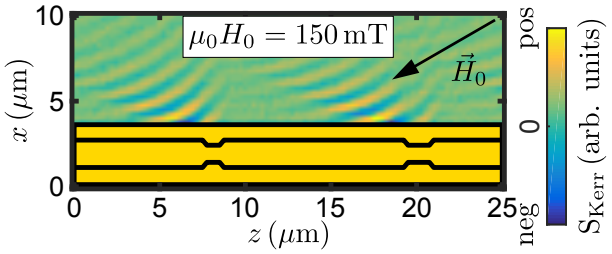

Figure 6.8. Simultaneous excitation of two diffractive SW beams at 150 mT using a type A1 antenna. The in-plane direction of the bias field is rotated with respect to the z direction. Consequential, the propagation direction of the diffractive SW beams is rotated as well with respect to the x direction.

much larger compared with the situation displayed in Fig. 6.4(a). Moreover, at first glance, it seems as if the slanted transitions would facilitate the SW beam steering or enable it in the first place, since one has to keep in mind that it is assumed that they also excite wave components having in-plane wave vectors for which $\vec{k} \not\parallel \vec{e}_x$ applies. However, to clarify whether the possibility of SW beam steering is actually either restricted or predetermined by the shape and size of the transitions and for a detailed analysis about the angular range in which the propagation direction can be set within the xz plane by rotating $\vec{H}_0$ in-plane, much more additional measurements using all types of nonuniform microwave antennas would be required, thus becoming the focus of a separate study.

6.5 Conclusion

It was experimentally proven that SW beams can be excited in a metallic NiFe film with the aid of properly designed nonuniform microwave antennas, thereby confirming an approach for the generation of SW beams suggested by Gruszecki *et al.* [202], which they studied only by micromagnetic simulations and in the exchange-dominated regime of the DE SW dispersion. This study focused on the dipolar-dominated regime of the DE SW dispersion, which was accessed magneto-optically by TRMOKE. Four different types of nonuniform microwave antennas—A1, A2, B1, and B2—were fabricated. In general, the SW beams excited by these antennas were diffractive, i.e., their width changed as they propagated. Furthermore, it was demonstrated that it is possible

(i) to excite multiple SW beams simultaneously using one single nonuniform microwave antenna, where the number of occurring SW beams is predetermined by the number of nonuniformities integrated into the antenna,

(ii) to tailor the diffractive behavior by the shape of the transitions between the individual CPW building blocks the nonuniform microwave antennas were composed of,

(iii) to set the initial width of the SW beam by the length of the CPW segment which excites the SW beam,

(iv) to tune the SW beam excitation frequency when the bias field magnitude is adjusted simultaneously, and

(v) to manipulate the propagation direction of the SW beams—excited by a type A1 antenna—by rotating the direction of the in-plane bias field.

Summary

Four different SW propagation experiments have been performed within the framework of this thesis. In each of them, the SWs propagating in the magnetic nanostructures were excited by microwave antennas and detected optically using TRMOKE, which provided the required spatial, temporal and phase resolution. The Kerr microscopy setup was operated both in the spectroscopy and the imaging mode. In the latter mode, real-space Kerr images of the propagating SWs were acquired. The analysis of these images enabled the observation of changes in specific SW propagation characteristics due to modifications in specific sample features as well as direct access to the two main quantities characterizing propagating SWs—dispersion and attenuation length. The detailed investigation of these two quantities provided the basis for the determination of a variety of fundamental parameters governing magnetization dynamics in different kinds of magnetic materials and systems. In combination and/or comparison with the results from other sample characterization techniques and micromagnetic simulations, the individual SW propagation experiments revealed the following results and findings:

(i) The interaction with a spin-polarized electric current caused changes in the characteristics of Damon-Eshbach SWs propagating in a 15 nm-thin, submicron-wide $Ni_{80}Fe_{20}$ stripe, which were studied in detail both qualitatively and quantitatively. The approach chosen for this study enabled to determine the values of the key STT parameters for $Ni_{80}Fe_{20}$ in a self-consistent and independent way: $\alpha = 0.0075$, $u = 5.1\,\mathrm{m/s}$, $P = 0.64$, and $\beta = 0.0035$.

(ii) The observation of an asymmetry in the characteristics of Damon-Eshbach SWs propagating in 70 μm-wide Pt(2 nm)/Co(0.4 nm)/Py(5 nm)/MgO(5 nm) stripes allowed to evidence the presence of an interfacial DMI at the Pt/Co interface arising due to the broken inversion symmetry of the system and to quantify it: $D_{\mathrm{eff}} = 0.165\,\mathrm{mJ/m^2}$ and $D_{\mathrm{int}} = 0.89\,\mathrm{pJ/m}$, respectively. Micromagnetic simulations confirmed that the observed signature of the asymmetry coincides with the one expected to occur due to an interfacial DMI as well as that it is opposite to the asymmetry induced solely by the PMA field originating from the same interface. Moreover, they revealed that the common approach to quantify the strength of the interfacial DMI from the experimental data underestimates its actual strength by up to 40%.

(iii) To check whether the binary $3d$ transition metal alloy $Co_{25}Fe_{75}$ is indeed a promising material for future magnonic devices as it exhibits the lowest intrinsic magnetic damping reported so far in case of a metallic system, the magnetic damping of 10 nm poly-crystalline $Co_{25}Fe_{75}$ grown by MBE was accessed both by the analysis of in-plane FMR measurements on a full film sample as well as by the assessement of the attenuation length of Damon-Eshbach SWs propagating in micrometer-wide stripes. The measurements revealed that the intrinsic magnetic Gilbert damping parameter was 2.6 times smaller than the effective magnetic SW damping parameter: $\alpha_{\mathrm{int}}^{\mathrm{FMR}} = 1.5 \times 10^{-3}$ vs. $\alpha_{\mathrm{eff}}^{\mathrm{SW}} = 3.9 \times 10^{-3}$. Micromagnetic simulations confirmed the assumption that the distinct difference arises due to the significant extrinsic contributions to the magnetic losses present in the poly-crystalline grown $Co_{25}Fe_{75}$.

(iv) It was evidenced by magnetic imaging that multiple SW beams can be excited locally and simultaneously in thin $Ni_{80}Fe_{20}$ full films by means of properly designed nonuniform microwave antennas. The diffractive nature of the occurring SW beams as well as their initial width could be tailored by the size and geometry of the nonuniformities. In addition, it was demonstrated that the excitation frequency of the SW beams can be tuned by the bias field magnitude while their propagation direction can be steered by the direction of the in-plane bias field.

In summary, all these results and findings prove that real-space imaging by TRMOKE of SWs propagating in magnetic nanostructures is a versatile and sensitive tool, which enables an accurate determination of fundamental SW, material and system parameters as well as the exploration of novel concepts and approaches for controlling the excitation and/or propagation of SWs. Either of which is relevant and essential for the realization of future logic and memory devices exploiting all the advantages that magnonics and spintronics offer for storing, transporting and processing information.

Appendix A

Derivation of Expressions for the Spin-Drift Velocity and the Nonadiabatic Parameter

The analytical model developed by Hans Bauer [138] yields expressions for the spin-drift velocity u and the nonadiabatic parameter β. The peculiarity of these expressions is the fact that all occurring quantities can be determined experimentally[121]. A detailed derivation of these expressions is presented in the following.

In case of DE SWs, the effect of the adiabatic and nonadiabatic STT terms in the extended LLG equation [cf. Eq. (1.29)] can be absorbed in the quantities H, ω and α by performing the following transformations:

$$\omega \to \omega + uk = \omega + \Delta\omega \tag{A1}$$

$$H \to H + i\,(\beta - \alpha)\,\frac{uk}{\gamma\mu_0} = H + \Delta H\,. \tag{A2}$$

Since the DE SW wave number is a function of ω and H, i.e., $k = k\,(\omega, H)$, the STT-induced changes in k can be expressed using $\Delta\omega$ and ΔH as follows:

$$\Delta k = \frac{\partial k}{\partial \omega}\Delta\omega + \frac{\partial k}{\partial H}\Delta H\,. \tag{A3}$$

Eq. (A3) represents a complex equation, which can be solved exactly for u and β yielding[122]

$$u = -\frac{\mathrm{Re}\left[\frac{\partial \underline{k}}{\gamma\mu_0\partial H}\cdot\left(\frac{\Delta\underline{k}}{\underline{k}}\right)\right]}{\mathrm{Re}\left[\frac{\partial \underline{k}}{\partial\omega}\cdot\left(\frac{\partial \underline{k}}{\gamma\mu_0\partial H}\right)\right]} \tag{A4}$$

$$\text{and} \qquad \beta = \frac{\mathrm{Im}\left[\frac{\partial \underline{k}}{\partial\omega}\left(\frac{\Delta\underline{k}}{\underline{k}}\right)^*\right]}{\mathrm{Re}\left[\frac{\partial \underline{k}}{\gamma\mu_0\partial H}\left(\frac{\Delta\underline{k}}{\underline{k}}\right)^*\right]} + \alpha, \tag{A5}$$

[121] These expressions are employed to evaluate the key STT parameters from SW Doppler experiments [cf. Sec. 3.4.3].

[122] $\underline{k}$ denotes a complex wave number, while * denotes the complex conjugate.

respectively. Several approximations[123] can be applied to Eqs. (A4) and (A5) [138, 139], which eventually result in the following expressions:

$$u \approx \mathrm{Re}\left(\frac{\Delta\underline{k}}{\underline{k}}\right) v_{\mathrm{gr}} \tag{A6}$$

and

$$\beta \approx \frac{-1}{v_{\mathrm{gr}} \cdot \mathrm{Re}\left(\frac{\partial\underline{k}}{\gamma\mu_0 \partial H}\right)} \left[\frac{\mathrm{Im}\left(\frac{\Delta\underline{k}}{\underline{k}}\right)}{\mathrm{Re}\left(\frac{\Delta\underline{k}}{\underline{k}}\right)} - \frac{\mathrm{Im}\left(\underline{k}\right) d}{1 - \mathrm{Re}\left(\underline{k}\right) d}\right] + \alpha\,. \tag{A7}$$

[123] The appropriability of these approximations was verified by micromagnetic simulations using mumax2 [161].

Appendix B

MuMax3 and the Implementation and Analysis of the Micromagnetic Simulations Performed

In this appendix, first, in B.1, details about the program used for the micromagnetic simulations are given, while further information about the implementation and analysis of the micromagnetic simulations discussed in Ch. 4 and 5 are addressed in B.2 and B.3, respectively.

B.1 MuMax3

MuMax3 is an open-source, GPU-accelerated micromagnetic simulation program [173]. This software is capable of calculating the space- and time-dependent magnetization dynamics in nano- to micro-sized magnetic structures. It employs finite-difference discretization, i.e., space is discretized using a two-dimensional or three-dimensional grid of orthorhombic cells. It calculates the evolution of the reduced magnetization $\vec{m}(\vec{r},t) = \vec{M}(\vec{r},t)/M_S$— which has unit length—by solving the following equation of motion

$$\frac{\partial \vec{m}}{\partial t} = \vec{\tau}\,, \tag{B1}$$

where the torque τ—units 1/s—has three contributions, namely

- the Landau-Lifshitz-torque[124] $\vec{\tau}_{LL}$ [cf. Eq. (1.24)], which is used by MuMax3 in its explicit form written as [84, 85]

$$\vec{\tau}_{LL} = \gamma_{LL}\frac{1}{1+\alpha^2}\left[\vec{m}\times\vec{B}_{eff} + \alpha\left(\vec{m}\times\left(\vec{m}\times\vec{B}_{eff}\right)\right)\right]\,, \tag{B2}$$

  with [cf. Eq. (1.22)]

$$\vec{B}_{eff} = \mu_0\vec{H}_{eff} = \mu_0\left(\vec{H}_0 + \vec{H}_{dip} + \vec{H}_{ex} + \vec{H}_{DMI} + \vec{H}_{ani}\right)\,, \tag{B3}$$

[124] In the micromagnetic simulations addressed in B.2 and B.3, only this torque term is relevant.

- the Zhang-Li STT $\vec{\tau}_{\mathrm{ZL}}$ [89], and
- the Sloczweski STT $\vec{\tau}_{\mathrm{SL}}$ [18, 203].

An advantage of the finite-difference discretization is the fact that the magnetostatic field $\vec{B}_{\mathrm{dip}} = \vec{H}_{\mathrm{dip}}/\mu_0$ in Eq. (B2) can be evaluated as a (discrete) convolution of the magnetization with a demagnetizing kernel $\overline{\overline{K}}$, i.e.,

$$\vec{B}_{\mathrm{dip,i}} = \overline{\overline{K}}_{ij} * \vec{M}_j \tag{B4}$$

with $\vec{M} = M_{\mathrm{S}}\vec{m}$, using a fast Fourier transform. $\overline{\overline{K}}$ itself is accessed by assuming a constant magnetization in each finite-difference cell [204] and averaging the resulting $\vec{B}_{\mathrm{dip}}$ over the cell volumes.
Moreover, MuMax3 offers optional periodic boundary conditions (PBC) in each direction, i.e., the magnetization is repeated N_i times along the periodic directions, thereby enabling the simulation of extended magnetic layers when taking advantage of the specific symmetries of the sample and/or the experimental geometry. When PBC are utilized, the magnetostatic field of the repeated magnetization building blocks is added to $\vec{B}_{\mathrm{dip}}$.
To simulate field or current excitations—e.g., the excitation of propagating DE SWs by the spatially inhomogeneous rf fields of a microwave antenna in the shape of a shorted CPW—MuMax3 offers the possibility to add an arbitrary number of time- and space-dependent vector fields in the form $g\,(x, y, z) \cdot f\,(t)$.
Furthermore, to model grains in a thin magnetic structure, MuMax3 provides a two-dimensional Voronoi tessellation, thus enabling the variation of specific material parameters within up to 256 different regions.

B.2 Micromagnetic Simulations on the Interfacial Dzyaloshinskii-Moriya Interaction in Pt/Co/Py/MgO

In the experiment, the influence of an interfacial DMI on the propagation of DE SWs is investigated in 70 μm-wide, 500 μm-long, and 5.4 nm-thick Pt/Co/Py/MgO stripes. In the corresponding micromagnetic simulations the stripes are modeled as follows:
First, a 20 μm-long (x direction), 5.7 nm-thick (y direction) and 200 nm-wide (z direction) stripe is defined. Its volume is divided into individual cells, where the number of cells along each direction is set in such a way that each cell dimension is shorter than the exchange length [117]: $N_x = 8192$ (length), $N_y = 4$ (thickness), and $N_z = 64$ (width), respectively. Then, due to symmetry arguments, PBC—64 repetitions—are employed along the z direction, thereby converting the initially very narrow stripe into an extended plain film[125]. In order to suppress SW reflection at the x edges absorbing boundary conditions are included by locally enhancing the Gilbert damping parameter α in the cells, which are located in

[125] As the width of the fabricated Pt/Co/Py/MgO stripes is on the order of several tens of micrometers, i.e., it is much larger than the thickness, these stripes can be regarded as a plain film.

the vicinity of these edges [102], where the strength of the enhancement increases towards the edges.

The initial random magnetization configuration is relaxed in the (first) bias field applied along the z direction prior to the excitation of DE SWs by the in-plane and out-of-plane rf fields of a 60 nm-thick microwave antenna in the shape of a shorted CPW [cf. Sec. 1.4.5]. Its signal line width is 600 nm, and the ratio "*signal line width : signal line to ground line gap : ground line width*" is set to 2 : 1 : 1. Based on these dimensions[126], the spatial profiles of the dynamic excitation fields within the xz-plane are calculated using the two-dimensional Biot-Savart law assuming a uniform current distribution within the CPW [cf. Sec. 1.4.5]. The duration of the excitation—which corresponds to the runtime of the simulation for a given set of parameters—is set to 10 ns, thereby covering at least 50 excitation periods depending on the excitation frequency.

The simulation data are analyzed as follows: As $N_y \neq 1$, they are first averaged over all N_y layers, thereby accounting for the fact that, in the experiment, the probing laser pulses sample the total thickness of the ferromagnet/ferromagnetic layers since it is smaller than their penetration depth [cf. Sec. 1.5 and Ch. 2]. The resulting modified simulation data are evaluated the same way as the Kerr images [cf. Sec. 4.3].

B.3 Micromagnetic Simulations on the Magnetic Damping in Poly-Crystalline $Co_{25}Fe_{75}$

The propagation of DE SWs is simulated in 80 μm-long, 1.15 μm-wide and 10 nm-thin stripes as well as, for comparison, in full films. In general, the number of cells is chosen in such a way that the in-plane dimensions of each cell are smaller than the exchange length [117]. To model the full film, PBC along the z direction are utilized. In order to suppress SW reflection at the x edges absorbing boundary conditions are included by locally enhancing the Gilbert damping parameter α in the cells, which are located in the vicinity of these edges [102], where the strength of the enhancement increases towards the edges. The material parameters used are listed in Table BI.

The initial random magnetization configuration is relaxed in the (first) bias field applied along the z direction prior to the excitation of DE SWs by the in-plane and out-of-plane rf fields of a 60 nm-thick microwave antenna in the shape of a shorted CPW with the following widths of the constituents: 600 nm

[126] In the simulations, the ratio "*signal line width : signal line to ground line gap : ground line width*" differs from the one of the microwave antennas patterned on top of the Pt/Co/Py/MgO stripes. Yet, differences in the dimensions of the constituents of the microwave antenna only result in a modified excitation spectrum, i.e., different excitation efficiencies for the individual wave numbers [cf. Sec. 1.4.5], but, at a given combination of f and H_0, the DE SW wave number is identical as this quantity is predetermined by the dispersion.

signal line, 300 nm gap, and 300 nm ground lines. Based on these dimensions, the spatial profiles of the dynamic excitation fields within the xz-plane are calculated using the two-dimensional Biot-Savart law assuming a uniform current distribution within the CPW [cf. Sec. 1.4.5]. The duration of the excitation is adjusted for each simulation individually, but comprises at least 100 excitation periods. In agreement with the experiment, the excitation frequency is varied between 13.68 GHz and 14.16 GHz in steps of 120 or 240 MHz, and the bias field magnitude is varied between 70 and 100 mT in steps of 5 mT.

The full film simulation data are analyzed the same way as the Kerr images [cf. Sec. 5.3]. In contrast, the stripe simulation data are analyzed slightly different. In order to mimic the optical detection method, these data are first convoluted with a Gaussian having a full width at half maximum of 300 nm in accordance with the Gaussian beam profile of the probing laser pulses. The resulting modified data are analyzed the same way as the full film simulation data.

quantity	value
α_{sim}	0.0015 / 0.0040
$\mu_0 M_{\mathrm{S}}$ [T]	2.40
$\mu_0 H_{\mathrm{u}}^{\perp}$ [T]	0.49
$\mu_0 H_{\mathrm{u}}^{\mathrm{ip}}$ [mT] (along the x or z direction)	1.7
A [J/m]	2.6×10^{-11}
γ [rad/(Ts)]	185×10^{9}

Table BI. Material parameters used throughout the CoFe simulations.

Inhomogeneities in the CoFe stripes are modeled by local variations in the saturation magnetization. For this purpose, grains, 10 nm in size, are implemented using the two-dimensional Voronoi tessellation algorithm inherently incorporated in MuMax3 [cf. Appendix B.1]. In each grain, the saturation magnetization is randomly varied by a certain percentage—0–5%—around the base value of 2.40 T. In simulations including inhomogeneities, the simulation Gilbert damping parameter α_{sim} is set to 0.0015.

Bibliography

[1] A. G. Gurevich and G. Melkov. *Magnetization Oscillations and Waves*. CRC Press, Boca Raton (1996).

[2] D. D. Stancil and A. Prabhakar. *Spin Waves–Theory and Applications*. Springer US, New York (2009).

[3] V. V. Kruglyak, S. O. Demokritov, and D. Grundler. *Magnonics*. J. Phys. D: Appl. Phys. **43**, 260301 (2010). https://doi.org/10.1088/0022-3727/43/26/260301.

[4] B. Lenk, H. Ulrichs, F. Garbs, and M. Münzenberg. *The building blocks of magnonics*. Phys. Rep. **507**, 107 (2011). https://doi.org/10.1016/j.physrep.2011.06.003.

[5] K. Perzlmaier, G. Woltersdorf, and C. H. Back. *Observation of the propagation and interference of spin waves in ferromagnetic thin films*. Phys. Rev. B **77**, 054425 (2008). https://doi.org/10.1103/PhysRevB.77.054425.

[6] H. G. Bauer, J.-Y. Chauleau, G. Woltersdorf, and C. H. Back. *Coupling of spinwave modes in wire structures*. Appl. Phys. Lett. **104**, 102404 (2014). https://doi.org/10.1063/1.4868250.

[7] J. Stigloher, M. Decker, H. S. Körner, K. Tanabe, T. Moriyama, T. Taniguchi, H. Hata, M. Madami, G. Gubbiotti, K. Kobayashi, T. Ono, and C. H. Back. *Snell's Law for Spin Waves*. Phys. Rev. Lett. **117**, 037204 (2016). https://doi.org/10.1103/PhysRevLett.117.037204.

[8] P. Grünberg, M. G. Cottam, W. Vach, C. Mayr, and R. E. Camley. *Brillouin scattering of light by spin waves in thin ferromagnetic films (invited)*. J. Appl. Phys. **53**, 2078 (1982). https://doi.org/10.1063/1.330751.

[9] J. Jorzick, S. O. Demokritov, C. Mathieu, B. Hillebrands, B. Bartenlian, C. Chappert, F. Rousseaux, and A. N. Slavin. *Brillouin light scattering from quantized spin waves in micron-size magnetic wires*. Phys. Rev. B **60**, 15194 (1999). https://doi.org/10.1103/PhysRevB.60.15194.

[10] T. Sebastian, K. Schultheiss, B. Obry, B. Hillebrands, and H. Schultheiss. *Micro-focused Brillouin light scattering: imaging spin waves at the nanoscale*. Front. Phys. **3**, 35 (2015). https://doi.org/10.3389/fphy.2015.00035.

[11] V. Vlaminck and M. Bailleul. *Current-Induced Spin-Wave Doppler Shift.* Science **322**, 410 (2008). https://doi.org/10.1126/science.1162843.

[12] M. Haidar and M. Bailleul. *Thickness dependence of degree of spin polarization of electrical current in permalloy thin films.* Phys. Rev. B **88**, 054417 (2013). https://doi.org/10.1103/PhysRevB.88.054417.

[13] O. Gladii, D. Halley, Y. Henry, and M. Bailleul. *Spin-wave propagation and spin-polarized electron transport in single-crystal iron films.* Phys. Rev. B **96**, 174420 (2017). https://doi.org/10.1103/PhysRevB.96.174420.

[14] S. Wintz, V. Tiberkevich, M. Weigand, J. Raabe, J. Lindner, A. Erbe, A. Slavin, and J. Fassbender. *Magnetic vortex cores as tunable spin-wave emitters.* Nat. Nanotechnol. **11**, 948 (2016). https://doi.org/10.1038/nnano.2016.117.

[15] G. Dieterle, J. Förster, H. Stoll, A. S. Semisalova, S. Finizio, A. Gangwar, M. Weigand, M. Noske, M. Fähnle, I. Bykova, D. A. Bozhko, H. Y. Musiienko-Shmarova, V. Tiberkevich, A. N. Slavin, C. H. Back, J. Raabe, G. Schütz, and S. Wintz. *Coherent excitation of heterosymmetric spin waves with ultrashort wavelengths.* arXiv:1712.00681 [cond-mat.mes-hall] (2017). https://arxiv.org/abs/1712.00681.

[16] L. Berger. *Exchange interaction between ferromagnetic domain wall and electric current in very thin metallic films.* J. Appl. Phys. **55**, 1954 (1984). https://doi.org/10.1063/1.333530.

[17] L. Berger. *Emission of spin waves by a magnetic multilayer traversed by a current.* Phys. Rev. B **54**, 9353 (1996). https://doi.org/10.1103/PhysRevB.54.9353.

[18] J. Slonczewski. *Current-driven excitation of magnetic multilayers.* J. Magn. Magn. Mater. **159**, L1 (1996). https://doi.org/10.1016/0304-8853(96)00062-5.

[19] M. I. Dyakonov and V. I. Perel. *Possibility of orienting electron spins with current.* JETP Lett. **13**, 467 (1971).

[20] M. Dyakonov and V. Perel. *Current-induced spin orientation of electrons in semiconductors.* Phys. Lett. A **35**, 459 (1971). https://doi.org/10.1016/0375-9601(71)90196-4.

[21] J. E. Hirsch. *Spin Hall Effect.* Phys. Rev. Lett. **83**, 1834 (1999). https://doi.org/10.1103/PhysRevLett.83.1834.

[22] S. Zhang. *Spin Hall Effect in the Presence of Spin Diffusion.* Phys. Rev. Lett. **85**, 393 (2000). https://doi.org/10.1103/PhysRevLett.85.393.

[23] Y. K. Kato, R. C. Myers, A. C. Gossard, and D. D. Awschalom. *Observation of the Spin Hall Effect in Semiconductors.* Science **306**, 1910 (2004). https://doi.org/10.1126/science.1105514.

[24] J. Sinova, S. O. Valenzuela, J. Wunderlich, C. H. Back, and T. Jungwirth. *Spin Hall effects*. Rev. Mod. Phys. **87**, 1213 (2015). https://doi.org/10.1103/RevModPhys.87.1213.

[25] I. Dzyaloshinsky. *A thermodynamic theory of "weak" ferromagnetism of antiferromagnetics*. J. Phys. Chem. Solids **4**, 241 (1958). https://doi.org/10.1016/0022-3697(58)90076-3.

[26] T. Moriya. *Anisotropic Superexchange Interaction and Weak Ferromagnetism*. Phys. Rev. **120**, 91 (1960). https://doi.org/10.1103/PhysRev.120.91.

[27] V. V. Zhirnov, R. K. Cavin, J. A. Hutchby, and G. I. Bourianoff. *Limits to binary logic switch scaling - a gedanken model*. Proc. IEEE **91**, 1934 (2003). https://doi.org/10.1109/JPROC.2003.818324.

[28] K. Bernstein, R. K. Cavin, W. Porod, A. Seabaugh, and J. Welser. *Device and Architecture Outlook for Beyond CMOS Switches*. Proc. IEEE **98**, 2169 (2010). https://doi.org/10.1109/JPROC.2010.2066530.

[29] D. E. Nikonov and I. A. Young. *Overview of Beyond-CMOS Devices and a Uniform Methodology for Their Benchmarking*. Proc. IEEE **101**, 2498 (2013). https://doi.org/10.1109/JPROC.2013.2252317.

[30] D. E. Nikonov and I. A. Young. *Benchmarking of Beyond-CMOS Exploratory Devices for Logic Integrated Circuits*. IEEE J. Explor. Solid-State Computat. Devices Circuits **1**, 3 (2015). https://doi.org/10.1109/JXCDC.2015.2418033.

[31] M. M. Waldrop. *The chips are down for Moore's law*. Nature **530**, 144 (2016). https://doi.org/10.1038/530144a.

[32] J. M. Owens, J. H. Collins, and R. L. Carter. *System applications of magnetostatic wave devices*. Circ. Syst. Signal Pr. **4**, 317 (1985). https://doi.org/10.1007/BF01600088.

[33] J. D. Adam. *Analog signal processing with microwave magnetics*. Proc. IEEE **76**, 159 (1988). https://doi.org/10.1109/5.4392.

[34] V. Cherepanov, I. Kolokolov, and V. L'vov. *The saga of YIG: Spectra, thermodynamics, interaction and relaxation of magnons in a complex magnet*. Phys. Rep. **229**, 81 (1993). https://doi.org/10.1016/0370-1573(93)90107-O.

[35] T. Balashov, P. Buczek, L. Sandratskii, A. Ernst, and W. Wulfhekel. *Magnon dispersion in thin magnetic films*. J. Phys.: Condens. Matter **26**, 394007 (2014). https://doi.org/10.1088/0953-8984/26/39/394007.

[36] T.-H. Chuang, K. Zakeri, A. Ernst, Y. Zhang, H. J. Qin, Y. Meng, Y.-J. Chen, and J. Kirschner. *Magnetic properties and magnon excitations in Fe(001) films grown on Ir(001)*. Phys. Rev. B **89**, 174404 (2014). https://doi.org/10.1103/PhysRevB.89.174404.

[37] A. V. Chumak, A. A. Serga, and B. Hillebrands. *Magnon transistor for all-magnon data processing*. Nat. Commun. **5**, 4700 (2014). https://doi.org/10.1038/ncomms5700.

[38] T. Schneider, A. A. Serga, A. V. Chumak, C. W. Sandweg, S. Trudel, S. Wolff, M. P. Kostylev, V. S. Tiberkevich, A. N. Slavin, and B. Hillebrands. *Nondiffractive Subwavelength Wave Beams in a Medium with Externally Controlled Anisotropy*. Phys. Rev. Lett. **104**, 197203 (2010). https://doi.org/10.1103/PhysRevLett.104.197203.

[39] A. A. Serga, A. V. Chumak, and B. Hillebrands. *YIG magnonics*. J. Phys. D: Appl. Phys. **43**, 264002 (2010). https://doi.org/10.1088/0022-3727/43/26/264002.

[40] A. V. Chumak, V. I. Vasyuchka, A. A. Serga, and B. Hillebrands. *Magnon spintronics*. Nat. Phys. **11**, 453 (2015). https://doi.org/10.1038/nphys3347.

[41] S. Dutta, S.-C. Chang, N. Kani, D. E. Nikonov, S. Manipatruni, I. A. Young, and A. Naeemi. *Non-volatile Clocked Spin Wave Interconnect for Beyond-CMOS Nanomagnet Pipelines*. Sci. Rep. **5**, 9861 (2015). https://doi.org/10.1038/srep09861.

[42] G. Csaba, Ádám Papp, and W. Porod. *Perspectives of using spin waves for computing and signal processing*. Phys. Lett. A **381**, 1471 - 1476 (2017). https://doi.org/10.1016/j.physleta.2017.02.042.

[43] M. Jamali, J. H. Kwon, S.-M. Seo, K.-J. Lee, and H. Yang. *Spin wave nonreciprocity for logic device applications*. Sci. Rep. **3**, 3160 (2013). https://doi.org/10.1038/srep03160.

[44] T. Schneider, A. A. Serga, T. Neumann, B. Hillebrands, and M. P. Kostylev. *Phase reciprocity of spin-wave excitation by a microstrip antenna*. Phys. Rev. B **77**, 214411 (2008). https://doi.org/10.1103/PhysRevB.77.214411.

[45] V. E. Demidov, M. P. Kostylev, K. Rott, P. Krzysteczko, G. Reiss, and S. O. Demokritov. *Excitation of microwaveguide modes by a stripe antenna*. Appl. Phys. Lett. **95**, 112509 (2009). https://doi.org/10.1063/1.3231875.

[46] V. E. Demidov, M. P. Kostylev, K. Rott, J. Münchenberger, G. Reiss, and S. O. Demokritov. *Excitation of short-wavelength spin waves in magnonic waveguides*. Appl. Phys. Lett. **99**, 082507 (2011). https://doi.org/10.1063/1.3631756.

[47] R. Gieniusz, H. Ulrichs, V. D. Bessonov, U. Guzowska, A. I. Stognii, and A. Maziewski. *Single antidot as a passive way to create caustic spin-wave beams in yttrium iron garnet films*. Appl. Phys. Lett. **102**, 102409 (2013). https://doi.org/10.1063/1.4795293.

[48] M. Zhu, C. L. Dennis, and R. D. McMichael. *Temperature dependence of magnetization drift velocity and current polarization in $Ni_{80}Fe_{20}$ by spin-wave Doppler measurements.* Phys. Rev. B **81**, 140407 (2010). https://doi.org/10.1103/PhysRevB.81.140407.

[49] K. Sekiguchi, K. Yamada, S.-M. Seo, K.-J. Lee, D. Chiba, K. Kobayashi, and T. Ono. *Time-Domain Measurement of Current-Induced Spin Wave Dynamics.* Phys. Rev. Lett. **108**, 017203 (2012). https://doi.org/10.1103/PhysRevLett.108.017203.

[50] K. An, D. R. Birt, C.-F. Pai, K. Olsson, D. C. Ralph, R. A. Buhrman, and X. Li. *Control of propagating spin waves via spin transfer torque in a metallic bilayer waveguide.* Phys. Rev. B **89**, 140405 (2014). https://doi.org/10.1103/PhysRevB.89.140405.

[51] V. E. Demidov, S. Urazhdin, A. B. Rinkevich, G. Reiss, and S. O. Demokritov. *Spin Hall controlled magnonic microwaveguides.* Appl. Phys. Lett. **104**, 152402 (2014). https://doi.org/10.1063/1.4871519.

[52] J.-H. Moon, S.-M. Seo, K.-J. Lee, K.-W. Kim, J. Ryu, H.-W. Lee, R. D. McMichael, and M. D. Stiles. *Spin-wave propagation in the presence of interfacial Dzyaloshinskii-Moriya interaction.* Phys. Rev. B **88**, 184404 (2013). https://doi.org/10.1103/PhysRevB.88.184404.

[53] K. Di, V. L. Zhang, H. S. Lim, S. C. Ng, M. H. Kuok, J. Yu, J. Yoon, X. Qiu, and H. Yang. *Direct Observation of the Dzyaloshinskii-Moriya Interaction in a Pt/Co/Ni Film.* Phys. Rev. Lett. **114**, 047201 (2015). https://doi.org/10.1103/PhysRevLett.114.047201.

[54] S. A. Wolf, D. D. Awschalom, R. A. Buhrman, J. M. Daughton, S. von Molnár, M. L. Roukes, A. Y. Chtchelkanova, and D. M. Treger. *Spintronics: A Spin-Based Electronics Vision for the Future.* Science **294**, 1488 (2001). https://doi.org/10.1126/science.1065389.

[55] I. Žutić, J. Fabian, and S. Das Sarma. *Spintronics: Fundamentals and applications.* Rev. Mod. Phys. **76**, 323 (2004). https://doi.org/10.1103/RevModPhys.76.323.

[56] D. A. Allwood, G. Xiong, C. C. Faulkner, D. Atkinson, D. Petit, and R. P. Cowburn. *Magnetic Domain-Wall Logic.* Science **309**, 1688 (2005). https://doi.org/10.1126/science.1108813.

[57] J. Katine and E. E. Fullerton. *Device implications of spin-transfer torques.* J. Magn. Magn. Mater. **320**, 1217 (2008). https://doi.org/10.1016/j.jmmm.2007.12.013.

[58] A. D. Kent and D. C. Worledge. *A new spin on magnetic memories.* Nat. Nanotechnol. **10**, 187 (2015). https://doi.org/10.1038/nnano.2015.24.

[59] S. S. P. Parkin, M. Hayashi, and L. Thomas. *Magnetic Domain-Wall Racetrack Memory.* Science **320**, 190 (2008). https://doi.org/10.1126/science.1145799.

[60] S. Parkin and S.-H. Yang. *Memory on the racetrack*. Nat. Nanotechnol. **10**, 195 (2015). https://doi.org/10.1038/nnano.2015.41.

[61] P. P. J. Haazen, E. Murè, J. H. Franken, R. Lavrijsen, H. J. M. Swagten, and B. Koopmans. *Domain wall depinning governed by the spin Hall effect*. Nat. Mater. **12**, 299 (2013). https://doi.org/10.1038/nmat3553.

[62] K.-S. Ryu, L. Thomas, S.-H. Yang, and S. Parkin. *Chiral spin torque at magnetic domain walls*. Nat. Nanotechnol. **8**, 527 (2013). https://doi.org/10.1038/nnano.2013.102.

[63] S. Emori, U. Bauer, S.-M. Ahn, E. Martinez, and G. S. D. Beach. *Current-driven dynamics of chiral ferromagnetic domain walls*. Nat. Mater. **12**, 611 (2013). https://doi.org/10.1038/nmat3675.

[64] W. F. Brown. *Micromagnetics*. Krieger, New York (1978).

[65] S. Blundell. *Magnetism in Condensed Matter*. Oxford University Press, USA (2000).

[66] A. Hubert and R. Schäfer. *Magnetic Domains–The Analysis of Magnetic Microstructures*. Springer-Verlag, Berlin Heidelberg (1998).

[67] G. Bertotti, I. D. Mayergoyz, and C. Serpico. *Nonlinear Magnetization Dynamics in Nanosystems*. Elsevier (2009).

[68] U. K. Rößler, A. N. Bogdanov, and C. Pfleiderer. *Spontaneous skyrmion ground states in magnetic metals*. Nature **442**, 797 (2006). https://doi.org/10.1038/nature05056.

[69] M. Uchida, Y. Onose, Y. Matsui, and Y. Tokura. *Real-Space Observation of Helical Spin Order*. Science **311**, 359 (2006). https://doi.org/10.1126/science.1120639.

[70] S. Mühlbauer, B. Binz, F. Jonietz, C. Pfleiderer, A. Rosch, A. Neubauer, R. Georgii, and P. Böni. *Skyrmion Lattice in a Chiral Magnet*. Science **323**, 915 (2009). https://doi.org/10.1126/science.1166767.

[71] S. D. Yi, S. Onoda, N. Nagaosa, and J. H. Han. *Skyrmions and anomalous Hall effect in a Dzyaloshinskii-Moriya spiral magnet*. Phys. Rev. B **80**, 054416 (2009). https://doi.org/10.1103/PhysRevB.80.054416.

[72] X. Z. Yu, Y. Onose, N. Kanazawa, J. H. Park, J. H. Han, Y. Matsui, N. Nagaosa, and Y. Tokura. *Real-space observation of a two-dimensional skyrmion crystal*. Nature **465**, 901 (2010). https://doi.org/10.1038/nature09124.

[73] X. Z. Yu, N. Kanazawa, Y. Onose, K. Kimoto, W. Z. Zhang, S. Ishiwata, Y. Matsui, and Y. Tokura. *Near room-temperature formation of a skyrmion crystal in thin-films of the helimagnet FeGe*. Nat. Mater. **10**, 106 (2011). https://doi.org/10.1038/nmat2916.

[74] S. Heinze, K. von Bergmann, M. Menzel, J. Brede, A. Kubetzka, R. Wiesendanger, G. Bihlmayer, and S. Blügel. *Spontaneous atomic-scale magnetic skyrmion lattice in two dimensions.* Nat. Phys. **7**, 713 (2011). https://doi.org/10.1038/nphys2045.

[75] S. X. Huang and C. L. Chien. *Extended Skyrmion Phase in Epitaxial* FeGe(111) *Thin Films.* Phys. Rev. Lett. **108**, 267201 (2012). https://doi.org/10.1103/PhysRevLett.108.267201.

[76] A. Fert, V. Cros, and J. Sampaio. *Skyrmions on the track.* Nat. Nanotechnol. **8**, 152 (2013). https://doi.org/10.1038/nnano.2013.29.

[77] H. Yang, A. Thiaville, S. Rohart, A. Fert, and M. Chshiev. *Anatomy of Dzyaloshinskii-Moriya Interaction at Co/Pt Interfaces.* Phys. Rev. Lett. **115**, 267210 (2015). https://doi.org/10.1103/PhysRevLett.115.267210.

[78] A. Fert and P. M. Levy. *Role of Anisotropic Exchange Interactions in Determining the Properties of Spin-Glasses.* Phys. Rev. Lett. **44**, 1538 (1980). https://doi.org/10.1103/PhysRevLett.44.1538.

[79] A. R. Fert. *Magnetic and Transport Properties of Metallic Multilayers.* In: Metallic Multilayers, Vol. 59, Materials Science Forum. Trans Tech Publications. pp. 439–480 (1991). https://doi.org/10.4028/www.scientific.net/MSF.59-60.439.

[80] A. N. Bogdanov and U. K. Rößler. *Chiral Symmetry Breaking in Magnetic Thin Films and Multilayers.* Phys. Rev. Lett. **87**, 037203 (2001). https://doi.org/10.1103/PhysRevLett.87.037203.

[81] A. Thiaville, S. Rohart, E. Jué, V. Cros, and A. Fert. *Dynamics of Dzyaloshinskii domain walls in ultrathin magnetic films.* Europhys. Lett. **100**, 57002 (2012). https://doi.org/10.1209/0295-5075/100/57002.

[82] A. Aharoni. *Introduction to the Theory of Ferromagnetism.* Oxford University Press (2001).

[83] N. Nakajima, T. Koide, T. Shidara, H. Miyauchi, H. Fukutani, A. Fujimori, K. Iio, T. Katayama, M. Nývlt, and Y. Suzuki. *Perpendicular Magnetic Anisotropy Caused by Interfacial Hybridization via Enhanced Orbital Moment in* Co/Pt *Multilayers: Magnetic Circular X-Ray Dichroism Study.* Phys. Rev. Lett. **81**, 5229 (1998). https://doi.org/10.1103/PhysRevLett.81.5229.

[84] L. Landau and E. Lifshitz. *On the theory of dispersion of magnetic permeability in ferromagnetic bodies.* Phys. Z. Sowjet. **8**, 153 (1935).

[85] T. L. Gilbert. *Lagrangian Formulation of the Gyromagnetic Equation of the Magnetization Field.* Phys. Rev. **100**, 1243 (1955).

[86] D. Ralph and M. Stiles. *Spin transfer torques.* J. Magn. Magn. Mater. **320**, 1190 (2008). https://doi.org/10.1016/j.jmmm.2007.12.019.

[87] A. Thiaville, Y. Nakatani, J. Miltat, and N. Vernier. *Domain wall motion by spin-polarized current: a micromagnetic study.* J. Appl. Phys. **95**, 7049 (2004). https://doi.org/10.1063/1.1667804.

[88] Z. Li and S. Zhang. *Domain-wall dynamics driven by adiabatic spin-transfer torques.* Phys. Rev. B **70**, 024417 (2004). https://doi.org/10.1103/PhysRevB.70.024417.

[89] S. Zhang and Z. Li. *Roles of Nonequilibrium Conduction Electrons on the Magnetization Dynamics of Ferromagnets.* Phys. Rev. Lett. **93**, 127204 (2004). https://doi.org/10.1103/PhysRevLett.93.127204.

[90] Y. B. Bazaliy, B. A. Jones, and S.-C. Zhang. *Modification of the Landau-Lifshitz equation in the presence of a spin-polarized current in colossal- and giant-magnetoresistive materials.* Phys. Rev. B **57**, R3213 (1998). https://doi.org/10.1103/PhysRevB.57.R3213.

[91] G. Tatara and H. Kohno. *Theory of Current-Driven Domain Wall Motion: Spin Transfer versus Momentum Transfer.* Phys. Rev. Lett. **92**, 086601 (2004). https://doi.org/10.1103/PhysRevLett.92.086601.

[92] Z. Li and S. Zhang. *Domain-Wall Dynamics and Spin-Wave Excitations with Spin-Transfer Torques.* Phys. Rev. Lett. **92**, 207203 (2004). https://doi.org/10.1103/PhysRevLett.92.207203.

[93] J. Fernández-Rossier, M. Braun, A. S. Núñez, and A. H. MacDonald. *Influence of a uniform current on collective magnetization dynamics in a ferromagnetic metal.* Phys. Rev. B **69**, 174412 (2004). https://doi.org/10.1103/PhysRevB.69.174412.

[94] J. P. Ansermet. *Classical description of spin wave excitation by currents in bulk ferromagnets.* IEEE Trans. Magn. **40**, 358 (2004). https://doi.org/10.1109/TMAG.2004.824120.

[95] A. Thiaville, Y. Nakatani, J. Miltat, and Y. Suzuki. *Micromagnetic understanding of current-driven domain wall motion in patterned nanowires.* Europhys. Lett. **69**, 990 (2005). https://doi.org/10.1209/epl/i2004-10452-6.

[96] X. Waintal and M. Viret. *Current-induced distortion of a magnetic domain wall.* Europhys. Lett. **65**, 427 (2004). https://doi.org/10.1209/epl/i2003-10089-y.

[97] J. Xiao, A. Zangwill, and M. D. Stiles. *Spin-transfer torque for continuously variable magnetization.* Phys. Rev. B **73**, 054428 (2006). https://doi.org/10.1103/PhysRevB.73.054428.

[98] G. Tatara, H. Kohno, J. Shibata, Y. Lemaho, and K.-J. Lee. *Spin Torque and Force due to Current for General Spin Textures.* J. Phys. Soc. Jpn. **76**, 054707 (2007). https://doi.org/10.1143/JPSJ.76.054707.

[99] Y. Tserkovnyak, A. Brataas, and G. E. Bauer. *Theory of current-driven magnetization dynamics in inhomogeneous ferromagnets.* J. Magn. Magn. Mater. **320**, 1282 (2008). https://doi.org/10.1016/j.jmmm.2007.12.012.

[100] I. Garate, K. Gilmore, M. D. Stiles, and A. H. MacDonald. *Nonadiabatic spin-transfer torque in real materials*. Phys. Rev. B **79**, 104416 (2009). https://doi.org/10.1103/PhysRevB.79.104416.

[101] S. Lepadatu, M. C. Hickey, A. Potenza, H. Marchetto, T. R. Charlton, S. Langridge, S. S. Dhesi, and C. H. Marrows. *Experimental determination of spin-transfer torque nonadiabaticity parameter and spin polarization in permalloy*. Phys. Rev. B **79**, 094402 (2009). https://doi.org/10.1103/PhysRevB.79.094402.

[102] S.-M. Seo, K.-J. Lee, H. Yang, and T. Ono. *Current-Induced Control of Spin-Wave Attenuation*. Phys. Rev. Lett. **102**, 147202 (2009). https://doi.org/10.1103/PhysRevLett.102.147202.

[103] S. E. Barnes and S. Maekawa. *Current-Spin Coupling for Ferromagnetic Domain Walls in Fine Wires*. Phys. Rev. Lett. **95**, 107204 (2005). https://doi.org/10.1103/PhysRevLett.95.107204.

[104] M. D. Stiles, W. M. Saslow, M. J. Donahue, and A. Zangwill. *Adiabatic domain wall motion and Landau-Lifshitz damping*. Phys. Rev. B **75**, 214423 (2007). https://doi.org/10.1103/PhysRevB.75.214423.

[105] H. Kohno, G. Tatara, and J. Shibata. *Microscopic Calculation of Spin Torques in Disordered Ferromagnets*. J. Phys. Soc. Jpn. **75**, 113706 (2006). https://doi.org/10.1143/JPSJ.75.113706.

[106] K. Gilmore, I. Garate, A. H. MacDonald, and M. D. Stiles. *First-principles calculation of the nonadiabatic spin transfer torque in Ni and Fe*. Phys. Rev. B **84**, 224412 (2011). https://doi.org/10.1103/PhysRevB.84.224412.

[107] L. Heyne, M. Kläui, D. Backes, T. A. Moore, S. Krzyk, U. Rüdiger, L. J. Heyderman, A. F. Rodríguez, F. Nolting, T. O. Mentes, M. A. Niño, A. Locatelli, K. Kirsch, and R. Mattheis. *Relationship between Nonadiabaticity and Damping in Permalloy Studied by Current Induced Spin Structure Transformations*. Phys. Rev. Lett. **100**, 066603 (2008). https://doi.org/10.1103/PhysRevLett.100.066603.

[108] M. Hayashi, L. Thomas, Y. B. Bazaliy, C. Rettner, R. Moriya, X. Jiang, and S. S. P. Parkin. *Influence of Current on Field-Driven Domain Wall Motion in Permalloy Nanowires from Time Resolved Measurements of Anisotropic Magnetoresistance*. Phys. Rev. Lett. **96**, 197207 (2006). https://doi.org/10.1103/PhysRevLett.96.197207.

[109] R. Moriya, L. Thomas, M. Hayashi, Y. B. Bazaliy, C. Rettner, and S. S. P. Parkin. *Probing vortex-core dynamics using current-induced resonant excitation of a trapped domain wall*. Nat. Phys. **4**, 368 (2008). https://doi.org/10.1038/nphys936.

[110] L. Thomas, M. Hayashi, X. Jiang, R. Moriya, C. Rettner, and S. S. P. Parkin. *Oscillatory dependence of current-driven magnetic domain wall motion on current pulse length*. Nature **443**, 197 (2006). https://doi.org/10.1038/nature05093.

[111] S. D. Pollard, L. Huang, K. S. Buchanan, D. A. Arena, and Y. Zhu. *Direct dynamic imaging of non-adiabatic spin torque effects*. Nat. Commun. **3**, 1028 (2012). https://doi.org/10.1038/ncomms2025.

[112] O. Boulle, J. Kimling, P. Warnicke, M. Kläui, U. Rüdiger, G. Malinowski, H. J. M. Swagten, B. Koopmans, C. Ulysse, and G. Faini. *Nonadiabatic Spin Transfer Torque in High Anisotropy Magnetic Nanowires with Narrow Domain Walls*. Phys. Rev. Lett. **101**, 216601 (2008). https://doi.org/10.1103/PhysRevLett.101.216601.

[113] R. W. Damon and J. R. Eshbach. *Magnetostatic modes of a ferromagnet slab*. J. Phys. Chem. Solids **19**, 308 (1961). https://doi.org/10.1016/0022-3697(61)90041-5.

[114] B. A. Kalinikos and A. N. Slavin. *Theory of dipole-exchange spin wave spectrum for ferromagnetic films with mixed exchange boundary conditions*. J. Phys. C: Solid State Phys. **19**, 7013 (1986). https://doi.org/10.1088/0022-3719/19/35/014.

[115] B. A. Kalinikos, M. P. Kostylev, N. V. Kozhus, and A. N. Slavin. *The dipole-exchange spin wave spectrum for anisotropic ferromagnetic films with mixed exchange boundary conditions*. J. Phys.: Condens. Matter **2**, 9861 (1990). https://doi.org/10.1088/0953-8984/2/49/012.

[116] K. Di, V. L. Zhang, H. S. Lim, S. C. Ng, M. H. Kuok, X. Qiu, and H. Yang. *Asymmetric spin-wave dispersion due to Dzyaloshinskii-Moriya interaction in an ultrathin Pt/CoFeB film*. Appl. Phys. Lett. **106**, 052403 (2015). https://doi.org/10.1063/1.4907173.

[117] G. S. Abo, Y. K. Hong, J. Park, J. Lee, W. Lee, and B. C. Choi. *Definition of Magnetic Exchange Length*. IEEE Trans. Magn. **49**, 4937 (2013). https://doi.org/10.1109/TMAG.2013.2258028.

[118] K. Y. Guslienko and A. N. Slavin. *Magnetostatic Green's functions for the description of spin waves in finite rectangular magnetic dots and stripes*. J. Magn. Magn. Mater. **323**, 2418 (2011). https://doi.org/10.1016/j.jmmm.2011.05.020.

[119] J. M. D. Coey. *Magnetism and Magnetic Materials*. Cambridge University Press (2010).

[120] M. Kostylev. *Non-reciprocity of dipole-exchange spin waves in thin ferromagnetic films*. J. Appl. Phys. **113**, 053907 (2013). https://doi.org/10.1063/1.4789962.

[121] O. Gladii, M. Haidar, Y. Henry, M. Kostylev, and M. Bailleul. *Frequency nonreciprocity of surface spin wave in permalloy thin films*. Phys. Rev. B **93**, 054430 (2016). https://doi.org/10.1103/PhysRevB.93.054430.

[122] S. Rao, J. Yoon, J. Rhensius, C. S. Bhatia, and H. Yang. *Spin wave non-reciprocity and beating in permalloy by the time-resolved magneto-optical Kerr effect*. J. Phys. D: Appl. Phys. **47**, 385002 (2014). https://doi.org/10.1088/0022-3727/47/38/385002.

[123] M. Haidar, M. Bailleul, M. Kostylev, and Y. Lao. *Nonreciprocal Oersted field contribution to the current-induced frequency shift of magnetostatic surface waves*. Phys. Rev. B **89**, 094426 (2014). https://doi.org/10.1103/PhysRevB.89.094426.

[124] M. Kostylev. *Strong asymmetry of microwave absorption by bilayer conducting ferromagnetic films in the microstrip-line based broadband ferromagnetic resonance*. J. Appl. Phys. **106**, 043903 (2009). https://doi.org/10.1063/1.3187547.

[125] V. Vlaminck and M. Bailleul. *Current-Induced Spin-Wave Doppler Shift—Supplemental Material*. Science **322**, 410 (2008).

[126] P. Lederer and D. L. Mills. *Possible Experimental Test of the Band Theory of Magnetism*. Phys. Rev. **148**, 542 (1966). https://doi.org/10.1103/PhysRev.148.542.

[127] T. P. Gill. *The Doppler Effect–An Introduction to the Theory of the Effect*. Logos Press, London (1965).

[128] D. D. Stancil, B. E. Henty, A. G. Cepni, and J. P. Van't Hof. *Observation of an inverse Doppler shift from left-handed dipolar spin waves*. Phys. Rev. B **74**, 060404 (2006). https://doi.org/10.1103/PhysRevB.74.060404.

[129] H. T. Nembach, J. M. Shaw, M. Weiler, E. Jue, and T. J. Silva. *Linear relation between Heisenberg exchange and interfacial Dzyaloshinskii-Moriya interaction in metal films*. Nat. Phys. **11**, 825 (2015). https://doi.org/10.1038/nphys3418.

[130] M. Belmeguenai, J.-P. Adam, Y. Roussigné, S. Eimer, T. Devolder, J.-V. Kim, S. M. Cherif, A. Stashkevich, and A. Thiaville. *Interfacial Dzyaloshinskii-Moriya interaction in perpendicularly magnetized Pt/Co/AlO$_x$ ultrathin films measured by Brillouin light spectroscopy*. Phys. Rev. B **91**, 180405 (2015). https://doi.org/10.1103/PhysRevB.91.180405.

[131] A. A. Stashkevich, M. Belmeguenai, Y. Roussigné, S. M. Cherif, M. Kostylev, M. Gabor, D. Lacour, C. Tiusan, and M. Hehn. *Experimental study of spin-wave dispersion in Py/Pt film structures in the presence of an interface Dzyaloshinskii-Moriya interaction*. Phys. Rev. B **91**, 214409 (2015). https://doi.org/10.1103/PhysRevB.91.214409.

[132] J.-Y. Chauleau, H. G. Bauer, H. S. Körner, J. Stigloher, M. Härtinger, G. Woltersdorf, and C. H. Back. *Self-consistent determination of the key spin-transfer torque parameters from spin-wave Doppler experiments*. Phys. Rev. B **89**, 020403(R) (2014). https://doi.org/10.1103/PhysRevB.89.020403.

[133] H. S. Körner, J. Stigloher, H. G. Bauer, H. Hata, T. Taniguchi, T. Moriyama, T. Ono, and C. H. Back. *Interfacial Dzyaloshinskii-Moriya interaction studied by time-resolved scanning Kerr microscopy*. Phys. Rev. B **92**, 220413(R) (2015). https://doi.org/10.1103/PhysRevB.92.220413.

[134] H. S. Körner, J. Stigloher, and C. H. Back. *Excitation and tailoring of diffractive spin-wave beams in NiFe using nonuniform microwave antennas.* Phys. Rev. B **96**, 100401 (2017). https://doi.org/10.1103/PhysRevB.96.100401.

[135] H. S. Körner, M. A. W. Schoen, T. Mayer, M. M. Decker, J. Stigloher, T. Weindler, T. N. G. Meier, M. Kronseder, and C. H. Back. *Magnetic damping in poly-crystalline $Co_{25}Fe_{75}$: Ferromagnetic resonance vs. spin wave propagation experiments.* Appl. Phys. Lett. **111**, 132406 (2017). https://doi.org/10.1063/1.4994137.

[136] V. Vlaminck and M. Bailleul. *Spin-wave transduction at the submicrometer scale: Experiment and modeling.* Phys. Rev. B **81**, 014425 (2010). https://doi.org/10.1103/PhysRevB.81.014425.

[137] H. G. Bauer, J.-Y. Chauleau, G. Woltersdorf, and C. H. Back. *k-vector distribution of magneto-static spin waves excited by micro-fabricated antenna structures.* In: Ultrafast Magnetism I: Proceedings of the International Conference UMC 2013 Strasbourg, France. Springer International Publishing, Cham. pp. 83–85 (2015). https://doi.org/10.1007/978-3-319-07743-7_27.

[138] H. Bauer. *Linear and nonlinear magnetization dynamics in thin ferromagnetic films and nanostructures.* Universität Regensburg, Dissertation (2015).

[139] J.-Y. Chauleau, H. G. Bauer, H. S. Körner, J. Stigloher, M. Härtinger, G. Woltersdorf, and C. H. Back. *Self-consistent determination of the key spin-transfer torque parameters from spin-wave Doppler experiments—Supplemental Material.* Phys. Rev. B **89**, 020403(R) (2014).

[140] Y. Henry, O. Gladii, and M. Bailleul. *Propagating spin-wave normal modes: A dynamic matrix approach using plane-wave demagnetizating tensors.* arXiv:1611.06153 [cond-mat.mes-hall] (2016). https://arxiv.org/abs/1611.06153.

[141] B. Hillebrands and A. Thiaville. *Spin Dynamics in Confined Magnetic Structures III.* Springer-Verlag, Berlin Heidelberg (2006).

[142] J. P. Park, P. Eames, D. M. Engebretson, J. Berezovsky, and P. A. Crowell. *Spatially Resolved Dynamics of Localized Spin-Wave Modes in Ferromagnetic Wires.* Phys. Rev. Lett. **89**, 277201 (2002). https://doi.org/10.1103/PhysRevLett.89.277201.

[143] V. E. Demidov, S. O. Demokritov, K. Rott, P. Krzysteczko, and G. Reiss. *Nano-optics with spin waves at microwave frequencies.* Appl. Phys. Lett. **92**, 232503 (2008). https://doi.org/10.1063/1.2945000.

[144] C. Kittel. *Excitation of Spin Waves in a Ferromagnet by a Uniform rf Field.* Phys. Rev. **110**, 1295 (1958). https://doi.org/10.1103/PhysRev.110.1295.

[145] P. Bruno, Y. Suzuki, and C. Chappert. *Magneto-optical Kerr effect in a paramagnetic overlayer on a ferromagnetic substrate: A spin-polarized quantum size effect.* Phys. Rev. B **53**, 9214 (1996). https://doi.org/10.1103/PhysRevB.53.9214.

[146] J. Zak, E. Moog, C. Liu, and S. Bader. *Universal approach to magneto-optics.* J. Magn. Magn. Mater. **89**, 107 (1990). https://doi.org/10.1016/0304-8853(90)90713-Z.

[147] S. Bader. *SMOKE.* J. Magn. Magn. Mater. **100**, 440 (1991). https://doi.org/10.1016/0304-8853(91)90833-V.

[148] Z. Q. Qiu and S. D. Bader. *Surface magneto-optic Kerr effect.* Rev. Sci. Instrum. **71**, 1243 (2000). https://doi.org/10.1063/1.1150496.

[149] W. Zinth and U. Zinth. *Optik: Lichtstrahlen–Wellen–Photonen.* Oldenbourg Wissenschaftsverlag, München (2005).

[150] E. Hecht. *Optik.* Oldenbourg Wissenschaftsverlag, München (2005).

[151] K. K. Tikuišis, L. Beran, P. Cejpek, K. Uhlířová, J. Hamrle, M. Vaňatka, M. Urbánek, and M. Veis. *Optical and Magneto-Optical Properties of Permalloy Thin Films in 0.7–6.4 eV Photon Energy Range.* Mater. Design **114**, 31 (2017). https://doi.org/10.1016/j.matdes.2016.10.036.

[152] D. A. Allwood, G. Xiong, M. D. Cooke, and R. P. Cowburn. *Magneto-optical Kerr effect analysis of magnetic nanostructures.* J. Phys. D: Appl. Phys. **36**, 2175 (2003). https://doi.org/10.1088/0022-3727/36/18/001.

[153] J. McCord. *Progress in magnetic domain observation by advanced magneto-optical microscopy.* J. Phys. D: Appl. Phys. **48**, 333001 (2015). https://doi.org/10.1088/0022-3727/48/33/333001.

[154] F. Hoffmann. *Magnetic anisotropies of (Ga,Mn)As films and nanostructures.* Universität Regensburg, Dissertation (2010).

[155] K. Yamada, S. Kasai, Y. Nakatani, K. Kobayashi, H. Kohno, A. Thiaville, and T. Ono. *Electrical switching of the vortex core in a magnetic disk.* Nat. Mater. **6**, 270 (2007). https://doi.org/10.1038/nmat1867.

[156] L. Thomas and S. Parkin. *Current Induced Domain-Wall Motion in Magnetic Nanowires.* Wiley, New York (2008).

[157] G. Tatara, H. Kohno, and J. Shibata. *Microscopic approach to current-driven domain wall dynamics.* Phys. Rep. **468**, 213 (2008). https://doi.org/10.1016/j.physrep.2008.07.003.

[158] H. Min, R. D. McMichael, M. J. Donahue, J. Miltat, and M. D. Stiles. *Effects of Disorder and Internal Dynamics on Vortex Wall Propagation.* Phys. Rev. Lett. **104**, 217201 (2010). https://doi.org/10.1103/PhysRevLett.104.217201.

[159] H. T. Nembach, J. M. Shaw, C. T. Boone, and T. J. Silva. *Mode- and Size-Dependent Landau-Lifshitz Damping in Magnetic Nanostructures: Evidence for Nonlocal Damping*. Phys. Rev. Lett. **110**, 117201 (2013). https://doi.org/10.1103/PhysRevLett.110.117201.

[160] A. Aharoni. *Demagnetizing factors for rectangular ferromagnetic prisms*. J. Appl. Phys. **83**, 3432 (1998). https://doi.org/10.1063/1.367113.

[161] A. Vansteenkiste, B. Van de Wiele, M. Dvornik, R. Lassalle-Balier, and G. Rowlands. *mumax2*. http://code.google.com/p/mumax2 (2012).

[162] L. Thomas, R. Moriya, C. Rettner, and S. S. Parkin. *Dynamics of Magnetic Domain Walls Under Their Own Inertia*. Science **330**, 1810 (2010). https://doi.org/10.1126/science.1197468.

[163] J. Cho, N.-H. Kim, S. Lee, J.-S. Kim, R. Lavrijsen, A. Solignac, Y. Yin, D.-S. Han, N. J. J. van Hoof, H. J. M. Swagten, B. Koopmans, and C.-Y. You. *Thickness dependence of the interfacial Dzyaloshinskii-Moriya interaction in inversion symmetry broken systems*. Nat. Commun. **6**, 7635 (2015). https://doi.org/10.1038/ncomms8635.

[164] V. L. Zhang, K. Di, H. S. Lim, S. C. Ng, M. H. Kuok, J. Yu, J. Yoon, X. Qiu, and H. Yang. *In-plane angular dependence of the spin-wave nonreciprocity of an ultrathin film with Dzyaloshinskii-Moriya interaction*. Appl. Phys. Lett. **107**, 022402 (2015). https://doi.org/10.1063/1.4926862.

[165] M. Kostylev. *Interface boundary conditions for dynamic magnetization and spin wave dynamics in a ferromagnetic layer with the interface Dzyaloshinskii-Moriya interaction*. J. Appl. Phys. **115**, 233902 (2014). https://doi.org/10.1063/1.4883181.

[166] B. Heinrich, S. T. Purcell, J. R. Dutcher, K. B. Urquhart, J. F. Cochran, and A. S. Arrott. *Structural and magnetic properties of ultrathin Ni/Fe bilayers grown epitaxially on Ag(001)*. Phys. Rev. B **38**, 12879 (1988). https://doi.org/10.1103/PhysRevB.38.12879.

[167] F. C. Nörtemann, R. L. Stamps, R. E. Camley, B. Hillebrands, and G. Güntherodt. *Effective-medium theory for finite magnetic multilayers: Effect of anisotropy on dipolar modes*. Phys. Rev. B **47**, 3225 (1993). https://doi.org/10.1103/PhysRevB.47.3225.

[168] S. Rüegg, G. Schütz, P. Fischer, R. Wienke, W. B. Zeper, and H. Ebert. *Spin-dependent x-ray absorption in Co/Pt multilayers*. J. Appl. Phys. **69**, 5655 (1991). https://doi.org/10.1063/1.347926.

[169] S. Ferrer, J. Alvarez, E. Lundgren, X. Torrelles, P. Fajardo, and F. Boscherini. *Surface x-ray diffraction from Co/Pt(111) ultrathin films and alloys: Structure and magnetism*. Phys. Rev. B **56**, 9848 (1997). https://doi.org/10.1103/PhysRevB.56.9848.

[170] J. Geissler, E. Goering, M. Justen, F. Weigand, G. Schütz, J. Langer, D. Schmitz, H. Maletta, and R. Mattheis. *Pt magnetization profile in a Pt/Co bilayer studied by resonant magnetic x-ray reflectometry.* Phys. Rev. B **65**, 020405 (2001). https://doi.org/10.1103/PhysRevB.65.020405.

[171] M. Suzuki, H. Muraoka, Y. Inaba, H. Miyagawa, N. Kawamura, T. Shimatsu, H. Maruyama, N. Ishimatsu, Y. Isohama, and Y. Sonobe. *Depth profile of spin and orbital magnetic moments in a subnanometer Pt film on Co.* Phys. Rev. B **72**, 054430 (2005). https://doi.org/10.1103/PhysRevB.72.054430.

[172] T. Kuschel, C. Klewe, J.-M. Schmalhorst, F. Bertram, O. Kuschel, T. Schemme, J. Wollschläger, S. Francoual, J. Strempfer, A. Gupta, M. Meinert, G. Götz, D. Meier, and G. Reiss. *Static Magnetic Proximity Effect in Pt/$NiFe_2O_4$ and Pt/Fe Bilayers Investigated by X-Ray Resonant Magnetic Reflectivity.* Phys. Rev. Lett. **115**, 097401 (2015). https://doi.org/10.1103/PhysRevLett.115.097401.

[173] A. Vansteenkiste, J. Leliaert, M. Dvornik, M. Helsen, F. Garcia-Sanchez, and B. Van Waeyenberge. *The design and verification of MuMax3.* AIP Adv. **4**, 107133 (2014). https://doi.org/10.1063/1.4899186.

[174] Y. Sun, H. Chang, M. Kabatek, Y.-Y. Song, Z. Wang, M. Jantz, W. Schneider, M. Wu, E. Montoya, B. Kardasz, B. Heinrich, S. G. E. te Velthuis, H. Schultheiss, and A. Hoffmann. *Damping in Yttrium Iron Garnet Nanoscale Films Capped by Platinum.* Phys. Rev. Lett. **111**, 106601 (2013). https://doi.org/10.1103/PhysRevLett.111.106601.

[175] H. Yu, O. d'Allivy Kelly, V. Cros, R. Bernard, P. Bortolotti, A. Anane, F. Brandl, R. Huber, I. Stasinopoulos, and D. Grundler. *Magnetic thin-film insulator with ultra-low spin wave damping for coherent nanomagnonics.* Sci. Rep. **4**, 6848 (2014). https://doi.org/10.1038/srep06848.

[176] A. Talalaevskij, M. Decker, J. Stigloher, A. Mitra, H. S. Körner, O. Cespedes, C. H. Back, and B. J. Hickey. *Magnetic properties of spin waves in thin yttrium iron garnet films.* Phys. Rev. B **95**, 064409 (2017). https://doi.org/10.1103/PhysRevB.95.064409.

[177] T. Sebastian, Y. Ohdaira, T. Kubota, P. Pirro, T. Brächer, K. Vogt, A. A. Serga, H. Naganuma, M. Oogane, Y. Ando, and B. Hillebrands. *Low-damping spin-wave propagation in a micro-structured $Co_2Mn_{0.6}Fe_{0.4}Si$ Heusler waveguide.* Appl. Phys. Lett. **100**, 112402 (2012). https://doi.org/10.1063/1.3693391.

[178] M. Zhu, B. D. Soe, R. D. McMichael, M. J. Carey, S. Maat, and J. R. Childress. *Enhanced magnetization drift velocity and current polarization in $(CoFe)_{1-x}Ge_x$ alloys.* Appl. Phys. Lett. **98**, 072510 (2011). https://doi.org/10.1063/1.3554755.

[179] H. Yu, R. Huber, T. Schwarze, F. Brandl, T. Rapp, P. Berberich, G. Duerr, and D. Grundler. *High propagating velocity of spin waves and temperature*

dependent damping in a CoFeB thin film. Appl. Phys. Lett. **100**, 262412 (2012). https://doi.org/10.1063/1.4731273.

[180] S. Mankovsky, D. Ködderitzsch, G. Woltersdorf, and H. Ebert. *First-principles calculation of the Gilbert damping parameter via the linear response formalism with application to magnetic transition metals and alloys.* Phys. Rev. B **87**, 014430 (2013). https://doi.org/10.1103/PhysRevB.87.014430.

[181] M. A. W. Schoen, D. Thonig, M. L. Schneider, T. J. Silva, H. T. Nembach, O. Eriksson, O. Karis, and J. M. Shaw. *Ultra-low magnetic damping of a metallic ferromagnet.* Nat. Phys. **12**, 839 (2016). https://doi.org/10.1038/nphys3770.

[182] M. Schön. *Magnetic damping in binary 3-d transition metal alloys and multilayers.* Universität Regensburg, Dissertation (2017).

[183] M. Haertinger, C. H. Back, J. Lotze, M. Weiler, S. Geprägs, H. Huebl, S. T. B. Goennenwein, and G. Woltersdorf. *Spin pumping in YIG/Pt bilayers as a function of layer thickness.* Phys. Rev. B **92**, 054437 (2015). https://doi.org/10.1103/PhysRevB.92.054437.

[184] J. W. Shih. *Magnetic Properties of Iron-Cobalt Single Crystals.* Phys. Rev. **46**, 139 (1934). https://doi.org/10.1103/PhysRev.46.139.

[185] R. D. McMichael, D. J. Twisselmann, and A. Kunz. *Localized Ferromagnetic Resonance in Inhomogeneous Thin Films.* Phys. Rev. Lett. **90**, 227601 (2003). https://doi.org/10.1103/PhysRevLett.90.227601.

[186] G. Woltersdorf, F. Hoffmann, H. G. Bauer, and C. H. Back. *Magnetic homogeneity of the dynamic properties of (Ga,Mn)As films from the submicrometer to millimeter length scale.* Phys. Rev. B **87**, 054422 (2013). https://doi.org/10.1103/PhysRevB.87.054422.

[187] M. A. W. Schoen, J. M. Shaw, H. T. Nembach, M. Weiler, and T. J. Silva. *Radiative damping in waveguide-based ferromagnetic resonance measured via analysis of perpendicular standing spin waves in sputtered permalloy films.* Phys. Rev. B **92**, 184417 (2015). https://doi.org/10.1103/PhysRevB.92.184417.

[188] V. E. Demidov, S. O. Demokritov, K. Rott, P. Krzysteczko, and G. Reiss. *Linear and nonlinear spin-wave dynamics in macro- and microscopic magnetic confined structures.* J. Phys. D: Appl. Phys. **41**, 164012 (2008). https://doi.org/10.1088/0022-3727/41/16/164012.

[189] T. Mayer. *Magnetic damping in Cobalt-Iron alloys.* Universität Regensburg, Masterarbeit (2017).

[190] X. Xing and Y. Zhou. *Fiber optics for spin waves.* NPG Asia Mater **8**, e246 (2016). https://doi.org/10.1038/am.2016.25.

[191] W. Yu, J. Lan, R. Wu, and J. Xiao. *Magnetic Snell's law and spin-wave fiber with Dzyaloshinskii-Moriya interaction*. Phys. Rev. B **94**, 140410 (2016). https://doi.org/10.1103/PhysRevB.94.140410.

[192] P. Gruszecki, J. Romero-Vivas, Y. S. Dadoenkova, N. N. Dadoenkova, I. L. Lyubchanskii, and M. Krawczyk. *Goos-Hänchen effect and bending of spin wave beams in thin magnetic films*. Appl. Phys. Lett. **105**, 242406 (2014). https://doi.org/10.1063/1.4904342.

[193] P. Gruszecki, M. Mailyan, O. Gorobets, and M. Krawczyk. *Goos-Hänchen shift of a spin-wave beam transmitted through anisotropic interface between two ferromagnets*. Phys. Rev. B **95**, 014421 (2017). https://doi.org/10.1103/PhysRevB.95.014421.

[194] V. E. Demidov, S. O. Demokritov, D. Birt, B. O'Gorman, M. Tsoi, and X. Li. *Radiation of spin waves from the open end of a microscopic magnetic-film waveguide*. Phys. Rev. B **80**, 014429 (2009). https://doi.org/10.1103/PhysRevB.80.014429.

[195] T. Sebastian, T. Brächer, P. Pirro, A. A. Serga, B. Hillebrands, T. Kubota, H. Naganuma, M. Oogane, and Y. Ando. *Nonlinear Emission of Spin-Wave Caustics from an Edge Mode of a Microstructured $Co_2Mn_{0.6}Fe_{0.4}Si$ Waveguide*. Phys. Rev. Lett. **110**, 067201 (2013). https://doi.org/10.1103/PhysRevLett.110.067201.

[196] J.-V. Kim, R. L. Stamps, and R. E. Camley. *Spin Wave Power Flow and Caustics in Ultrathin Ferromagnets with the Dzyaloshinskii-Moriya Interaction*. Phys. Rev. Lett. **117**, 197204 (2016). https://doi.org/10.1103/PhysRevLett.117.197204.

[197] T. Brächer, O. Boulle, G. Gaudin, and P. Pirro. *Creation of unidirectional spin-wave emitters by utilizing interfacial Dzyaloshinskii-Moriya interaction*. Phys. Rev. B **95**, 064429 (2017). https://doi.org/10.1103/PhysRevB.95.064429.

[198] S. Neusser, G. Duerr, H. G. Bauer, S. Tacchi, M. Madami, G. Woltersdorf, G. Gubbiotti, C. H. Back, and D. Grundler. *Anisotropic Propagation and Damping of Spin Waves in a Nanopatterned Antidot Lattice*. Phys. Rev. Lett. **105**, 067208 (2010). https://doi.org/10.1103/PhysRevLett.105.067208.

[199] S. Neusser, H. G. Bauer, G. Duerr, R. Huber, S. Mamica, G. Woltersdorf, M. Krawczyk, C. H. Back, and D. Grundler. *Tunable metamaterial response of a $Ni_{80}Fe_{20}$ antidot lattice for spin waves*. Phys. Rev. B **84**, 184411 (2011). https://doi.org/10.1103/PhysRevB.84.184411.

[200] G. Duerr, K. Thurner, J. Topp, R. Huber, and D. Grundler. *Enhanced Transmission through Squeezed Modes in a Self-Cladding Magnonic Waveguide*. Phys. Rev. Lett. **108**, 227202 (2012). https://doi.org/10.1103/PhysRevLett.108.227202.

[201] K. Wagner, A. Kákay, K. Schultheiss, A. Henschke, T. Sebastian, and H. Schultheiss. *Magnetic domain walls as reconfigurable spin-wave nanochannels*. Nat. Nanotechnol. **11**, 432 (2016). https://doi.org/10.1038/nnano.2015.339.

[202] P. Gruszecki, M. Kasprzak, A. E. Serebryannikov, M. Krawczyk, and W. Śmigaj. *Microwave excitation of spin wave beams in thin ferromagnetic films*. Sci. Rep. **6**, 22367 (2016). https://doi.org/10.1038/srep22367.

[203] J. Xiao, A. Zangwill, and M. D. Stiles. *Boltzmann test of Slonczewski's theory of spin-transfer torque*. Phys. Rev. B **70**, 172405 (2004). https://doi.org/10.1103/PhysRevB.70.172405.

[204] R. D. McMichael, M. J. Donahue, D. G. Porter, and J. Eicke. *Comparison of magnetostatic field calculation methods on two-dimensional square grids as applied to a micromagnetic standard problem*. J. Appl. Phys. **85**, 5816 (1999). https://doi.org/10.1063/1.369929.

List of Abbreviations

ALD atomic layer deposition

BBO barium borate

BLS Brillouin light scattering

BV backward volume

CAIBE chemically assisted ion beam etching

CMOS complementary metal-oxide semiconductor

CPW coplanar waveguide

DE Damon-Eshbach

DMI Dzyaloshinskii-Moriya interaction

DW domain wall

EBL electron beam lithography

FMR ferromagnetic resonance

FV forward volume

ip in-plane

LLG Landau-Lifshitz-Gilbert

MBE molecular beam epitaxy

MOKE magneto-optical Kerr effect

MRAM magnetic random access memory

oop out-of-plane

PBC periodic boundary conditions

PMA perpendicular magnetic anisotropy

PSWS propagating spin wave spectroscopy

rf radio-frequency

SEM scanning electron microscopy

SHE spin Hall effect

SOC spin-orbit coupling

SQUID superconducting quantum interference device

STT spin-transfer torque

STXM scanning transmission X-ray microscopy

SW spin wave

TRMOKE time-resolved magneto-optical Kerr microscopy

VC vortex core

XPS X-ray photoelectron spectroscopy

YIG yttrium iron garnet

Acknowledgment

My big thanks go to the following persons:

Prof. Dr. Christian Back for the chance to do my PhD in his group on exciting and challenging topics in the hot research fields of magnonics and spintronics, for our fruitful discussions during the various projects I worked on as well as for giving me the opportunities to attend the summer school at the Radboud University and to present the results of our work on several conferences in Germany, Europe and the USA.

Dr. Jean-Yves Chauleau for familiarizing me with the TRMOKE setup, with the basics about SWs and with the myriads of challenging issues concerning the fabrication of well-performing samples, for his significant contributions to the implementation and analysis of the SW Doppler experiments, and for his never-ending positive attitude and motivation: "It is going in a good direction!". I enormously benefited from his support during my first year as a PhD student in the following years.

Hiroshi Hata, Takuya Taniguchi, and Dr. Takahiro Moriyama from the group of Prof. Dr. Teruo Ono at the Kyoto University, who were involved in the DMI project, for the fabrication of the multi-layered films and patterned samples and for the characterization of these using FMR and SQUID.

Hans Bauer for his profound answers to my various questions concerning SWs during my first year as a PhD student as well as for the many beneficial discussions we had about the evaluation and interpretation of experimental data and findings.

Johannes Stigloher for his support on the TRMOKE setup and his assistance on the TRMOKE measurements and on the evaluation of the resulting raw data using Python as well as for familiarizing me with the implementation of micromagnetic simulations using MuMax3.

Martin Decker for the many fruitful and profound discussions on the interpretation of experimental data and their verification by micromagnetic simulations as well as on crucial issues concerning different sample fabrication processes and steps.

Tobias Weindler for being my best buddy at the chair, with whom I spent countless hours not only in the clean room during sample fabrication, but also in the seminar room watching soccer matches.

Dr. Matthias Kronseder for the growth of the poly-crystalline $Co_{25}Fe_{75}$ full films in the metal MBE system.

Markus Härtinger, Martin Schön, Thomas Mayer, and Robert Islinger for the implementation and evaluation of the FMR measurements on the various magnetic samples.

Thomas Meier for the implementation and evaluation of the XPS measurements on the poly-crystalline $Co_{25}Fe_{75}$ full film.

All the other former and current group members who contributed to the nice atmosphere that made working at the chair a great pleasure.

Prof. Dr. Dieter Weiss for giving me the opportunity to use the different machines for sample fabrication and characterization in the labs and in the clean room at his chair.

Imke Gronwald for her assistance during certain steps in the sample fabrication process.

Markus Hollberger for his active support on keeping the SQUID almost continuously running throughout the past years as well as for his contributions and helping hands to the assembly and maintenance of the evaporation chamber.

Magdalena Pfleger, Sylvia Hrdina, Claudia Zange and Doris Meier for their assistance on all kind of administrative issues.

All the persons, who were involved in proof-reading (parts of) this thesis, for their valuable feedback, comments and suggested improvements.

Jana Nottensteiner for cheering me up with her loving and positive attitude whenever needed. Our relationship suffuses me with deep love, great pleasures, and the necessary diversion beyond work.

My family for their continuous support in all areas of life.

The financial support by the European Union via the European Research Council starting grant “ERC-2011-StG_20101014—ECOMAGICS” as well as by the Deutsche Forschungsgemeinschaft via the Collaborative Research Center “SFB 689—Spinphänomene in reduzierten Dimensionen” is gratefully acknowledged since fabricating samples and performing experiments would not be possible without a proper equipment in the various facilities.

List of Publications[127]

Covered in this thesis:

H. S. Körner, M. A. W. Schoen, T. Mayer, M. M. Decker, J. Stigloher, T. Weindler, T. N. G. Meier, M. Kronseder, and C. H. Back. *Magnetic damping in poly-crystalline $Co_{25}Fe_{75}$: Ferromagnetic resonance vs. spin wave propagation experiments*. Appl. Phys. Lett. **111**, 132406 (2017). https://doi.org/10.1063/1.4994137. [cf. Ch. 5]

H. S. Körner, J. Stigloher, and C. H. Back. *Excitation and tailoring of diffractive spin-wave beams in NiFe using nonuniform microwave antennas*. Phys. Rev. B **96**, 100401(R) (2017). https://doi.org/10.1103/PhysRevB.96.100401. [cf. Ch. 6]

H. S. Körner, J. Stigloher, H. G. Bauer, H. Hata, T. Taniguchi, T. Moriyama, T. Ono, and C. H. Back. *Interfacial Dzyaloshinskii-Moriya interaction studied by time-resolved scanning Kerr microscopy*. Phys. Rev. B **92**, 220413(R) (2015). https://doi.org/10.1103/PhysRevB.92.220413. [cf. Ch. 4]

J.-Y. Chauleau, H. G. Bauer, **H. S. Körner**, J. Stigloher, M. Härtinger, G. Woltersdorf, and C. H. Back. *Self-consistent determination of the key spin-transfer torque parameters from spin-wave Doppler experiments*. Phys. Rev. B **89**, 020403(R) (2014). https://doi.org/10.1103/PhysRevB.89.020403. [cf. Ch. 3]

Other contributions (while in Regensburg):

J. Stigloher, T. Taniguchi, **H. S. Körner**, M. Decker, T. Moriyama, T. Ono, and C. H. Back. *Observation of a Goos-Hänchen-like Phase Shift for Magnetostatic Spin Waves*. Phys. Rev. Lett. **121**, 137201 (2018). https://doi.org/10.1103/PhysRevLett.121.137201.

Johannes Stigloher, Takuya Taniguchi, Marco Madami, Martin Decker, **Helmut S. Körner**, Takahiro Moriyama, Gianluca Gubbiotti, Teruo Ono, and Christian H. Back. *Spin-wave wavelength down-conversion at thickness steps*. Appl. Phys. Express **11**, 053002 (2018). https://doi.org/10.7567/APEX.11.053002.

[127] Full record is available at https://orcid.org/0000-0001-8153-5610 or http://www.researcherid.com/rid/F-2299-2018.

L. Chen, S. Mankovsky, S. Wimmer, M. A. W Schoen, **H. S. Körner**, M. Kronseder, D. Schuh, D. Bougeard, H. Ebert, D. Weiss, and C. H. Back. *Emergence of anisotropic Gilbert damping in ultrathin Fe layers on GaAs(001).* Nat. Phys. **14**, 490 (2018). https://doi.org/10.1038/s41567-018-0053-8.

M. M. Decker, M. S. Wörnle, A. Meisinger, M. Vogel, **H. S. Körner**, G. Y. Shi, C. Song, M. Kronseder, and C. H. Back. *Time Resolved Measurements of the Switching Trajectory of* Pt/Co *Elements Induced by Spin-Orbit Torques.* Phys. Rev. Lett. **118**, 257201 (2017). https://doi.org/10.1103/PhysRevLett.118.257201.

A. Talalaevskij, M. Decker, J. Stigloher, A. Mitra, **H. S. Körner**, O. Cespedes, C. H. Back, and B. J. Hickey. *Magnetic properties of spin waves in thin yttrium iron garnet films.* Phys. Rev. B **95**, 064409 (2017). https://doi.org/10.1103/PhysRevB.95.064409.

J. Stigloher, M. Decker, **H. S. Körner**, K. Tanabe, T. Moriyama, T. Taniguchi, H. Hata, M. Madami, G. Gubbiotti, K. Kobayashi, T. Ono, and C. H. Back. *Snell's Law for Spin Waves.* Phys. Rev. Lett. **117**, 037204 (2016). https://doi.org/10.1103/PhysRevLett.117.037204.

Joachim Hubmann, Benedikt Bauer, **Helmut S. Körner**, Stephan Furthmeier, Martin Buchner, Günther Bayreuther, Florian Dirnberger, Dieter Schuh, Christian H. Back, Josef Zweck, Elisabeth Reiger, and Dominique Bougeard. *Epitaxial Growth of Room-Temperature Ferromagnetic MnAs Segments on GaAs Nanowires via Sequential Crystallization.* Nano Lett. **16**, 900 (2016). https://doi.org/10.1021/acs.nanolett.5b03658.

Quirin M. Kainz, Soraia Fernandes, Corina M. Eichenseer, Francesca Besostri, **Helmut Körner**, Rainer Müller, and Oliver Reiser. *Synthesis of functionalized, dispersible carbon coated cobalt nanoparticles for potential biomedical applications.* Faraday Discuss. **175**, 27 (2014). https://doi.org/10.1039/C4FD00108G.

G. Woltersdorf, J. Stigloher, **H. S. Körner**, F. Hoffmann, M. Kiessling, V. Novak, J.-Y. Chauleau, and C. H. Back. *Spatial constraints on the source of uniaxial anisotropy in (Ga,Mn)As films.* J. Phys. D: Appl. Phys. **47**, 195001 (2014). https://doi.org/10.1088/0022-3727/47/19/195001.